

CARDIFF
UNIVERSITY

PRIFYSGOL
CAERDYDD

Acknowledgements

There is a multitude of ways by which people during the completion of this PhD

I would like to thank my mother and father for their support and for looking after me along the way. I very much appreciate the many and thank you for your love

Experimental and numerical study of the fracture and self-healing of cementitious materials

Christopher Joseph

MEng (Hons.)

Submitted for the degree of Doctor of Philosophy

School of Engineering

Cardiff University, UK

October 2008

UMI Number: U585302

All rights reserved

INFORMATION TO ALL USERS

The quality of this reproduction is dependent upon the quality of the copy submitted.

In the unlikely event that the author did not send a complete manuscript and there are missing pages, these will be noted. Also, if material had to be removed, a note will indicate the deletion.



UMI U585302

Published by ProQuest LLC 2013. Copyright in the Dissertation held by the Author.
Microform Edition © ProQuest LLC.

All rights reserved. This work is protected against
unauthorized copying under Title 17, United States Code.



ProQuest LLC
789 East Eisenhower Parkway
P.O. Box 1346
Ann Arbor, MI 48106-1346

Acknowledgements

I have been assisted in a multitude of ways by many people during the completion of this PhD thesis.

I would like to thank my mother and father for bringing me into this world and for looking after me along the way. I very much appreciate the moral and financial support that you have given me throughout the course of my academic studies.

I would like to acknowledge Tony Jefferson, Bhushan Karihaloo, Bob Lark, and the School of Engineering for providing me with the financial support to embark on this path of discovery. I would sincerely like to thank Tony for his unwavering support and continued faith in my ability to complete this project.

I would also like to thank the laboratory technical staff, Des, Carl, Brian, and Len and graduates Mauro and Ben for their assistance with the self-healing experimental work.

I am also indebted to my friends old and new within the department who have joined me in the good times and supported me through the 'not so good' times. Terry, Xiao, Pat, Reza, Rami, Laura, Phil and Tim, I am very grateful for your friendship over the years. In addition, I would like to acknowledge the support provided by my wider circle of friends and family as well as the boundless mettā offered by the Sangha of the Cardiff Buddhist centre. I am eternally grateful to you all.

Finally, I would like to thank my wife, Sharon, for her unconditional love and support over the 12 years that I have known her, and for producing (with a little help) our son, Aled. The unbounded energy with which he lives his life has been a true inspiration to me during the completion of this thesis, which in his own words was 'hard to do'! His extensive experimental programmes on the fracture toughness of ceramics and glass, and fatigue testing of door hinges, augurs well for his own scientific development! This thesis is therefore dedicated to my son Aled.

Summary

This thesis presents details of an experimental and numerical programme of study undertaken on the fracture and self-healing of cementitious materials at Cardiff University.

The experimental component reported in the thesis consists of an extensive programme of tests conducted on reinforced mortar specimens, autonomically healed with a low viscosity cyanoacrylate adhesive. The development of the self-healing experimental procedure is explained and results of a series of three point bending tests are presented. These examine the effect of reinforcement, pre-notching, and rate of loading, on the healing performance of the beams. Both primary and secondary healing behaviour was observed during the first and second loading cycles, respectively.

The numerical component of this thesis describes development work undertaken on the discrete lattice beam modelling method. The aim of these developments is to improve the quantitative aspects of the model, including mesh orientation and size dependency, and over-brittleness of the force-displacement response. The orientation effect of the lattice is discussed and various failure criteria which minimise, or omit, this effect are presented and compared. The effect of mesh size (lattice resolution) on the specific fracture energy is also examined. A new regularisation method, which is based on the application of statistical distributions of beam strengths that are linked to the beam length, is presented. This method is shown to significantly improve the objectivity of the force-displacement results, whilst maintaining the qualitative ability to capture the main phases of crack formation, namely; macrocrack growth, crack branching and bridging.

In the final chapter the lattice method is used to simulate the self-healing response observed during the experiments. The method was found to be capable of capturing realistic pre- and post-healing fracture patterns, in addition to the stiffness increase observed during primary healing, which occurs shortly after the release of adhesive from the glass supply tubes.

Symbols and abbreviations

The following symbols and abbreviations are used in this thesis:

A	cross-sectional area of beam
A_{ξ}	axial area of beam
A_{η}	shear area of beam
a_p	percolation limit
b, t	breadth (thickness) of beam
b	width of crack plane opening
b_0	crack opening at the bottom of the cavity
b_h	crack opening at the top of the cavity
\mathbf{C}	elastic plane stress compliance matrix
c_l	exponential softening curve coefficient
D_{max}, D_{min}	maximum and minimum aggregate particle size
E	Young's modulus
E_b	Young's modulus of beam
E_c	Young's modulus of continuum
F	axial force
F_{ξ}	local axial force in beam
f_{cu}	cube strength (100mm cubes)
\mathbf{F}_L	local force vector for beam
f_{split}	splitting tensile strength (100mm ϕ , 200mm long cylinders)
f_t	tensile strength of material
f_{tb}	tensile strength of beam
F_{η}	local shear force in beam
g	gravitational constant
G_f	specific fracture energy
h	height of beam
I	second moment of area
\mathbf{k}, \mathbf{k}_e	element stiffness matrix
\mathbf{K}_{CR}	global stiffness matrix stored in compressed row format
\mathbf{k}_L	local stiffness matrix of element
l	length of beam
M	bending moment
\mathbf{M}	Jacobian preconditioning matrix
m	Weibull constant
N	total number of beams in lattice

n	total number of beams in an RME
n_p	number of beam with strengths from lower strength distribution
n_ω	number of broken beams in RME at failure (i.e. $\omega=1$)
p_c	capillary potential
P_k	prescribed aggregate content
P_{pre}	prescribed load
Q, V	shear force
r_{eff}	relative effective stress ($=\sigma_{eff}/f_{tb}$)
s_ξ	local axial stress in beam
s_η	local shear stress in beam
\mathbf{T}_σ	stress transformation matrix
tn	scaled total force norm.
u	displacement
u_ξ, u_η	local displacements of beam
u_0	crack opening at failure
\mathbf{u}_L	local displacement vector for beam
u_p	prescribed displacement
$u_{x/l}, u_{y/l}$	displacements at end of beam
W	elastic section modulus ($=bh^2/6$)
z	distance of fluid front from reservoir
α, β, α_s	scaling factors in failure criteria
α	orientation of local element axes
α_l	orientation of principal stress axes
α_s	shear area correction factor
β_1, β_2	axial and shear stress correction factors
γ	surface tension of the fluid
γ_{xy}	engineering shear strain
ε	effective strain
$\varepsilon_{\xi\xi}, \varepsilon_{\eta\eta}, \gamma_{\xi\eta}$	local strain components of beam
ζ_j	beam strain
θ	angle that the meniscus forms with the face of the crack
θ	orientation of principal axes
λ	non-dimensional lattice size
μ	M-C shear/normal strength ratio
μ	viscosity of fluid
ν	Poisson's ratio
ρ	residual effective energy

ρ	density of liquid
σ_{eff}	effective stress in beam
σ_I, σ_{II}	major and minor principal stresses
τ	shear stress
ϕ	inclination angle of capillary or crack
φ_1, φ_2	rotations at end of beam
ω	rotation tensor
ω, ω	damage parameter or tensor
<i>AAR</i>	aggregate alkaline reaction
<i>CG</i>	conjugate gradient
<i>CMOD</i>	crack mouth opening displacement
<i>CPU</i>	central processing unit
<i>CR</i>	compressed row
<i>C-S-H</i>	calcium silica hydrates
<i>CSL</i>	confined shear lattice
<i>DEM</i>	discrete element model
<i>DEN</i>	double edge notched
<i>DTI</i>	Department of Trade and Industry, U.K.
<i>ECC</i>	engineered cementitious composite
<i>FE</i>	finite element
<i>fpz</i>	fracture process zone
<i>GUI</i>	graphical user interface
<i>hcp</i>	hardened cement paste
<i>ITZ</i>	interfacial transition zone
<i>LEFM</i>	linear elastic fracture mechanics
<i>LVDT</i>	linear variable differential transducer
<i>M-C</i>	Mohr-Coulomb
<i>NDT</i>	non-destructive testing
<i>PCA</i>	Portland cement association
<i>RBSM</i>	rigid body spring model
<i>RFM</i>	random fuse model
<i>RILEM</i>	Réunion Internationale des Laboratoires d'Essais et de Recherches sur les Matériaux et les Constructions.
<i>RME</i>	representative material element
<i>RVE</i>	representative volume element
<i>SEM</i>	scanning electron microscope
<i>SH</i>	self-healing
<i>XFEM</i>	extended finite element model

Contents

CHAPTER 1	INTRODUCTION	1
1.1	CEMENTITIOUS MATERIALS	1
1.2	DURABILITY ISSUES	2
1.3	INSPECTION, MAINTENANCE AND REPAIR OF CONCRETE STRUCTURES	3
1.4	MOTIVATION FOR THE RESEARCH	4
1.4.1	Development of self-healing cementitious materials	4
1.4.2	Numerical modelling	6
1.5	SCOPE AND OBJECTIVES OF THE RESEARCH	6
1.6	OUTLINE OF THE THESIS	7
CHAPTER 2	STATE OF THE ART REVIEW	9
2.1	INTRODUCTION	9
2.1.1	Definition of terms	9
2.1.2	Addressing the durability issues of concrete through advanced material science	12
2.2	AUTONOMIC HEALING OF POLYMERS	12
2.2.1	The self-healing concept in polymers	13
2.2.2	The technology of self-healing in polymers	14
2.2.3	Mechanical response of self-healed specimens	16
2.3	SELF-HEALING OF CEMENTITIOUS COMPOSITES	18
2.3.1	Autogenic healing of cementitious composites	19
2.3.2	Autonomic healing of cementitious composites	20
2.3.3	Mechanical response of self-healed specimens	25
2.4	MODELLING THE SELF-HEALING PROCESS	30
2.5	NUMERICAL MODELLING OF FRACTURE IN CEMENTITIOUS MATERIALS	33
2.5.1	Introduction	33
2.5.2	Continuum finite element modelling	33
2.5.3	Discrete lattice modelling	38
2.6	CONCLUSIONS	42
2.6.1	Self-healing materials - Blue sky or pie in the sky?	42
2.6.2	Modelling autonomic healing in concrete	44
CHAPTER 3	LATTICE BEAM MODELLING – <i>THE FUNDAMENTALS</i>	46
3.1	INTRODUCTION	46
3.1.1	Historical development	46

3.1.2	Basic concept	47
3.2	LATTICE CONFIGURATION	49
3.3	LATTICE ELEMENT	51
3.3.1	Element type	51
3.3.2	FE formulation	53
3.3.3	Element geometry	54
3.4	REPRESENTING HETEROGENEITY.....	56
3.4.1	Particle overlay method	57
3.4.2	Statistical distributions of beam strengths.....	59
3.5	FAILURE CRITERIA	61
3.6	DAMAGE EVOLUTION	63
3.7	CURRENT LIMITATIONS	64
3.7.1	Computational demand	64
3.7.2	Mesh orientation dependency	64
3.7.3	Mesh size dependency	66
3.7.4	Over-brittleness.....	68
3.8	CONCLUSIONS.....	69
CHAPTER 4	COMPUTATIONAL IMPLEMENTATION	71
4.1	INTRODUCTION	71
4.2	PRE-PROCESSOR.....	71
4.2.1	Main features.....	71
4.2.2	Particle overlay implementation	72
4.2.3	Statistical distribution of beams strengths implementation.....	73
4.3	FE CODE.....	74
4.3.1	Overview	74
4.3.2	Compressed row storage	75
4.3.3	Conjugate gradient solver	76
4.4	POST-PROCESSOR.....	78
4.5	SUMMARY AND CONCLUSIONS	79
CHAPTER 5	FAILURE CRITERIA DEVELOPMENT.....	81
5.1	INTRODUCTION	81
5.2	EXISTING FAILURE CRITERIA	82
5.3	MOHR-COULOMB BASED FAILURE CRITERIA	83
5.3.1	Continuum equivalence and isotropy of the Mohr-Coulomb failure criterion.....	85
5.4	PRINCIPAL STRESS BASED FAILURE CRITERION	97

5.4.1	Matching strains in plane beams	97
5.4.2	Failure criterion development	100
5.4.3	Continuum equivalence and isotropy of the principal stress failure criterion.....	101
5.5	FURTHER FAILURE CRITERIA CONSIDERATIONS	105
5.5.1	Mohr-Coulomb criterion based on continuum stresses.....	105
5.5.2	Modified Mohr-Coulomb criterion based on continuum stresses.....	106
5.5.3	Modified Mohr-Coulomb criterion based on beam stresses	106
5.6	STRAIN ENERGY EQUIVALENCE.....	108
5.7	SUMMARY AND COMPARISON OF DIFFERENT FAILURE CRITERIA.....	111
5.8	CONCLUSIONS AND FUTURE WORK	122
CHAPTER 6	STOCHASTIC REGULARISATION OF LATTICE MODELLING	124
6.1	INTRODUCTION	124
6.2	MESH SIZE DEPENDENCY	124
6.3	OPTIONS FOR REGULARISATION	130
6.4	1D PARALLEL BAR MODEL.....	133
6.5	2D LATTICE MODEL WITHOUT MESOSTRUCTURE	136
6.6	RME (REPRESENTATIVE MATERIAL ELEMENT).....	138
6.7	DOUBLE STRENGTH DISTRIBUTION OVER AN RME	139
6.8	PERCOLATION LIMIT	140
6.9	OBJECTIVITY OF DOUBLE STRENGTH DISTRIBUTION	142
6.10	CONCLUSIONS AND FUTURE WORK	147
CHAPTER 7	EXPERIMENTAL STUDY ON SELF-HEALING CEMENTITIOUS MATERIALS	150
7.1	INTRODUCTION	150
7.2	PRELIMINARY INVESTIGATIONS	151
7.2.1	Healing agent	151
7.2.2	Encapsulation method	153
7.2.3	Cementitious matrix.....	154
7.2.4	Reinforcement.....	155
7.2.5	Summary of preliminary investigation work	155
7.3	EXPERIMENTAL PROCEDURE	158
7.3.1	Programme of study	158
7.3.2	Specimen preparation procedure.....	161
7.3.3	Testing procedure.....	162
7.4	RESULTS AND DISCUSSION	164

7.4.1	Typical healing response.....	164
7.4.2	Effect of reinforcement level	167
7.4.3	Effect of loading rate.....	168
7.4.4	Effect of pre-notching	170
7.4.5	Effect of specimen age	171
7.4.6	Qualitative results	172
7.5	CONCLUSIONS AND FUTURE WORK	176
CHAPTER 8 MODELLING OF SELF-HEALING CEMENTITIOUS MATERIALS		179
8.1	INTRODUCTION	179
8.2	LATTICE MODELLING OF THE SELF-HEALING PROCESS	179
8.2.1	Healing algorithm in 1D	180
8.2.2	Extension of healing algorithm to 2D	182
8.2.3	Glue flow theory	183
8.3	2-D MODELLING EXAMPLE	187
8.4	CONCLUSIONS AND FUTURE WORK	193
CHAPTER 9 CONCLUSIONS AND FUTURE OUTLOOK.....		195
REFERENCES.....		200
APPENDIX A – DATA SHEET FOR RITE-LOK EC5 CYANOACRYLATE		211
APPENDIX B – SELF-HEALING EXPERIMENTAL RESULTS		213

Chapter 1

Introduction

1.1 Cementitious materials

The Romans used pozzolanic materials such as quicklime, volcanic ash and pumice to create pozzolanic mortars. This was then mixed with aggregate to form concrete, which was used in many structures including the domed roof of the Pantheon in Rome. It was not until the discovery of Portland cement in the middle of the nineteenth century, however, that the use of concrete as a building material accelerated. Today, cementitious materials including mortar and concrete are the most commonly used man made materials on the planet. Cement is used to make approximately 2.5 metric tonnes (over one cubic metre) of concrete per person alive per year (van Oss, 2005).

Concrete is a truly multiscale material, containing hydration products such as calcium-silica-hydrates (C-S-H) at the nanoscale, cement particles at the microscale, and aggregate at the mesoscale. In addition, it is a heterogenic material which behaves isotropically in the case of plain concrete and anisotropically when reinforced with steel.

The compressive strength of concrete may vary between 20 and 60MPa for traditional concrete, although strengths of up to 200MPa have been achieved with the use of special additives and compaction techniques. Cementitious materials including concrete are, however, quasi-brittle in nature. This means that whilst they are relatively strong in compression, they are relatively weak in tension. The tensile strength of concrete is usually about 10 times less than its compressive strength. In order to account for the relatively low tensile strength of concrete, most structures are reinforced with steel reinforcing bars. Nevertheless, before the tensile strength of the steel can be utilised in a reinforced member the concrete must crack up to the level of the reinforcement. In addition to cracking caused by structural loading, other more common causes of cracking include plastic shrinkage, drying shrinkage, and thermal effects as illustrated in Figure 1.1.



(a)



(b)

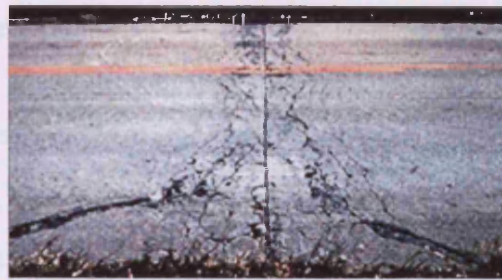


(c)

Figure 1.1. Common causes of cracking in concrete: (a) Plastic shrinkage; (b) Drying shrinkage, and (c) Thermal effects (PCA, 2008)

1.2 Durability issues

Whilst cracking of concrete, especially microcracking, is extremely common, and is not classed as 'failure', it invariably leads to an increase in the number of pathways open to the ingress of saline water, acid rain, and carbon dioxide. Depending on the type of concrete, the environmental conditions and the chemical makeup of the infiltrating fluid, various degrading processes can occur which cause further cracking and substantially reduce the durability of the structure. These processes include freeze-thaw action, aggregate alkaline reaction, and reinforcement corrosion, as illustrated in Figure 1.2. In addition to reducing the structural integrity of the concrete, cracking is aesthetically unsightly and also increases the porosity of the material, thus potentially compromising the water tightness of the concrete that the structure is formed from. This is a very important requirement for water retaining structures such as dams and storage tanks, but also for other critical housing facilities such as nuclear reactors and disposal facilities for radioactive waste.



(a)



(b)



(c)

Figure 1.2. Common accelerated effects of cracking in concrete: (a) Freeze-thaw action; (b) Aggregate alkaline reaction (AAR), and (c) Reinforcement corrosion (PCA, 2008)

1.3 Inspection, maintenance and repair of concrete structures

The durability problems associated with concrete structures are currently addressed through regular monitoring and maintenance programmes. Currently, maintenance work on concrete structures generally relies on regular inspection programmes, which are expensive, and depend on a combination of non destructive testing (NDT) and human perception. As discussed by Kessler et al. (2003), NDT can offer some degree of accuracy, however, human perception, due to its very nature can include a large degree of subjectivity. In addition, these inspection programmes are costly, both in terms of time and money, since a high degree of training and expertise is generally required to complete the inspection and interpret the results. It is also worth noting that NDT may not always produce conclusive results, hence intrusive, or partially destructive testing, such as core drilling may be required. Core drilling, and the subsequent testing of cores, is generally used in order to investigate suspected large internal defects that NDT, such as acoustic emissions analysis, may highlight. However, such activities may well compromise the integrity of the structure.

The periodic nature of inspection programmes also means that the occurrence of structural defects will only be addressed, at the earliest, during the next scheduled inspection. Thus, the regularity of inspections is usually related to the risk associated with failure of the structure,

both in respect to serviceability and ultimate criteria. The concept of continual ‘health monitoring’ of structures through the use of real-time sensors connected to centralised computers is therefore appealing (Mihashi et al., 2000).

The repair methods, which have been used to date, include techniques such as resin or grout injection into macro cracks, bolting or gluing fibre reinforced strips to the tension face, ‘remove and replace’ techniques for parts of members, or in the most severe cases, replacement of structural members in their entirety. As noted by Kessler et al. (2003), access to the structure, in order to inspect and, if necessary, complete remedial works, may be difficult, if not hazardous. There are, in fact, many examples of structures, in which thorough inspection is extremely difficult, if not practically impossible e.g. buried concrete pipes, nuclear reactor chambers, waste disposal facilities, undersea structures, buried foundations etc. Even if continuous, automated inspection of such structures (as discussed above) were installed, subsequent remediation of identified defects would remain a significant problem.

1.4 Motivation for the research

1.4.1 Development of self-healing cementitious materials

The financial cost of traditional monitoring and maintenance programmes, as described above, is very large. Figure 1.3 illustrates the annual expenditure in billions of pounds (relative to 2000 prices) on construction work in the UK between 1995 and 2005. It can be seen that repair and maintenance costs account for over 45% of the total expenditure on construction, of which concrete structures form a large proportion.

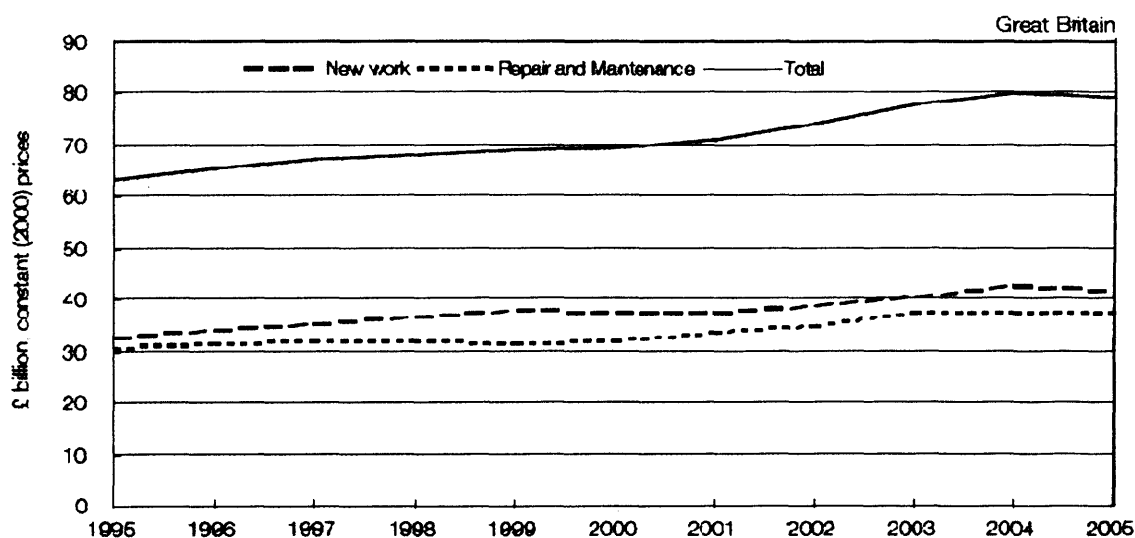


Figure 1.3. Billions of pounds spent on repair and maintenance and new construction work in Great Britain between 1995 and 2005 (DTI, 2006).

These issues are not just confined to the United Kingdom. In the USA, the annual maintenance cost for bridges is estimated at \$5.2 billion, and the cost for bridge reconstruction is estimated to be between \$20 billion and \$200 billion (Yunovich and Thompson, 2003). In addition, as discussed by Freyermuth (2001), comprehensive life cycle analyses indicate that the indirect costs due to traffic jams and associated loss of productivity are more than 10 times the direct cost of maintenance and repair.

As well as financial penalties, poor durability of concrete, which causes the need for the refurbishment or even complete replacement of structures, also has a significant environmental impact. The production of 1 tonne of Portland cement, for example, produces approximately 1 tonne of CO₂ when the emissions due to calcination and fuel combustion required to power the kiln are both taken into account (van Oss, 2005). Considering that about 2.35×10^9 tonnes of cement are used annually worldwide, the CO₂ emissions associated with the production of cement are very significant, and are estimated to be in the order of 5 - 7% of the total CO₂ production in the world.

In order to enhance the durability of our built infrastructure, and reduce mankind's impact on the stability of the biosphere, material scientists have recently turned their attention towards the creation of smarter materials that have the ability to adapt to their environment. Researchers have therefore begun to challenge the traditional and long established view that structural materials should be designed to pre-defined specifications and are assumed to meet these specifications throughout the lifetime of the structure. In practice, not only do the external demands on such materials invariably change over time, but the materials ability to meet these demands often diminishes. Significant evidence of such developments was evident recently, at the first international conference on self-healing materials which was held in the Netherlands during April 2007. This conference was also succeeded by the first book devoted solely to self-healing materials (van der Zwaag, 2007). Examples of these 'smarter' materials include smart coatings which are able to heal scratches, autonomic healing of polymers and bacterial enhanced autogenous healing in concrete. Many researchers are gaining the inspiration for the development of these sophisticated materials from nature e.g. blood supply system in humans, water uptake mechanisms in plants and trees, and bone healing in mammals. These materials are, therefore, often referred to as bio-mimetic materials.

In concrete, early research in this self-healing area has focused on both the natural ability of hydrates to heal cracks over time, and artificial means of crack repair from adhesive reservoirs embedded within the matrix. It is the latter concept that is investigated in this thesis. The

motivation for developing this self-healing cementitious material is therefore to achieve a material with improved durability and service life and reduced lifetime costs, both in terms of money and environmental impact.

1.4.2 Numerical modelling

“How does a heterogeneous solid break when an externally applied displacement is slowly increased?” (Herrmann et al., 1989).

This is a question postulated by Hans Herrmann, Alex Hansen, and Stephane Roux almost 20 years ago. It is a question, however, that has pre-occupied the minds of mathematicians, material scientists, and engineers alike many years prior to, and since, the publication of this paper. Therefore, in relation to heterogeneous solid materials such as concrete, the question stated above should now be extended to include the words: “...and how does a partially damaged heterogeneous material recover its physical properties over time, when subjected to a self-healing process?”

The motivation for the development of the modelling work presented in this thesis is therefore to complement the observations made during the experimental programme, and to begin to shed some light on the answer to this question, particularly in respect to the autonomic adhesive based healing of cementitious materials.

A suitable modelling approach should be capable of:

- Capturing the heterogeneity of the cementitious material.
- Predicting realistic crack patterns for given boundary conditions.
- Predicting a realistic constitutive response which is objective.
- Capturing the primary physical aspects of the self-healing process in a simple way.

1.5 Scope and objectives of the research

The scope and objectives of the research presented in this thesis are to:

1. Undertake novel autonomic healing experiments to better understand the kinematics of the healing process, and to obtain reliable data on the mechanical properties of the healed material for the development of numerical models;
2. Improve the quantitative abilities of the discrete lattice beam modelling method in respect to modelling the damage of cementitious materials, and;

3. Model the fracture and autonomic healing process within cementitious materials using the discrete lattice beam modelling method.

1.6 Outline of the thesis

This thesis is divided into 9 chapters with 2 appendices. Chapter 2 describes the recent state of the art developments that have occurred in the field of self-healing materials with specific focus given to applications in cementitious materials. The use of modelling techniques applied to self-healing materials and cementitious materials in general is also discussed, and the main differences between continuum and discrete approaches are highlighted.

Chapter 3 focuses specifically on the fundamental aspects of the discrete lattice beam modelling method, including the mesh geometry, element type and failure criteria. The main advantages of the method are presented together with an appraisal of its current limitations. In Chapter 4 a brief overview of the computational implementation of the lattice method is presented, with specific attention being given to the issue of computational efficiency. Details are presented of the pre and post processor programs in addition to the main finite element code, all of which have been developed as part of this thesis.

A detailed investigation of the most appropriate failure criterion to be used in the lattice model is then presented in Chapter 5. A theoretical framework based on the equivalence between the discrete lattice and the underlying continuum is formulated. This is then used to investigate the isotropic properties of various failure criteria, which are partly responsible for the mesh orientation dependency of the method. The influence that the choice of failure criterion has on the fracture pattern and force-displacement response for a lattice simulation is also investigated.

The mesh size dependency of the lattice modelling method is discussed in chapter 6. A regularisation procedure based on a statistical distribution of beam strengths that are linked to the element length is then proposed and evaluated.

Chapter 7 presents the body of experimental work completed at Cardiff on adhesive based self-healing of cementitious materials. The findings from the initial investigations and the development of the current experimental procedure are described. The results of several series of three-point beam bending experiments are then presented and discussed.

Finally, the application of the discrete lattice beam method to the modelling of the self-healing process in cementitious materials is presented in chapter 8, and some general conclusions and an outlook towards future research in this area is presented in chapter 9.

Chapter 2

State of the art review

2.1 Introduction

This state of the art review investigates the current situation in relation to the development of self-healing materials within the construction and manufacturing industries. Particular focus has been placed on the process of autonomic healing and its associated technology. The application of this technology to both cementitious materials and polymeric materials has been considered. This is because a far larger body of research has been completed on the autonomic healing of polymeric materials, and therefore, this offers potential opportunity for technology transfer between the different material types.

A summary of the limited numerical modelling work which has been undertaken to date on self-healing polymeric and cementitious materials is discussed. In section 2.5 a brief overview is also given of the far larger body of work that has been completed on the modelling of fracture in cementitious materials. The purpose of this overview is to identify an appropriate numerical technique for capturing the primary mechanisms occurring in the experimental self-healing work presented later in this thesis.

2.1.1 Definition of terms

There are many terms which are being used within the literature to describe the development of new composite materials designed to possess some 'higher-order' function. There is some ambiguity regarding the definition of these terms, however, as reported by Joseph and Jefferson (2006a), Mihashi et al. (2000) and Sharp and Clemeña (2004) give some insight to their meaning, and attempt to differentiate between them.

2.1.1.1 *Intelligent materials*

Intelligent materials, as defined by Mihashi et al. (2000), are materials which 'incorporate the notion of information as well as physical indexes such as strength and durability'. This higher

level function or 'intelligence' is achieved through the systematic corporation of various individual functions. As a result, intelligent materials exhibit a self-control capability whereby they are not only able to sense and respond to various external stimuli, but conduct this response in a regulated manner. This is analogous to the behaviour exhibited by many natural materials such as skin, bone, and tendons. Schmets (2003) identifies this inherent 'intelligent' adaptability of natural materials, and states that their outstanding mechanical properties are a consequence of their highly organised hierarchical structure, which is omnipresent at all levels (length scales) of the material.

Given their complexity, it is not surprising that such materials are currently not used in practice. The development of man made intelligent materials are still largely at the conceptual and early design stages, and are confined mainly to the fields of medicine, bionics, and aeronautics/astronautics.

2.1.1.2 Smart materials

Smart materials, on the other hand, are engineered materials which are able to provide a unique beneficial response when a particular change occurs in its surrounding environment (Sharp and Clemena, 2004). Examples of smart materials include piezoelectric materials, magnetostrictive materials, shape memory materials, temperature-responsive polymers which are able to change colour with temperature, and smart gels which are able to shrink or swell by factors of up to 1000 in response to chemical or physical stimuli. The difference between a smart material and an intelligent material is therefore defined by the degree to which the material can gather information, process this information and react accordingly.

2.1.1.3 Smart structures

Smart structures differ from smart materials, in that they are engineered composites of conventional materials, which exhibit sensing and actuation properties, due to the properties of the individual components.

2.1.1.3.1 Self-healing materials

Many self-healing materials fall into the category of smart structures, since they contain encapsulated healing agents which are released when damage occurs, thereby 'healing' the 'injury', and increasing the materials' functional life.

Self-healing studies have been performed on polymers, coatings, and composites (inc. concrete), however, all of these 'structures' rely on previous knowledge of the damage

mechanisms to which they are susceptible, and are therefore classed as smart rather than intelligent. Self-healing polymers and cementitious composites are discussed at greater length in sections 2.2 and 2.3, respectively.

2.1.1.3.2 *Autonomic and autogenic healing*

A composite material which exhibits self-healing capabilities due to the release of encapsulated resins or glues, as a result of cracking from the onset of damage, is categorised as having autonomic healing properties.

If the healing properties of a material are generic to that material, then the material could potentially be classed as a smart material, and the healing process is termed autogenic healing. Cementitious materials have this innate ability to self-repair, since re-submersion of a concrete specimen in water, can serve to kick-start the hydration process, when the water reacts with pockets of unhydrated cement in the matrix.

2.1.1.3.3 *Passive and active modes*

Smart self-healing structures may also be classified depending on the passive or active nature of their healing abilities. A passive mode smart structure has the ability to react to an external stimulus without the need for human intervention, whereas an active mode smart structure requires intervention in order to complete the healing process. Both systems have been tested, in respect to concrete by Dry (1994), and are illustrated in Figures 2.1 and 2.2.

A fully passive release system draws its main benefits from the omission of the need for human inspection, repair and maintenance. The requirement for human intervention in an active mode system, nonetheless, allows for a larger degree of control to be exercised, and is thus likely to inspire greater confidence within the end user.

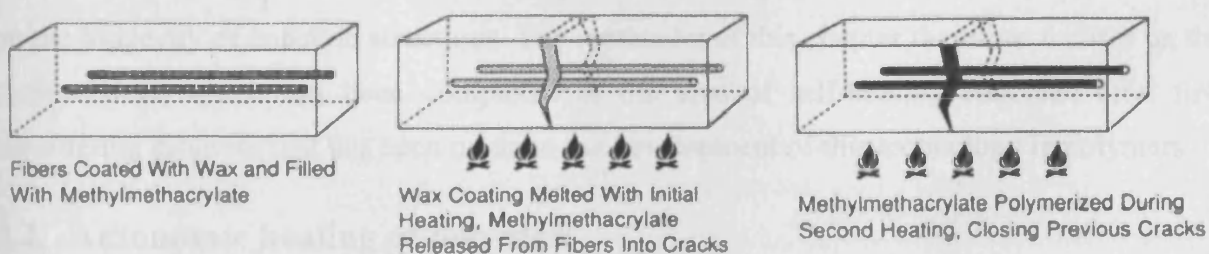
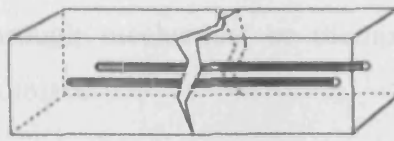


Figure 2.1. Active release mode illustrated through the melting of a wax coating on porous fibres containing methylmethacrylate healing agent (Dry, 1994)



Adhesive Released By Cracking

Figure 2.2. Passive release mode illustrated through the physical cracking of the brittle fibre under loading (Dry, 1994)

2.1.1.4 Sensory structures

Sensory structures are the fourth and least intelligent of the advanced materials categories. These structures have sensing capabilities but lack actuating properties. Examples of sensory structures include: smart brick which are able to monitor temperature, vibration and movements within buildings; smart optical fibres which are able to sense undesirable chemicals, moisture, and strain; and, smart paints which contain silicon-microsphere sensors, and are able to monitor their condition and protection effectiveness.

2.1.2 Addressing the durability issues of concrete through advanced material science

Conventional methods for improving the durability of concrete, involve the reduction of cracking through the use of fibre reinforcing, or the reduction in permeability through the use of waterproofing agents, sealants, or the creation of denser microstructures with reduced porosity.

It is evident, however, from the previous section that the field of advanced materials potentially has a significant amount to contribute to the areas of civil and structural engineering. In the context of concrete durability, in particular, the ability to self-repair microcracks through the release of an encapsulated healing agent, will have a profound effect on the longevity of concrete structures. The remainder of this chapter therefore focuses on the current work which has been completed in the area of self-healing concrete, after first considering progress that has been made in the development of this technology in polymers.

2.2 Autonomic healing of polymers

Structural thermosetting polymers are susceptible to damage in the form of cracks, which form deep within the structure where detection is difficult and repair is almost impossible (White et al., 2001). Cracking leads to mechanical degradation of fibre reinforced polymer composites, and in microelectronic polymer components it can also lead to electrical failure.

White et al. (2001) stress that regardless of the application, once cracks have formed within polymeric materials, either through mechanical or thermal fatigue, the integrity of the structure is significantly compromised.

It is therefore no surprise that autonomic-healing polymers have been the subject of much attention since their initial creation in the material laboratories of the University of Illinois at Urbana-Champaign. Their recent development is widely credited to the team at this institution led by Prof. White (Helmer, 2001), and significant literature has been published in this area recently by White et al. (2001), Kessler et al. (2003), and Brown et al. (2002, 2003a, 2003b, 2004, 2005a, and 2005b). The novel properties of these polymeric materials have also gained interest with the press, and numerous articles have appeared in *Nature* (Helmer, 2001), *The Washington Post* (Gugliotta, 2001), *The Chicago Sun-Times* (Wisby, 2001) and *U.S. News and World Reports* (Fischer, 2001).

2.2.1 The self-healing concept in polymers

The self-healing concept in polymers is illustrated in Figure 2.3 below.

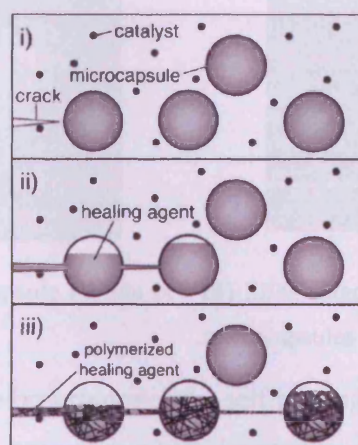
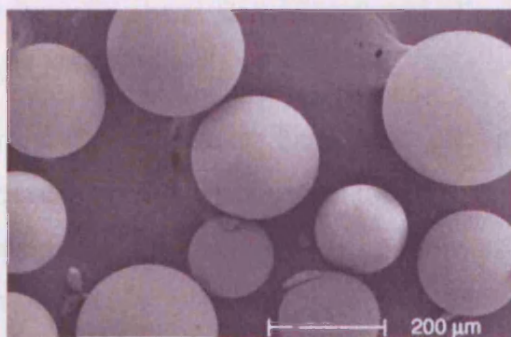


Figure 2.3. The three stages in the concept of self-healing in polymers (Kessler et al., 2003)

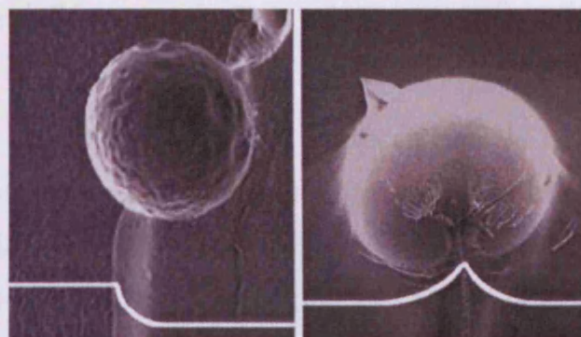
Initially a microcapsule is embedded in a structural matrix containing a catalyst. The first stage shows a crack propagating through the matrix due to the occurrence of damage, such as fatigue loading. The second stage illustrates the rupturing of the microcapsule, thereby releasing the healing agent into the crack plane through capillary action. The third, and final, stage illustrates the contact between the healing agent and the catalyst, resulting in polymerisation and 'healing' via bonding of the crack faces.

This self-healing process has been realised by the group at the University of Illinois using Urea-formaldehyde microcapsules embedded alongside a Grubbs catalyst inside a polymer

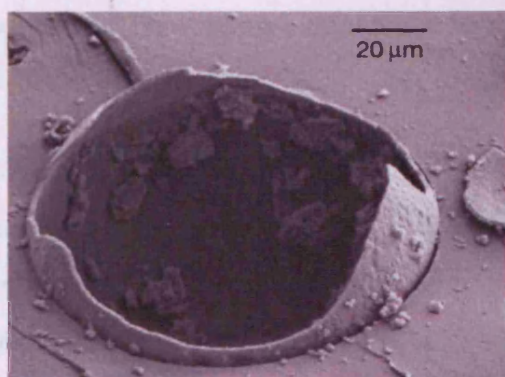
matrix. The scanning electron microscope (SEM) images (Figure 2.4) illustrate the above process in an actual polymeric material.



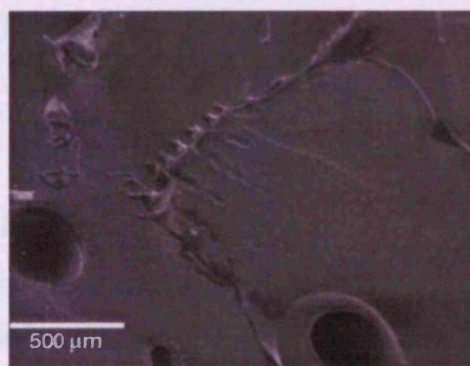
(a) SEM image of Urea-formaldehyde microcapsules microencapsulating dicyclopentadiene liquid. (Brown et al., 2004).



(b) SEM image of Urea-formaldehyde microcapsules breaking and tail formation in the wake of the crack (propagation is from top to bottom) (Brown et al., 2004).



(c) SEM image of a ruptured microcapsule (White et al., 2001).



(d) SEM image of a healed crack plane and depleted microcapsules (White et al., 2001).

Figure 2.4. SEM images of the occurrence of the self-healing process in polymeric materials

2.2.2 The technology of self-healing in polymers

The technology of self-healing in polymers inevitably involves a large amount of polymer chemistry, which is unfortunately outside the scope of this thesis. Stinson (2001), however, offers a brief and simplified description of the associated technology:

2.2.2.1 Microcapsules

The microcapsules are formed by high speed stirring of an aqueous mixture of urea and formaldehyde, dicyclopentadiene, resorcinol acid catalyst, and ethylene-maleic anhydride resin emulsifying agent. The product is microcapsules of urea-formaldehyde resin containing dicyclopentadiene, a liquid tricyclic diolefin (Figure 2.4 (b)). As discussed by Stinson (2001)

the microcapsule properties are crucial: “They must be small enough so that their inclusion does not degrade the strength or stiffness of the epoxy. The walls must be thick enough to survive the shear stresses of moulding and yet thin enough to burst upon meeting the lengthening crack”.

Further investigations have also shown that the stiffness of the microcapsules is also important. If the capsules are too stiff, stress distribution in the surrounding plastic will cause crack paths to deflect away from the capsules. Helmer (2001) reports that if the microcapsules exhibit greater yielding, they will, in fact, serve to attract propagating cracks rather than deflect them, thus increasing the efficiency and effectiveness of the self-healing process. Further information on crack-microcapsule interaction is presented in section 2.4.

A detailed analysis of the microencapsulation technology associated with the autonomic healing of polymers is presented by Brown et al. (2003a). The size of the microcapsules produced by the authors range from 10 micron to 1000 microns, depending on the revolution rate of the centrifuge.

2.2.2.2 Polymerising catalyst

The polymerising catalyst used in the current work is a ruthenium carbene complex invented by chemistry professor Robert H. Grubbs of California Institute of Technology. The Grubbs catalyst remains active even on exposure to air, moisture, or most organic functional groups.

Figure 2.5(a) illustrates a test component moulded from epoxy resin, containing 10% microcapsules by weight. Components are cured for 24 hours at room temperature, and then baked at 40°C for a further 24 hours.

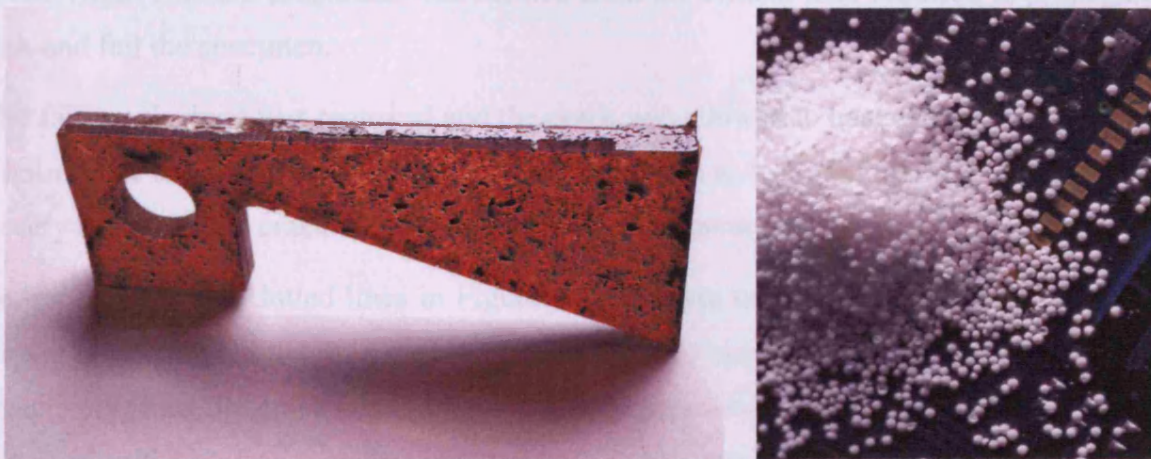


Figure 2.5. (a) Image of a broken epoxy resin component (black spots are embedded powder catalyst)
(b) Image of microcapsules on a microchip. (White, 2005).

The usual failure mechanism of plastics (Stinson 2001) is the creation of minute fatigue cracks, from repeated thermo-mechanical loading, which propagate to become microcracks, then macrocracks, and eventually through-cracks. As reported by Kabat (2001), the self-healing process in polymers heals these initial cracks before they grow beyond 100 microns in length. This 'repair' process is initiated when the healing agent comes into contact with the Grubbs catalyst. 'The catalyst mediates gelation of dicyclopentadiene by ring-opening metathesis polymerisation' (Stinson 2001). This is a highly cross-linked polymerisation which effectively stitches the crack up, as shown in Figure 2.4(d).

2.2.3 Mechanical response of self-healed specimens

The ultimate aim of a self-healing polymer is that the self-healing system: must not degrade the physical properties of the plastic; must sense damage; must initiate healing; and, must restore the original strength and stiffness of the material (Stinson 2001).

These aims have been engineered and tested by the Illinois self-healing group at Urbana Champagne in a series of scientific papers, since 2001 (Brown et al. 2003b; Brown et al. 2002; Brown et al. 2004, 2005a, 2005b; Kessler et al. 2003; Rule et al. 2005; White et al. 2001).

The early work of White et al. (2001) focused on examining the fracture toughness of tapered double cantilever beam (TDCB) specimens, with sharp embedded pre-cracks. Control samples consisting of (1) neat epoxy containing no Grubbs' catalyst or microspheres; (2) epoxy with Grubbs' catalyst but no microspheres; and (3) epoxy with microspheres but no catalyst were examined. Load was applied in a direction perpendicular to the pre-crack (Mode I). The virgin fracture toughness was defined from the critical load required to propagate the crack and fail the specimen.

After failure, the load was removed and the crack was allowed to heal at room temperature for 48 hours. The amount of healing was quantified through re-loading to failure (Figure 2.6), and in every specimen the crack was observed to propagate along the original (virgin) crack plane.

The upper and lower dotted lines in Figure 2.6 represent the average peak loads obtained by manually injecting a mixture of dicyclopentadiene and Grubbs' catalyst, and neat epoxy resin, respectively, into the crack plane of the control specimens. The representative curves for a virgin and self-healed composite show that both failure mechanisms are elastically brittle, and that the self-healing has effectively recovered about 75% of the virgin fracture load. As

highlighted by the authors, this is in sharp contrast to all three types of control samples that showed no healing and were unable to carry any load upon re-loading.

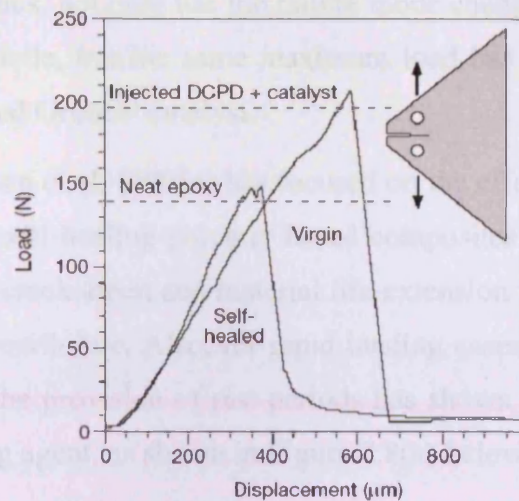


Figure 2.6. Self-healing efficiency of an epoxy polymer, illustrated through fracture toughness testing of tapered double-cantilever beam (TDCB) specimens (White et al., 2001).

A recent study by Rule et al. (2005) has considered, in detail, the role of the catalyst, and proposed the embedment of the catalyst in a wax protected microsphere. This protective embedment has not only served to enhance the distribution of the catalyst, but has also helped reduce the effect of the epoxy's curing agent, diethylenetriamine (DETA), which destructively attacks the Grubbs' catalyst as the epoxy initially cures.

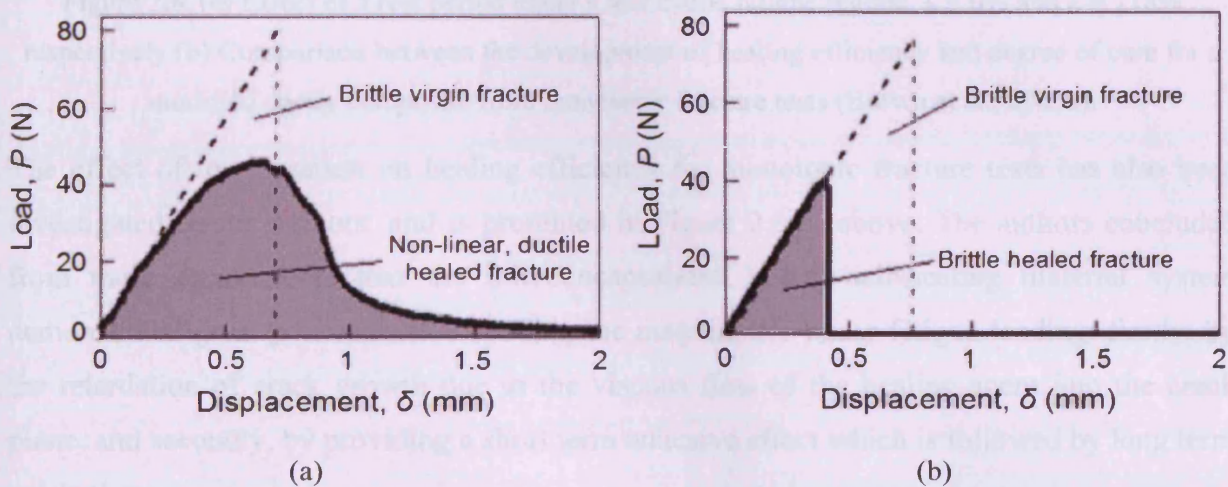


Figure 2.7. Representative virgin and healed load-displacement curves for samples with (a) 5% wt. microspheres containing 5% wt. Grubbs' catalyst, and (b) 2.5% wt. unprotected Grubbs' catalyst. Both samples contain 10% wt. DCPD microcapsules with an average diameter of 180 microns (Rule et al., 2005).

Due to the presence of the wax, the failure mode of the healed specimen has changed from the perfectly elastic, brittle response, shown in Figure 2.7(b), to a non-linear, ductile response, as shown in Figure 2.7(a). Thus, not only has the failure mode changed from a sudden explosive mode to a safer ductile mode, but the same maximum load has been achieved whilst using only 10% wt. of the original Grubbs' catalyst.

More recent work by Brown et al. (2005a) has focused on the effect of low and high intensity cyclic fatigue loading on self-healing polymer based composites. These materials have been found to show significant crack arrest and material life-extension when the in-situ healing rate is faster than the crack growth rate. Also, for rapid loading cases (i.e. rate of loading greater than the rate of healing) the provision of rest periods has shown to dramatically increase the performance of the healing agent, as shown in Figure 2.8(a) below.

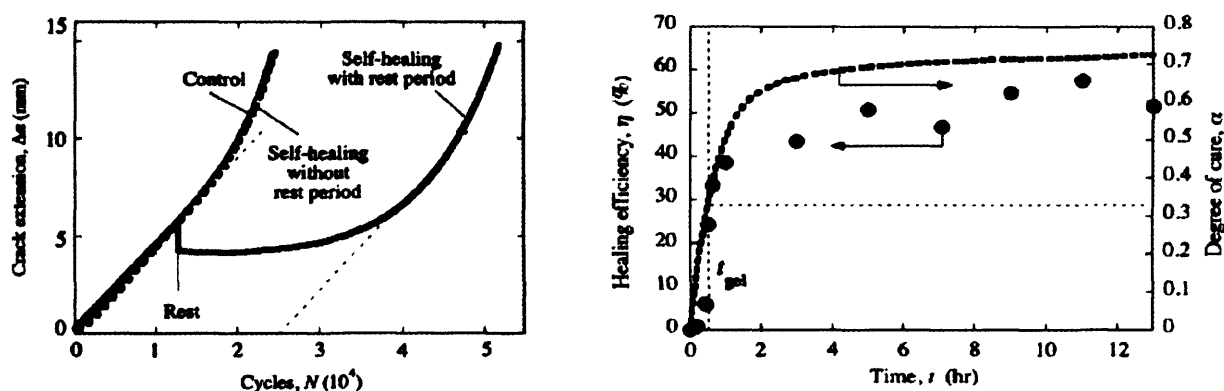


Figure 2.8. (a) Effect of a rest period under a low cyclic fatigue regime. $\lambda = 0\%$ and $\lambda = 118\%$ respectively (b) Comparison between the development of healing efficiency and degree of cure for a modified epoxy composite from monotonic fracture tests (Brown et al., 2005a).

The effect of rest duration on healing efficiency for monotonic fracture tests has also been investigated by the authors, and is presented in Figure 2.8(b) above. The authors concluded from these experiments that the microencapsulated in-situ self-healing material system demonstrated great potential for extending the material life under fatigue loading; firstly, by the retardation of crack growth due to the viscous flow of the healing agent into the crack plane, and secondly, by providing a short term adhesive effect which is followed by long term crack closure.

2.3 Self-healing of cementitious composites

As indicated in the introduction, cementitious composites have the ability to self-heal in one of two ways, either autonomically or autogenically.

2.3.1 Autogenic healing of cementitious composites

The autogenic healing of cementitious materials is a natural self-repair phenomenon which has been known about for many years. There are several processes that are considered to be responsible for this phenomenon. These include chemical, physical and mechanical interactions as discussed by Kishi et al. (2007). The main processes are: (i) swelling and hydration of cement pastes; (ii) precipitation of calcium carbonate crystals, and; (iii) blockage of flow paths due to deposition of water impurities or movement of concrete fragments that detach during the cracking process.

The autogenous healing effect is generally acknowledged as one of the reasons why so many old buildings and structures have survived for so long with limited servicing and maintenance. Westerbeek (2005) attributes the unexpected longevity of many old bridges in Amsterdam to this phenomenon. It is believed that this longevity is due to the high levels of chalk or calcium in the cement of that area. Under the presence of water, this calcium is believed to dissolve and then deposit in cracks, thus partially healing them and hindering their propagation. Recently the autogenic healing of microcracks has been the suggested reason for the reduction in diffusion coefficient of concrete marine structures with time. For non-submerged structures, however, the durability benefit that the self-healing of microcracks affords is reduced, and whilst periodic ‘wetting’ of these structures may enhance healing, such a process is expensive and generally impracticable for most situations.

As described by Schlangen (2005), one of the first works on the healing of cementitious materials was published more than 20 years ago. It was shown that the so called Kaiser effect (absence of acoustic emission, which is usually observed at repeated loading of structural elements, until the load exceeds the previously achieved level) disappeared for concrete which had been kept under water for a long period of time before re-loading: i.e. acoustic emissions were recorded during reloading of the structure, thus indicating that partial healing of the cracks caused during the first loading cycle had taken place.

Over recent years many authors have continued to investigate this natural self-healing ability: Reinhardt and Joos (2003) have examined the effect of temperature on permeability and self-healing of cracked concrete; Zhong and Yao (2008) have investigated the effect of the degree of damage on the self-healing ability of normal strength and high strength concrete; Şahmaran and Li (2008) have considered the effect of autogenous healing on engineered cementitious materials (ECCs), and; Jacobsen and Sellevold (1996) have examined the efficacy of autogenic healing on strength recovery of ‘well cured’ concrete beams exposed to rapid

freeze/thaw cycles. The latter paper concluded that only a 4-5% recovery of compressive strength by means of autogenous healing was possible. Edvardsen (1999) noted, however, that the greatest potential for autogenous healing exists in early age concrete. More recent work by Ter Heide et al. (2005) has therefore focused on examining both the mechanical strength gain and reduction in permeability of early age concrete which has been cracked and allowed to heal autogeneously. The authors examined the extent of healing under a range of factors including the specimen age at the time of cracking, width of the crack opening, compressive strength applied during healing, and the curing conditions post-damage. The main results of this study were that crack healing was only observed to occur for specimens stored under water, and that the compressive stress applied to the crack faces did little to improve the healing behaviour other than to close the crack opening. Since the specimens that were cracked at an earlier age and then stored in water showed the greatest strength recovery, the authors concluded that the primary healing mechanism was ongoing hydration.

An interesting recent development has been the autogenous healing of expansive concretes as studied by Japanese researchers: Kishi et al. (2007); Hosoda et al. (2007), and; Yamada et al. (2007). They have found, through microscopic observations and subsequent water permeability tests, that the inclusion of expansive agents in the concrete has allowed even large cracks of up to 0.3 – 0.4mm to heal (Hosoda et al., 2007). The authors have also found that the addition of small amounts of various carbonates such as bicarbonate of soda increase the self-healing ability of the concrete by allowing more calcium carbonate (CaCO_3) to be precipitated (Yamada et al., 2007).

2.3.2 Autonomic healing of cementitious composites

The autonomic healing of cementitious composites has received significantly less attention than its polymer counterpart, and the research efforts to date have been far more piecewise and sporadic. Nevertheless, several authors (Dry 1994, 1996a, 1996b, 1996c, 1996d, 2000; Dry and Corsaw 2003; Dry and Unzicker 1998; Li et al. 1998; Mihashi et al. 2000) have completed studies in this area.

2.3.2.1 The concept of autonomic healing in cementitious composites

The concept of autonomic healing in concrete was originally proposed for cementitious materials by Dry (1994). This concept, as illustrated in Figure 7.1, is similar to that described previously for polymers (Figure 2.3). Due to the vastly different structure of concrete compared to plastic and the infancy of this research area, the sophistication of the

encapsulating methods and the encapsulated materials are somewhat different, although the underlying philosophy is the same.

2.3.2.2 Healing agents

Various healing agents have been proposed in the studies which have been undertaken on the self-healing of concrete. In contrast to the specialist healing agents employed in polymers, these healing agents have generally been 'off the shelf' agents. The relatively 'low cost' and readily available nature of 'off the shelf' products are important assets which must be possessed by any healing agent proposed for application to a large bulk material, such as concrete.

The main healing materials which have been proposed to date are epoxy resins, cyanacrylates, and alkali-silica solutions. It is obvious that the effectiveness of the healing process is not only dependent on the capillary forces, which are dictated by the crack width, but also on the viscosity of the repair agent; the lower the viscosity the larger the potential repair area. Another pre-requisite for the agent is that it must form a sufficiently strong bond between the surfaces of the crack, in order to prevent the re-opening of the crack, and thus force other new cracks to open, hence increasing the total fracture energy that is required to break the specimen.

2.3.2.2.1 Epoxy resins

Low viscosity epoxy resins currently form the principle healing agent used in the post-damage 'active' remediation of critical concrete floors, and bridge decks. Sikadur 52 (Sika Ltd., 2001), and Tecroc Epoxy Injection Grout (Tecroc Products Ltd., 2004), have viscosities at room temperature (20°C) in the order of 500 and 200 centipose, respectively (Note: Water has a viscosity of 1 centipose (1m.Pa.s), milk is 3 centipose, and grade 10 light oil is 85-140 centipose). Epoxy resins are durable materials that generally have good thermal, moisture and light resistance. They are available in either one or two part systems: a one part epoxy is activated by the presence of heat; and, a two part epoxy is cured by the presence of both a hardener and resin component.

Nishiwaki et al. (2006) have recently designed and developed a single agent epoxy resin based self-healing system for concrete. The low viscosity epoxy resin is stored in an organic (ethylene vinyl acetate) film pipe which melts at 93°C. The authors have managed to maintain a passive system by embedding a 'self-diagnosis composite' sensor adjacent to the repair agent supply tube in the concrete. This sophisticated self-diagnosis composite sensor is made

from a fibre reinforced composite and an electro-conductive material. When a crack forms the sensor detects the increase in strain through reduced electrical conductivity, and as a result of the corresponding increase in resistance, heat is generated which melts the organic supply tube and cures the epoxy resin after it has flowed into the crack

The main problem with the application of two-part epoxy resins to the autonomic healing of concrete is the fact that both components have to be simultaneously present at a crack location. Given that both liquids must be encapsulated, the likelihood of both capsules being present at a crack location, and cracking at the same time, is extremely small. Mihashi et al. (2000), tried to overcome this by manually placing the two components in adjacent tubes. Despite both tubes cracking and releasing their respective agents, poor mechanical behaviour was observed due to insufficient mixing of the fluid blend.

The chemical reaction which occurs between the hardener and the resin is an exothermic reaction which, unfortunately, does not rely on the presence of oxygen to perpetuate. An encapsulated mixture of both agents will therefore only remain liquid for the duration of the 'pot-life' of the resin, which is usually in the order of hours.

2.3.2.2.2 Cyanacrylates

Cyanoacrylates (superglues) are one part systems that react to the presence of moisture, and are noted for their ability to cure rapidly (pot life in the order of seconds-minutes) and provide a bond strength that often exceeds the strength of the substrate, certainly in the case of concrete. They also have very low viscosities (<10 centipose), and therefore possess the ability to heal cracks less than 100 microns in thickness. Li et al. (1998) studied the effectiveness of an ethyl cyanoacrylate as a healing agent, as described in section 2.3.3.

An important property of cyanoacrylates in relation to their use in concrete is the fact that they are acidic solutions. Contact with concrete, which is an alkaline environment, will result in neutralisation of the glue and thus quicker setting times. This quicker gain of bond strength can be beneficial in rapid cyclic loading conditions; however, if the setting time is too quick, the dispersion of the healing agent within the crack may be insufficient.

2.3.2.2.3 Alkali-silica solution

Mihashi et al. (2000) present the use of a diluted and undiluted alkali-silica solution as a healing agent in concrete (see section 2.3.3). The alkali-silica solution in the presence of oxygen causes hydration and thus bonding of the original crack faces. The strength of the

bond is less than that of glue, although, this is immaterial so long as the bond strength is greater than the tensile strength of the surrounding material. The use of an alkali-silica based healing material in concrete is also likely to cause less material compatibility problems, than its polymer based counterparts.

2.3.2.3 Encapsulation techniques

Various encapsulation techniques have been proposed in the literature. Mihashi et al. (2000) discuss two encapsulation techniques, namely: a micro-capsule enclosing repairing agent mixed in concrete; and, a continuous glass supply pipe enclosing repairing agent, embedded in concrete, whilst Li et al. (1998) used cyanacrylycate enclosed in capillary tubes, sealed with silicon.

The shape of the embedded capsule is a factor which should be considered. A spherically shaped capsule will provide a more controlled and enhanced release of the healing agent upon breakage, and will also reduce the stress concentrations around the void left from the empty capsule. A tubular capsule, however, will cover a larger internal area of influence on the concrete for the same volume of healing agent (higher surface area to volume ratio). The release of the healing agent upon cracking however will be of inferior quality since localised and multiple cracking may occur inhibiting the effective distribution of the healing agent.

2.3.2.3.1 Microcapsules

The advantage of dispersed microcapsule inclusion is that the concrete can react to diffuse cracking at multiple locations; however, the disadvantage is that additional repairing agent cannot be supplied once the original agent has been exhausted.

In preliminary investigations by Mihashi et al. (2000), urea-formaldehyde microcapsules (diameter 20-70 microns) filled with epoxy resin, and gelatine microcapsules (diameter 125-297 micron) filled with acrylic resin were used in compression and splitting tests. In addition to the aforementioned problems of blending two agent epoxies, the authors concluded that the quantity of repairing agent provided by microencapsulation is very small and limited, and the bond strength between the micro-capsule and the matrix needs to be stronger than the strength of the microcapsule, to ensure that cracks propagate through and not around the capsules.

2.3.2.3.2 Glass capillary tubes

Li et al. (1998) utilised capillary tubes, developed for blood testing in the medical industry, as encapsulating containers for an ethyl cyanoacrylate healing agent. Their initial test regime

was aimed at confirming the sensing and actuation mechanisms of an engineered cementitious composite (ECC), through forced cracking of single hollow capillary tubes, under the eye of an environmental scanning electron microscope (ESEM). Custom made hollow capillary tubes, 500 microns in diameter, and 60 microns wall thickness were used, as illustrated in Figure 2.9.

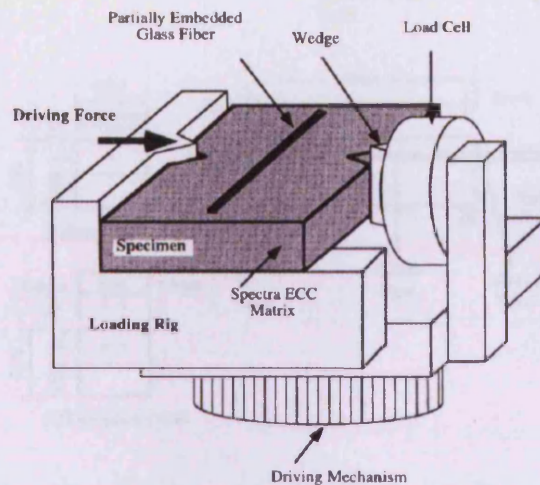


Figure 2.9. ESEM specimen loading configuration (Specimen dimensions are 10mm x 10mm x 1.5mm) (Li et al. 1998).

It was observed in the experiments that as the angle between the crack plane and the longitudinal direction of the capillary tube became more acute, the failure of the tube changed from a simple tensile mode (Figure 2.10(a)) to a flexural mode (Figure 2.10(b)). Some localised debonding between the borosilicate tube and cement matrix was also observed, however, subsequent testing of dye filled tubes illustrated the success of the sensing and actuation mechanisms.

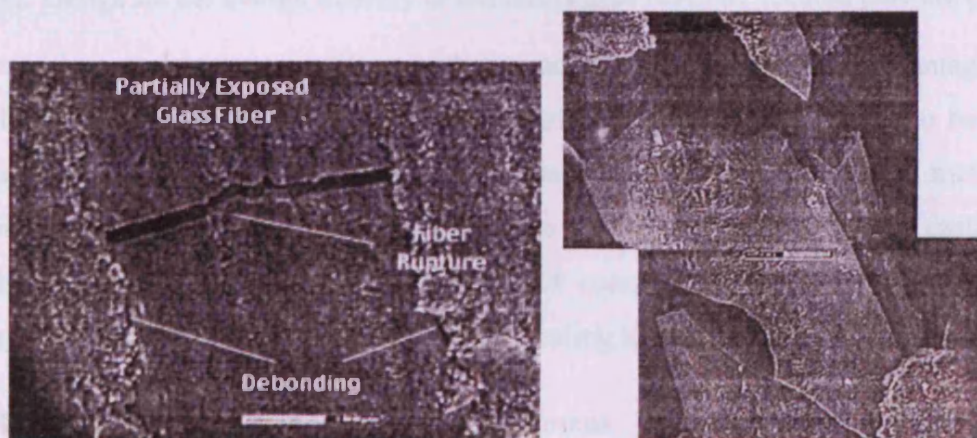


Figure 2.10. ESEM images showing (a) tensile failure (b) flexural failure of hollow capillary tubes (Li et al., 1998)

2.3.2.3.3 Continuous glass supply pipes

In later experimental work conducted by Mihashi et al. (2000) the authors reverted to the use of glass supply pipes, as oppose to individual microcapsules or capillary tubes, as shown in Figure 2.11.

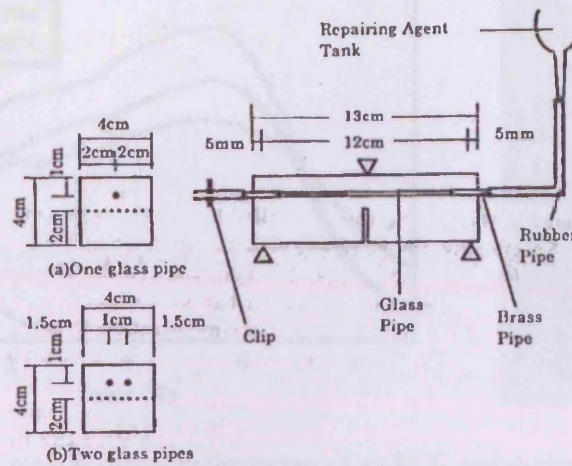


Figure 2.11. Three-point bending experimental setup illustrating the continuous supply of healing agent through glass pipes (Internal diameter 0.8mm, external diameter 2mm) (Mihashi et al., 2000)

In early work presented by Dry (1994), the active provision of healing agent was proposed via the use of an internal delivery vacuum pressure system, as shown in Figure 2.12 below.

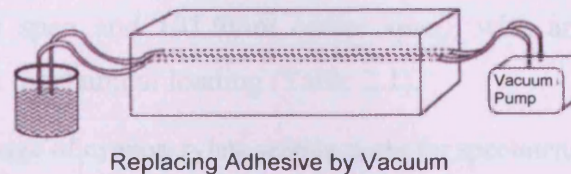


Figure 2.12. Design for the interior delivery of chemicals from fibres by vacuum pressure (Dry, 1994)

Continuous glass supply pipes, with or without vacuum pumps, have the advantage of being able to allow the type of repairing agent to be varied, and additional supply to be provided, thereby allowing larger fractures to be healed than with other encapsulation methods. The significant disadvantage of the method is the care that must be taken during casting, hence this method is not suitable for in-situ casting of concrete. It does, however, provide an interesting feasibility test for the concept of self-healing in cementitious materials.

2.3.3 Mechanical response of self-healed specimens

As mentioned above, Li et al. (1998) undertook their self-healing experiments within the matrix of an ECC. An ECC is essentially a fibre reinforced cementitious composite that

exhibits significant tensile strain-hardening characteristics (Figure 2.13(a)) due to the inclusion of high-modulus polyethylene fibres. These fibres serve to constrain the crack width opening of the matrix, thus giving a large, controlled, ductile mechanical response.

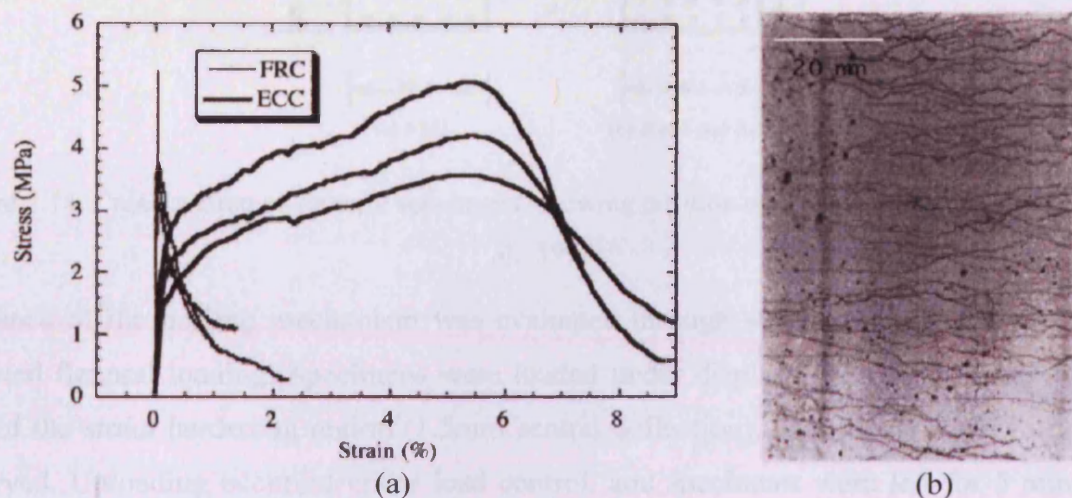


Figure 2.13. (a) Uniaxial tensile stress-strain curves of an ECC and normal FRC, and (b) Multiple cracking in an ECC with fine crack width control (specimen has been tensile strained to 4.6%) (Li et al., 1998)

After investigating the sensing and actuation response of embedded glass capillary tubes in small ESEM specimens, as described above, the authors investigated the mechanical response of three-point beam members (76.2mm deep x 38.1mm wide x 203.2mm span), and four-point beams (304.8mm span and 101.6mm centre span), with and without healing agent, subjected to damage via mechanical loading (Table 2.1).

Table 2.1. Dosage of cyanoacrylate sealing agent for specimens (Li et al., 1998)

Specimens	No. of specimens	No. of SAC fibers	No. glass fiber w/ink	Amount of SA (ml)
N-M1	1	—	—	—
N-M2	5	—	—	—
N-M1-4	2	—	—	—
I-M1	2	—	10	—
S-M1	2	20	—	1.0
S-M2	6	20	—	1.0
S-M1-4	1	32*	8*	3.2

SA, sealing agent (Superglue)

*200 mm length and 100 μ l capacity glass fibers with the same cross-section specified in the "Passive Smart Self-healing Concept: Implementation" section

Note: M1 and M2 in Table 2.1 refer to different fibre types included in the ECC. The average crack width for M1 specimens was 50 microns and 30 microns for M2 specimens. The three four-point bending tests are indicated by a '4' following the specimen name.

The arrangement of capillary tubes in the test specimens is illustrated in Figure 2.14.

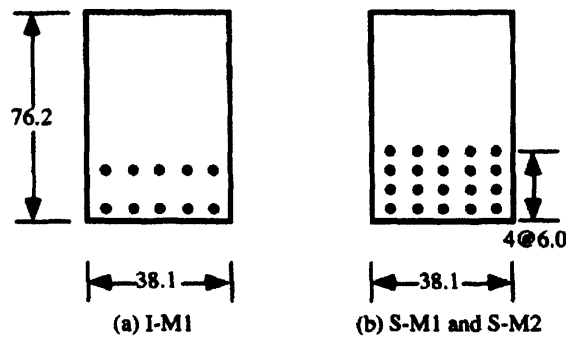


Figure 2.14. Cross-section of flexural specimens, showing position of glass fibres (units in mm) (Li et al., 1998)

Evidence of the healing mechanism was evaluated through studying the beam stiffness on repeated flexural loading. Specimens were loaded under displacement control into the early part of the strain hardening region (1.5mm central deflection), and visible microcracks were observed. Unloading occurred under load control, and specimens were left for 5 minutes in order to allow setting of the healing agent to occur. This loading-unloading process was repeated once more for a central beam deflection of 2.5mm (larger damage), and thereafter the beams were loaded to failure.

The authors used a linear curve fitting function to compute the stiffnesses, which were normalised to the initial uncracked stiffness. The normalised stiffnesses are presented in Figure 3.7 below.

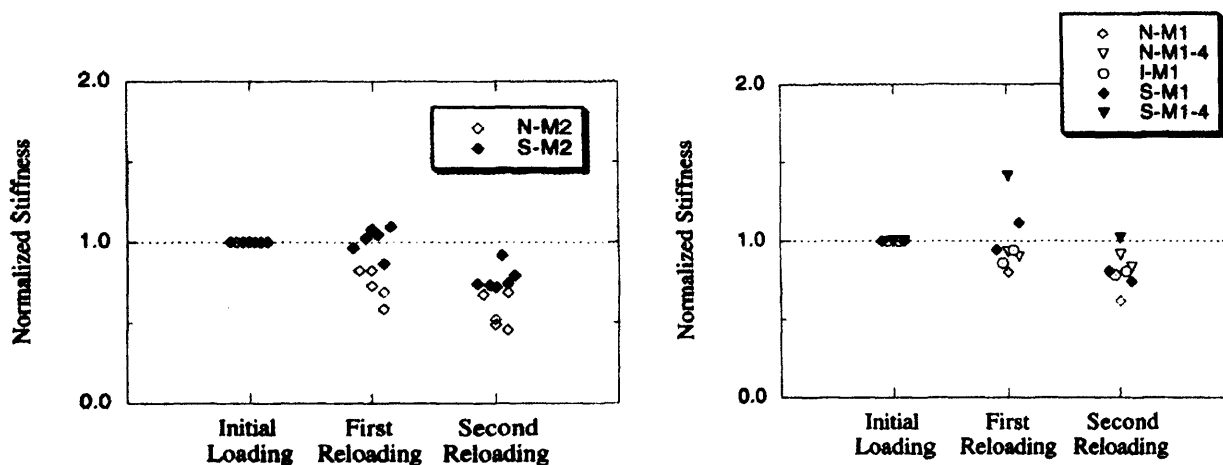


Figure 2.15. Normalised stiffness in flexural beams (Li et al., 1998)

It can be seen from Figure 2.15 that six out of the nine specimens showed higher regained stiffness on first reloading than the initial stiffness. In contrast, specimens having no SAC fibres all suffered stiffness degradation from 10% to 40%. For the self-healing specimens that did not perform as well, post-mortem investigations indicated hardened sealing agent inside

the capillary tubes, as shown in Figure 2.16. This indicates that the sealing agent may have hardened prior to testing due to poor sealing of the tubes.

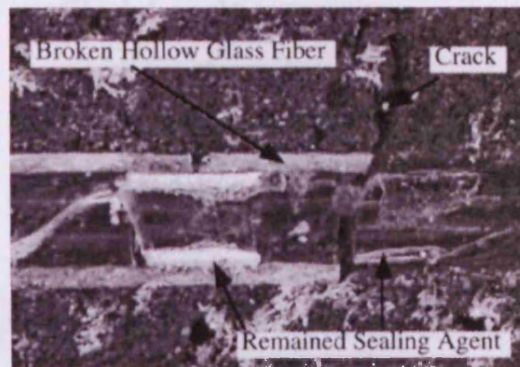


Figure 2.16. Cut section of a specimen with SAC fibres after flexural testing (Li et al., 1998)

It is also noticeable from the results that the regaining of stiffness in the second reloading cycle is less significant. As suggested by the authors, this is probably due to exhaustion of available sealing agent in the first damage/healing cycle. It is probably due to this reason that the crack shown in Figure 2.16 does not appear to have been healed; i.e. the healing agent has already been used to heal another crack which is not visible in the picture.

The most significant stiffness increase was observed for the four-point bend specimen (S-M1-4). This specimen exhibited an increase of 1.4 and 1.0 for first and second loading cycles, respectively. This result is believed by the authors to be a direct result of the significantly larger amount of healing agent that this specimen contains (3ml compared to 1ml for all other self-healing specimens).

Mihashi et al. (2000) also performed a study on the mechanical response of self healed three-point bend specimens. However, unlike Li et al. (1998) the authors examined the effect of self-healing on normal notched concrete beams, subjected to the continuous supply of healing agent through glass tubes, as illustrated in Figure 2.11. The healing properties of both epoxy resin and alkali-silica solutions were investigated, and compared to control specimens, and specimens where the healing agent had been actively injected into surface cracks.

Unlike Li et al. (1998) the specimens were initially loaded beyond their maximum flexural load, and unloaded at load level P_1 , as shown in Figure 2.17 below. The maximum load attained on reloading after healing is P_r , and thus the strength recovery ratio is defined as P_r/P_1 .

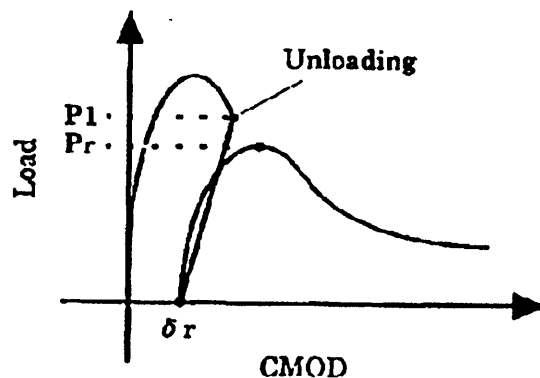
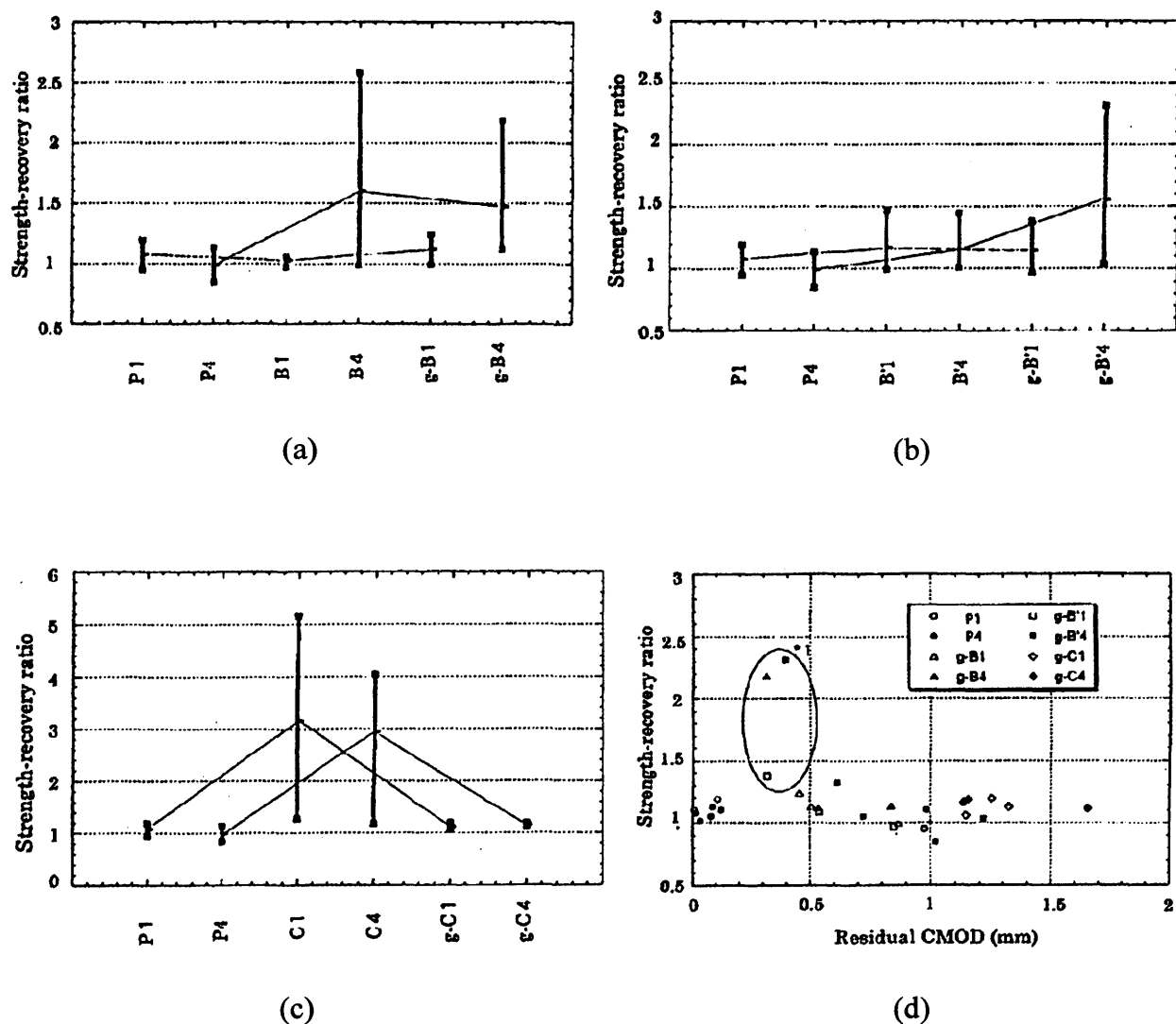


Figure 2.17. Typical Load v CMOD for test specimens (Mihashi et al., 2000)

The results obtained for the experiments are reproduced in Figure 2.18 below.



NOTE: P = Control specimens / g = glass tubes (as oppose to manually injected)
 B = Alkali-silica solution (27% diluted solution) / B' = Alkali-silica solution
 C = Two-part epoxy resin (low viscosity type)

Figure 2.18. Results of self-healing experiments (Mihashi et al., 2000)

Both the diluted and undiluted alkali-silica solutions showed increases in the strength recovery ratios, 1.12, 1.48, 1.15, and 1.56 for test series g-B1, g-B4, g-B'1, and g-B'4 respectively. A large strength recovery was observed for the manual injection of the diluted alkali-silica solution (B4); however, the authors believe that this was not replicated in the case of the undiluted solution due to its higher viscosity. As expected, the manual injection of the epoxy resin (C1 and C4) produced very good strength recovery results; however, no significant effect was measured when this healing agent was encapsulated. This is due to insufficient mixing of the two agents, as mentioned previously. The final trend highlighted by the authors relates to the effect of damage on self-healing ability. Despite the continuous supply of healing agents in these experiments Figure 2.18(d) illustrates that self-healing is significant when the CMOD is less than approximately 0.5mm (see ringed zone *1). For damage greater than this level the size of the cracks are believed to be too large to self-heal effectively.

Further results demonstrating the feasibility of the autonomic healing of cementitious materials are presented by: Dry (1994), (1996b), (1996c), (1996d), and (2000); Dry and Corsaw (2003); and, Dry and Unzicker (1998).

These studies consider various self-healing applications, including glass tube supply networks in loaded small scale rigid-framed structures, grids of scored glass tubes in large scale concrete decks subject to shrinkage cracking, and hollow adhesive filled fibres in RC three-point bending samples. The majority of the results obtained from these studies are, however, largely qualitative, and are therefore not presented here.

2.4 Modelling the self-healing process

Given the natural tendency for the numerical modelling fraternity to lag behind the field of material science, and the fact that self-healing polymers and concrete are very new materials, still at the development stage, it is unsurprising that there is a lack of published modelling literature on the subject.

Some early work has nevertheless been completed on the modelling of self-healing polymers. White et al. (2001) attempted to capture the complex 3D effect of the interaction between a crack and a microcapsule using micromechanical modelling with the aid of the Eshelby-Mura equivalent inclusion method. An illustrative result from these studies is presented in Figure 2.19. This figure shows the effect of the relative stiffness of the microcapsule on the propagation path of an approaching crack.

The crack, the sphere, and the surrounding matrix are subjected to far-field tensile loading, σ_∞ perpendicular to the crack plane. The σ_{22} stress distribution in the equatorial plane of the sphere illustrates the fact that the stiffness of the sphere relative to the matrix, strongly affects the stress state in the proximity of the crack tip and around the sphere itself. As stated by the authors; “in the case of a stiffer inclusion, the stress field in the immediate vicinity of the crack tip shows an asymmetry that indicates an undesirable tendency of the crack to be deflected away from the inclusion”. This is shown in the left hand stress contour of Figure 2.19 below. The stress contour on the right hand side illustrates the reverse situation for the case of a more compliant spherical inclusion, where the crack is attracted toward the microcapsule.

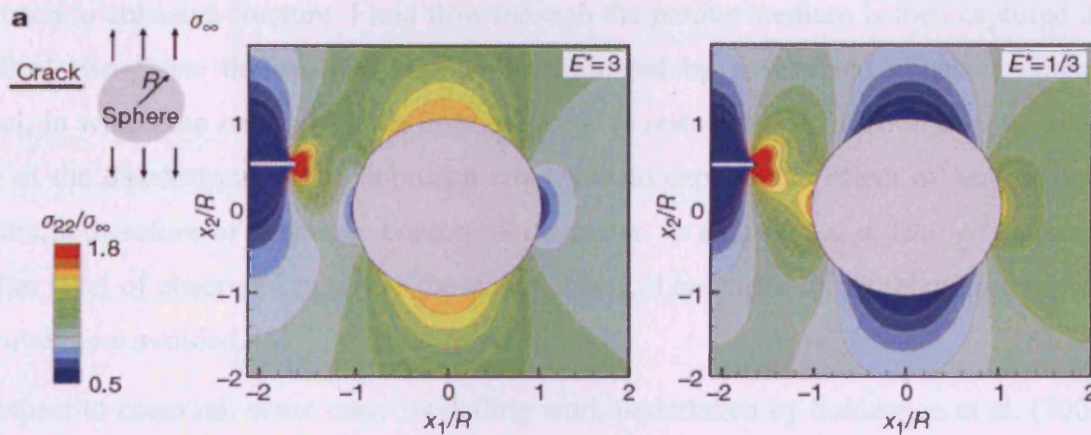


Figure 2.19. Stress state in the vicinity of a planar crack as it approaches a spherical inclusion embedded in a linearly elastic matrix and subjected to a remote tensile loading perpendicular to the fracture plane. ($E^* = E_{\text{sphere}}/E_{\text{matrix}}$ and ν of sphere and matrix = 0.3) (White et al., 2001)

Barbero and Lonetti (2003) present a continuum damage healing mechanics model, based on the theory of generalised thermodynamics, with specific application to the damage, yielding, and healing of fibre-reinforced polymer-matrix composites.

The model does not consider the propagation of damage through the growth of discrete microcracks, but considers homogenised properties of the material through the inclusion of parameters such as damage evolution, yield evolution, and healing evolution. These parameters are obviously dependent on the properties of the material, and the properties and density of healing agents, in the case of healing. Expressions for the various domains, potentials, and evolution equations are based on insight gained from experimental observations. This method is therefore essentially a parameter based modelling method which lies towards the phenomenological side of numerical modelling.

Further work on the self-healing of polymer composites has been completed by Maiti and Geubelle (2006). Their proposal pertains to the numerical modelling of fatigue crack growth retardation induced by artificial crack closure. Their model is therefore a fictitious crack continuum model, which relies on the combination of cohesive modelling and a contact algorithm in the wake of the advancing crack, to account for the effect of the introduced wedge. This model has a greater physical background than the previous model, however, modelling diffuse, or even a localised network of discrete cracks, in a concrete specimen using the cohesive crack model carries a large computational overhead.

More recently, Remmers and de Borst (2007) have developed a model which predicts crack growth using the method of cohesive segments. This is an extension of the partition of unity approach to cohesive fracture. Fluid flow through the porous medium is then captured using a classical two-phase theory, and healing is simulated by a reversed cohesive constitutive model, in which the strength of the cohesive zone is restored as a function of time and stress state at the discontinuity. The approach employed to capture the effect of healing by these authors is therefore of a phenomenological character, in so much as a detailed analysis on a smaller level of observation, where the actual chemical reactions of the rebonding process are important, are avoided.

In respect to concrete, some early modelling work undertaken by Schlangen et al. (2006) has investigated autogenous healing of early age cracks. The authors have used the finite element module MLS of FEMMASSE (FEMMASSE, 2008) to confirm the validity of their hypothesis that ongoing hydration is responsible for the crack healing observed during experiments. This model is based on the state parameter concept, which means that the material properties are assumed to be a function of the state of the material. This state can be considered as maturity, degree of hydration, temperature or moisture potential.

Currently, no modelling work specific to the autonomic-healing of cementitious materials appears to be available within the literature. Therefore, in order to identify suitable candidate methods for application to self-healing concrete, a brief overview of numerical models currently applied to cementitious materials is considered useful.

2.5 Numerical modelling of fracture in cementitious materials

2.5.1 Introduction

The numerical modelling of cementitious materials has been a very active research area over the past 40 years, since the advent of affordable computational power, and a comprehensive review is outside the scope of this thesis. Therefore, only a general overview of the main techniques is presented here. For a more comprehensive overview see de Borst (2002).

Concrete is a highly heterogeneous material whose microstructure not only affects the geometry of crack propagation but also the stress re-distribution which occurs during the fracture process. Crack propagation in cementitious materials is therefore described through techniques based on iterative calculations. These techniques may generally be split into the two main categories of continuum and discrete modelling.

Continuum models, which may be considered as the classical approach, generally exclude explicit consideration of the micro- and meso-structure of the material from the model, and treat the material as a continuum at the macro level. The constitutive relation of the material at the macro-level must therefore be non-linear, and hence the damage process is described by a macroscopic evolution function which depends upon material properties. Conversely, in discrete models, such as lattice, particle and DEMs (Discrete element models), the global softening response is obtained from consideration of a finite configuration of discrete elements. The constitutive law at the element level may be brittle or a simple softening function, and the heterogeneity of the material is generally represented by some pre-defined variation in material properties.

2.5.2 Continuum finite element modelling

In continuum modelling of quasi-brittle materials, such as concrete, a number of different approaches have been developed. These can be considered to fall broadly into two categories. There are constitutive theories which relate to assumed stress-strain, or stress-relative displacement, behaviour, and there are computational approaches by which cracks are represented within, or at the boundaries of, finite elements.

The constitutive theories were originally developed separately and included the cohesive crack model of Hillerborg (1985), damage mechanics (Krajcinovic, 1996), and directional fracture models (Rots, 1993). However, the close relationship between these approaches has

since been recognised and they can all, essentially, be classed as types of damage models (de Borst, 2002).

Continuum damage mechanics deals with the study of crack formation and growth in structures which may contain initial defects. Material integrity is considered to progressively diminish due to the growth and coalescence of microcracks, microvoids or other material defects. Damage evolution may therefore be modelled at the macroscopic level through degradation of the overall constitutive response of the material. This is often described by a scalar damage state variable ω , or tensor $\boldsymbol{\omega}$, whose evolution is prescribed along the gradient of a damage loading surface. Various damage models for concrete are described in detail by Karihaloo (2003).

The bulk behaviour of the material may either be described by phenomenological damage models (Lemaitre and Chaboche (1990), Krajcinovic (1996), Bažant and Planas (1997)) or homogenised micromechanics based models (Budiansky and O'Connell (1976), Kunin (1982), Frantziskonis et al. (2001)). The former are frequently based on the notion of effective stress and the constitutive response is described by a phenomenological strain energy function, while the latter approach considers an averaged response of the materials microstructural features over a representative volume element (RVE). It should be noted however, that homogenisation of the material response is only valid so long as the material is statistically homogenous. Gitman (2006) has shown that for concrete undergoing distributed microcracking in the pre-peak hardening zone, the size of the RVE must increase to conform to this requirement, whereas in the post-peak softening regime, localisation of cracking effectively destroys the notion of a statistically representative material element, and homogenisation based approaches are therefore no longer applicable. The reason for this is that the crack localises to one element, or a band of elements, and creates a discontinuity that cannot be represented by an RVE.

The second broad category of continuum models deals with computational approaches to cracking. These have traditionally been divided into two classes; smeared cracking (Rashid, 1968), in which cracks (or damage) are represented at the integration points of elements (Figure 2.20(a)), and discrete approaches (Nilson, 1968) in which cracks are represented by separations between elements (Figure 2.20(b)). More recently, approaches based on embedding strong discontinuities within elements have also become popular (Sukumar et al., 2000 and Oliver et al., 2002 and 2003).

Traditional smeared models for cracking are essentially directional damage models but were not classified as such when they were developed. Examples of finite element models based on the smeared crack approach are given by Rots (1993), Bažant and Planas (1997), and Jefferson (2003a and 2003b). This approach is illustrated in Figure 2.20(a) below. Here, the cracks are not explicitly modelled but, in the simplest sense, are assumed to form a band of distributed microcracks across the finite element. Therefore, rather than considering a crack explicitly as a discrete displacement jump, the effect is spread or smeared to all Gauss points of the finite elements that contain the crack, by degrading the material properties at these points. The initially isotropic element stiffness is therefore transformed to an anisotropic form, and gradually the stiffness of the element in the direction of the principal stress is reduced to zero. This method can be thought of being synonymous with the crack band model of Bažant and Oh (1983), where the fracture process zone may be considered to be equal to the element size. Consequently, as noted by Vervuurt, mesh size and orientation significantly influence the results, however, consideration of higher order continua have been shown to decrease mesh dependency (de Borst and Muhlhaus, (1991)).

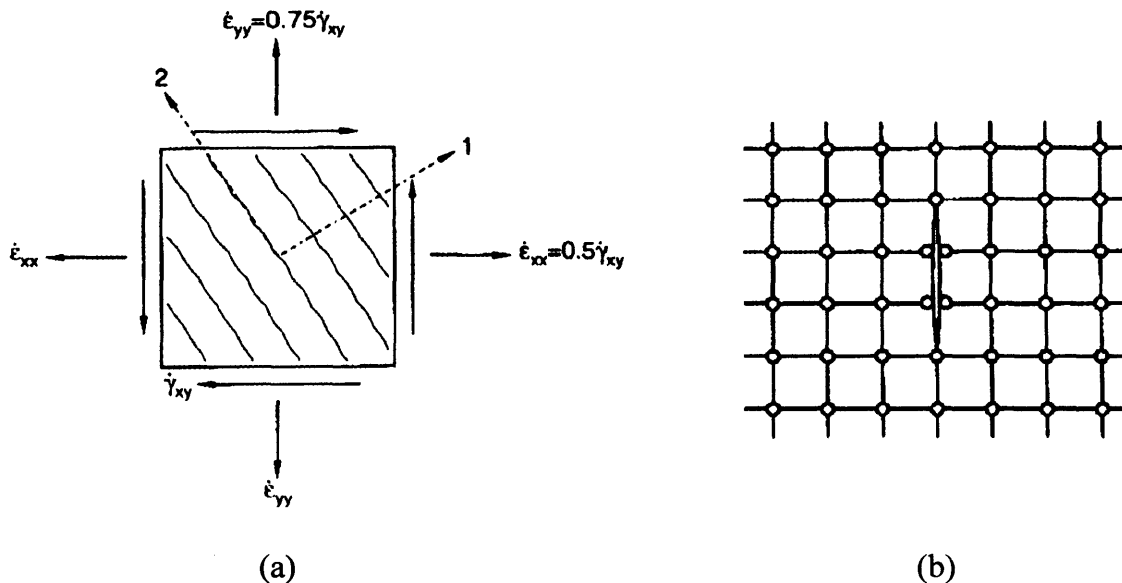


Figure 2.20. Illustration of (a) smeared crack approach (Rots, 1993), and (b) discrete crack approach (Hillerborg, 1985)

An alternative computational approach is one which explicitly studies how a pre-existing crack or crack-like defect is likely to grow within a structure. A common application of this approach is the discrete crack method which is often implemented with a cohesive crack model (Hillerborg (1985), Bažant and Planas (1997)). In this model (Figure 2.20(b)) the crack is represented as a discrete entity through the use of interface or special crack tip finite

elements. The zero thickness interface elements are embedded between the edges of adjacent ordinary finite elements by splitting the node (or allowing separation of double nodes) where the crack occurs, and their constitutive behaviour is governed by a traction-displacement cohesive law. This law is used to evaluate interface traction, S which depends upon normal and tangential displacement jumps, or non-dimensional displacement jump parameters. Crack propagation is simulated through progressive failure of these interface elements, however, in the absence of re-meshing, crack patterns are confined to the finite element edges, and the fracture is constrained to a discrete number of paths, decided *a priori*. The crack prediction capabilities of such models are therefore limited. Re-meshing techniques (Ingraffea and Saouma (1985), Valente (1991)), which modify the finite element mesh topology to explicitly capture a discontinuity, have a large computational overhead and are not readily applicable to non-linear problems (Alava et al, 2006).

The limitations of the traditional continuum damage models and computational approaches, as outlined above, have spurred a whole new array of models to be developed over recent years. For example, the problem of strain localisation, which is characterised by a concentration of deformations into a region of finite size in a real cementitious material, but which is found to localise to a single element (1D) or a single line of elements (2D), irrespective of their size, in the FE method. This has been addressed by various strain localisation limiting techniques, including those based on nonlocal continuum concepts (Pijaudier-Cabot and Bažant, 1987), higher-order gradient theories (Peerlings et al., 1996), and micropolar or Cosserat continuum descriptions (de Borst et al., 1993). These techniques ensure a finite localisation zone, and finite energy dissipation, however, their implementation into standard finite element codes is problematic. Traditionally, Bažant and Oh's (1983) crack band model has been used to regularise meshes but this method doesn't improve solution stability in contrast to the more recent models described above.

The issue of restricted fracture patterns produced by the discrete crack method has been addressed by the development of extended or generalised finite element methods (XFEM) (Daux et al., 2000) based on the partition of unity (Malenk and Babuska, 1996). The method is not only capable of modelling arbitrary propagation of cracks within elements, but is also capable of representing multiple cracks with secondary branches, thereby eliminating the need for remeshing. In addition, enhanced coarse mesh accuracy may be obtained by enriching the crack tip with true asymptotic displacement field information (Xiao and Karihaloo, 2006).

Finally, the limitation of homogenisation methods in the post-peak regime, and the need to achieve more realistic crack growth in concrete, has motivated recent investigations to use finite element simulations that explicitly model the microstructure. In these models heterogeneity can be implemented by assigning different properties to the finite elements. As reported in Schlangen (1993) and Vervuurt (1997), Rossi and Richer (1987) proposed a stochastic based model, whereby distributed fracture energy (E) properties are assigned to the planar continuum elements and failure is modelled along contact interface elements which have an elastic-brittle constitutive relationship with a distributed failure stress (σ_N) (Figure 2.21(a)).

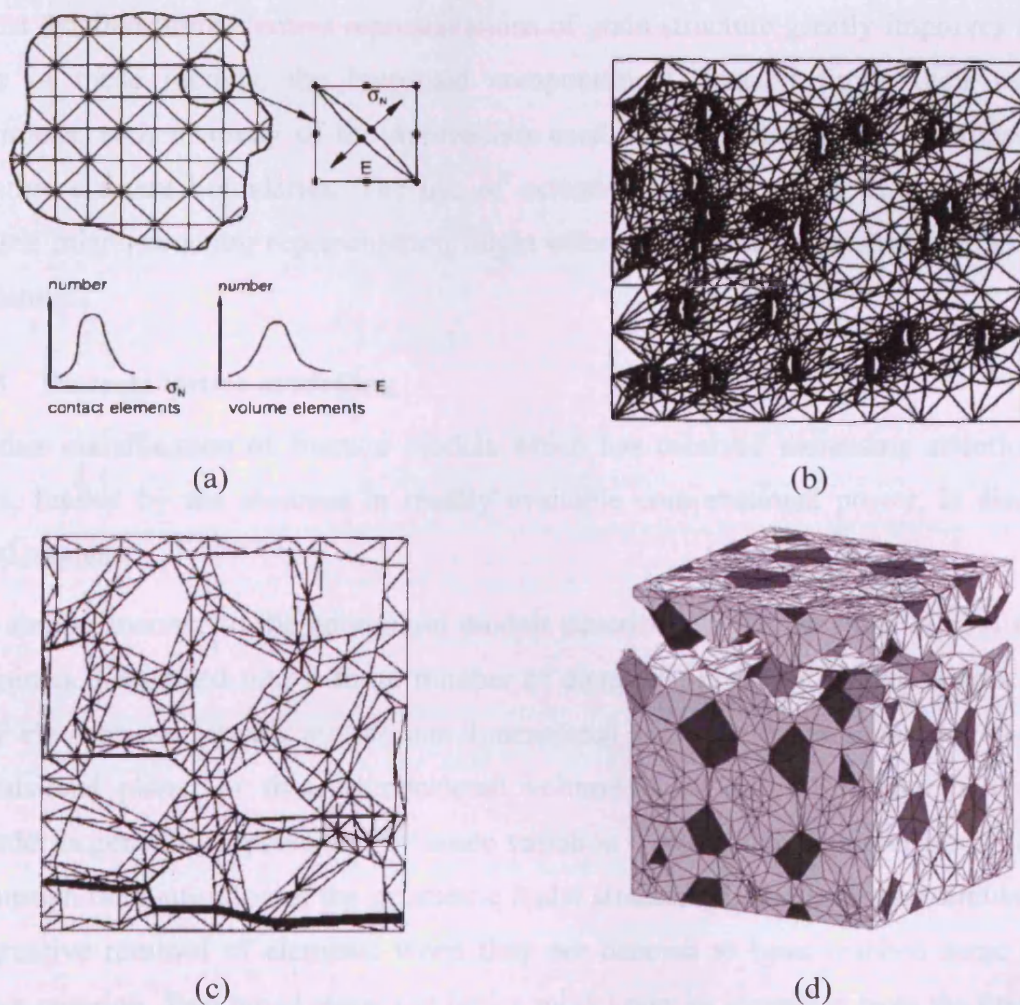


Figure 2.21. Continuum model discretisations containing heterogeneity: (a) Stochastic model (Rossi and Richer, 1987); (b) LEFM FE model (Wang et al., 1992); (c) 2D microstructural model (Carol et al., 2001), and (d) 3D microstructural model (Caballero et al., 2006).

Later models have explicitly represented the material structure to various degrees, as shown in Figure 2.21(b), (c), and (d). Wang et al. (1992 and 1997) represented the aggregate as fine

discretisations of circular inclusions of various sizes. The authors adopted a linear elastic fracture mechanics (LEFM) approach, with cracks initiating from minor imperfections embedded in the matrix-aggregate interface (Figure 2.21 (b)). Carol et al. (2001) undertook a microstructural analysis of concrete fracture using interface elements embedded between linear elastic triangular elements (Figure 2.21 (c)), in a similar manner to the earlier model of Vonk et al. (1991). A regular array of aggregate particles is prescribed, and then randomised during the discretisation process according to the numerical work of Stankowski (1990). This work has recently been extended to the third dimension (Figure 2.21(d)), although only coarse aggregate is currently captured in the model (Caballero et al., 2006).

Whilst detailed finite element representations of grain structure greatly improves the physical basis of these models, the increased computational demand limits their use to small specimens, and, in many of the approaches used, crack paths are still restricted to micro-structure element boundaries. The use of extended finite elements in conjunction with an explicit micro-structure representation might offer an interesting solution to this problem in the future.

2.5.3 Discrete lattice modelling

Another classification of fracture models which has received increasing attention in recent years, fuelled by the increase in readily available computational power, is discrete lattice based models.

In a similar manner to the continuum models described in the previous section the material domain is discretised into a finite number of elements, however, unlike continuum models these elements are usually simple one dimensional spring or beam elements rather than two dimensional planar or three dimensional volumetric elements. Material heterogeneity or disorder is generally represented by some variation in the material properties of the elements or through randomisation of the geometric nodal structure. Damage is then simulated through progressive removal of elements when they are deemed to have reached some pre-defined failure criterion. Two broad classes of lattice model may be identified from the literature.

2.5.3.1 Lattice spring or beam model

The first class is termed lattice spring or beam modelling and refers to the case whereby the material continuum is represented by a truss of bars or a frame of beams, and the properties of the bars or beams are derived from the phase of the material which they are considered to represent (e.g. aggregate, matrix, or interface in concrete). The elements may connect

neighbouring nodes, as in the Delft lattice model described in Chapter 3 (Schlangen and van Mier (1992a), Schlangen (1993), Lilliu and van Mier (2007)), or longer range connections may be defined, as in the random lattice model described by Burt and Dougill (1977). Combinations of short- and long-range connections have also been used to represent the respective plain concrete phase and fibre phase of fibre reinforced concrete, as illustrated in Figure 2.22(a) (Leite et al., 2007).

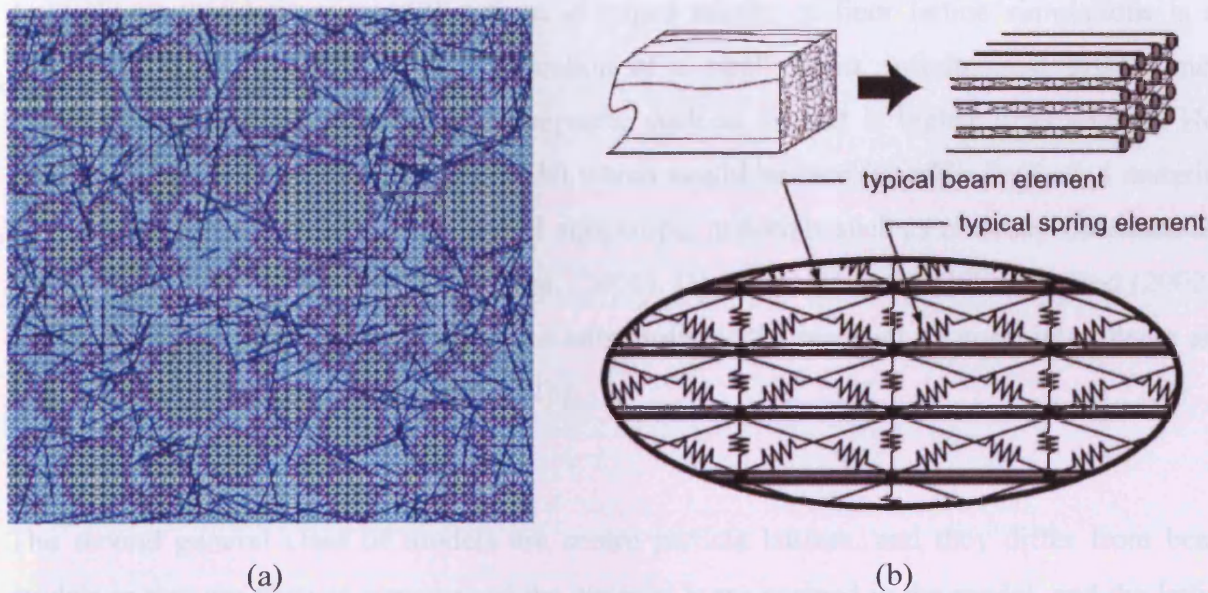


Figure 2.22. (a) 2D lattice discretisation of three phase concrete (matrix-interface-aggregate) and fibre reinforcement represented by long range nodal connections (Leite et al., 2007) (b) Combined anisotropic beam and spring model for wood (Vasic et al., 2005)

Lattice beam models have been shown to possess very good qualitative properties, and have been used to correctly predict crack patterns in concrete under uniaxial tension (Prado and van Mier, 2003), four-point shear (Schlangen, 1993), mixed mode tension and shear (Noor-Mohamed et al., 1993) and anchor pull-out (Vervuurt et al., 1994). In addition, the model has been shown to capture the effect of varying boundary conditions under uniaxial tension (van Mier et al. (1995), van Vliet (2000)) and to a lesser degree uniaxial compression (Schlangen and Garboczi, 1997). It is the good qualitative properties and the flexibility to represent a multitude of varying types of heterogeneity that has made lattice beam modelling a popular choice for researches in many different fields.

Lattice beam or bar models have been used extensively in physics for simulating problems of electrical conductivity and cracking in disordered materials, (e.g. Hermann and Roux (1990), Meakin (1991), and Alava et al. (2006)), and more recently by engineers studying the fracture of different heterogenic materials such as concrete (Schlangen and van Mier, 1992a),

sandstone (Vervuurt et al. (1996), van Mier et al. (1996)), cement paste (Copuroglu (2005), Tan et al. (2007)). They have also been applied to a wide range of other materials, including: clay (Meakin et al., 1989); polymer fibres (Termonia et al., 1985); paper (Ostoja-Starzewski and Stahl, 2000), pharmaceutical tablets (Kuentz et al., 1999), bone (Bruyere et al., 1998) and; ceramics (Curtin and Scher (1990), Jagota and Bennison (1994)). Feng (2003) presents a multiscale lattice approach to the modelling of fatigue cracking in hot mixed asphalt. The determination of lattice properties from averaged results of finer lattice simulations is an interesting concept, although the application of a small strain, infinitesimal displacement model to a large strain viscoelastic composite such as asphalt is highly questionable. Hou (2007) presents a large strain lattice model which would be more suitable for such a material. The method has also been used to model anisotropic materials such as masonry (Beranek and Hobbelman, 1998) and wood (Vasic et al. (2005), Davids and Landis (2003), Parrod (2002)). The authors have chosen to represent the anisotropy of the material by combining beam and spring elements as shown in Figure 2.22(b).

2.5.3.2 Centre particle lattice model

The second general class of models are centre particle lattices, and they differ from beam models in that the particle structure of the material is maintained in the model, and the lattice elements now represent presumed inter-particle stress transfer mechanisms, as shown in Figure 2.23(a).

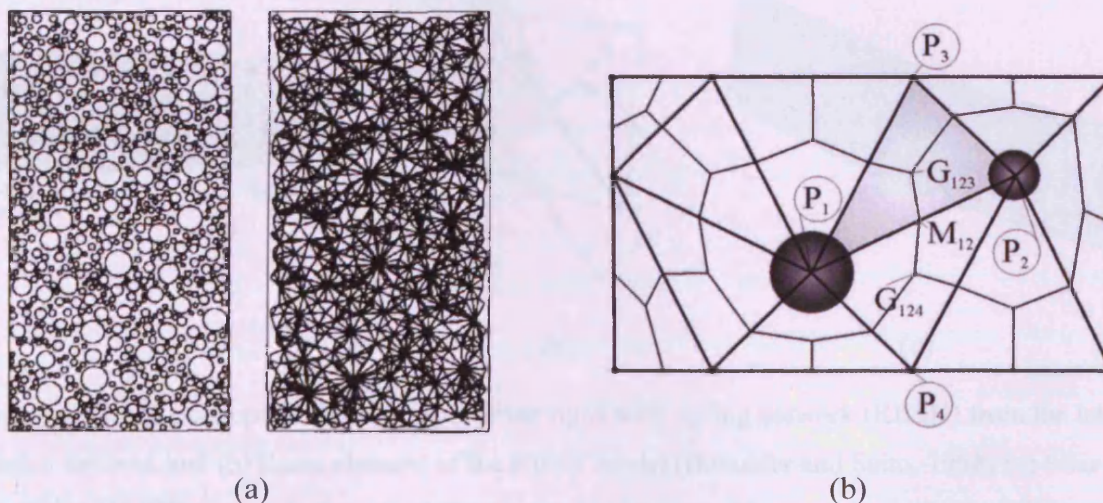


Figure 2.23. (a) Centre particle lattice model (Bažant et al., 1990) (b) Voronoi tessellation of a Delaunay triangulation (Cusatis et al., 2006)

Bažant et al. (1990) and Beranek and Hobbelman (1994) applied central particle lattices to the constitutive modelling of concrete through the assemblage of spheres. In centre particle

lattices, elements are assumed to span between particle centres, and therefore comprise part aggregate, matrix and interface. Determination of element properties is therefore more complicated, and softening is usually considered to be solely a material phenomenon since it is built into the constitutive relationship of every lattice element.

These forms of centre particle lattices have been developed extensively for application to concrete in recent literature. Cusatis, Bažant and Cedolin (2003a, 2003b, 2006) and Cusatis and Cedolin (2007) present a confined shear lattice (CSL) model in two and three dimensions. In this model, nodal geometry is generated randomly according to a given grain (aggregate) size distribution. Lattice connections are then obtained from a Delaunay triangulation of nodal points, and the effective cross-sectional areas of connecting struts, which are also potential crack planes, are obtained from a Voronoi tessellation, as shown in Figure 2.23(b) for the 2D case. The displacements and rotations at lattice nodes are defined by rigid body kinematics according to Zubelewicz and Bažant (1987), and each strut connecting adjacent particles can transmit both axial and shear forces. Quite a complicated constitutive law is implemented which is intended to simulate fracture, friction and cohesion at the meso-level. Transversal confining strains, obtained by assuming linear displacement fields within each tetrahedron of the Delaunay triangulation govern the behaviour in tension and shear.

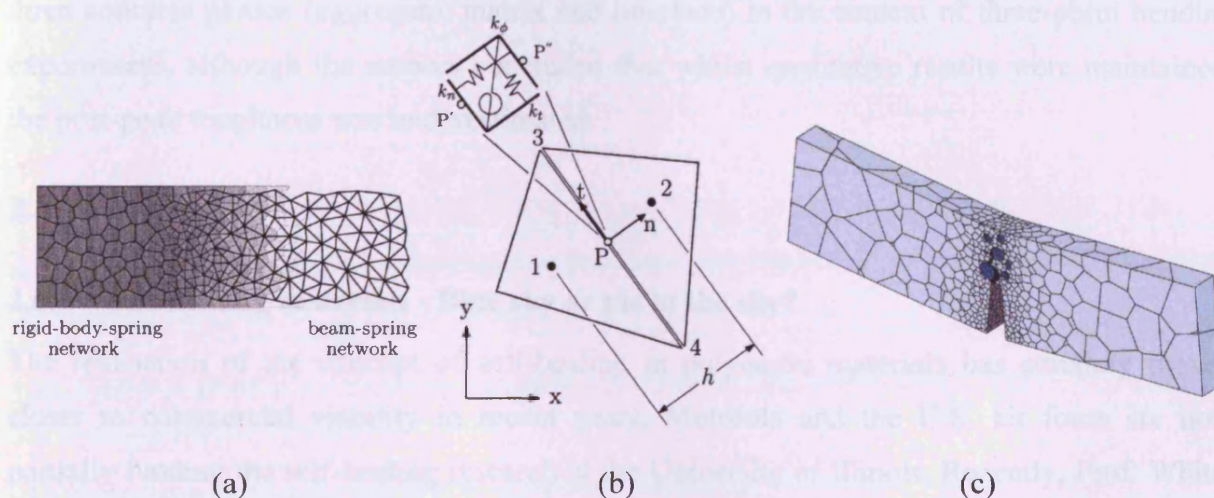


Figure 2.24. (a) Conceptual development of the rigid body spring network (RBSN) from the lattice beam network and (b) Basic element of the RBSN model (Bolander and Saito, 1998) (c) Slice of fractured 3D RBSN model of notched three point bend beam with aggregate inclusions (Yip et al., 2006).

A similar model has also been developed over the last decade by Bolander and co-workers at the University of California (Bolander and Saito (1998), Bolander and Le (1999), Bolander et

al. (2000, 2001), Bolander and Berton (2004), Bolander and Sukumar (2005), Yip et al. (2005, 2006), and Li et al (2006)). In the rigid body spring network (RBSN) model, Voronoi tessellations of Delaunay triangulations between randomly generated nodal structures have also been implemented, as in the CSL model described above, however, nodes are no longer confined to representing aggregate particle centres. The model is therefore used at a much finer scale than the CSL model, as shown by the Voronoi discretisation of individual aggregate particles in Figure 2.24(c).

The RBSN model may be thought of as a modification to the classical lattice beam model (Figure 2.24(a)), whereby the rigid particle is essentially obtained by considering the unit cell created by joining the ends of half beams emanating from individual nodes. For a regular periodic triangular lattice this equates to a hexagonal shape in two dimensions (Figure 3.7). The two dimensional lattice element consists of a mass-less set of normal, tangential, and rotational springs connected to the lattice nodes via rigid arms, as shown in Figure 2.24(b). The analysis is again non-linear since a cohesive crack approach is adopted to maintain objectivity in terms of fracture energy dissipation. As a result, adaptive mesh refinement is required in order to obtain sufficient fracture information without excessive computation overhead. Yip et al. (2006) did examine the use of locally brittle fracture properties for the three concrete phases (aggregate, matrix and interface) in the context of three-point bending experiments, although the authors concluded that whilst qualitative results were maintained, the post-peak toughness was underestimated.

2.6 Conclusions

2.6.1 Self-healing materials - Blue sky or pie in the sky?

The realisation of the concept of self-healing in polymeric materials has certainly moved closer to commercial viability in recent years. Motorola and the U.S. air force are now partially funding the self-healing research at the University of Illinois. Recently, Prof. White, team leader at Illinois, has also been quoted, in relation to future development time frames, as saying that 'self-healing circuit boards are probably only three to five years away'. The issue regarding the cost of Grubbs' catalyst (over \$100 per kg (Dry, 2004)) has been recently addressed by the work on microencapsulation of the catalyst in wax, however, questions remain regarding the long term shelf-life, and temperature resistance of this material.

The progress made in recent years on the development of self-healing polymers suggests that this material is certainly on the way to becoming commercially viable, particularly for

specialist uses, where it is not possible, or practical, to repair a material when in service; such as prosthetics, artificial organs, satellites, etc. Recent studies on self-healing polymeric material specimens have shown the great potential that microencapsulation of a healing agent has in increasing the longevity and durability of these materials.

Concrete is a material which is in serious need of improvements aimed at solving its long term durability problems, and thus meeting its prescribed design life, without the need for the implementation of intensive inspection and maintenance regimes.

Concrete and polymers are very different materials, however. Thermosetting plastics are essentially hydrocarbons with various monomer inclusions, which have undergone a polymerisation process, and generally exhibit perfectly elastic brittle failure. Concrete, on the other hand, is a complex quasibrittle composite material which has length scales ranging from macro aggregate inclusions, to micro cement particles, down to C-S-H formation at the nano-scale. In addition, concrete does not (generally) have specialist applications, where cost becomes secondary to performance. Therefore, any self-healing technology proposed for use in concrete, must not only produce the necessary mechanical and durability properties, but must also be readily available and at a commercially viable cost.

As highlighted in this chapter, autonomically healed concrete has a significant leap to make in order to catch up with its polymer counterpart. To date, the feasibility of autonomic healing in cementitious materials has been shown through the active release of epoxy resin and alkali-silika solutions from continuous supply systems into concrete, and through the active release of cyanoacrylate from hollow glass fibres into an engineered cementitious material. However, no 'prototype' system for direct application to the construction industry has yet been developed.

The potential gains of developing an effective self-healing concrete are enormous: both in terms of addressing the durability issues of concrete, and the resulting socio-economic impact that this would have. This potential socio-economic impact would be felt by many countries through: (i) an increase in the safety of civil infrastructure and structures constructed from self-repairing concrete; (ii) a reduction in repair, refurbishment and replacement operations and costs, with consequential reductions in construction related injuries and deaths, and; (iii) a reduction in construction wastes, raw material and energy consumption, and production of greenhouse emissions.

In a recent report (Sharp and Clemena, 2004) which studied the potential application of advanced materials specifically to the civil engineering area of highway infrastructure, self-healing concrete gained acknowledgement as offering potential benefit in the future, and was rated 12th out of the 48 advanced materials studied. Given the very early stages at which the development of this material is currently at, and the recommendation of the authors that “this material should not be ignored”, it is felt that the creation of a low cost, passive, and distributed self-healing mechanism for concrete is a research area which should be given serious attention in the future.

2.6.2 Modelling autonomic healing in concrete

It is clear from the literature that both continuum based and discrete modelling methods may be applied to the numerical analysis of self-healing cementitious materials. The choice of a suitable modelling method is dependent primarily on the type of problem, the scale of the specimens to be considered, and the nature of the information required, rather than the ‘correctness’ of the model.

In respect to continuum models, since the complex constitutive material relationships, damage, and potential healing evolution are incorporated within the model formulation, the computational overhead of continuum models is considerably less than that of discrete methods. They are therefore far more adept at providing global response predictions for full scale structural elements, although this is often at the expense of detailed fracture process information. In addition, parameter identification requirements of continuum models can be problematic, since experimental determination of material properties can introduce undesirable size effect and boundary effect conditions (van Mier et al., 1995).

Conversely, the simplicity of the constitutive relations often employed in lattice models drastically limits the material input parameters to just the stiffness and strength properties of the material phases. The simple but yet effective consideration of damage evolution within cementitious materials offered by the lattice modelling method also opens up the potential of an equally simplified, yet potentially informative consideration of the healing process. In addition, since the microstructure is explicitly included, discrete lattice models may be classified as offering a more physical-based approach because detailed information about the fracture processes in relation to the material structure is obtained. In this respect, the lattice beam method is considered to offer greater flexibility at representing material microstructure than centre particle lattices, since several different material phases may be included and the

model is not confined to presumed stress transfer mechanisms between individual particles. This has been confirmed by the wide range of heterogeneous isotropic and anisotropic materials that the method has been applied to within the literature.

Therefore, with respect to the autonomic healing of small scale laboratory based specimens, it is considered that the additional fracture information offered by the discrete lattice beam model could prove useful in determining the onset of healing, modelling the degree of healing, and subsequently determining specimen fracture under loading post-healing. The lattice beam modelling method has therefore been described in further detail in Chapter 3.

Chapter 3

Lattice beam modelling – *the fundamentals*

3.1 Introduction

This chapter contains an overview of the fundamental aspects of the lattice spring or beam modelling technique, as previously outlined in section 2.5.3.1. Particular focus is given to the current application of the method to the modelling of cementitious materials, and the main advantages and current limitations of the method are highlighted where appropriate.

3.1.1 Historical development

In 1941 Alexander Hrennikoff, in an attempt to overcome the mathematical difficulties associated with the solution of differential equations of the theory of elasticity, developed the ‘framework method’:

“Essentially, the method consists in replacing the continuous material of the elastic body being studied by a framework of bars arranged according to a definite pattern, the elements of which are endowed with elastic properties suitable to the type of problem”

(Hrennikoff, 1941).

Hrennikoff developed distribution factors which determined the stresses caused in various members by the movement of a single main joint. Subsequent successive movement of nodes were then undertaken in order to minimise the out of balance forces at internal nodes. These laborious calculations were undertaken manually, and therefore it was not until the advent of computers that the method was given further attention and due acknowledgement as being of landmark status and a true predecessor to the more common finite element method.

Burt and Dougill (1977) then extended the method for simulating progressive failure of heterogeneous materials through successive beam removal, and more recently lattice models have been widely used in the form of the random fuse model (RFM) for solving conductivity problems through the application of Kirchhoff’s Laws to fuse networks (see Krajcinovic, 1996

for a comprehensive description). In addition, the lattice method has been used extensively within the field of physics for studying cracking in disordered materials (Herrmann and Roux, 1990), and as a natural extension to pseudo one-dimensional fibre-bundle models, for developing statistical based fracture models, as extensively reviewed recently by Alava (2006).

Bažant et al. (1990) and Schlangen and van Mier (1992) were the first to extend the method to the simulation of progressive failure within concrete, using truss (pin-jointed) and frame (Euler-Bernoulli) beams, respectively. Since 1992, the lattice beam method has been used extensively by the group in Delft to examine various aspects of concrete failure, including the effect of specimen size (van Vliet (2000), Man and van Mier (2008)), the effect of aggregate type (Schlangen and van Mier, 1992b), and the physical reasons behind the softening behaviour of quasi-brittle materials, such as crack face bridging (Schlangen and van Mier, 1992a) and self-affine fractality (van Mier et al. (1997), Chiaia et al. (1997)). More recently, application of the model has been further extended to examining deterioration mechanisms in cementitious materials such as autogenous shrinkage (Schlangen et al., 2007), frost salt scaling (Copuroglu et al., 2005), and alkali-silica reaction (Schlangen and Copuroglu (2005), Schlangen and van Breugel (2005)).

3.1.2 Basic concept

The basic concept of lattice spring or beam models is that the material continuum is approximated *a priori* by a system of discrete one dimensional elements that are connected together at nodes. The generation of the nodal structure may be of a regular or random format and element connectivities may be defined on the basis of nearest neighbour, next nearest neighbour, or some other pre-defined rule. The connecting elements may be trusses or beams according to the number of degrees of freedom they possess and they may be further classified according to the constitutive relationship employed.

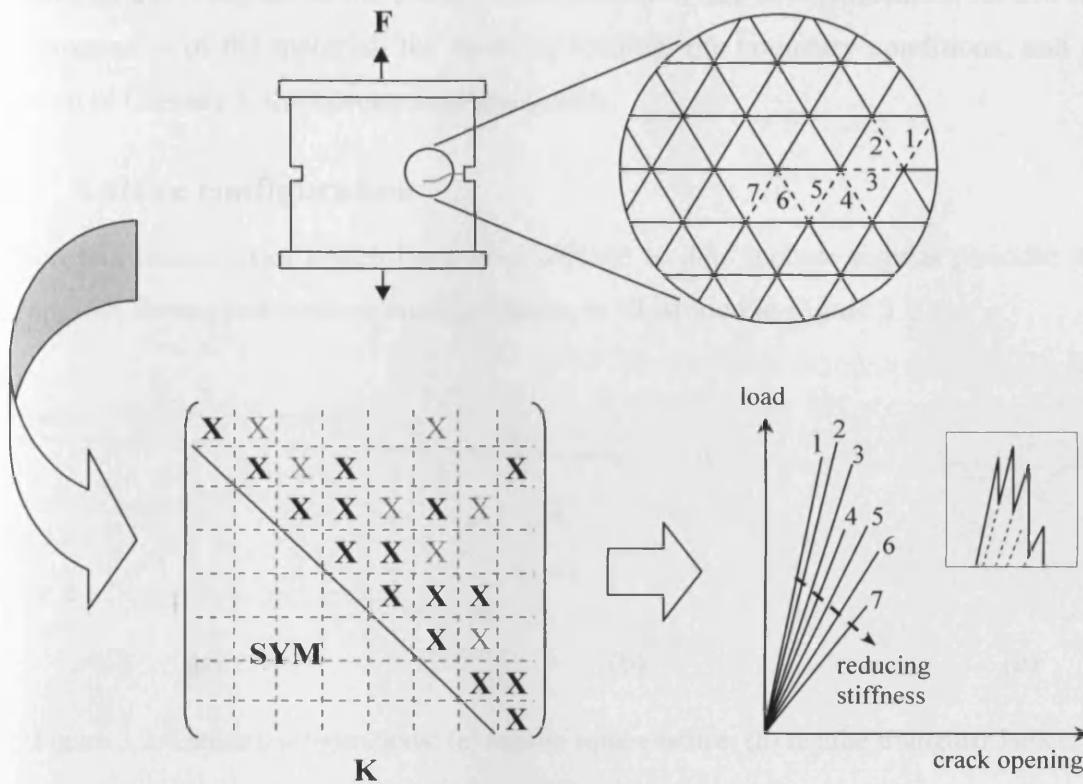


Figure 3.1. Schematic representation of the basic concept of the lattice beam modelling method

By means of compensation for this simplified approach, meshes are generally far finer than for continuum methods, and this allows for explicit representation of material disorder and justifies the common adoption of very simple elastic-brittle material behaviour at the local element level. It is in fact the adoption of such an idealised constitutive relationship that allows such fine meshes, with vast numbers of degrees of freedom, to be solved economically. This is of critical importance, since fracture is simulated through progressive removal of individual elements that are deemed to have reached some pre-defined fracture condition. By adopting linear elastic perfectly brittle material behaviour the problem is reduced to the solution of a set of linear equations for each stage of the dilution process i.e. the fracture process may be followed step by step, in a series of quasi-equilibria. This ‘physical’ dilution process is mirrored numerically by the gradual degradation of the global stiffness matrix due to element stiffness removal. This results in a decaying macroscopic stiffness response for the specimen, as illustrated in Figure 3.1 by the diminishing gradients of the linear force-displacement relationships of the lattice at various stages of lattice dilution (damage). The envelope of these linear lines of ever decreasing gradient gives rise to the non-

linear global hardening and softening response for the system. The nature of this response is related to the evolution of the crack pattern, which in turn is dependent on factors such as the heterogeneity of the material, the mode of loading, the boundary conditions, and as will be shown in Chapter 5, the failure criterion chosen.

3.2 Lattice configuration

The main lattice types which have been utilised to date include regular periodic square and triangular forms, and random configurations, as illustrated in Figure 3.2.

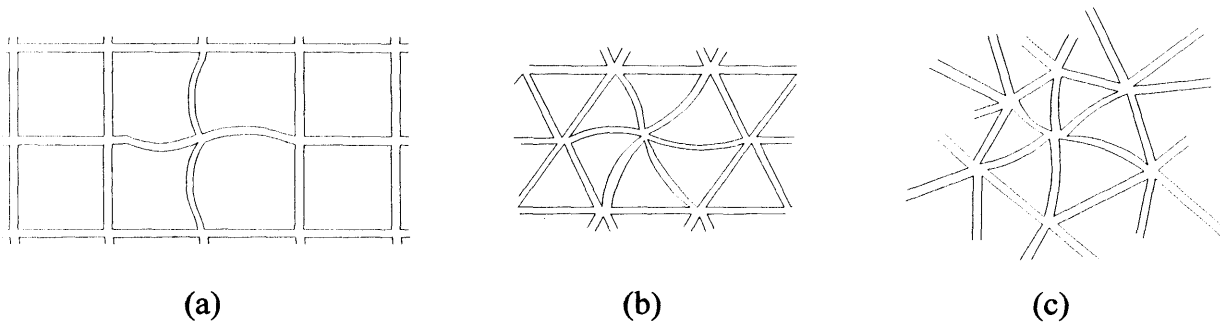


Figure 3.2. Lattice configurations: (a) regular square lattice; (b) regular triangular lattice, and; (c) random lattice.

Herrmann et al. (1989) and Herrmann (1991) originally used a regular square lattice to study the fracture of two dimensional elastic lattices with random disorder, and more recently Arslan et al. (2002) and Ince et al. (2003) have applied this type of lattice to the fracture of concrete. Van Mier (2004) highlights the fact, however, that the regular square lattice yields a Poisson's ratio of zero, which makes it unsuitable for modelling concrete, which has a Poisson's ratio of approximately 0.2. In addition, Karihaloo et al. (2003) showed that the square Euler Bernoulli beam lattice is a special case of an orthotropic micropolar continuum, and is therefore not suitable for representing an isotropic material such as concrete. Various modifications to the square (or cubic in 3D) configuration have been proposed, including the introduction of diagonal members connecting opposing corner nodes (Rocha and Riera (1991), Leite et al. (2004)). The adoption of overlapping lattice elements seems to be rather arbitrary, however, and direct equivalence with the underlying continuum is less obvious.

Crossing of elements was also another disadvantage of the earlier random lattice model of Burt and Dougill (1977), as reported by Schlangen (1993). The randomness was intended to reduce the predisposition of global crack orientations to follow heterogeneities in regular meshes, however, visualisation of the fracture process even in two dimensions proved

extremely difficult. This problem has since been overcome by Schlangen (1993) and others through the development of a random lattice based on a regular square grid, S (Figure 3.3(a)).

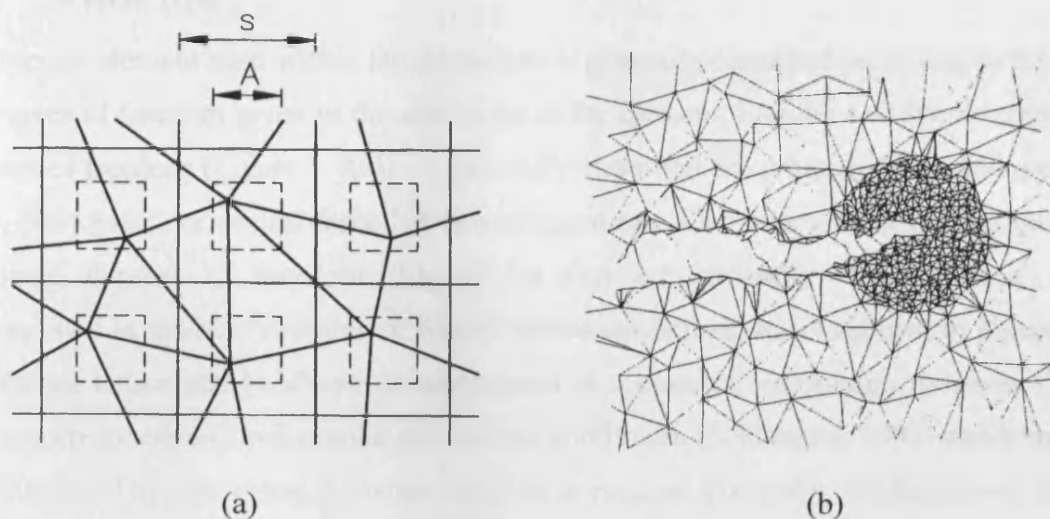


Figure 3.3. (a) Generation of a random lattice based on a regular square grid (b) Re-meshing procedure during crack growth (Vervuurt, 1997)

Nodes are allocated randomly within boxes of size A and the three closest nodes are connected using the Voronoi construction. The randomness of the mesh may then be altered by changing the ratio $A:S$ from 0 to 1. Vervuurt (1997) extended this procedure even further by implementing the random lattice within a re-meshing procedure (Figure 3.3(b)). In this procedure, the coarse mesh around a crack tip is replaced with a circular 'zone' of random mesh which has a finer resolution. Only elements contained within this finer discretisation are then allowed to fracture. The centre of this circular 'zone' is moved to the new location of the crack tip when this tip is about to penetrate the coarse mesh.

This method is clearly capable of capturing more information about the post-localisation fracture process zone, however, the inability of beams to break outside of this zone means that the model is not capable of capturing long-range interactions and distributed microcracking prior to the localisation of strains. The author also concludes, following a comparison of various lattice configurations, that the regular triangular lattice when combined with a microstructure overlay (section 3.4.1) offers an equal if not more realistic crack pattern than the random lattice.

All of the succeeding work presented in this thesis therefore focuses on the use of the regular periodic triangular lattice as illustrated in Figure 3.2 (b).

3.3 Lattice element

3.3.1 Element type

The type of element used within lattice models is generally classified according to the number of degrees of freedom given to the end nodes of the element. Elements with only translational degrees of freedom (Figure 3.4(a)) are generally classified as springs or bars, and are used in truss, pin-jointed, or central force lattice configurations. Elements with both translational and rotational degrees of freedom (Figure 3.4 (b)) are generally called beams, and are incorporated in moment resisting or framed lattice configurations. As shown in Figure 3.4 the simple bar lattice can be shown to correspond to a classical continuum, whereas the beam lattice corresponds to a micropolar or Cosserat continuum (Schlangen (1993) and Karihaloo et al. (2003)). The bar element, when used in a regular triangular configuration, can only represent materials with a fixed Poisson's ratio of $1/3$, and therefore only a limited range of materials like steel and ice can be studied (van Vliet and van Mier, 1996). The beam element, however, is theoretically able to represent any general Poisson's ratio between -1 and $1/3$, although Karihaloo et al. (2003) comments that due to the slenderness assumptions of the Euler Bernoulli beam (see section 3.3.2), when this element type is used the model does not admit a ratio of below approximately 0.2 .

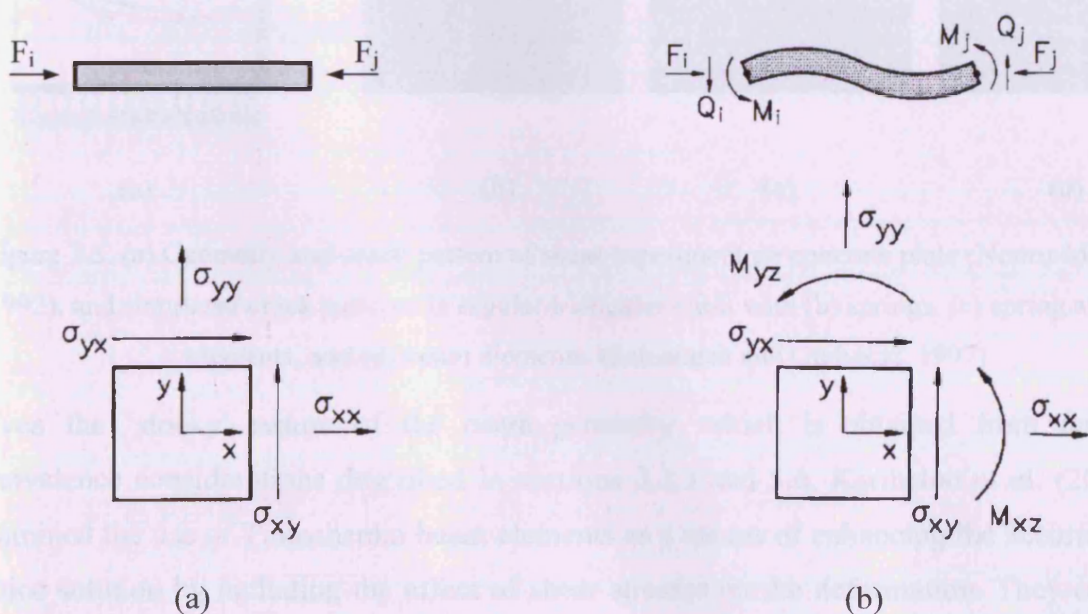


Figure 3.4. Stress in (a) classical continuum represented by a bar element, and (b) micropolar continuum represented by a beam element (Schlangen, 1993)

Both element types have been used extensively to model disordered materials within the literature. Curtin and Scher (1990), Jagota and Bennison (1994), and Schlangen and Garboczi (1996) among others have examined spring models, and Herrmann (1991), Schlangen and van Mier (1992a), and van Mier and van Vliet (2003) have utilised the additional rotational rigidity offered by beam models. Schlangen and Garboczi (1996 and 1997) undertook an interesting study on the effect of element type on the crack patterns produced by a shear plate test, as investigated experimentally by Nooru-Mohamed (1992). They examined the two cases presented in Figure 3.4, and an intermediate case whereby the lattice elements had both axial and shear capacity but no moment capacity. The fracture patterns for the three cases without any heterogeneity are presented in Figure 3.5. It can be seen that the micropolar continuum represented by the beam discretisation (Figure 3.5 (d)) gives the best agreement with the experimentally observed crack pattern. Overlapping cracks at the scale shown in Figure 3.5, or locally in the form of crack face bridges around aggregate inclusions (van Mier, 1997), are not captured very well by spring networks since local rotations of the material cannot be accounted for (Schlangen and van Mier, 1995).

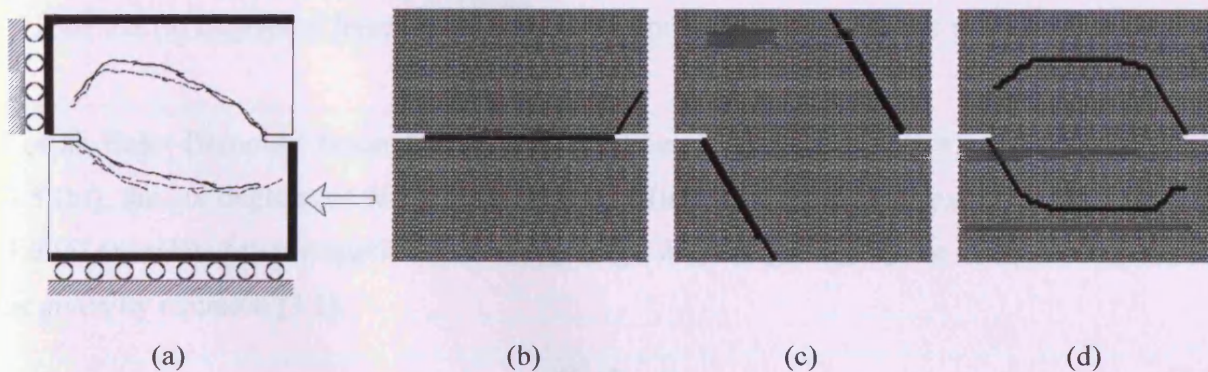


Figure 3.5. (a) Geometry and crack pattern of shear experiment on concrete plate (Nooru-Mohamed, 1992), and simulated crack patterns in regular triangular mesh with (b) springs, (c) spring and shear elements, and (d) beam elements. (Schlangen and Garboczi, 1997)

Given the ‘stocky’ nature of the beam geometry, which is obtained from the energy equivalence considerations described in sections 3.3.3 and 5.6, Karihaloo et al. (2003) also examined the use of Timoshenko beam elements as a means of enhancing the accuracy of the lattice solution by including the effect of shear stresses on the deformation. They concluded that the shear deformation does little to alter the pre-peak load-displacement response, but it was found to suppress interfacial debonding and produce a more diffuse crack pattern, thereby increasing the amount of energy absorbed before fracture, when compared to the Euler-Bernoulli beam. It should be noted, however, that their comparison was for the case whereby

finite deformation was also considered through a simplified update of the nodal coordinates at every loading increment. As a result of this the effect of the shear deformation would have been exaggerated when compared to an infinitesimal displacement model.

The Euler-Bernoulli beam has therefore been used exclusively in the development and modelling work reported in this thesis.

3.3.2 FE formulation

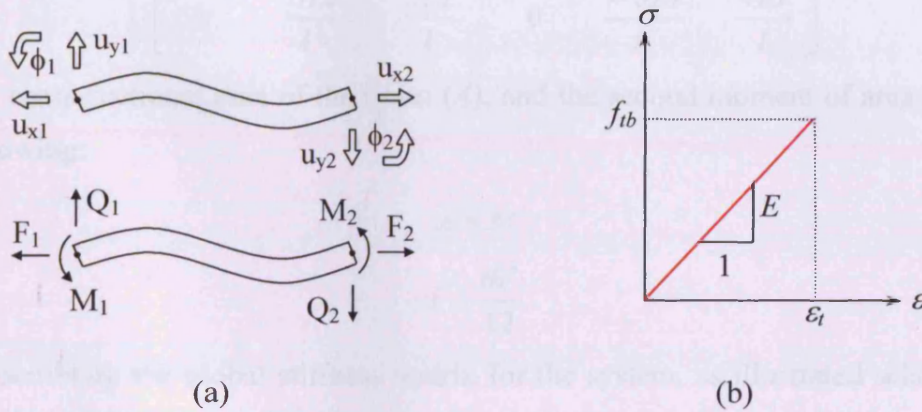


Figure 3.6. (a) Degrees of freedom and forces acting on beam (b) Constitutive relationship for single beam

For an Euler-Bernoulli beam with a perfectly linear elastic constitutive relationship (Figure 3.6 (b)), the six degrees of freedom per beam, \mathbf{u} (u_{x1} , u_{y1} , ϕ_1 , u_{x2} , u_{y2} , ϕ_2) as shown in Figure 3.6 (a) are related to the applied forces, \mathbf{F} (F_1 , Q_1 , M_1 , F_2 , Q_2 , M_2) by the element stiffness, \mathbf{k}_e , as given by equation (3.1):

$$\mathbf{F} = \mathbf{k}_e \cdot \mathbf{u} \quad (3.1)$$

For a beam with Young's modulus E , length l , height h , and thickness t this can be written as (Coates et al., 1988):

$$\begin{bmatrix} F_1 \\ Q_1 \\ M_1 \\ F_2 \\ Q_2 \\ M_2 \end{bmatrix} = \begin{bmatrix} \frac{EA}{l} & 0 & 0 & -\frac{EA}{l} & 0 & 0 \\ 0 & \frac{12EI}{l^3} & \frac{6EI}{l^2} & 0 & -\frac{12EI}{l^3} & \frac{6EI}{l^2} \\ 0 & \frac{6EI}{l^2} & \frac{4EI}{l} & 0 & -\frac{6EI}{l^2} & \frac{2EI}{l} \\ -\frac{EA}{l} & 0 & 0 & \frac{EA}{l} & 0 & 0 \\ 0 & -\frac{12EI}{l^3} & -\frac{6EI}{l^2} & 0 & \frac{12EI}{l^3} & -\frac{6EI}{l^2} \\ 0 & \frac{6EI}{l^2} & \frac{2EI}{l} & 0 & -\frac{6EI}{l^2} & \frac{4EI}{l} \end{bmatrix} \begin{bmatrix} u_{x1} \\ u_{y1} \\ \phi_1 \\ u_{x2} \\ u_{y2} \\ \phi_2 \end{bmatrix} \quad (3.2)$$

Where the cross-sectional area of the beam (A), and the second moment of area (I) are given by the following:

$$A = ht \quad (3.3)$$

And:
$$I = \frac{th^3}{12} \quad (3.4)$$

Prior to assembling the global stiffness matrix for the system, as illustrated schematically in Figure 3.1, the equilibrium condition must be written in terms of the global reference axes, thereby taking account of the individual orientations of the beams (Figure 3.7(b)). Equation (3.1) therefore becomes:

$$\bar{F} = \mathbf{T}^T \mathbf{k}_e \mathbf{T} \cdot \bar{u} \quad (3.5)$$

where \mathbf{T} is the rotational transformation matrix:

$$\mathbf{T} = \begin{bmatrix} \cos(\theta) & \sin(\theta) & 0 & 0 & 0 & 0 \\ -\sin(\theta) & \cos(\theta) & 0 & 0 & 0 & 0 \\ 0 & 0 & 1 & 0 & 0 & 0 \\ 0 & 0 & 0 & \cos(\theta) & \sin(\theta) & 0 \\ 0 & 0 & 0 & -\sin(\theta) & \cos(\theta) & 0 \\ 0 & 0 & 0 & 0 & 0 & 1 \end{bmatrix} \quad (3.6)$$

3.3.3 Element geometry

For a regular periodic triangular lattice the length of the beam element has traditionally been selected based upon the minimum size of mesostructure that one wishes to represent (see section 3.4.1). For the case of concrete Schlangen (1993) suggests a beam length of the order of two to three times smaller than the minimum aggregate diameter. The thickness of the beam is generally set to unity for the two dimensional plane stress representation, and the

height of the beam is determined from consideration of the equivalence in strain energy stored in a unit cell of the lattice compared to its continuum counterpart, under constant strains:

$$U_{cell} = U_{continuum} \quad (3.7)$$

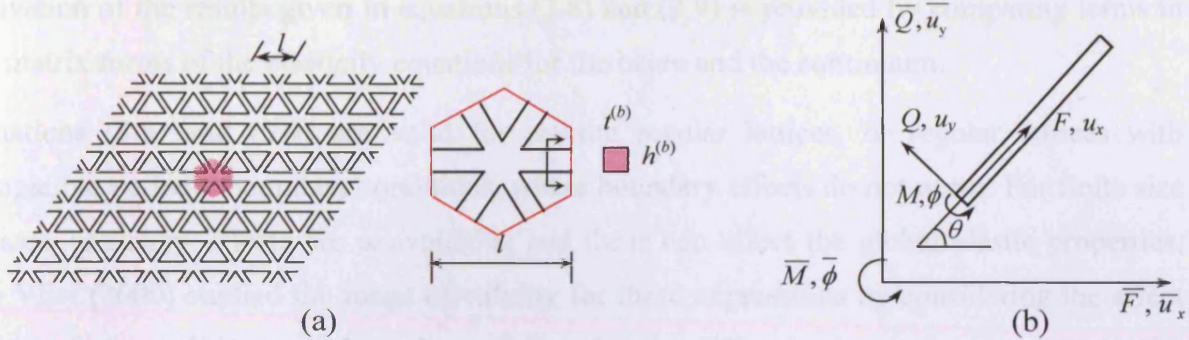


Figure 3.7. (a) A regular triangular beam lattice with a hexagonal unit cell (b) Element forces and displacements in global and local coordinates

This equivalence is presented by Schlangen and Garboczi (1997), and a rigorous mathematical derivation is given by Karihaloo et al. (2003), the main results of which are presented in equations (3.8) and (3.9) below.

$$\nu = \frac{1 - \left(\frac{h}{l}\right)^2}{3 + \left(\frac{h}{l}\right)^2} \quad (3.8)$$

$$\frac{E}{E^{(b)}} = 2\sqrt{3} \frac{h}{l} \frac{1 + \left(\frac{h}{l}\right)^2}{3 + \left(\frac{h}{l}\right)^2} \frac{t^{(b)}}{t} \quad (3.9)$$

where E , ν , and t are Young's Modulus, Poisson's ratio, and the thickness of the continuum, and $E^{(b)}$, h , l , and $t^{(b)}$ are the Young's Modulus, height, length, and the thickness of the beam. In order to model a Poisson's ratio of 0.2 for concrete, equation (3.8) gives an aspect ratio for the beam of:

$$\frac{h}{l} = \frac{1}{\sqrt{3}} \quad (3.10)$$

In the results presented in later chapters the height of the beam has therefore been set to $l/\sqrt{3}$ so that a global Poisson's ratio value of 0.2 is maintained. It should be noted, however, that

substituting this aspect ratio into equation (3.9) suggests that Young's modulus of the beam should be 1.25 times that of the continuum it is representing.

The issue of strain energy equivalence is revisited in section 5.6. In this section a full derivation of the results given in equations (3.8) and (3.9) is provided by comparing terms in the matrix forms of the elasticity equations for the beam and the continuum.

Equations (3.8) and (3.9) are valid for infinite regular lattices, or regular lattices with compatible periodic boundary conditions, where boundary effects do not occur. For finite size lattices, boundary effects are unavoidable and these can affect the global elastic properties. van Vliet (2000) studied the range of validity for these expressions by considering the effect of boundary conditions on the values of E and ν for different size lattices under uniaxial tension. (Note: size is defined as the number of elements in the horizontal or vertical direction). He concluded that as the size of the lattice increased the numerical values of E and ν converged to the theoretically predicted values. The regular triangular mesh was also found to perform better when the base of the triangle was perpendicular to the direction of uniaxial loading.

3.4 Representing heterogeneity

In order to simulate fracturing of heterogeneous materials such as concrete, the disorder contained within the material must be represented in some form. For lattice discretisations utilising linear elastic perfectly brittle beam elements (Figure 3.6), only three properties of the beams may be altered, namely: stiffness; strength, and; beam length. The main options for representing heterogeneity therefore include:

1. Randomly assigning individual element stiffnesses or strengths to a regular triangular lattice, usually according to some form of statistical distribution. (Schlangen (1993), van Mier et al. (2002)).
2. Overlaying a regular triangular lattice on top of a generated microstructure (particle overlay), and assigning beam properties according to their position, as illustrated in Figure 3.8. (Schlangen (1993), Lilliu and van Mier (2007)).
3. Adopting a 'geometric' heterogeneity, by using a random mesh (Figure 3.2(c) and Figure 3.3) with identical mechanical beam properties. (Vervuurt (1997), van Vliet (2000)).

4. Using a combination of random geometry and generated microstructure. (van Vliet (2000), van Mier and van Vliet (2003)).

The first option has been investigated extensively in Chapter 6 in respect to regularising the fracture energy released from lattice simulations and also achieving realistic force-displacement response for cementitious materials.

It should be noted that altering the stiffness of the beams affects the local equivalence of the stored strain energy between the lattice unit cell and its continuum counterpart, as described above. Disorder has therefore been primarily introduced within the literature through variation of the element beam strengths. In addition, adopting a random lattice with identical elastic beam properties (Young's Modulus, E , cross-sectional area, A , and second moment of area, I) introduces an additional 'geometric' heterogeneity. For the centre particle method (Figure 2.23(a), Bažant, 1990) and for fibrous materials (Ostoja-Starzewski, 2002) the random mesh represents the underlying microstructure of the material, and hence the equivalence is unique. However, when random lattices are used to model concrete, with or without explicit particle overlay, the randomness is not representative of the microstructure and the additional heterogeneity it provides serves only to obscure the effect that the true material heterogeneity has on the fracture process. Schlangen and Garboczi (1996) recognised this fact and devised an iterative method of altering the values of A and I for each and every beam so that a random geometry lattice was capable of representing an elastically homogenous medium. The method proved successful; however, negative values of A and I , which are obviously physically meaningless, were obtained for a small number of beams.

3.4.1 Particle overlay method

The particle overlay method has been the primary method of representing the microstructure of concrete in the lattice model. Concrete may be classed as a three phase material consisting of aggregate particles embedded in a cementitious matrix, with the third phase being attributed to the interfacial transitional zone (ITZ) between the two. At the simplest level, aggregate particles may be considered to be perfectly spherical objects distributed at an optimum density according to a Fuller curve:

$$p = 100\sqrt{(D/D_{\max})} \quad (3.11)$$

where p denotes the percentage by weight passing a sieve with aperture diameter D and D_{\max} is the diameter of the largest aggregate particle.

For 3D lattice simulations (Lilliu and van Mier, 2003), this distribution may then be projected onto the lattice mesh with strength and stiffness properties being assigned to the lattice elements according to the phase in which they fall (Figure 3.8). For two dimensional discretisations which may be considered as slices through the three dimensional domain, the aggregate particles take the form of circles which may be distributed according to a cumulative probability function. Equation (3.12), as derived by Walraven (1980), is commonly used within the literature for this purpose.

$$P_c(D < D_o) = P_k (1.455 D_o^{0.5} D_{\max}^{-0.5} - 0.5 D_o^2 D_{\max}^{-2} + 0.036 D_o^4 D_{\max}^{-4} + 0.006 D_o^6 D_{\max}^{-6} + 0.002 D_o^8 D_{\max}^{-8} + 0.001 D_o^{10} D_{\max}^{-10}) \quad (3.12)$$

where P_c represents the probability that an arbitrary point in the body, lying on an intersection plane, is located in an intersection circle with a diameter $D < D_o$, and P_k is the ratio of total aggregate volume to concrete volume. For a given concrete mix with a maximum aggregate particle diameter (D_{\max}) equation (3.12) allows the percentage of aggregate particles passing various sieve sizes to be determined, and hence an approximation for the particle distribution, based on integer valued aggregate sizes, may be obtained (Schlangen, 1993). The algorithm for the random distribution of the aggregate is described in section 4.2.2.

The strength and stiffness properties of the beams are then assigned in a similar fashion to the three dimensional case given above, as schematised in Figure 3.8.

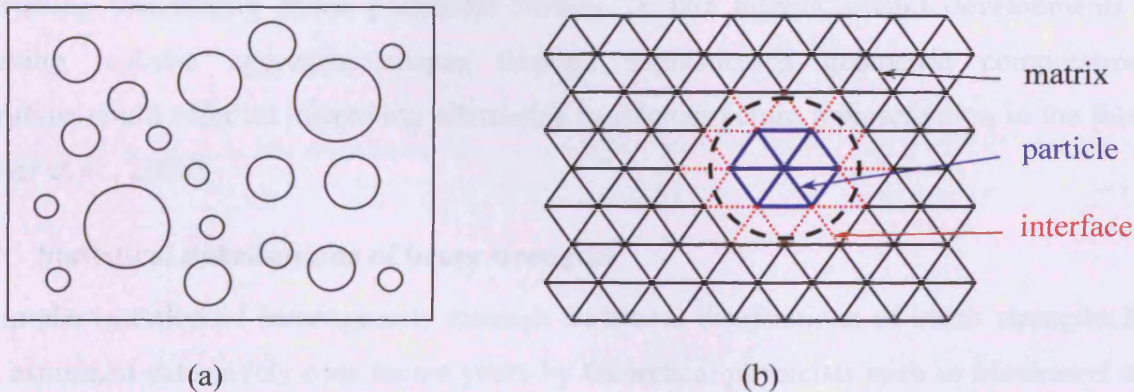


Figure 3.8. Schematic illustration of particle overlay method (a) randomly generated aggregate distribution (b) projection onto regular triangular lattice mesh and assignment of aggregate, matrix and interface element properties.

The typical material parameters adopted in the literature and used in the standard three phase particle overlay tests described in section 6.2 are given in Table 3.1.

Table 3.1. Typical parameters used in regular triangular lattice analysis with particle overlay (van Mier and van Vliet, 2003)

	E (MPa)	f_t (MPa)
Particle	87514	10.0
Interface	31255	1.5
Matrix	31255	5.0

One disadvantage in adopting simple spherical or circular aggregate geometries is that the actual modelled shape changes with lattice resolution or aggregate size. As the lattice resolution becomes finer or the aggregate size increases, the boundary becomes more spherical or circular. This is illustrated in the different lattice discretisations shown in Figure 6.1. In the coarse representation the aggregate takes on the appearance of crushed limestone, whereas in the finer representation it is more akin to rounded river gravel.

In an effort to obtain a more realistic representation of material microstructure, digitised images of real material specimen cross-sections have also been used (Schlangen and Garboczi (1997), Schlangen and Copuroglu (2005)). Whilst this method clearly offers significant improvements, the time consuming production of such images means that it is not suitable for undertaking statistically based parameter studies. In this respect, recent developments in achieving realistic aggregate shapes through sophisticated geometric computational algorithms could offer an interesting alternative to microstructure representation in the future (Häfner et al., 2006).

3.4.2 Statistical distributions of beam strengths

The implementation of heterogeneity through statistical distributions of beam strengths has been examined extensively over recent years by theoretical physicists such as Moukarzel and Duxbury (1994) and Duxbury et al. (1995), as reviewed by Hermann and Roux (1990), Krajcinovic (1996), and Alava (2007). Work in this field has focused on issues such as phase percolation limits, fractality, scaling theories, criticality and avalanche behaviour. Invariably, this work has focused on the use of the random fuse model (RFM). This is analogous to the elastic lattice model, whereby the current is comparable to stress, the voltage is representative of strain, and the conductivity is akin to elastic stiffness (Zapperi et al., 1997). The strengths (or fuse current thresholds, I_c) are often randomly assigned values from arbitrary, often

uniform distributions, and the dielectric breakdown under increasing voltage is analysed in a statistical sense. Whilst mathematical treatment of such cases is often rigorous, the direct relevance to real materials such as concrete, where disorder is far more complicated, is not always clear.

van Mier et al. (2002) tried to capture the nature of disorder in cementitious materials by exploring the statistical aspects of lattice simulations. The authors specifically examined whether or not it was possible to mimic the effects, in terms of fracture patterns and mechanical response, obtained from explicit representation of the microstructure (particle overlay) with random distributions of beams strengths (and or stiffnesses) drawn from Weibull or Gaussian distributions (Figure 3.9).

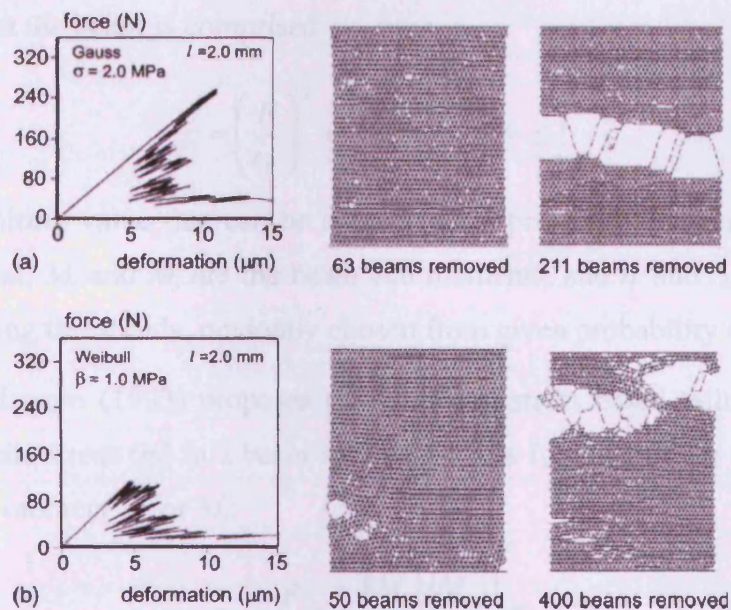


Figure 3.9. Force-deformation diagrams and fracture patterns for 80mm square specimens under uniaxial tension, with random strength distributions drawn from (a) Gaussian (b) Weibull distribution.
(van Mier et al., 2002)

The authors surmised that whilst force-deformation behaviour comparable with the particle overlay method may be obtained for a given statistical distribution, the crack patterns are generally unrealistic, particularly for the case of the Gaussian distribution. The Weibull distribution seems to capture crack face bridging due to the larger number of high strength beams, although the crack tortuosity observed when aggregate particles are considered is not represented.

3.5 Failure criteria

The traditional lattice beam modelling method represents isotropic damage within a material through the gradual dilution of the lattice via beam removal. In order to determine when a beam should be removed some form of failure criterion must be implemented. Several forms of failure criteria have been proposed within the literature in relation to the lattice beam model.

Herrmann et al. (1989) considered the fracture of heterogeneous solids through the use of two dimensional square elastic lattices composed of beams with both longitudinal and flexural rigidity, and specified breaking thresholds. They adopted the rupture criterion given by equation (3.13), which can be derived from Tresca's or von Mises's general yielding criteria for the material that the beam is comprised.

$$p = \left(\frac{F}{t_F} \right)^2 + \frac{\left(|M_i|, |M_j| \right)_{\max}}{t_M} \leq 1 \quad (3.13)$$

where p is the limiting value that can be related to the probability of failure, F is the axial force in the element, M_i and M_j are the beam end moments, and t_F and t_M are the elongation and flexural breaking thresholds, randomly chosen from given probability distributions.

Alternatively, Schlangen (1993) proposes the following stress based failure criterion, where the maximum tensile stress (σ_t) in a beam is taken to be a function of the normal force F and the maximum end moment M_i or M_j :

$$\sigma_t = \frac{F}{A} + \alpha \frac{\left(|M_i|, |M_j| \right)_{\max}}{W} \quad (3.14)$$

where A is the cross-sectional area of the beam ($b \cdot h$), and W is the section modulus ($b \cdot h^2/6$). The scaling parameter α controls the contribution of the moment term to the final failure mode. The external load carrying capacity of the lattice, P , at each stage of system dilution (successive beam removal) is given by:

$$P = P_{pre} \beta \left(\frac{f_t}{\sigma_t} \right) \quad (3.15)$$

where P_{pre} is the prescribed load, f_t is the tensile strength of the beam, and β is a further scaling parameter charged with matching the numerical peak response to that of an experimental specimen under uniaxial tension.

It should be noted, for the purposes of clarity, that the scaling parameter β has often been introduced directly into equation (3.14), by authors such as Vervuurt (1997), van Mier (1997), and van Vliet (2000). In this case, β effectively becomes the reciprocal of the original scaling parameter proposed by Schlangen (1993), although its purpose remains the same.

For the simpler bar or spring system the failure criteria is a truncated version of equation (3.14), whereby the axial stress ($\sigma_t = F/A$) is compared directly to the tensile strength of the beam, f_t .

Schlangen and Garboczi (1997) proposed a nodal stress based failure criterion in order to account for mesh orientation bias of the old failure criterion presented in equation (3.14). They applied this new criterion to uniaxial tensile, tensile splitting, and compression tests on mortar plate specimens with both free and fixed platen boundary conditions, and achieved good crack pattern prediction. Further details of this procedure are given in section 3.7.2.

Additional work on improving the predictive qualities of the lattice model in compression was investigated by van Vliet and van Mier (1996). They also acknowledged the limitations of the original failure criterion (eqn. (3.14)) in respect to modelling biaxial compression, and therefore proposed the use of a principle stress based failure criterion, similar to Beranek and Hobbelman (1994). A simpler, alternative, method for considering compression has recently been proposed by Abreu et al. (2007). The failure criterion given by eqn. (3.14) is used in this model, however, the stiffness of the beams are degraded in a two stage process. On first failure, the beam is converted to a bar by removing the bending and shear stiffnesses, and then on second failure the axial stiffness of the remaining bar is removed completely. Whilst this staged method has given reasonable failure patterns the physical basis for such a staged failure criteria remains highly questionable.

More recently Karihaloo et al. (2003) implemented a strain based failure criterion within their model, whereby the longitudinal strain, ε of each beam element was calculated from the nodal displacements according to equation (3.16). A strain based failure criterion was required in order to satisfy the linear tension softening relationship that was implemented within the matrix and ITZ phases.

$$\varepsilon = \frac{1}{l} \left(\Delta_x \cos \theta + \Delta_y \sin \theta + |\varphi_1 - \varphi_2| \frac{h}{2} \alpha_s \right) \quad (3.16)$$

where l is the length of the beam, Δ_x and Δ_y are the extensions along the global x and y axes, θ is the angle of the beam in respect to the global x-axis (Figure 3.7(b)), h is the height of the

beam, and φ_1 and φ_2 are the nodal rotations at the ends of the beam. α_s , taken to be 0.005, is essentially the same as α in equation (3.14) and is chosen so that the tail of the softening curve matches the measured one.

It should be noted that the failure criteria discussed above for the local lattice beam element allow for both shear and tension and hence could fail under a compressive shear mode, however, they have been developed by considering predominantly tensile failure cases. The issue of which is the most appropriate failure criterion to use is discussed further in Chapter 5.

3.6 Damage evolution

As outlined at the beginning of this chapter, damage evolution in lattice models is generally modelled in an isotropic fashion through successive beam removal. Usually, only a single beam is removed from the lattice before the system is allowed to relax and the effect of the localised stress re-distribution, from the removal of the beam, is analysed. The internal nodal displacements are solved following each and every beam removal, and the global parameters of force and displacement are obtained. This method results in a series of linear elastic relationships, as illustrated in Figure 3.1, which may be simplified to the ‘saw tooth’ external envelope schematised in the enlarged view of Figure 3.1.

The flexibility of the lattice method means that it is also possible to simulate some form of pseudo-dynamic effect by multiple beam removal, although in order to do this, some form of phenomenological relationship between actual loading rate and the number of elements removed would be required (Schlangen and Garboczi, 1997). Alternatively, Herrmann (1991) discusses a form of staged damage whereby the breaking threshold of bonds, in the vicinity of the crack, are reduced by an amount proportional to their strain. These bonds are therefore predisposed to complete failure during subsequent loading steps. This method can be thought of as physically representing the fracture process zone which is believed to contain a microcracked region in the highly stressed zone ahead of a crack tip (Mihashi and Nomura, 1992). This method is effectively a primitive implementation of a multiscale concept, whereby individual beams are considered to represent a finer underlying structure which degrades in a piecewise fashion. Whilst this has the potential to offer additional information about the mechanical response of the system, it incurs an increased computational overhead due to the larger number of solution steps required for complete failure of the specimen.

In order to maintain simplicity and limit computational demand, damage evolution through single beam removal has been implemented exclusively in the simulations presented in this thesis.

3.7 Current limitations

3.7.1 Computational demand

As previously mentioned, the original development of the ‘framework’ method proposed by Hrennikoff (1941) was initially stalled by the need to undertake repetitive calculations. Despite the recent advent of fast, readily available computational power, the numerical overhead attributed to the method has remained, and always will remain, its single most limiting factor.

Concrete is a truly multiscale material, containing hydration products such as calcium-silica-hydrates (C-S-H) at the nanoscale, cement particles at the microscale, and aggregate at the macroscale. Whilst lattice models may be considered to be physically accurate at the atomistic scale, providing suitable interaction potentials are implemented in the elements, applying a lattice model over the full range of scales is computationally impossible.

Therefore, in all lattice simulations a compromise must be made between the lattice mesh (domain) size and individual element length, or in material science terms; specimen size and size of internal material structure. Currently, an element to mesh size ratio of 1:200–1:300 is common for square 2D plane stress simulations, and 1:20–1:30 for cubic 3D simulations (Lilliu and van Mier, 2007). Lilliu and van Mier (2007) also give an indication of the computational time involved in such analyses. For a 3D random lattice simulation on a 24mm cube, with a 1.3mm maximum beam length, the number of beams and degrees of freedom are approximately 450,000, and 430,000 respectively. This simulation was reported to take 2-3 weeks on the 512 processor TERAS parallel computer in The Netherlands during 2002. The authors also comment that in light of Moore’s law, and barring any significant technological developments, it is likely to be decades before an appreciable improvement in computational capacity allows the element to mesh size ratio given above to be increased significantly.

3.7.2 Mesh orientation dependency

When a continuum is represented by an interconnecting series of one dimensional finite elements there will inevitably be some form of mesh orientation dependency, at least at the

local level. This dependency can affect both the global fracture pattern which results from a sequence of localised failures, and the load-displacement response of the system.

Schlangen and Garboczi (1997) studied the effect of lattice type and orientation on the fracture patterns produced from shear plate experiments, as illustrated in Figure 3.5 (a). The results for square, triangular, and random configurations without material heterogeneity are given in Figure 3.10. It should also be noted that the geometric heterogeneity introduced naturally by the random lattice mesh has been removed by altering the values of A and I for every beam, as previously described in section 3.4.

If the elements of the lattice model are considered to represent bonds between material regions and crack propagation, which is instigated by beam removal, is considered to occur perpendicular to the longitudinal axis of the elements, then even random lattice configurations will show localised mesh orientation dependency. However, on a global specimen scale this dependency becomes less obvious due to the randomness of the mesh. The authors recognise this fact since even though Figure 3.10 suggests that the random lattice offers the most realistic crack pattern, a regular triangular mesh which directly implements material disorder, through beam strength or stiffness variation, is also believed to be able to yield similar quality overlapping crack patterns. For this to be true the beam size would have to be small relative to the length scale of the inhomogeneous material.

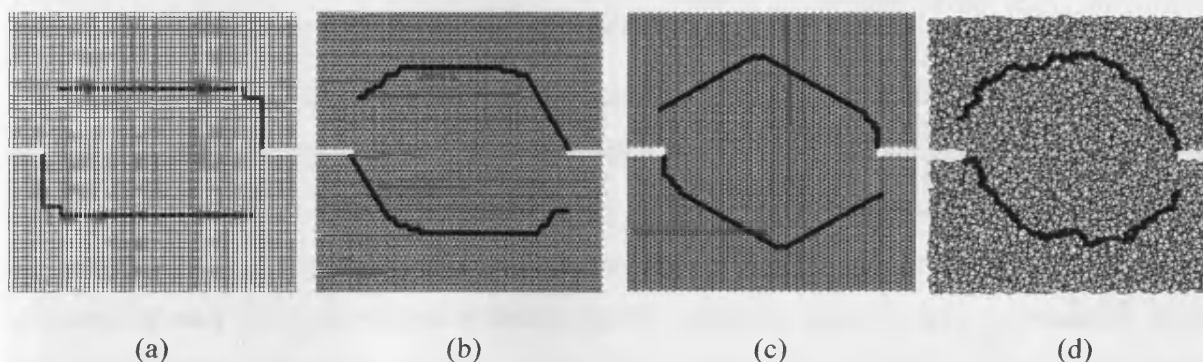


Figure 3.10. Simulated crack patterns in (a) square mesh, (b) regular triangular mesh, (c) rotated triangular mesh, and (d) random triangular mesh. (Schlangen and Garboczi, 1997)

In addition to the mesh orientation affecting the crack patterns, it has also been shown to affect the mechanical force-displacement response of the lattice system. Schlangen and Garboczi (1997) state that for a regular periodic triangular mesh orientated as shown in Figure 3.1, the maximum beam stress is 33% higher when the lattice is under constant horizontal strain than vertical strain. This result was obtained for a beam lattice with a simple axial

failure criterion as given in equation (3.14) but with the moment contribution ignored. The reason for this discrepancy is that, under this failure criterion, beams whose axis is aligned with the principal direction of loading are more pre-disposed to failure than other beams. Incidentally, including the flexural component of equation (3.14) in the fracture law does not correct this problem of mesh orientation dependence.

Since this issue of directional dependence is intrinsically linked to the isotropy of the failure criterion, Schlangen and Garboczi (1997) developed a new failure criterion based on consideration of the resultant axial and shear stresses at nodes rather than in beams. The methodology for this criterion is illustrated in Figure 3.11.

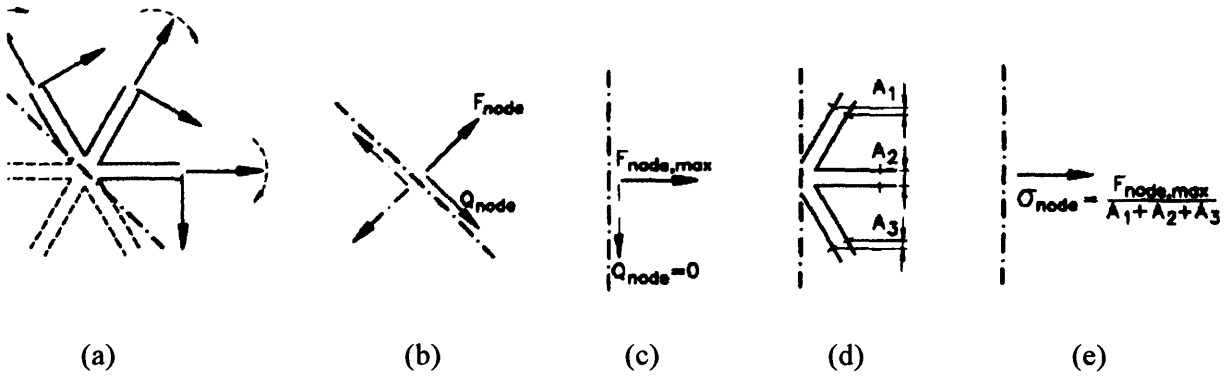


Figure 3.11. (a) Lattice with forces in beam elements, (b) resulting normal and shear forces perpendicular to a nodal cut, (c) maximum normal force $F_{node,max}$, (d) cross sections corresponding to angle with $F_{node,max}$ and (e) resulting stress in the node

The nodal stress σ_{node} calculated in 3.11(e) is assigned to each beam attached to this node, and the beam with the highest relative effective stress ($r_{eff} = \sigma_{node}/f_t$) is broken and removed from the lattice. Whilst the authors obtained good agreement for both the fracture patterns and force-displacement response between lattices tested in orthogonal directions using this criterion, it may be argued that a beam failure criterion based solely on stresses within individual beams has more physical relevance. As a result of this, an alternative Mohr-Coulomb based criterion is proposed in Chapter 5 and its isotropy properties are investigated.

3.7.3 Mesh size dependency

Increasing the resolution of a lattice and therefore decreasing the element length, clearly increases the ability of the mesh to capture fracture patterns in greater detail. However, the objectivity (independence to element length) of the force-displacement response obtained, as the element length is reduced, has been raised as a key limitation of the method in the literature. The objectivity of this mechanical response has been discussed within the statistical

physics field (Krajcinovic (1996)), although it has been given relatively limited coverage within the engineering community.

Schlangen and Garboczi (1997) discuss the influence of lattice resolution (number of beams per unit length of specimen) on the mechanical response of the specimen. They examined four different lattice mesh resolutions tested under uniaxial tension. Heterogeneity was modelled in a simple manner by randomly assigning low (1.0) or high (3.0) strengths to the individual beams in the ratio of 1:3. Whilst the crack patterns were comparable, although obviously varying in detail, the load-crack opening response showed significant variation in ductility, as shown in Figure 3.12.

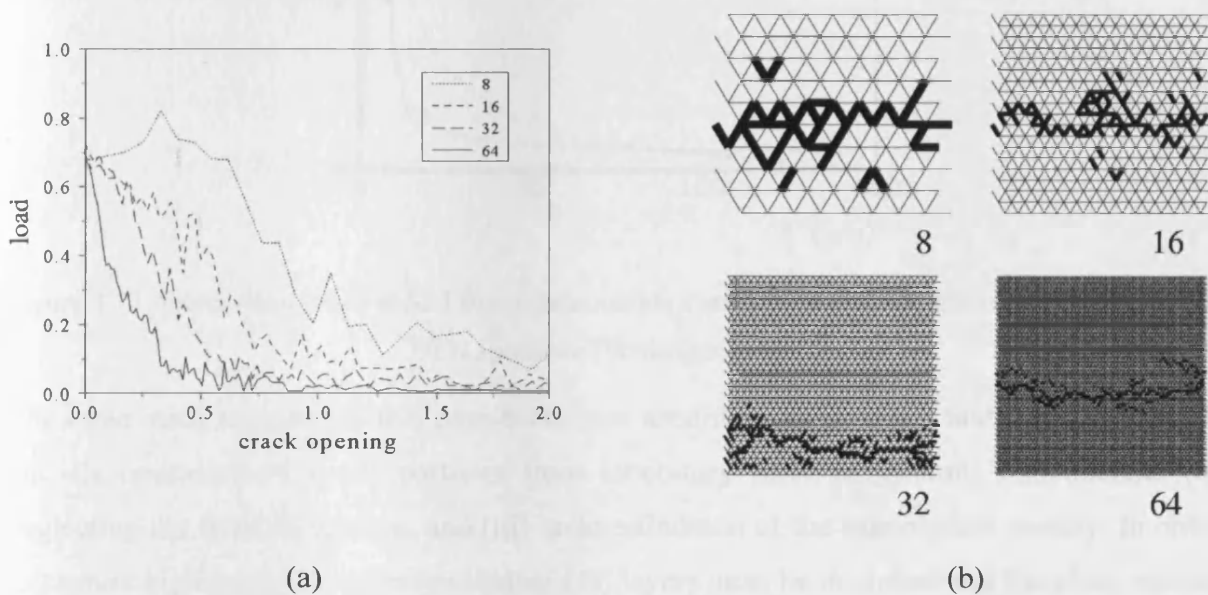


Figure 3.12. (a) Load-crack opening, and (b) crack patterns for various lattice resolutions. Note: Load and crack opening displacement units are arbitrary. (Schlangen and Garboczi, 1997)

This mesh size dependency is due to the fact that the energy released per unit area of new crack changes as the beam size changes. Since the ductility of the response is represented by the specific fracture energy, which is in turn related to the strain energy released following beam removal, the non-unique response is to be expected. Given that an increased percentage of microstructure inclusion generally increases the ductility of the response prior to ITZ percolation (Lilliu and van Mier, 2007), then linking the size of the smallest aggregate inclusion to the size of the lattice beam may reduced the mesh size dependency effect shown in Figure 3.12. This method is, however, likely to mask the numerical deficiency highlighted here, rather than scientifically correct it. A fuller explanation of this response and suggestions on how to correct for it are given in Chapter 6.

3.7.4 Over-brittleness

The final key limitation of the lattice modelling technique as identified from the literature is the over-brittleness of the force-displacement response when compared to experimental observations. An example of this is given by Schlangen (1993) for a uniaxial tensile test on a double edged notched (DEN) specimen, as shown in Figure 3.13.

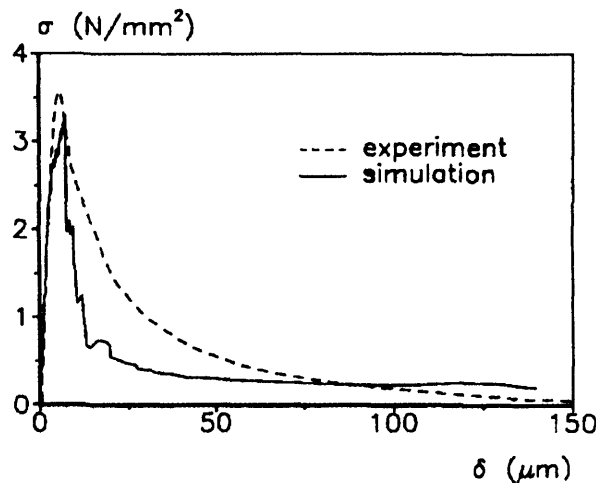


Figure 3.13. Experimental and model stress-deformation curves for a uniaxial tensile test on a standard DEN specimen (Schlangen (1993))

The three main reasons for this over-brittleness according to van Mier and van Vliet (2003) are: (i) omission of small particles from laboratory scale simulations on concrete; (ii) neglecting the third dimension, and (iii) underestimation of the true particle density. In order to capture higher particle densities thinner ITZ layers must be modelled and therefore smaller beam elements are required. Likewise, in order to model smaller particle inclusions finer resolution meshes are required. Both of these solutions increase the number of degrees of freedom that must be considered, and moving to three dimensions further increases this by an order of magnitude. The solutions to the problems outlined above are therefore all essentially related to the computational overhead of the method, as discussed previously in section 3.7.1.

Three dimensional lattice analyses have nevertheless been completed by Lilliu and van Mier (2003), Lilliu and van Mier (2007) and Man and van Mier (2008). It should be noted however, that due to computational limitations the length of the elements have to be increased or the size of the specimens reduced in these 3D analyses. Lilliu and van Mier (2007) have, nevertheless, compared two dimensional and three dimensional tensile analyses on concrete specimens with the same particle density (34%). It is not clear if these analyses were completed with the same beam length, thereby eliminating the mesh size effect described in

the previous section, however, the 3D analysis showed far greater post-peak ductility when compared to the 2D analysis, as shown in Figure 3.14.

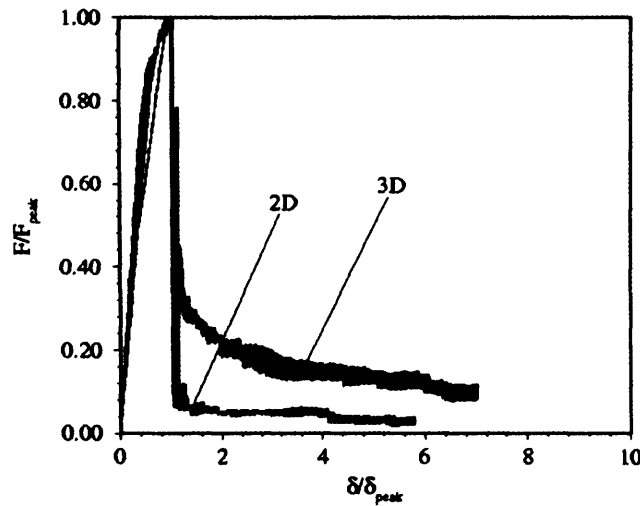


Figure 3.14. Comparison of 2D and 3D relative load-displacement behaviour for the same particle density (34%)

Due to the plane stress assumptions made in two dimensional lattice analyses, aggregate particles are essentially considered as cylinders and cracks that occur around these particles are assumed to propagate along the entire length of the cylinder (i.e. thickness of specimen) instantly. In three dimensional laboratory experiments and also lattice models, aggregate particles take on a spherical form and cracks may occur at discrete locations in the third spatial dimension. It is therefore unsurprising that the 2D plane stress simplification underestimates the ductility of the fracture response in quasi-brittle materials.

In this thesis, however, only two dimensional plane stress lattice examples have been considered. This is primarily because quicker run times greatly aid the model development process. The issue of over-brittleness, and the need to achieve better agreement with experimental force-displacement results has nevertheless been addressed in Chapter 6.

3.8 Conclusions

The lattice beam modelling method offers an extremely simple approach to capturing the fracture of materials. The main ingredients of the model are: (i) the lattice of elements; (ii) the representation of heterogeneity, and (iii) the adopted fracture criterion.

The model has been applied to a wide range of materials, from paper and wood to quasi-brittle materials such as cement and concrete. In respect to the latter, the model, despite its simplicity, has been shown to correctly predict failure patterns under a range of loading

conditions. These include uniaxial tension, tensile splitting, shear plate failure, and uniaxial compression with both free and fixed boundary conditions.

The qualitative properties of the model are therefore very good, and the main limitations of the model primarily relate to its quantitative capabilities. These limitations have been identified from the literature as being:

- Computational demand – in order to represent material mesostructure in laboratory scale specimens, the number of degrees of freedom in lattice simulations is commonly in the hundreds of thousands, and the run time can therefore be considerable.
- Mesh orientation dependency – due to the discrete representation of the continuum and the anisotropic properties of the failure criterion both the fracture pattern and mechanical load-displacement response may be influenced by the orientation of the mesh.
- Mesh size dependency – due to the difference in strain energy stored in beams of different lengths under constant strain conditions the fracture energy released during cracking is not unique for simulations with varying lattice resolutions.
- Over-brittleness – owing to computational limitation, the inability to model fine particles and therefore realistic particle densities, and also omission of the third dimension, results in an overly brittle mechanical response when compared to laboratory experiments.

These issues, which are felt to be restricting an even wider application of the method, have been addressed further in the following three chapters. In doing so, the specific type of lattice model which has been considered is a regular triangular configuration comprising beam elements.

Chapter 4

Computational implementation

4.1 Introduction

In this brief chapter the computational implementation of the lattice theory presented in Chapter 3 is discussed. This theory has been implemented in two separate computer codes, namely: the pre-processor, and the main finite element (FE) code. Both of these programs have been written in Fortran 90 using the Compaq Visual Fortran development studio. Visualisation of the input and output data from the model has been undertaken using a bespoke application, which has been written in Visual Basic 5. The main features of these individual programs are summarised in this chapter. Particular attention has also been given to the issue of computational efficiency within the numerical algorithms implemented in the main finite element engine.

4.2 Pre-processor

4.2.1 Main features

The main features of the pre-processor are:

1. Automatic creation of regular triangular lattice, including nodal coordinate generation, node and element numbering, and topology assignment;
2. Automatic creation of specimen pre-notches through element removal;
3. Representation of material heterogeneity, through assignment of beam properties, according to the particle overlay or statistical distribution of beam strengths methods, and;
4. Assignment of boundary conditions.

Two methods of representing material heterogeneity have been discussed in this thesis, as presented in Chapter 6. These are the particle overlay method and the statistical distribution of beam strengths method. Both of these methods have been implemented in the pre-processor.

4.2.2 Particle overlay implementation

The particle overlay method has been implemented in a similar manner to that described by Schlangen (1993). As outlined in section 3.4.1, aggregate particles are assumed to be represented by spheres in three dimensions, which then produce circles when 3D specimens are cut to obtain 2D specimens. For a given specimen size, and aggregate content, P_k , the probability density function given in equation (3.12), as derived by Walraven (1980), is used to obtain an approximate particle size distribution in terms of integer valued particle diameters. The particle sizes, which are actually overlaid onto the lattice mesh, range from D_{min} to D_{max} , where D_{min} is taken to be twice the lattice resolution length, and D_{max} is set to the maximum aggregate size in the concrete specimen being modelled. A typical particle size distribution for a 50mm x 50mm two dimensional specimen, with an aggregate content, P_k of 55%, and a maximum aggregate size of 8mm, is shown in Table 4.1. It should be noted that for a lattice beam length resolution of 1mm, the smallest particle size represented would be 2mm.

Table 4.1. Particle size distribution for 50mm x 50mm specimen with $P_k = 55\%$, $D_{max} = 8\text{mm}$

D_0 (mm)	1	2	3	4	5	6	7	8
No.	887	83	24	9	4	1	0	0

The structure of the particle overlay, illustrated in Figure 4.1, is created using the following method:

1. The particles are distributed in order of size, starting with the largest.
2. Random coordinates are selected within the specimen domain for the centre point of the first particle.
3. For every particle distributed thereafter, a check is made on the distance between its centre point and the centre point of the previously allocated particles. The minimum distance between the centres of two particles A and B is taken to be $1.1(D_A + D_B)/2$. If the chosen coordinates violate this criterion, new coordinates are repeatedly chosen until the criterion is met.

4. The particle structure is then overlaid on top of the lattice mesh and beam properties are assigned, as described in section 3.4.1.

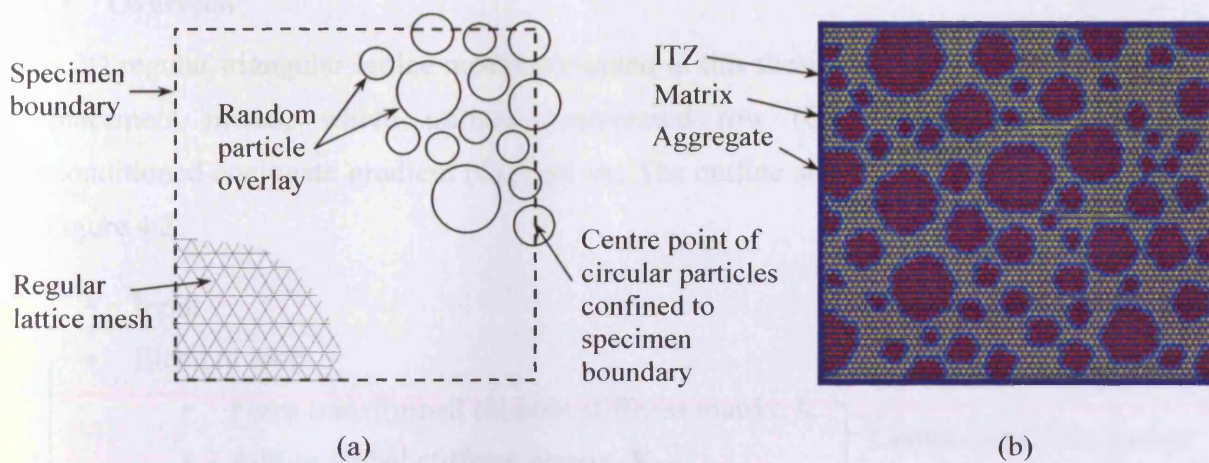


Figure 4.1. (a) Schematic illustration of two dimensional particle structure, and (b) Final appearance of a typical lattice mesh

It should be noted, that since the centre points of the particles, rather than their circumferences, have been confined to the specimen boundary, then the specimens produced using this method are more akin to cores taken from larger samples, than individually cast samples. This is evident in the final appearance of a typical lattice mesh, as illustrated in Figure 4.1(b).

4.2.3 Statistical distribution of beams strengths implementation

The procedure for representing material heterogeneity via a statistical distribution of beam strengths, according to the theory presented in section 6.7, is as follows:

1. The specimen domain is subdivided into a grid of smaller RMEs (Representative material elements), as illustrated in Figure 6.9.
2. The exact numbers of elements, n in each RME are counted.
3. Equation (6.9) is solved for $j=1$ to n to obtain the beam strains, ζ_j for each beam in a particular RME. The beam strengths for each beam are then obtained by multiplying the beam strain by the elastic modulus of the beam, E_b .
4. These strengths are then allocated randomly to all beams within the RME.

4.3 FE code

4.3.1 Overview

The 2D regular triangular lattice model presented in this thesis is a small strain, infinitesimal displacement model, which utilises compressed row (CR) storage and a Jacobian preconditioned conjugate gradient (CG) solver. The outline structure of the code is presented in Figure 4.2.

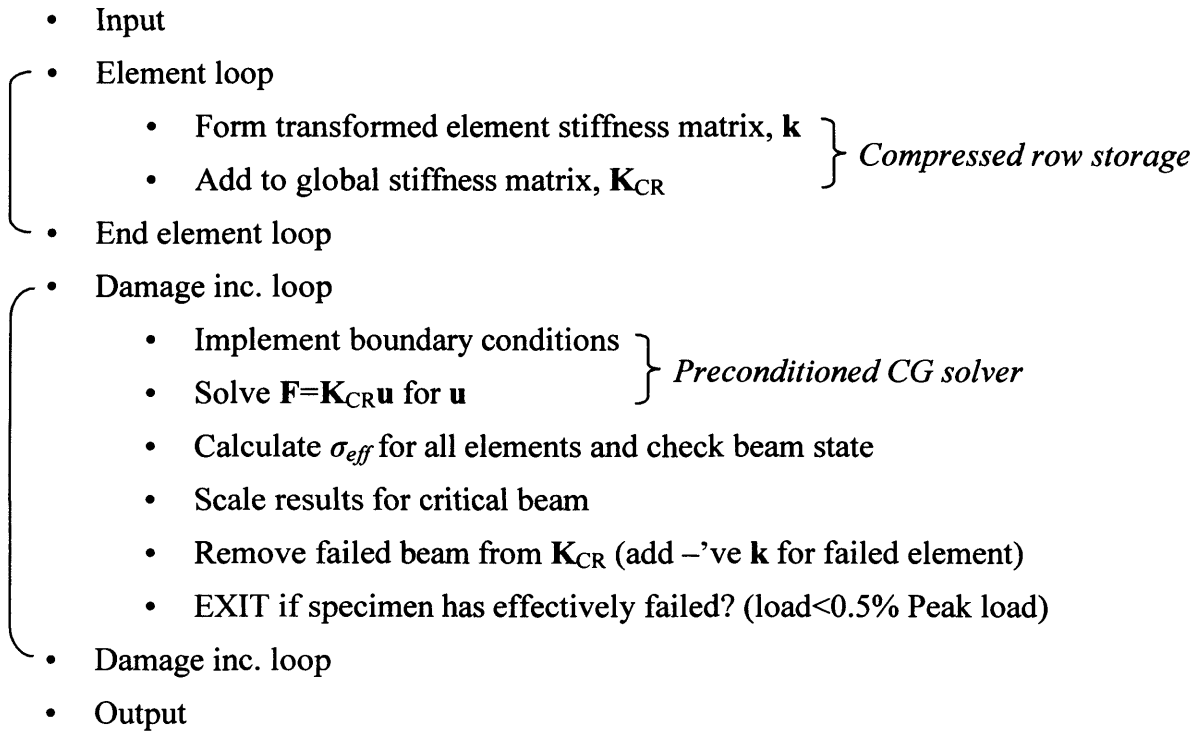


Figure 4.2. Outline structure of the lattice FE code

Following the initial input and variable initialisation stages, the global stiffness matrix is formed from the assemblage of the element stiffness matrices, which have been transformed into the global coordinate system. It should be noted that the global stiffness matrix is assembled using the compressed row storage scheme, as described in section 4.3.2.

The implementation of the boundary conditions and the solution of the system of equations, for a chosen value of the initial prescribed displacement, are then undertaken using a Jacobian preconditioned conjugate gradient solver. Further details of the solver are given in section 4.3.3.

The effective stress, σ_{eff} , in each and every beam is then calculated, according to the chosen failure criterion, as discussed in Chapter 5. This then allows the relative effective stress, r_{eff} , to be calculated for every beam according to:

$$r_{eff} = \frac{\sigma_{eff}}{f_{tb}} \quad (4.1)$$

where f_{tb} is the beam strength.

Since the lattice system is linear elastic, the relative effective stress for the most critical beam, $r_{effCRIT}$, may be used to determine the exact value of the prescribed displacement which would cause the most critical beam to break, i.e. $\sigma_{eff} = f_{tb}$. This may be achieved by scaling the originally prescribed displacement by $1/r_{effCRIT}$. In fact, the full solution previously obtained for the internal displacements may simply be scaled by $1/r_{effCRIT}$ without the need to resolve. It should be noted that since $r_{effCRIT}$ may be greater than 1, the scaling factor may be less than 1, and this method is therefore able to capture any snap-back behaviour of the lattice model.

The stiffness of the most critical beam is then removed from the global stiffness matrix by adding the negative component of the broken beams elements stiffness matrix to the global stiffness matrix. As a result, the compressed row version of the global stiffness matrix is only formed once in the code, for the case of the pristine, undamaged lattice. Thereafter, it is simply degraded as the lattice becomes diluted due to progressive beam failures.

From Figure 4.2 it can then be seen that, following a check on the degree of damage of the overall lattice, the system of equations is resolved for the new reduced global stiffness. The prescribed displacement, and the initial ‘guess’ for the displacement vector, \mathbf{u} in the CG solver are set to the scaled values from the previous iteration. This is done in order to minimise the initial residual within the solver, as discussed in section 4.3.3.

4.3.2 Compressed row storage

The global stiffness matrix which is created from the assemblage of the transformed element stiffness matrices is extremely sparse for lattice models, as noted by Schlangen and Garboczi (1997). The memory storage requirements of the method can therefore be dramatically reduced, by either solving element by element, or by storing only the non-zero terms of the global stiffness matrix. The latter approach has been implemented in this code, by adopting the compressed row storage technique.

This technique is based upon traversing the global stiffness matrix in a row-wise fashion, and recording all non-zero values (*val*), their column index (*col_ind*) and the row pointer (*row_ptr*). The latter stores the index locations in the ‘*val*’ vector, of the values that start rows in the full matrix. This method is described in detail by Barrett et al. (1994), and is illustrated in Figure 4.3.

$$A = \begin{pmatrix} 10 & 0 & 0 & 0 & -2 & 0 \\ 3 & 9 & 0 & 0 & 0 & 3 \\ 0 & 7 & 8 & 7 & 0 & 0 \\ 3 & 0 & 8 & 7 & 5 & 0 \\ 0 & 8 & 0 & 9 & 9 & 13 \\ 0 & 4 & 0 & 0 & 2 & -1 \end{pmatrix}$$

val	10	-2	3	9	3	7	8	7	3.....9	13	4	2	-1
col_ind	1	5	1	2	6	2	3	4	1.....5	6	2	5	6
row_ptr	1	3	6	9	13	17	20						

Figure 4.3. Compressed row storage of a non-symmetrical matrix **A** (Barrett et al., 1994)

The disadvantage of the method, as presented in Figure 4.3, is that the full global stiffness matrix must be assembled, and therefore stored, prior to being compressed. This is avoided in the current code, by creating a ‘*block_ptr*’ matrix, which stores the connectivity of each node; i.e. all the nodes which are connected to any given node in the lattice mesh. The ‘*block_ptr*’ matrix can then be used to populate the ‘*col_ind*’ and ‘*row_ptr*’ vectors. This allows the components of the element stiffness matrices to be inserted directly into the correct locations in the ‘*val*’ vector during assemblage.

It should be noted that this modified method does not remove the zero components of the element stiffness matrices which are used to populate ‘*val*’. However, the sparsity which this creates is very small compared to the sparsity generated by non-connected nodes.

4.3.3 Conjugate gradient solver

For a loaded lattice mesh, the solution of the displacement vector, **u** may be determined by either a direct method, such as Gaussian elimination, or an indirect iterative method, such as the conjugate gradient method. Since the conjugate gradient method is the most prominent iterative method for solving sparse systems of linear equations (Shewchuk, 1994), and is significantly faster than Gaussian elimination (Press et al., 1996), it has been implemented in

the current code. In addition, as noted by Schlangen and Garboczi (1997), the modelling of fracture using the lattice method is based on successive removal of beams, which each result in a relaxation of the mesh. This relaxation is, in general, a localised effect. This implies that changes between successive solutions of the displacement vector will also include primarily localised effects around the vicinity of the removed element; i.e. changes in the translational and rotational movement of nodes will be relatively large in nodes located around the removed element, but small elsewhere. This, therefore, makes the lattice method particularly suited to an iterative solver. This is because the solution of the displacement vector from the previous lattice mesh is likely to offer a very good starting guess for the solution to the current mesh, which will only have one new additional beam removed. Experience has shown that this results in fewer iterations and improved solver efficiency.

Iterative solver efficiency, however, is known to reduce as the ill-conditioning of the stiffness matrix increases. This occurs when property differences between adjacent parts of the system become large, such as is often the case when material heterogeneity is represented. In order to improve the conditioning of the stiffness matrix and the efficiency of the solver, a Jacobian preconditioner (**M**) has been used in the implemented solver. This is a simple explicit preconditioner which is based on the reciprocal of the trace of the global stiffness matrix, **K**.

The preconditioned CG algorithm implemented in this code is given in Figure 4.4.

```

Compute  $r^{(0)} = b - Ax^{(0)}$  for some initial guess  $x^{(0)}$ 
for  $i = 1, 2, \dots$ 
    solve  $Mz^{(i-1)} = r^{(i-1)}$ 
     $\rho_{i-1} = r^{(i-1)T} z^{(i-1)}$ 
    if  $i = 1$ 
         $p^{(1)} = z^{(0)}$ 
    else
         $\beta_{i-1} = \rho_{i-1} / \rho_{i-2}$ 
         $p^{(i)} = z^{(i-1)} + \beta_{i-1} p^{(i-1)}$ 
    endif
     $q^{(i)} = Ap^{(i)}$ 
     $\alpha_i = \rho_{i-1} / p^{(i)T} q^{(i)}$ 
     $x^{(i)} = x^{(i-1)} + \alpha_i p^{(i)}$ 
     $r^{(i)} = r^{(i-1)} - \alpha_i q^{(i)}$ 
    check convergence; continue if necessary
end

```

Figure 4.4. Preconditioned conjugate gradient algorithm (Barrett et al., 1994)

In the present work the residual effective energy (ρ) is normalised by the square root of the inner product of the total load (F_T) and the reactions (F_r) based on the initial displacement vector. This gives the following convergence criterion:

$$\frac{\sqrt{\rho_i}}{tn} \leq \text{tol} \quad (4.2)$$

where tn is the scaled total force norm, given by:

$$tn = \sqrt{(F_T + F_r)^T \cdot K^{-1} \cdot (F_T + F_r)} \quad (4.3)$$

and the error tolerance (tol) is taken as 10^{-6} .

Preliminary benchmark tests on the Jacobian preconditioned CG solver, presented above, compared with a direct Gaussian elimination solver implemented by Karihaloo et al. (2003), have shown that a speed-up factor of at least 20 can be achieved, with respect to the CPU time required per solution of the system of linear equations.

Finally, it should be noted that during all stages of general code and solver development, the results obtained from the Fortran code have been verified, for individual small scale lattice meshes, by comparing them with simulations undertaken in a commercial FE program called LUSAS (2008).

4.4 Post-processor

A bespoke post-processor has been specifically designed and developed in order to display the output generated by the FE code. This post-processor has been written in Visual Basic 5, and a screen shot of the graphical user interface (GUI) is shown in Figure 4.5.

The main features of the post-processor include the ability to:

1. Visually check the applied boundary conditions and locations of pre-notches;
2. View the pristine mesh, including the three phase mesostructure, displayed in user defined colours;
3. Display useful information such as the number of nodes, number of elements, and how many of these elements have been assigned to the different mesostructure phases;
4. Plot fractured meshes at any load step, and at any scaled displacement value. In addition to the basic fractured mesh, broken beams may be plotted on their own, as well as graphical representations of various properties of the beams. These include the beam strength, f_{ib} , the effective stress in the beam, σ_{eff} , and the relative effective stress

- (stress ratio) of the beam, r_{eff} , as defined by equation (4.1). The spatial distribution of values for each of these variables is represented by a coloured plot, whose range may be manually altered, in order to examine specific areas of interest;
5. Add any plot to an animation sequence, or to automatically generate and save an animation sequence for the entire fracture process of a specimen, for any chosen variable settings, and;
 6. Plot the force-displacement graph, including labelling of the load steps, to allow comparison with the corresponding fracture plots.

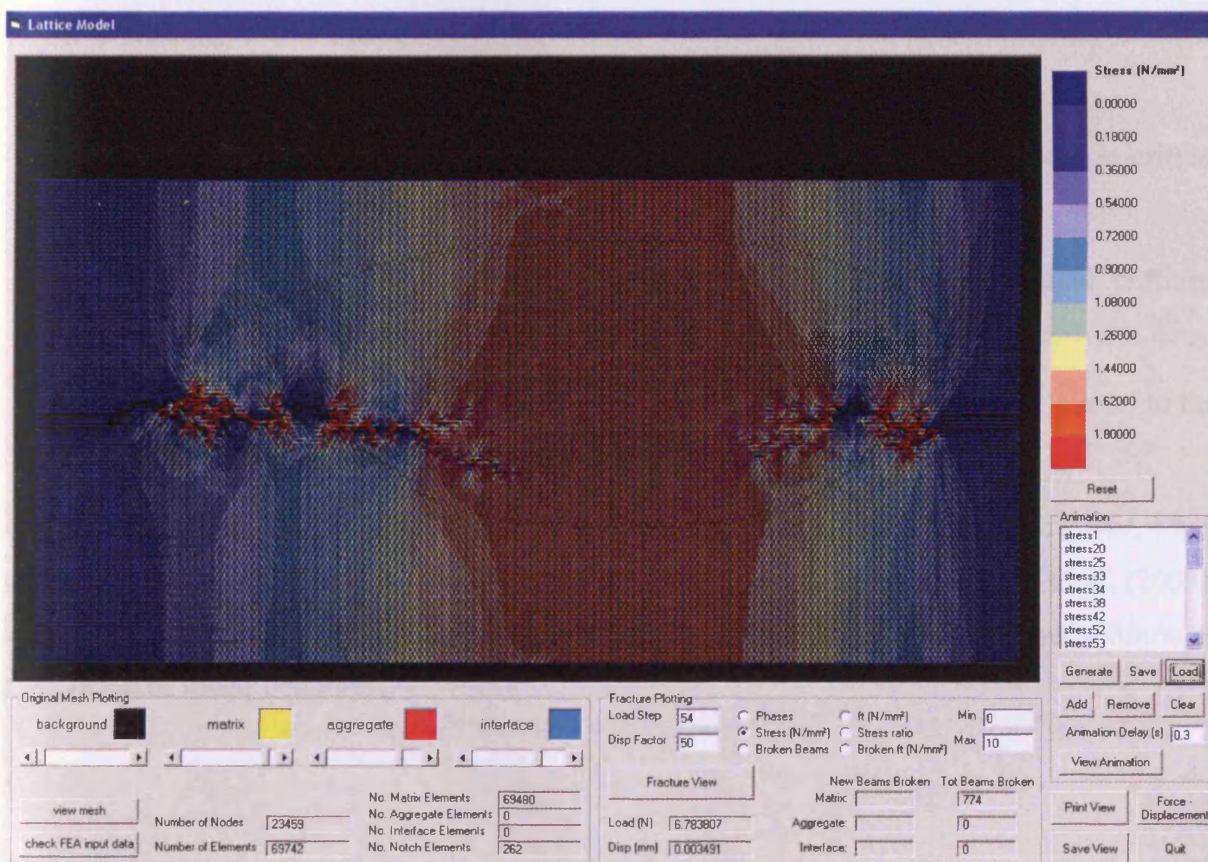


Figure 4.5. Screen shot of the post-processor GUI

4.5 Summary and conclusions

A brief overview of the computational implementation of the lattice modelling method has been given in this chapter. The primary features of the pre- and post-processors have been described, in addition to the main FE engine.

The pre-processor is able to automatically generate a regular triangular lattice mesh of any size, and represent material heterogeneity through either a particle overlay or a statistical

distribution of beam strengths. The post-processor is able to automatically plot, and animate, fracture patterns and coloured contour plots of beam stresses, as well as illustrating the force-displacement response for the specimen.

The main FE engine, which has been written in Fortran 90, assembles and solves the system of linear equations for each stage of the fracture process. Various features have been implemented within the FE code in order to improve its computational efficiency. These include:

1. Assembly of the global stiffness matrix using the compressed row storage technique;
2. Solution of the linear set of equations using a Jacobian preconditioned iterative conjugate gradient solver;
3. Scaling of results to achieve a stress state of 1 (i.e. failure point) in the most critical beam, without the need for re-solving;
4. Individual removal of element stiffnesses of broken beams from global stiffness matrix, without the need for re-assembly, and;
5. Minimisation of the initial residual in the CG solver by setting the initial 'guess' to the scaled value of the previous solution.

Preliminary benchmark tests have indicated that the Jacobian preconditioned CG solver, when compared with a direct Gaussian elimination solver implemented by Karihaloo et al. (2003), can achieve speed-up factors of at least 20, in respect to the CPU time required per solution of the system of linear equations.

Chapter 5

Failure criteria development

5.1 Introduction

This chapter focuses on the analysis and development of various failure criteria that may be used for capturing damage propagation with the lattice beam model. A brief summary of the existing failure criteria used within the literature is given initially, together with some comment on their efficacy and practical meaning.

A Mohr-Coulomb (M-C) type failure criterion is then proposed, which is based on beam forces. The isotropy of this criterion is examined under a theoretical framework. This framework is based on consideration of the equivalence between the lattice mesh and the underlying continuum. The optimum form of the Mohr-Coulomb criterion, which minimises the degree of anisotropy, is thereby obtained.

The theoretical equivalence theory is then developed further, and the possibility of obtaining stresses from the lattice mesh, which are directly equivalent to the continuum stresses at that location, is investigated. As a result, an isotropic failure criterion, based on principal stresses, is proposed for an elastic regular triangular mesh. The true isotropy of the principal stress failure criterion is then tested for a pristine lattice mesh which is subject to separate constant strain conditions in two orthogonal directions.

Finally, a continuum stress based version of the M-C criterion is proposed. This is based on the stresses in the continuum at the mid-plane location of a lattice beam. The axial and shear components for the continuum are then compared to the equivalent components in a beam and a modified M-C criterion based on beam stresses is developed.

For completeness, the theoretical formulations used for analysing the equivalence between the continuum and the lattice mesh are extended further to derive the geometric properties required for the beam cross-section. In doing so, the tensorial derivation of beam properties as

given by Karihaloo et al. (2003), which is based upon matching the components of the elasticity tensor, is reworked using the explicit matrix forms of the equations adopted in this chapter.

The chapter is concluded with a summary and comparison of all of the failure criteria presented.

5.2 Existing failure criteria

As opposed to a simple truss or spring systems, elastic beams can break in various modes including stretching, bending, shearing and even twisting if the third dimension is considered. Ideally, the mechanical breaking rule or failure criterion implemented in the model should be able to reflect all of these different modes.

The various failure criteria which have been used in the literature to date have been presented and discussed in section 3.5 of this thesis. Two of these failure criteria, which have been used for beam elements, have been considered further in this chapter. The first of these is the stress based failure criterion used extensively by the Delft group in the Netherlands (Schlangen and van Mier (1992a), Chiaia et al. (1997), and van Mier et al. (2002)). This failure criterion, as given previously by equation (3.14), is:

$$\sigma_t = \frac{F}{A} + \alpha \frac{(|M_i|, |M_j|)_{\max}}{W} \quad (5.1)$$

where σ_t is the maximum tensile stress in a beam, F is the axial force, A is the cross-sectional area of the beam ($b \cdot h$), M_i and M_j are the end moments, W is the section modulus ($b \cdot h^2/6$), and α is the scaling parameter for the tail which is usually taken to be 0.005. It should also be noted that, as described in section 3.5, it is possible to scale the peak force by a factor β (equation (3.15)). However, β has been taken to be 1 in this chapter.

The second failure criterion considered, is that used by Karihaloo et al. (2003), as given previously by equation (3.16):

$$\varepsilon = \frac{1}{l} \left(\Delta_x \cos \theta + \Delta_y \sin \theta + |\varphi_1 - \varphi_2| \frac{h}{2} \alpha_s \right) \quad (5.2)$$

where ε is the effective strain, l is the length of the beam, Δ_x and Δ_y are the extensions along the global x and y axes, θ is the angle of the beam in respect to the global x axis (Figure 3.7), h is the height of the beam, φ_1 and φ_2 are the nodal rotations at the ends of the beam, and α_s is the scaling parameter taken to be 0.005.

This is essentially the strain equivalent of the Delft criterion, however, the difference between the end rotations of the beam are considered, rather than the maximum moment. As a result of this, it should be noted that if such a loading case arises whereby the end nodes experience equal rotation, no extension, but with some lateral translation, then, despite the beam being under constant shear, the effective strain, ε , given by equation (5.2) will always be zero, irrespective of the shear stress.

Both of these failure criteria are based on combinations of actual physical beam properties when the lattice is in a stressed (or strained) state. The Delft criterion is based upon the axial force in the beam and the maximum end moment which also indirectly includes a shear force component. Karihaloo et al's criterion considers the translational and rotational movement of the ends of the beam. They have both been shown to offer very good qualitative predictions of the failure envelope for lattice simulations (Schlangen (1993) and Karihaloo et al. (2003)), and with the correct choice of scaling parameters can also predict the quantitative properties. However, for both cases the scaling parameter does not have an underlying physical basis, and its value is obtained in an empirical manner from curve matching of experimental results.

5.3 Mohr-Coulomb based failure criteria

The beams in a lattice mesh can be considered to essentially connect the centres of continuum unit cells together, as shown in Figure 5.2. Under the framework of Bolander and Saito (1998) these unit cells can actually be thought of as rigid bodies, or particles in a material, as illustrated in Figure 2.24. If this concept is applied to the lattice beam modelling method, then the mid-plane surface of the beams can be considered to represent the interface between particles. Furthermore, if beams are considered to only break at particle interfaces (i.e. beam mid-planes), then a failure criterion may be developed which is based on the stresses at the mid-plane of every beam. It should be noted, that unlike the rigid body model, which includes the effects of rigid body mechanics and has separate normal, tangential and rotational springs at each interface, the assumption that the lattice beam mid-plane represents a particle interface is more conceptual than physical. However, it does serve as justification for developing a mid-plane failure criterion. Given this notion of the beam mid-plane representing the interface between two particles, then a suitable failure criterion may be one based on the theory of Mohr-Coulomb.

The individual contribution of axial, shear, and centre-span moment may then be considered explicitly in determining the effective stress state of the beam, as follows:

$$\mu(\sigma - f_{tb}) + |\tau| = 0 \quad (5.3)$$

where τ is the shear stress (Q/A), f_{tb} is the rupture strength of the beam, μ is the shear/normal strength ratio, and σ is the axial stress at the centroid of the beam which includes the contribution from the centre span moment:

$$\sigma = \frac{F}{A} + \frac{|M_c|}{W} \quad (5.4)$$

where F is the axial force, A is the cross-sectional area of the beam ($b \cdot h$), M_c is the bending moment at the beam centre, and W is the section modulus ($b \cdot h^2/6$). It should be noted that since the shear force has been considered explicitly in the chosen failure criterion, the bending moment has been taken to be the value at the centre span (mid-plane), rather than the maximum end value, as for the Delft criterion (eqn. (5.1)).

The failure envelope for the beam is given by equation (5.3), and represented graphically by the diagonal line in Figure 5.1. This expression may be rearranged to give a general expression for the ‘effective’ stress (σ_{eff}) in a beam:

$$\sigma_{eff} = \sigma + \frac{|\tau|}{\mu} \quad \text{for: } 0 \leq \sigma_{eff} < f_{tb} \quad (5.5)$$

It is the beam with the highest relative effective stress ($r_{eff} = \sigma_{eff}/f_{tb}$) that is removed from the lattice during the progression of damage, as discussed in section 4.3.1.

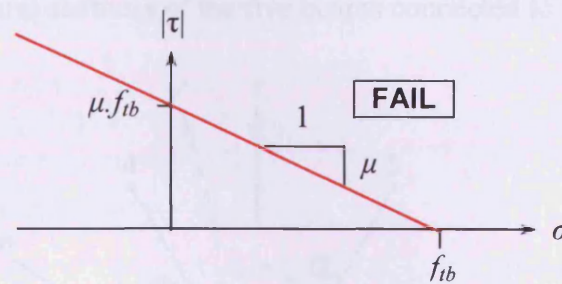


Figure 5.1. Mohr-Coulomb failure envelope

The effect of mesh orientation dependency of the lattice modelling method has been discussed in section 3.7.2. In respect to the force-displacement response of the system, the effect of the mesh orientation is primarily due to the anisotropy of the failure criterion being used. The Delft failure criterion (equation (5.1)) has been shown to exhibit mesh orientation dependency even for the elastic (pre-damaged) phase (Schlangen and Garboczi, 1997). Therefore, the isotropy properties of the M-C failure criterion proposed above should be examined to see if this failure criterion offers any improvements in this area.

A detailed, theoretically based, investigation has therefore been completed, as presented in the following section. During this investigation particular focus has been given to the determination of the most appropriate value to be used for the shear/normal strength ratio, μ , in addition to examining the equivalence between the M-C and continuum stresses.

5.3.1 Continuum equivalence and isotropy of the Mohr-Coulomb failure criterion

5.3.1.1 Outline of the investigation

The aims of this investigation are therefore to see if it is possible to achieve:

- (i) An isotropic failure criteria (i.e. first beam to break always occurs at the same principal tensile stress, regardless of the angle of the principal axes), and;
- (ii) A match between the mid-surface beam stresses and the continuum stresses.

In order to investigate the relationship between continuum stresses and those in the beams it will be assumed that the lattice star (Figure 5.2) is fixed to the underlying continuum, to which a stress field is applied. The star is formed from the six lattice beams connected to an internal node of a regular triangular lattice within an infinite domain. The displacement at the centre of the star is assumed to be zero. The dotted hexagon formed from the intersection of the lines normal to the beam mid-surfaces represents the unit cell for the lattice, as illustrated previously in Figure 3.7. It is further assumed that each beam is effectively restrained rotationally by the flexural stiffness of the five beams connected to each of its ends.

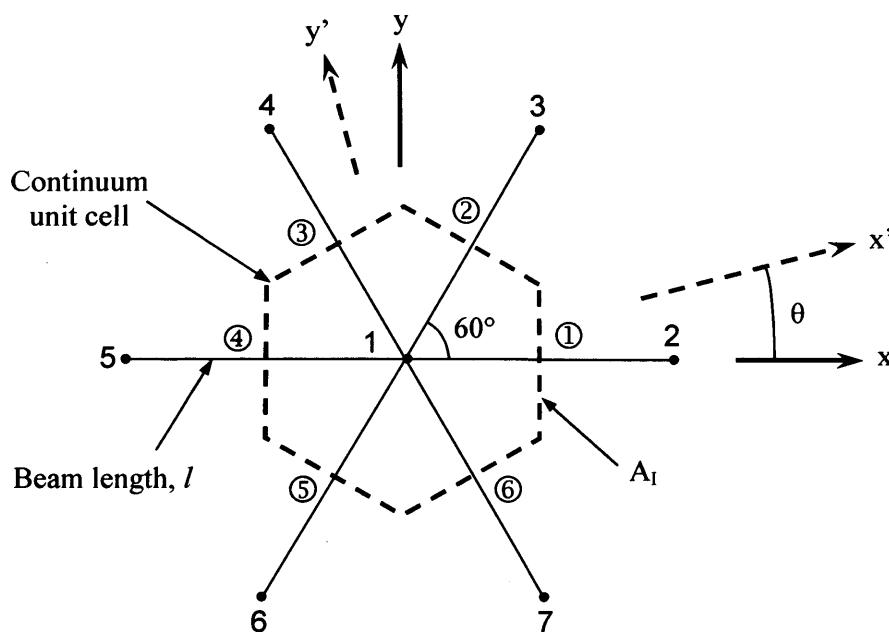


Figure 5.2. Representation of lattice star and hexagonal unit cell

The procedure that has been adopted for comparing the lattice star mid-beam stresses with the continuum stresses is as follows:

1. Initially a uniform stress field is assumed in the continuum in the $x'-x'$ direction, at an angle of θ to the x -axis.
2. The associated strain field is computed for an assumed homogenous material, and the displacements corresponding to the outer nodal positions of the star in Figure 5.2 are calculated.
3. These displacements, together with the stiffness properties of the beams, are then used to compute the resultant forces M , V , and F in the beams.
4. The effective (or nominal) stress in the beams is then calculated according to the Mohr-Coulomb criterion given in equation (5.3).

5.3.1.2 Stress transformation

As outlined above, a stress field is to be assumed in the $x'-x'$ axis, which is at an angle of θ to the x -axis. Before the associated strain field in the reference (x - y) axes may be computed, the stress field must be transformed into the reference axes system using the inverse of the stress transformation matrix, \mathbf{T}_σ . Therefore:

$$\boldsymbol{\sigma} = \mathbf{T}_\sigma^{-1} \boldsymbol{\sigma}' \quad (5.6)$$

where:

$$\mathbf{T}_\sigma^{-1} = \begin{bmatrix} \cos^2 \theta & \sin^2 \theta & -2 \sin \theta \cos \theta \\ \sin^2 \theta & \cos^2 \theta & 2 \sin \theta \cos \theta \\ \sin \theta \cos \theta & -\sin \theta \cos \theta & \cos^2 \theta - \sin^2 \theta \end{bmatrix} \quad (5.7)$$

5.3.1.3 Constitutive relationship

The strains may then be obtained from the transformed stresses using the constitutive relationship for the continuum. Therefore:

$$\boldsymbol{\varepsilon} = \mathbf{C} \boldsymbol{\sigma} \quad (5.8)$$

where \mathbf{C} is the elastic plane stress compliance matrix given by:

$$\mathbf{C} = \frac{1}{E} \begin{bmatrix} 1 & -\nu & 0 \\ -\nu & 1 & 0 \\ 0 & 0 & 1+\nu \end{bmatrix} \quad (5.9)$$

and E and ν are Young's modulus and Poisson's ratio for the material.

5.3.1.4 Continuum strain-displacement relationships

In a two-dimensional continuum there are three independent strain components but only two displacement components. Therefore, the direct displacement derivative-strain relationships are not sufficient to fully define the displacements, and thus a compatibility condition must be introduced. Considering the flexural stiffness of the 5 other beams at a connection, as mentioned previously, the rotation tensor (ω) may be taken to be zero:

$$\omega = \frac{1}{2} \left(\frac{\partial u_x}{\partial y} - \frac{\partial u_y}{\partial x} \right) = 0 \quad (5.10)$$

which implies:

$$\frac{\partial u_x}{\partial y} = \frac{\partial u_y}{\partial x} \quad (5.11)$$

The shear strain in the continuum is defined as usual by:

$$\varepsilon_{xy} = \frac{\gamma_{xy}}{2} = \frac{1}{2} \left(\frac{\partial u_x}{\partial y} + \frac{\partial u_y}{\partial x} \right) \quad (5.12)$$

and substituting (5.11) into (5.12) gives:

$$\varepsilon_{xy} = \frac{\gamma_{xy}}{2} = \frac{\partial u_x}{\partial y} = \frac{\partial u_y}{\partial x} \quad (5.13)$$

where γ_{xy} is the engineering shear strain.

The displacements at any given point in the continuum can now be uniquely determined if the strain field is uniform across the region and the displacements at one point in the region are known. In this case, $u_x=u_y=0$ at $x=y=0$. The nodal displacements for the end node j of a beam, in respect to the reference axes, can now be written in terms of the continuum strains:

$$\begin{bmatrix} u_x \\ u_y \end{bmatrix}_j = \begin{bmatrix} \varepsilon_{xx} & \frac{\gamma_{xy}}{2} \\ \frac{\gamma_{xy}}{2} & \varepsilon_{yy} \end{bmatrix} \cdot \begin{bmatrix} x \\ y \end{bmatrix}_j \quad (5.14)$$

These displacements, including the assumed zero rotation ($\phi_j=0$), can be transformed to the element local axes using the displacement transformation matrix, \mathbf{T}_u .

$$\mathbf{u}_L = \mathbf{T}_u \mathbf{u}_j = \begin{bmatrix} \cos \alpha & \sin \alpha & 0 \\ -\sin \alpha & \cos \alpha & 0 \\ 0 & 0 & 1 \end{bmatrix} \cdot \begin{bmatrix} u_x \\ u_y \\ \phi \end{bmatrix}_j \quad (5.15)$$

where α is the angle between the reference (x-y) axes and the local element axes, as shown in Figure 5.3.

5.3.1.5 Local stiffness relationship for a single element

The degrees of freedom and forces acting on a beam for the general case have already been discussed in section 3.3.2, and illustrated in Figure 3.6. For the specific case presented here, where node i is completely restrained and node j is restrained in the rotational sense, the nodal displacements in the local (ξ - η) axes are given by:

$$\mathbf{u}_i = \begin{bmatrix} u_\xi \\ u_\eta \\ \phi \end{bmatrix}_i = \begin{bmatrix} 0 \\ 0 \\ 0 \end{bmatrix} \quad (5.16)$$

and:

$$\mathbf{u}_j = \begin{bmatrix} u_\xi \\ u_\eta \\ \phi \end{bmatrix}_j = \begin{bmatrix} u_\xi \\ u_\eta \\ 0 \end{bmatrix} = \mathbf{u}_L \quad (5.17)$$

where \mathbf{u}_L is the local displacement vector. The deformed shape of a beam subject to such displacements is illustrated in Figure 5.3.

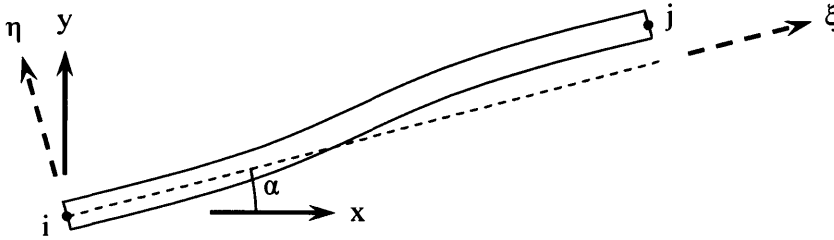


Figure 5.3. Element in local and global axis with rotations constrained

The local force vector which gives rise to these displacements is given by:

$$\mathbf{F}_L = \begin{bmatrix} F_\xi \\ F_\eta \\ M \end{bmatrix} \quad (5.18)$$

And this is related to the local displacement vector by the local stiffness matrix, \mathbf{k}_L :

$$\mathbf{F}_L = \mathbf{k}_L \mathbf{u}_L \quad (5.19)$$

Due to the translational and rotational restraint on node i the local stiffness matrix, \mathbf{k}_L is given by the lower right 3x3 sub-matrix obtained from the full element stiffness matrix, \mathbf{k}_e given previously in equation (3.2). Therefore:

$$\mathbf{k}_L = E \begin{bmatrix} \frac{A}{l} & 0 & 0 \\ 0 & \frac{12I}{l^3} & \frac{-6I}{l^2} \\ 0 & \frac{-6I}{l^2} & \frac{4I}{l} \end{bmatrix} \quad (5.20)$$

where A , l and I are the cross-sectional area, length and second moment of area of the beam, respectively. If we take unit breadth for the beam in the z -axis ($b=1$) then $A=h \cdot b$ becomes $A=h$, and $I= b \cdot h^3/12$ becomes $I= h^3/12$. Equation (5.20) for \mathbf{k}_L may then be re-written as:

$$\mathbf{k}_L = E \begin{bmatrix} \frac{h}{l} & 0 & 0 \\ 0 & \frac{h^3}{l^3} & \frac{-h^3}{2l^2} \\ 0 & \frac{-h^3}{2l^2} & \frac{h^3}{3l} \end{bmatrix} \quad (5.21)$$

where h is the height of the beam.

5.3.1.6 Failure criterion in terms of local beam axes

The general form of the criterion as expressed in equation (5.3) may be re-written in terms of the local beam axes as:

$$F(\underline{s}) = \mu(s_\xi - f_{tb}) + |s_\eta| = 0 \quad \text{at failure} \quad (5.22)$$

where s_ξ is the local nominal axial stress ($s_\xi = F_\xi/A_\xi$), s_η is the local nominal shear stress ($s_\eta = F_\eta/A_\eta$), f_{tb} is the failure strength of the beam, and μ is the shear/normal strength ratio. It should be noted that ideally, mid-section beam stresses should match those in the continuum when $A_\xi = A_\eta = A$, however for certain cases, as outlined in section 5.3.1.9, this does not hold true.

5.3.1.7 Examples

In order to examine the isotropy of the M-C failure criterion, and the equivalence between mid-section beam stresses and continuum stresses, let us consider the application of a tensile stress in the $x'-x'$ axis, which is equal to the ultimate strength of the material, f_t . Therefore $\sigma_{x'-x'} = \sigma_I = f_t$ and $\sigma_{y'-y'} = \sigma_{II} = 0$. In addition, let us also consider, initially, the uniaxial case where Poisson's ratio is zero ($\nu=0$). Therefore equation (5.8) reduces to:

$$\boldsymbol{\varepsilon} = \frac{1}{E} \boldsymbol{\sigma} \quad (5.23)$$

(i) Case 1 ($\theta=0^\circ$)

For this case:

$$\begin{bmatrix} \sigma_{xx} \\ \sigma_{yy} \\ \tau_{xy} \end{bmatrix} = \begin{bmatrix} \sigma_{x'x'} \\ \sigma_{y'y'} \\ \tau_{x'y'} \end{bmatrix} = \begin{bmatrix} f_t \\ 0 \\ 0 \end{bmatrix} \quad (5.24)$$

And therefore from equation (5.23):

$$\begin{bmatrix} \varepsilon_{xx} \\ \varepsilon_{yy} \\ \gamma_{xy} \end{bmatrix} = \begin{bmatrix} \varepsilon_{xx} \\ \varepsilon_{yy} \\ 2\varepsilon_{xy} \end{bmatrix} = \frac{1}{E} \begin{bmatrix} f_t \\ 0 \\ 0 \end{bmatrix} \quad (5.25)$$

If elements 1 and 2 of the lattice star given in Figure 5.2 are considered, the coordinates of the 'j' nodes of these elements (i.e. nodes 2 and 3) are $(x_2, y_2) = (l, 0)$ and $(x_3, y_3) = (l/2, \sqrt{3}l/2)$, respectively. The displacements of these nodes in the reference axes for the computed strain field are given from equation (5.14) by:

$$\begin{bmatrix} u_x \\ u_y \end{bmatrix}_2 = \begin{bmatrix} \varepsilon_{xx} & \frac{\gamma_{xy}}{2} \\ \frac{\gamma_{xy}}{2} & \varepsilon_{yy} \end{bmatrix} \cdot \begin{bmatrix} x \\ y \end{bmatrix}_2 = \frac{1}{E} \begin{bmatrix} f_t & 0 \\ 0 & 0 \end{bmatrix} \cdot \begin{bmatrix} l \\ 0 \end{bmatrix} = \frac{f_t}{E} \begin{bmatrix} l \\ 0 \end{bmatrix} \quad (5.26)$$

And:

$$\begin{bmatrix} u_x \\ u_y \end{bmatrix}_3 = \frac{1}{E} \begin{bmatrix} f_t & 0 \\ 0 & 0 \end{bmatrix} \cdot \begin{bmatrix} l/2 \\ \sqrt{3}l/2 \end{bmatrix} = \frac{f_t}{E} \begin{bmatrix} l/2 \\ 0 \end{bmatrix} \quad (5.27)$$

For element 1; $\alpha=0^\circ$, and therefore from equation (5.15), and assuming zero rotation of node 2 due to reasons cited previously:

$$u_L = \begin{bmatrix} u_x \\ u_y \\ \phi \end{bmatrix}_2 = \frac{f_t}{E} \begin{bmatrix} l \\ 0 \\ 0 \end{bmatrix} \quad (5.28)$$

From equations (5.19), (5.21) and (5.28) the local forces for element 1 are given by:

$$(\mathbf{F}_L)_1 = \begin{bmatrix} F_\xi \\ F_\eta \\ M \end{bmatrix}_1 = E \begin{bmatrix} \frac{h}{l} & 0 & 0 \\ 0 & \frac{h^3}{l^3} & \frac{-h^3}{2l^2} \\ 0 & \frac{-h^3}{2l^2} & \frac{h^3}{3l} \end{bmatrix} \cdot \frac{f_t}{E} \begin{bmatrix} l \\ 0 \\ 0 \end{bmatrix} = \begin{bmatrix} f_t h \\ 0 \\ 0 \end{bmatrix} \quad (5.29)$$

Taking $A_\xi = A_\eta = h$ (recalling that beam breadth is unity) gives:

$$s_\xi = \frac{F_\xi}{A_\xi} = \frac{f_t h}{h} = f_t \quad (5.30)$$

and $s_\eta=0$. These are equivalent to the applied axial and shear stress, as expected. From equation (5.22), the M-C failure function is given by:

$$F(\underline{s}) = \mu(s_\xi - f_{tb}) + |s_\eta| = \mu(f_t - f_{tb}) + |0| = 0 \quad (5.31)$$

which suggests that failure in the beam is also consistent with failure in the continuum.

For element 2; $\alpha=60^\circ$, and therefore from equation (5.15) and (5.27):

$$\mathbf{u}_L = \begin{bmatrix} \cos \alpha & \sin \alpha & 0 \\ -\sin \alpha & \cos \alpha & 0 \\ 0 & 0 & 1 \end{bmatrix} \cdot \begin{bmatrix} u_x \\ u_y \\ \phi \end{bmatrix}_3 = \begin{bmatrix} 1/2 & \sqrt{3}/2 & 0 \\ -\sqrt{3}/2 & 1/2 & 0 \\ 0 & 0 & 1 \end{bmatrix} \cdot \frac{f_t}{E} \begin{bmatrix} l/2 \\ 0 \\ 0 \end{bmatrix} = \frac{f_t}{E} \begin{bmatrix} l/4 \\ -\sqrt{3}l/4 \\ 0 \end{bmatrix} \quad (5.32)$$

From equations (5.19), (5.21) and (5.32) the local forces for element 2 are given by:

$$(\mathbf{F}_L)_2 = \begin{bmatrix} F_\xi \\ F_\eta \\ M \end{bmatrix}_2 = E \begin{bmatrix} \frac{h}{l} & 0 & 0 \\ 0 & \frac{h^3}{l^3} & -\frac{h^3}{2l^2} \\ 0 & -\frac{h^3}{2l^2} & \frac{h^3}{3l} \end{bmatrix} \cdot \frac{f_t}{E} \begin{bmatrix} l/4 \\ -\sqrt{3}l/4 \\ 0 \end{bmatrix} = f_t \begin{bmatrix} h/4 \\ -\sqrt{3}h^3/4l^2 \\ \sqrt{3}h^3/8l \end{bmatrix} \quad (5.33)$$

Therefore, noting that for a beam subject to zero end rotations and constant shear stress the bending moment at the mid-span reference surface is zero. Taking $A_\xi=A_\eta=h$ as before gives:

$$s_\xi = \frac{F_\xi}{A_\xi} = \frac{f_t h}{4h} = \frac{f_t}{4} \quad (5.34)$$

And:

$$s_\eta = \frac{F_\eta}{A_\eta} = \frac{-\sqrt{3}h^3}{4l^2} f_t \frac{1}{h} = \frac{-\sqrt{3}h^2}{4l^2} f_t \quad (5.35)$$

These values may be compared to the continuum stresses in this direction by transforming the stresses in the reference axes by 60° . Therefore:

$$\boldsymbol{\sigma}_{60^\circ} = \mathbf{T}_\sigma \boldsymbol{\sigma} = \begin{bmatrix} \cos^2 \theta & \sin^2 \theta & 2\sin \theta \cos \theta \\ \sin^2 \theta & \cos^2 \theta & -2\sin \theta \cos \theta \\ -\sin \theta \cos \theta & \sin \theta \cos \theta & \cos^2 \theta - \sin^2 \theta \end{bmatrix} \cdot \begin{bmatrix} \sigma_{xx} \\ \sigma_{yy} \\ \tau_{xy} \end{bmatrix} \quad (5.36)$$

$$\Rightarrow \begin{bmatrix} \sigma_{xx} \\ \sigma_{yy} \\ \tau_{xy} \end{bmatrix}_{60^\circ} = \begin{bmatrix} 1/4 & 3/4 & \sqrt{3}/2 \\ 3/4 & 1/4 & -\sqrt{3}/2 \\ -\sqrt{3}/4 & \sqrt{3}/4 & -1/2 \end{bmatrix} \cdot \begin{bmatrix} f_t \\ 0 \\ 0 \end{bmatrix} = f_t \begin{bmatrix} 1/4 \\ 3/4 \\ -\sqrt{3}/4 \end{bmatrix} \quad (5.37)$$

Therefore, from equations (5.34) and (5.37) it can be seen that $s_\xi = \sigma_{xx}(60^\circ)$ irrespective of the cross-sectional area of the beam. From equations (5.35) and (5.37), however, it can be seen that $s_\eta = \tau_{xy}(60^\circ)$ only if $h=l$. This result is consistent with equation (5.96) which gives $h=l$ for zero Poisson's ratio.

By substituting these values into equation (5.22) a minimum value of μ can be derived which ensures the 'inclined' beams do not fail before the primary horizontal beams in this case:

$$F(\underline{s}) = \mu \left(\frac{f_t}{4} - f_t \right) + \left| \frac{\sqrt{3}h^2}{4l^2} f_t \right| < 0 \quad (5.38)$$

$$\Rightarrow \mu > \frac{h^2}{\sqrt{3}l^2} \quad (5.39)$$

Therefore, if $h=l$ then $\mu > 1/\sqrt{3}$.

(ii) Case 2 ($\theta=30^\circ$)

The stresses in the reference (x - y) axes are given from equations (5.6) and (5.7) by:

$$\begin{bmatrix} \sigma_{xx} \\ \sigma_{yy} \\ \tau_{xy} \end{bmatrix} = \begin{bmatrix} \cos^2 30 & \sin^2 30 & -2\sin 30 \cos 30 \\ \sin^2 30 & \cos^2 30 & 2\sin 30 \cos 30 \\ \sin 30 \cos 30 & -\sin 30 \cos 30 & \cos^2 30 - \sin^2 30 \end{bmatrix} \cdot \begin{bmatrix} f_t \\ 0 \\ 0 \end{bmatrix} = f_t \begin{bmatrix} 3/4 \\ 1/4 \\ \sqrt{3}/4 \end{bmatrix} \quad (5.40)$$

And, therefore, from equation (5.25):

$$\begin{bmatrix} \varepsilon_{xx} \\ \varepsilon_{yy} \\ \gamma_{xy} \end{bmatrix} = \begin{bmatrix} \varepsilon_{xx} \\ \varepsilon_{yy} \\ 2\varepsilon_{xy} \end{bmatrix} = \frac{f_t}{E} \begin{bmatrix} 3/4 \\ 1/4 \\ \sqrt{3}/2 \end{bmatrix} \quad (5.41)$$

Therefore, considering elements 1 and 2 again, as for the previous case, the displacements of nodes 2 and 3, under the given strain field, are given by equation (5.14):

$$\begin{bmatrix} u_x \\ u_y \end{bmatrix}_2 = \begin{bmatrix} \varepsilon_{xx} & \frac{\gamma_{xy}}{2} \\ \frac{\gamma_{xy}}{2} & \varepsilon_{yy} \end{bmatrix} \cdot \begin{bmatrix} x \\ y \end{bmatrix}_2 = \frac{f_t}{E} \begin{bmatrix} 3/4 & \sqrt{3}/4 \\ \sqrt{3}/4 & 1/4 \end{bmatrix} \cdot \begin{bmatrix} l \\ 0 \end{bmatrix} = \frac{f_t l}{E} \begin{bmatrix} 3/4 \\ \sqrt{3}/4 \end{bmatrix} \quad (5.42)$$

$$\text{And: } \begin{bmatrix} u_x \\ u_y \end{bmatrix}_3 = \frac{f_t}{E} \begin{bmatrix} 3/4 & \sqrt{3}/4 \\ \sqrt{3}/4 & 1/4 \end{bmatrix} \cdot \begin{bmatrix} l/2 \\ \sqrt{3}l/2 \end{bmatrix} = \frac{f_t l}{E} \begin{bmatrix} 3/4 \\ \sqrt{3}/4 \end{bmatrix} \quad (5.43)$$

For element 1; $\alpha=0^\circ$, and therefore from equation (5.15), and assuming zero rotation of node 2 due to reasons cited previously:

$$u_L = \begin{bmatrix} u_x \\ u_y \\ \phi \end{bmatrix}_2 = \frac{f_t l}{E} \begin{bmatrix} 3/4 \\ \sqrt{3}/4 \\ 0 \end{bmatrix} \quad (5.44)$$

From equations (5.19), (5.21) and (5.28) the local forces for element 1 are given by:

$$(\mathbf{F}_L)_1 = \begin{bmatrix} F_\xi \\ F_\eta \\ M \end{bmatrix}_1 = E \begin{bmatrix} \frac{h}{l} & 0 & 0 \\ 0 & \frac{h^3}{l^3} & \frac{-h^3}{2l^2} \\ 0 & \frac{-h^3}{2l^2} & \frac{h^3}{3l} \end{bmatrix} \cdot \frac{f_t l}{E} \begin{bmatrix} 3/4 \\ \sqrt{3}/4 \\ 0 \end{bmatrix} = f_t \begin{bmatrix} 3h/4 \\ \sqrt{3}h^3/4l^2 \\ -\sqrt{3}h^3/8l \end{bmatrix} \quad (5.45)$$

Therefore, taking $A_\xi = A_\eta = h$ (recalling that beam breadth is unity) gives:

$$s_\xi = \frac{F_\xi}{A_\xi} = \frac{3h}{4h} f_t = \frac{3}{4} f_t \quad (5.46)$$

And:

$$s_\eta = \frac{F_\eta}{A_\eta} = \frac{\sqrt{3}h^3}{4l^2 h} f_t = \frac{\sqrt{3}h^2}{4l^2} f_t \quad (5.47)$$

As noted previously for case 1 ($\theta=0^\circ$), equations (5.40), (5.46) and (5.47) show that irrespective of the cross-sectional area of the beam, the axial beam stress is equivalent to the direct continuum stress ($s_\xi = \sigma_{xx}$), but the shear stresses are only equivalent ($s_\eta = \tau_{xy}$) if $h=l$. Before checking the failure criterion lets first consider the local stresses on element 2.

For element 2; $\alpha=60^\circ$, and therefore since the principal axis for case 2 ($\theta=30^\circ$) is a line of symmetry for elements 1 and 2, not only are the displacements of nodes 2 and 3 identical (equations (5.42) and (5.43)), but the local displacements and local forces can also be shown to be identical, apart from the direction (sign) of the displacement normal to the beam and also the shear force within the beam.

In addition, due to the symmetry of case 2 ($\theta=30^\circ$) both elements (1 and 2) should fail at the same time and ideally at a continuum principal stress value of f_t . Therefore, from equation (5.22), the M-C failure function is given by:

$$F(\underline{s}) = \mu(s_\xi - f_t) + |s_\eta| = \mu\left(\frac{3}{4} f_t - f_{tb}\right) + \left|\frac{\sqrt{3}h^2}{4l^2} f_t\right| = 0 \quad (5.48)$$

$$\Rightarrow \mu = \frac{\sqrt{3}h^2}{l^2} \quad (5.49)$$

If $h=l$ then in order for elements 1 and 2 to fail when $\sigma_{x'-x'} = \sigma_I = f_t$ at $\theta=30^\circ$ then $\mu=\sqrt{3}$. This is greater than $1/\sqrt{3}$ and therefore compliant with the requirements of equation (5.39).

5.3.1.8 General case

It has been shown for the two case examples described in detail above that when the Poisson's ratio is taken to be zero, and therefore $h=l$, the mid-plane axial and shear stresses in the elements of the lattice star (Figure 5.2) are equivalent to the axial and shear stresses in the continuum after transformations to the direction of the respective elements have been undertaken. This stress equivalence can be shown to hold true for all directions of principal stress ($0^\circ \leq \theta \leq 360^\circ$) and for all elements ($\alpha=0^\circ, 60^\circ, 120^\circ, 180^\circ, 240^\circ, 300^\circ$).

It has also been shown above that if these mid-plane stresses are combined in a M-C criterion then when the major principal axis is half way between two elements (e.g. $\theta=30^\circ$), both elements become simultaneously critical and therefore fail at an effective stress equal to the continuum stress, f_t , only when the shear/normal strength ratio, $\mu=\sqrt{3}$. In addition, when the major principal axis is in line with an element axis (e.g. $\theta=0^\circ$), this element, which is by definition critical, fails at the same effective stress as the continuum principal stress in pure tension, and the failure stress of such an element is independent of the value of μ . For other values of θ the value of the Mohr-Coulomb function as expressed in equation (5.3) has been calculated and is illustrated in Figure 5.4(a).

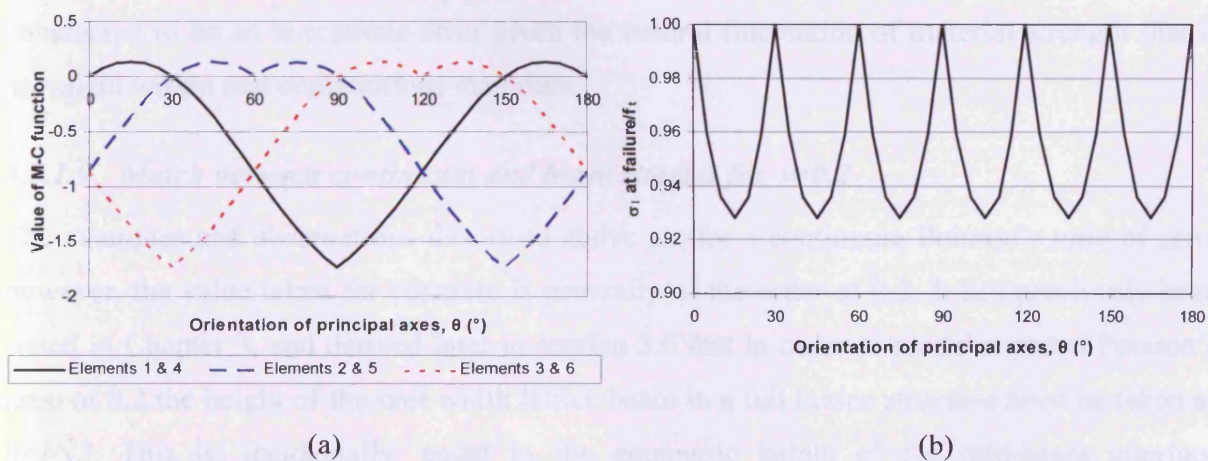


Figure 5.4. (a) Value of M-C function for elements within lattice star, and (b) The value of the continuum major principal stress, σ_I at failure normalised to the tensile strength, f_t , for varying θ .

It can be seen from Figure 5.4(a) that the value of the Mohr-Coulomb function for each element fluctuates in an oscillatory manner as the principal axes rotate. The function has a wavelength of 180° and has a discontinuity in the gradient every 90° due to the use of the absolute value of the shear stress in the Mohr-Coulomb function (equation (5.3)). It should be noted that due to the assumption that the lattice star (Figure 5.2) is fixed to the underlying continuum, and that both are restrained at $x=y=0$, then the stress state of elements 4, 5, and 6 are identical to that of elements 1, 2, and 3, respectively, for any given principal stress, σ_I .

For a rotating principal stress value, $\sigma_I = f_t = 1 \text{ MPa}$, the value of the Mohr-Coulomb function in the most critical element is either equal to or greater than zero as shown in Figure 5.4(a). The most critical elements are initially elements 1 and 4, when $\theta = 0^\circ$, and the critical status changes to elements 2 and 5 at $\theta = 30^\circ$ and elements 3 and 6 at $\theta = 90^\circ$. The critical status then continues to cycle over the three pairs of elements every 60° . This behaviour is consistent with what one would intuitively expect from a rotating principal tensile stress, as illustrated in Figure 5.2. Therefore, the correct elements become critical for different orientations of the principal tensile stress, however, the value of the M-C function for the most critical element fluctuates between 0 and 0.13 every 15° , indicating that this failure criterion is not perfectly isotropic. The degree of this anisotropy is best quantified by considering the value of the principal tensile stress, σ_I , at failure, normalised to the tensile strength of the material, f_t . This is illustrated in Figure 5.4(b), for varying θ . It can be seen from this figure that the normalised value of principal stress fluctuates between 1 and 0.93. The degree of anisotropy of the Mohr-Coulomb failure criterion is therefore only of the order of approximately 7%. This is considered to be an acceptable error given the natural fluctuation of material strength that is prevalent within real cementitious materials.

5.3.1.9 Match between continuum and beam stresses for $\nu=0.2$

The examples and observations discussed above are for a continuum Poisson's ratio of zero, however, the value taken for concrete is generally of the order of 0.2. It has previously been stated in Chapter 3, and derived later in section 5.6 that in order to model a global Poisson's ratio of 0.2 the height of the unit width lattice beam in a full lattice structure must be taken as $h=l/\sqrt{3}$. This is, incidentally, equal to the geometric height of the mid-beam interface represented by one side of the hexagonal unit cell shown in Figure 5.2.

The isolated single lattice 'star' considered above, however, is not capable at a local level of matching the continuum stresses generated by the biaxial straining that occurs due to a non-



zero Poisson's ratio. After damage in the form of cracking has occurred, however, the Poisson's ratio of a continuum, certainly at the local level, may be assumed to be zero. The accuracy of this assumption generally increases with the amount of damage that has occurred within the continuum.

As a result of the above, for a typical lattice simulation of concrete, the height of the beam elements are usually taken as $l/\sqrt{3}$ to represent an initial Poisson's ratio of 0.2 for the material in its elastic state. But, as noted previously, following damage to the material the value of Poisson's ratio tends towards zero. It is therefore worthwhile considering how the axial and shear mid-plane beam stresses compare to the 'damaged' continuum stresses for a plane stress beam with a height, and therefore cross-sectional area, of $l/\sqrt{3}$.

We may now reconsider the two examples given above: For case 1 ($\theta=0^\circ$), element 1 ($\alpha=0^\circ$), the mid-plane stress and failure criterion are independent of the cross-sectional area of the beam and the results are as previously given. For element 2 ($\alpha=60^\circ$) however, the axial stress s_ξ remains the same but for $h=l/\sqrt{3}$ the shear stress at the mid-surface of the beam becomes:

$$s_\eta = \frac{F_\eta}{A_\eta} = \frac{-\sqrt{3}h^2}{4l^2} f_t = \frac{-\sqrt{3}\left(\frac{l}{\sqrt{3}}\right)^2}{4l^2} f_t = \frac{-\sqrt{3}}{12} f_t \quad (5.50)$$

This is one third of the continuum shear stress at this point (equation (5.37)).

For case 2 ($\theta=30^\circ$), element 1 ($\alpha=0^\circ$), the axial stress is again independent of the cross-sectional area of the beam and the shear stress is equal to that given for element 2 of case 1 in equation (5.37) above. This is again one third of the continuum shear stress at this point.

It can be shown that generally for all orientations of the principal tensile stress ($0^\circ \leq \theta \leq 360^\circ$), that the axial stress in the elements and continuum are equivalent, irrespective of the cross-sectional area of the elements, and that the shear stresses in the elements are consistently one third of their continuum counterparts. In addition, if we consider the value of the shear/normal strength ratio, μ , that causes elements 1 and 2 to fail at the same time for a principal stress orientation of 30° , then from equation (5.49):

$$\mu = \frac{\sqrt{3}h^2}{l^2} = \frac{\sqrt{3}\left(\frac{l}{\sqrt{3}}\right)^2}{l^2} = \frac{1}{\sqrt{3}} \quad (5.51)$$

Alternatively, equivalence may be obtained between the element and continuum shear stresses if the shear area of the beam, A_η , is taken to be one third of the beam cross-sectional area:

$$A_\eta = \frac{A}{3} = \frac{h}{3} = \frac{l}{3\sqrt{3}} \quad (5.52)$$

If this revised definition for the shear area is adopted then the Mohr-Coulomb function given by equation (5.3) remains unchanged and elements 1 and 2 both fail, as previously, when $\mu = \sqrt{3}$.

5.4 Principal stress based failure criterion

5.4.1 Matching strains in plane beams

The concept of a lattice ‘star’ fixed on top of a continuum as introduced above, may be extended in order to try and obtain a match between the strain state at element mid-surfaces and the strain state at the same location in the continuum. The nodal displacements of the end nodes j of the six beams of the lattice star shown in Figure 5.2, have already been expressed in terms of the continuum strains in the reference coordinate system by equation (5.14). As illustrated in Figure 5.5, the nodal coordinates may subsequently be written in terms of the element length, l , and the angle between the reference axes and the local element axes, α , giving:

$$\begin{bmatrix} x \\ y \end{bmatrix}_j = l \begin{bmatrix} \cos \alpha \\ \sin \alpha \end{bmatrix}_j \quad (5.53)$$

Equation (5.14) therefore becomes:

$$\begin{bmatrix} u_x \\ u_y \end{bmatrix}_j = l \begin{bmatrix} \epsilon_{xx} & \frac{\gamma_{xy}}{2} \\ \frac{\gamma_{xy}}{2} & \epsilon_{yy} \end{bmatrix} \cdot \begin{bmatrix} \cos \alpha \\ \sin \alpha \end{bmatrix}_j \quad (5.54)$$

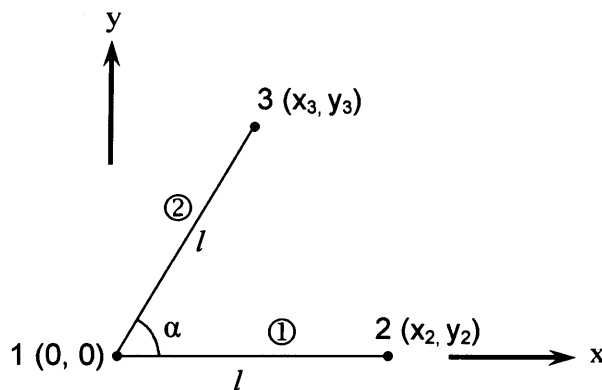


Figure 5.5. Enlarged detail of lattice ‘star’

The nodal coordinates given above may then be transformed into the local element axes using equation (5.15). If the nodal rotations are assumed to be zero due to reasons cited previously, then from (5.15) and (5.54):

$$\mathbf{u}_L = \mathbf{T}_u \mathbf{u}_j = \begin{bmatrix} \cos \alpha & \sin \alpha \\ -\sin \alpha & \cos \alpha \end{bmatrix} \cdot l \begin{bmatrix} \varepsilon_{xx} & \frac{\gamma_{xy}}{2} \\ \frac{\gamma_{xy}}{2} & \varepsilon_{yy} \end{bmatrix} \cdot \begin{bmatrix} \cos \alpha \\ \sin \alpha \end{bmatrix}_j \quad (5.55)$$

$$= l \begin{bmatrix} \varepsilon_{xx} \cos^2 \alpha + \gamma_{xy} \sin \alpha \cos \alpha + \varepsilon_{yy} \sin^2 \alpha \\ -\varepsilon_{xx} \sin \alpha \cos \alpha + \frac{\gamma_{xy}}{2} (\cos^2 \alpha - \sin^2 \alpha) + \varepsilon_{yy} \sin \alpha \cos \alpha \end{bmatrix} \quad (5.56)$$

Therefore from (5.56), the local axial and shear strain components in the beam, noting that the engineering shear strain, γ_η , is twice the true shear strain, ε_η , are given by:

$$\begin{bmatrix} \varepsilon_\xi \\ \gamma_\eta \end{bmatrix} = \frac{1}{l} \begin{bmatrix} u_\xi \\ 2u_\eta \end{bmatrix} = \begin{bmatrix} \varepsilon_{xx} \cos^2 \alpha + \gamma_{xy} \sin \alpha \cos \alpha + \varepsilon_{yy} \sin^2 \alpha \\ -2\varepsilon_{xx} \sin \alpha \cos \alpha + \gamma_{xy} (\cos^2 \alpha - \sin^2 \alpha) + 2\varepsilon_{yy} \sin \alpha \cos \alpha \end{bmatrix} \quad (5.57)$$

These should match the respective local strain components in the continuum. Therefore, considering the standard continuum strain transformation:

$$\varepsilon'_{ij} = \mathbf{n}_i \mathbf{n}_j \varepsilon_{ij} \quad (5.58)$$

And, in explicit matrix form for a transformation angle of α :

$$\begin{bmatrix} \varepsilon_{\xi\xi} \\ \varepsilon_{\eta\eta} \\ \gamma_{\xi\eta} \end{bmatrix} = \begin{bmatrix} \cos^2 \alpha & \sin^2 \alpha & \cos \alpha \sin \alpha \\ \sin^2 \alpha & \cos^2 \alpha & -\cos \alpha \sin \alpha \\ -2 \sin \alpha \cos \alpha & 2 \sin \alpha \cos \alpha & \cos^2 \alpha - \sin^2 \alpha \end{bmatrix} \cdot \begin{bmatrix} \varepsilon_{xx} \\ \varepsilon_{yy} \\ \gamma_{xy} \end{bmatrix} \quad (5.59)$$

Therefore, by expanding (5.59) it can be seen that the axial and shear strains are equivalent to those derived in (5.57), and in addition:

$$\varepsilon_{\eta\eta} = \sin^2 \alpha \varepsilon_{xx} + \cos^2 \alpha \varepsilon_{yy} - \gamma_{xy} (\cos^2 \alpha - \sin^2 \alpha) \quad (5.60)$$

In the beam elements $\varepsilon_{\eta\eta}$ is not available, and hence at the local level the lattice star is incapable of capturing a non-zero Poisson's ratio as previously described. This is due to the fact that when $\nu \neq 0$ the stress components depend not only on direct strains but also on orthogonal strains. This problem may be addressed by considering the full lattice star, as illustrated in Figure 5.6, and evaluating $\varepsilon_{\eta\eta}$ for a particular element mid-surface by considering the displacements in adjacent nodes.

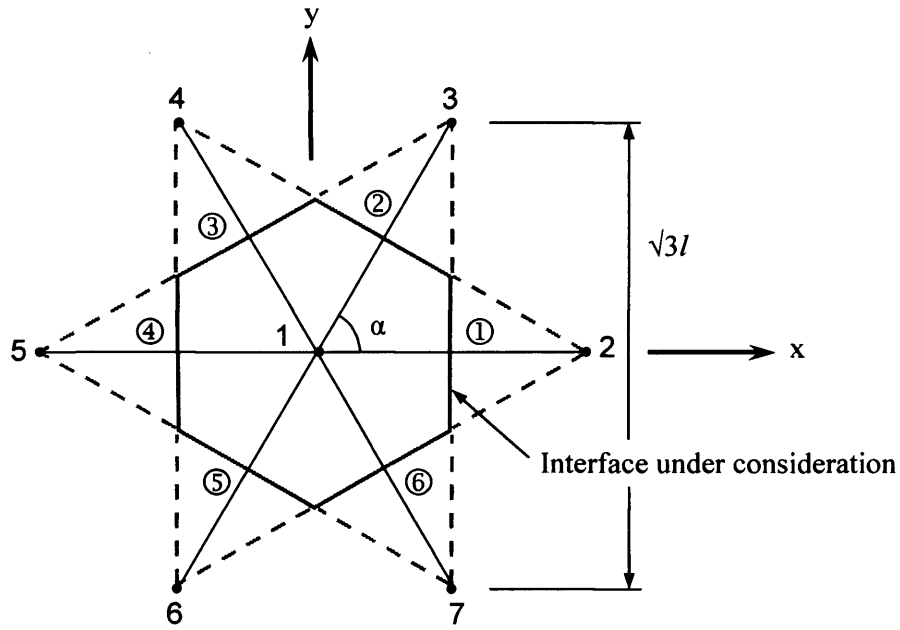


Figure 5.6. Full lattice star highlighting alignment of element mid-surface and end nodes of adjacent elements for determination of $\varepsilon_{\eta\eta}$

It can be seen from Figure 5.6 that due to the geometry of the regular triangular lattice the element mid-surfaces are in alignment with the nodal positions of the end nodes of adjacent elements. Considering element 1, the relative displacements may be defined as follows:

$$\begin{bmatrix} \bar{u}_{\xi\xi} \\ \bar{u}_{\eta\eta} \\ \bar{u}_{\xi\eta} \end{bmatrix}_{el=1} = \begin{bmatrix} u_{\xi 2} - u_{\xi 1} \\ u_{\eta 3} - u_{\eta 7} \\ u_{\eta 2} - u_{\eta 1} \end{bmatrix} \quad (5.61)$$

where ξ and η are the local axes of the element under consideration (i.e. element 1 above). Therefore, whilst the nodal displacements are all calculated in the reference axes for a strain field obtained from an applied stress field, as described previously, the transformations of these nodal displacements must relate to the orientation of the element under consideration. From equation (5.15), and ignoring nodal rotations:

$$\begin{bmatrix} u_{\xi} \\ u_{\eta} \end{bmatrix}_j = \begin{bmatrix} \cos \alpha & \sin \alpha \\ -\sin \alpha & \cos \alpha \end{bmatrix}_i \cdot \begin{bmatrix} u_x \\ u_y \end{bmatrix}_j \quad (5.62)$$

where i is the element number under consideration and j is the node number of the nodes required for calculating the full strain state at the interface of element i . For the above example, $i=1$ and $j=1, 2, 3$ & 7 . Once the respective nodal displacements have been obtained in the local axes, and the relative displacements calculated according to (5.61), then the strains at the element interface may be obtained from:

$$\begin{bmatrix} \varepsilon_{\xi\xi} \\ \varepsilon_{\eta\eta} \\ \gamma_{\xi\eta} \end{bmatrix}_i = \frac{1}{l} \begin{bmatrix} \bar{u}_{\xi\xi} \\ \bar{u}_{\eta\eta} / \sqrt{3} \\ 2\bar{u}_{\xi\eta} \end{bmatrix}_i \quad (5.63)$$

noting that the reference length between the end nodes of elements adjacent to the one under consideration (e.g. nodes 3 and 7 for element 1) is $\sqrt{3}l$, as shown in Figure 5.6.

The equivalent stress components at the element mid-surface must then be calculated from the elastic D-matrix for the material, as oppose to the element stiffness matrix for the beam as used previously. This is because the element stiffness matrix does not take into consideration the additional displacements orthogonal to the axis of the beam, as described above.

Therefore:

$$\begin{bmatrix} \sigma_{\xi\xi} \\ \sigma_{\eta\eta} \\ \tau_{\xi\eta} \end{bmatrix} = \frac{E}{1-\nu^2} \begin{bmatrix} 1 & \nu & 0 \\ \nu & 1 & 0 \\ 0 & 0 & \frac{1-\nu}{2} \end{bmatrix} \cdot \begin{bmatrix} \varepsilon_{\xi\xi} \\ \varepsilon_{\eta\eta} \\ \gamma_{\xi\eta} \end{bmatrix} \quad (5.64)$$

5.4.2 Failure criterion development

In light of the extended theoretical consideration of the strain state at the mid-surface of the elements forming the lattice star, the most appropriate failure criterion should be re-evaluated.

It has been shown previously that if the lattice is viewed as a plane in 2D, then the Mohr-Coulomb failure criterion is suitable, but never perfectly isotropic. An alternative continuum failure criterion, which is isotropic, is one based on principal stresses. This may be expressed as follows:

$$\sigma_I - f_t \geq 0 \text{ implies failure} \quad (5.65)$$

where:

$$\sigma_I = \frac{\sigma_{\xi\xi} + \sigma_{\eta\eta}}{2} + \sqrt{\left(\frac{\sigma_{\xi\xi} - \sigma_{\eta\eta}}{2}\right)^2 + \tau_{\xi\eta}^2} \quad (5.66)$$

and f_t is the failure strength of the material.

The orientation of the principal stress axis (α_I), which has zero shear stress, is then given relative to the direction of the beam axes by:

$$\alpha_I = \frac{1}{2} \tan^{-1} \left(\frac{2\tau_{\xi\eta}}{\sigma_{\xi\xi} - \sigma_{\eta\eta}} \right) \quad (5.67)$$

5.4.3 Continuum equivalence and isotropy of the principal stress failure criterion

The theory presented above suggests that the principal stress failure criterion, for the mid-surface stresses of a plane beam in a single lattice ‘star’, is isotropic when the lattice is considered to represent an elastic continuum (i.e. all elements in the ‘star’ are intact). In order to confirm this for the more general case of an entire mesh, the failure criterion has been applied to a discrete regular triangular lattice mesh, which is loaded in orthogonal directions, as shown in Figure 5.7.

Figure 5.7 shows two 10x10 lattice meshes, which are undamaged and have an element length of 1mm. The continuum domain which has been discretised by the meshes is 10mm wide and 8.660mm high. The two meshes are subject to prescribed displacement boundary conditions so that constant states of strain are set up in orthogonal directions. The strain is constant in the vertical direction in Figure 5.7(a) and in the horizontal direction in Figure 5.7(b).

For the purpose of this investigation $E=1000MPa$, and $u_y=8.6603 \times 10^{-3}mm$. For an original mesh height of 8.660mm this gives a uniform vertical strain, $\epsilon_y=0.001$. In order to generate the same strain field in the horizontal direction (Figure 5.7(b)), the prescribed displacements for the outer (u_{xo}) and inner (u_{xi}) nodes must be varied to account for the oscillating boundary caused by the geometry of the regular lattice configuration. Considering the case where prescribed displacements are applied to both sides of the mesh (Figure 5.7(b)), the original reference lengths for the inner and outer prescribed displacements are 4.5 and 5.0mm, respectively. In order to achieve a horizontal strain, $\epsilon_x=0.001$, the prescribed inner and outer displacements are therefore $u_{xi}=4.5 \times 10^{-3}mm$ and $u_{xo}=5 \times 10^{-3}mm$, respectively.

As a result of the prescribed displacements given above a constant value of principal stress of 1MPa should be generated in both meshes ($\sigma=E.\epsilon=1000 \times 0.001=1MPa$) if the results are to be consistent with the underlying continuum. Also, the direction of this principal stress from the x-axis for case (a) and case (b) should be 90° and 0° respectively.

The continuum equivalence and isotropy of the principal stress criterion may now be evaluated by comparing the actual principal stress values and the calculated angle of the principal axes, for all of the individual lattice beams from the two orthogonal cases, with the continuum values given above. It should be noted that this has been undertaken for the elastic case only, where no elements have been broken.

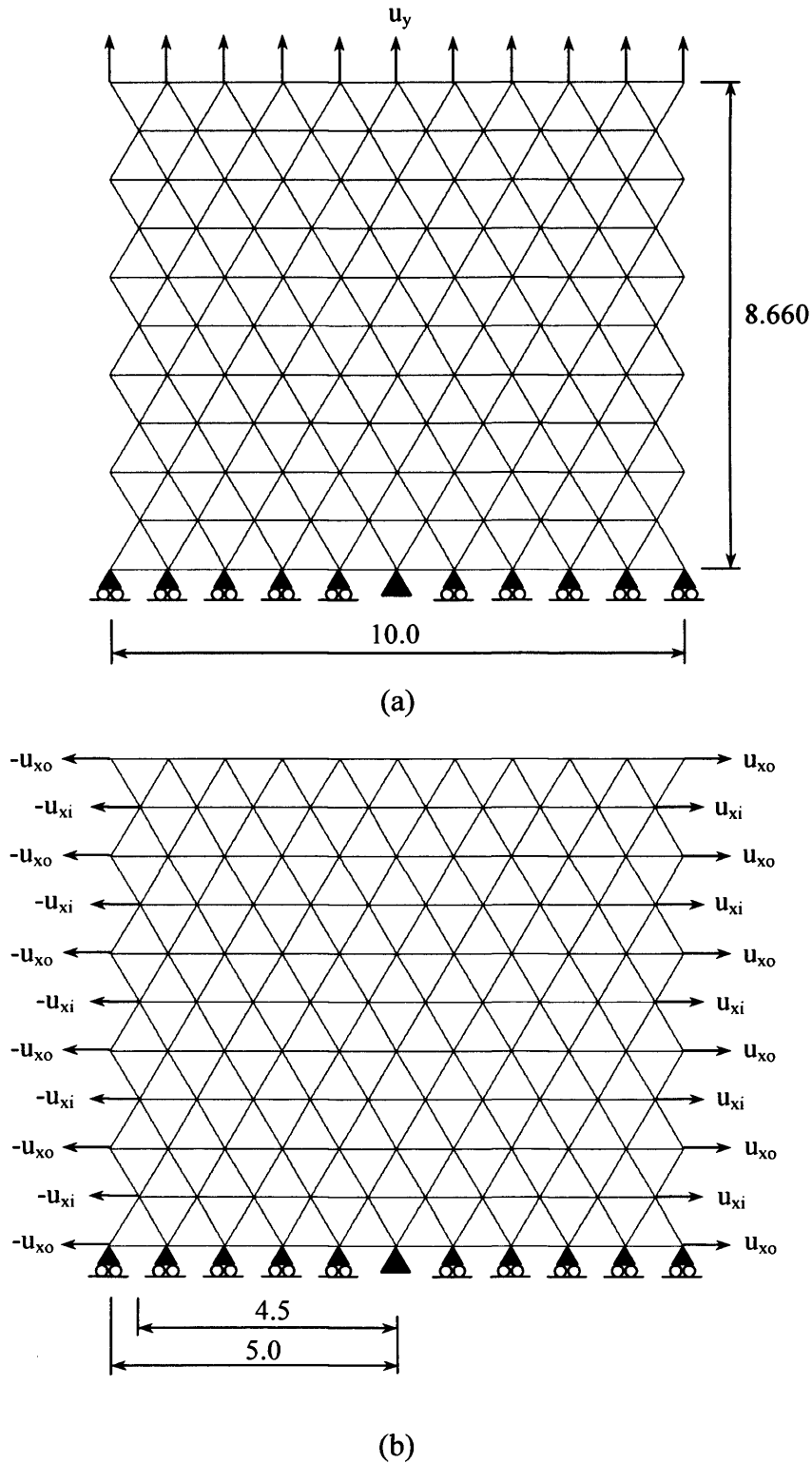


Figure 5.7. Boundary conditions used to cause constant strain in 10x10 lattice mesh at (a) 0° and (b) 90° orientation.

The values of the major principal stress for every lattice beam of the mesh under constant vertical and horizontal strains are shown by the colour plots in Figure 5.8.

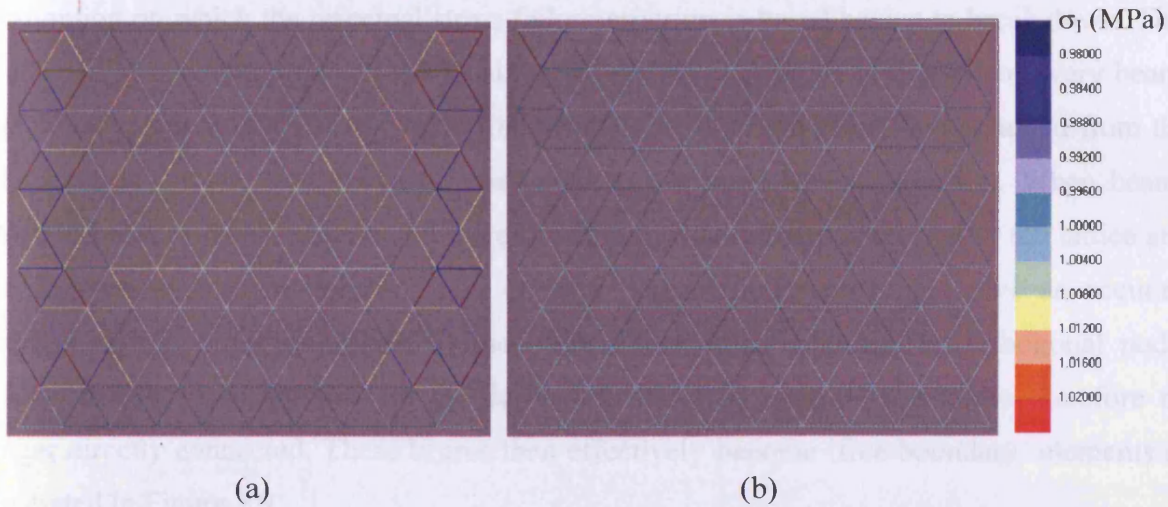


Figure 5.8. Major principal stress variation in lattice elements under constant (a) vertical and (b) horizontal strain fields

It can be seen that the variation in the value of the major principal stress for both the constant vertical and horizontal strain cases is very small. The values range from 0.944 to 1.077MPa for the constant vertical strain case (Figure 5.8(a)), and from 0.974 to 1.041MPa for the constant horizontal strain case (Figure 5.8(b)). Due to the periodically varying width of the lattice domain in Figure 5.7(a), the variation of the major principal stress is far greater at the left and right boundaries of Figure 5.8(a) than for the top and bottom boundaries of Figure 5.8(b). However, for both orientations of the constant strain field it can be seen from Figure 5.8 that the variation of the major principal stress is very small away from the boundaries, and within 1% of the true continuum value of 1MPa.

The values obtained for the orientation of the principal stress (α_l) relative to the beam axes are also equally as accurate as the values of the principal stresses themselves. The expected values of α_l for case (a) when the principal stress is in the vertical direction are 90° , 30° and -30° for the horizontal, upward diagonal and downward diagonal elements, respectively. For case (b) when the principal stress is in the horizontal direction, the expected values are 0° , -60° , and 60° . The values obtained for the internal elements were within 0.1% or less of the expected values for both cases. The outer elements show greater fluctuation due to boundary effects, with the error being greater for case (a) than case (b), as observed previously for the principal stress values.

The principal stress failure criterion described above has been verified to be isotropic for the elastic case of a pristine lattice mesh which represents an underlying continuum which is undamaged. However, once elements of the lattice begin to break, the fundamental

assumption on which the principal stress failure criterion is based begins to break down. This fundamental assumption is that the local ‘cross’ strains ($\epsilon_{\eta\eta}$) at the mid-plane of every beam, which are required in order to capture the local Poisson’s ratio effect, are obtained from the displacements of the two nodes perpendicular to the mid-plane in question. When beams begin to break, a displacement, and therefore strain, discontinuity is created in the lattice and the displacements from one (or both) of these ‘cross’ nodes no longer give an accurate estimate of $\epsilon_{\eta\eta}$ at the mid-plane of the beam under consideration. The orthogonal nodal displacements which are used in the derivation of $\epsilon_{\eta\eta}$ in equation (5.63) are therefore no longer directly connected. These beams then effectively become ‘free-boundary’ elements as illustrated in Figure 5.9.

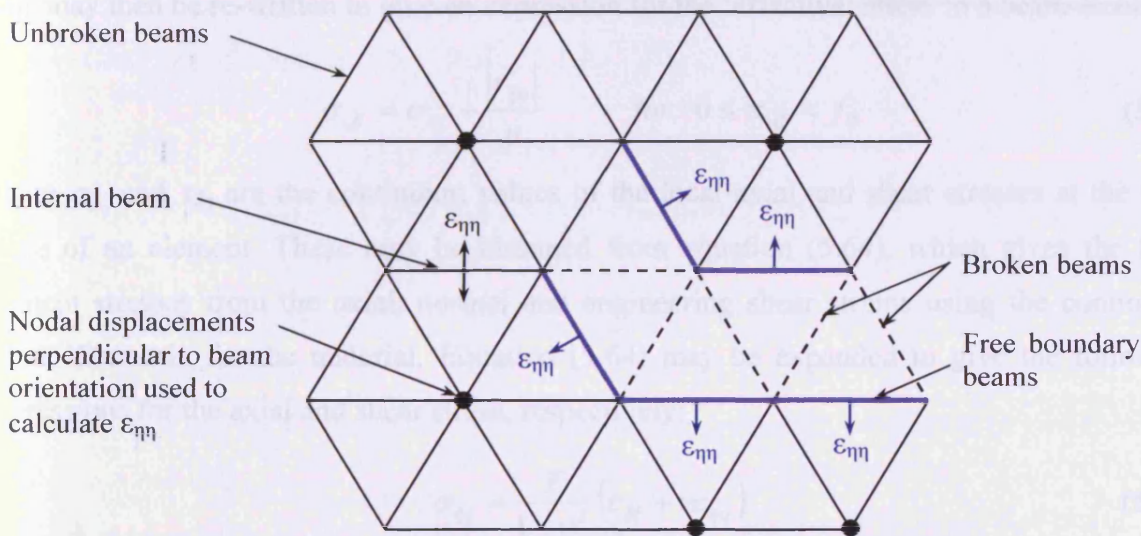


Figure 5.9. Creation of free boundary beams due to beam breakages

Following beam breakage it is still possible to calculate a value of $\epsilon_{\eta\eta}$ at the mid-plane of the free boundary elements using the perpendicular displacements from the remaining cross node, in the same manner as is originally done for the boundary elements of the mesh (Figure 5.7). However, once damage has started to occur the idealisation of a star representing part of a continuum is no longer valid, and a failure criterion, such as Mohr-Coulomb, which is based on local beam stresses then becomes the most appropriate. In addition, a Mohr-Coulomb criterion which considers the shear/normal strength ratio, μ at an interface has more practical relevance than a principal stress criterion, especially when microstructure is considered. The value of μ , for example, can be calculated from experiments on hcp/aggregate interface properties, as discussed by van Mier (1997).

5.5 Further failure criteria considerations

5.5.1 Mohr-Coulomb criterion based on continuum stresses

In order to achieve the most accurate version of the Mohr Coulomb failure criterion it is therefore worth considering a version of the criterion which is based on the continuum stresses at the mid-plane of a beam, whilst these are valid.

The general form of the Mohr-Coulomb criterion as given in equation (5.3) can be written in terms of the local beam axes (Figure 5.3) to give:

$$\mu(\sigma_{\xi\xi} - f_{tb}) + |\tau_{\xi\eta}| = 0 \quad (5.68)$$

This may then be re-written to give an expression for the ‘effective’ stress in a beam element:

$$\sigma_{eff} = \sigma_{\xi\xi} + \frac{|\tau_{\xi\eta}|}{\mu} \quad \text{for: } 0 \leq \sigma_{eff} < f_{tb} \quad (5.69)$$

where $\sigma_{\xi\xi}$ and $\tau_{\xi\eta}$ are the continuum values of the local axial and shear stresses at the mid-plane of an element. These may be obtained from equation (5.64), which gives the local element stresses from the axial, normal and engineering shear strains using the continuum elastic D-matrix for the material. Equation (5.64) may be expanded to give the following expressions for the axial and shear stress, respectively:

$$\sigma_{\xi\xi} = \frac{E}{1-\nu^2} (\varepsilon_{\xi\xi} + \nu\varepsilon_{\eta\eta}) \quad (5.70)$$

And:

$$\tau_{\xi\eta} = \frac{E}{2(1+\nu)} \gamma_{\xi\eta} \quad (5.71)$$

The values of the local strain components $\varepsilon_{\xi\xi}$, $\varepsilon_{\eta\eta}$ and $\gamma_{\xi\eta}$ given above may be obtained, as for the principal stress criterion, from equation (5.63). These strain components have been derived from the displacements of the end nodes of the beam and the ‘cross’ nodes perpendicular to the beam mid-plane, as illustrated by equation (5.61) and Figure 5.6.

Since the above version of the Mohr-Coulomb failure criterion is based on strains calculated from the displacement of these ‘cross’ nodes, the criterion becomes invalid as the lattice becomes damaged due to reasons cited previously for the principal stress criterion. The local Poisson’s ratio then tends towards zero.

5.5.2 Modified Mohr-Coulomb criterion based on continuum stresses

An alternative, modified form of the continuum stress based Mohr-Coulomb criterion given above may therefore be developed. If the axial stress component along the local beam axis $\sigma_{\xi\xi}$ is calculated from only the axial strain, $\varepsilon_{\xi\xi}$, then considering the behaviour as uniaxial:

$$\sigma_{\xi\xi} = E\varepsilon_{\xi\xi} \quad (5.72)$$

This definition of $\sigma_{\xi\xi}$ may then be adopted in the Mohr-Coulomb criterion given in equation (5.68). This modified criterion may then be used throughout the entire duration of a fracture test on a lattice mesh since the normal strain, $\varepsilon_{\eta\eta}$ which is obtained from the ‘cross’ nodes, is no longer considered. It should be noted, however, that as a result of this, the accuracy of the stress state captured by the criterion for an elastic mesh is less than that offered by the criterion described in section 5.5.1 above.

5.5.3 Modified Mohr-Coulomb criterion based on beam stresses

Considering that the lattice method is a discrete modelling method, the most appropriate form of a Mohr-Coulomb type failure criterion is one that is based on the stresses in a beam. Given this, it is therefore worthwhile investigating whether a criterion may be developed which is based on the stresses calculated from the forces in the beam, but that can also match the true continuum stresses for a pristine lattice. This would therefore avoid the need to switch failure criteria mid analysis.

By comparing stress terms for the beam and continuum it is possible to determine what corrections are required in order to satisfy this requirement.

If the rotation is assumed to be zero due to the restraint of the adjoining neighbouring elements, then the beam forces from equations (5.18), (5.19) and (5.20) are:

$$F_L = \begin{bmatrix} F_\xi \\ F_\eta \end{bmatrix} = \frac{E_b}{l} \begin{bmatrix} A & 0 \\ 0 & \frac{12I}{l^2} \end{bmatrix} \begin{bmatrix} u_\xi \\ u_\eta \end{bmatrix} \quad (5.73)$$

Therefore, the local beam stresses are given by:

$$\sigma_L = \begin{bmatrix} s_\xi \\ s_\eta \end{bmatrix} = \begin{bmatrix} \frac{F_\xi}{A} \\ \frac{F_\eta}{\alpha_s A} \end{bmatrix} = \frac{E_b}{l} \begin{bmatrix} \frac{u_\xi}{A} \\ \frac{u_\eta}{\alpha_s A} \end{bmatrix} = E_b \begin{bmatrix} \frac{u_\xi}{l} \\ \frac{u_\eta}{l \alpha_s} \end{bmatrix} \quad (5.74)$$

where α_s is the shear area correction factor, and the other variables are as previously defined.

But:

$$\frac{12I}{l^2 \alpha_s A} = \frac{12bh^3}{l^2 \alpha_s bh} = \frac{h^2}{l^2 \alpha_s} \quad (5.75)$$

Therefore:

$$\sigma_L = \begin{bmatrix} s_\xi \\ s_\eta \end{bmatrix} = E_b \begin{bmatrix} \frac{u_\xi}{l} \\ \frac{u_\eta}{l} \frac{h^2}{l^2 \alpha_s} \end{bmatrix} \quad (5.76)$$

The axial and shear stresses in the continuum are given from equations (5.64) and (5.63) by:

$$\sigma_c = \begin{bmatrix} \sigma_{\xi\xi} \\ \tau_{\xi\eta} \end{bmatrix} = \frac{E_c}{1-\nu^2} \begin{bmatrix} 1 & \nu & 0 \\ 0 & 0 & \frac{1-\nu}{2} \end{bmatrix} \frac{1}{l} \begin{bmatrix} \bar{u}_{\xi\xi} \\ \bar{u}_{\eta\eta} / \sqrt{3} \\ 2\bar{u}_{\xi\eta} \end{bmatrix} = \frac{E_c}{1-\nu^2} \begin{bmatrix} \frac{\bar{u}_{\xi\xi}}{l} + \nu \frac{\bar{u}_{\eta\eta}}{\sqrt{3}l} \\ (1-\nu) \frac{\bar{u}_{\xi\eta}}{l} \end{bmatrix} \quad (5.77)$$

Assuming that, once a crack has occurred, uniaxial conditions apply locally:

$$\varepsilon_{\eta\eta} = -\nu \varepsilon_{\xi\xi} \quad (5.78)$$

Therefore, from equation (5.63):

$$\frac{\bar{u}_{\eta\eta}}{\sqrt{3}l} = -\nu \frac{\bar{u}_{\xi\xi}}{l} \quad (5.79)$$

Substituting this into equation (5.77) gives:

$$\sigma_{\xi\xi} = \frac{E_c}{1-\nu^2} \left(\frac{\bar{u}_{\xi\xi}}{l} (1-\nu^2) \right) = E_c \frac{\bar{u}_{\xi\xi}}{l} \quad (5.80)$$

The uniaxial stress terms between the beam (s_ξ) and the continuum ($\sigma_{\xi\xi}$), which are obtained from equations (5.76) and (5.80), may now be compared. Hence if $\sigma_{\xi\xi}$ is taken as being correct, then:

$$\sigma_{\xi\xi} = \beta_1 s_\xi \quad (5.81)$$

where β_1 is the correction factor applied to the axial stress in the beam so that it matches the continuum value, and is given by:

$$\beta_1 = \frac{\sigma_{\xi\xi}}{s_\xi} = \frac{E_c \frac{\bar{u}_{\xi\xi}}{l}}{E_b \frac{\bar{u}_{\xi\xi}}{l}} = \frac{E_c}{E_b} \quad (5.82)$$

Comparing the shear stress terms between the beam (s_η) and the continuum ($\tau_{\xi\eta}$), which are given by equations (5.76) and (5.77), and taking $\tau_{\xi\eta}$ as being correct, gives:

$$\tau_{\xi\eta} = \beta_2 s_\eta \quad (5.83)$$

where β_2 is the correction factor applied to the shear stress in the beam so that it matches the continuum value. Since $\bar{u}_{\xi\eta} = u_\eta$, β_2 is given by:

$$\beta_2 = \frac{\tau_{\xi\eta}}{s_\eta} = \frac{\frac{E_c}{E_b} \frac{\bar{u}_{\xi\eta}}{u_\eta} \frac{l}{h^2}}{\frac{1+\nu}{l^2 \alpha_s}} = \frac{E_c}{E_b} \frac{1}{(1+\nu)} \left(\frac{l^2 \alpha_s}{h^2} \right) \quad (5.84)$$

If the axial and shear stresses calculated from the beam forces are modified using the correction factors given above, then, in general, better agreement should be obtained with the true continuum stresses for a pristine elastic lattice.

Prior to examining the effect that the choice of failure criterion has on the mechanical response of an actual lattice mesh, the cross-sectional geometric properties of the lattice beams are derived for completeness.

5.6 Strain energy equivalence

As described in section 3.3.3, the geometric properties of the lattice beams have traditionally been chosen in order to satisfy equivalence between the strain energy stored in the unit cell of the lattice and the continuum. The tensorial derivation of these beam properties, as given by Karihaloo et al. (2003), which is based upon matching the components of the elasticity tensor, is reworked in this section using the explicit matrix forms of the equations previously adopted in this chapter.

For the strain energies to match under a constant strain field the terms in the constitutive relationship for the continuum (D-matrix) must be equivalent to those in the constitutive relationship for the beam (stiffness matrix, \mathbf{k}_L).

Therefore:

$$\frac{1}{2} \int_V \boldsymbol{\varepsilon}^T \mathbf{D} \boldsymbol{\varepsilon} dv = \frac{1}{2} \int_V \mathbf{u}_L^T \mathbf{k}_L \mathbf{u}_L dv = \frac{1}{2} \int_V \mathbf{u}_L^T \mathbf{F}_L dv \quad (5.85)$$

Noting that in the present derivation the hexagonal unit cell, as illustrated in Figure 5.2, comprises of six ‘half-beams’ rather than full beams, the total strain energy W_L is given by:

$$W_L = \frac{1}{2} \int_V \mathbf{u}_L^T \mathbf{k}_L \mathbf{u}_L dv = \frac{1}{2} \cdot \frac{1}{2} \sum_6 \mathbf{u}_{L,i}^T \mathbf{k}_L \mathbf{u}_{L,i} = \frac{1}{4} \sum_6 \mathbf{u}_{L,i}^T \mathbf{F}_{L,i} \quad (5.86)$$

Recalling the assumption that the displacement at the central node is zero, and also that the rotation ϕ is assumed zero due to the effective restraint of the five additional connecting elements, then from equations (5.19), (5.20) and (5.56) the local element force is given by:

$$\mathbf{F}_{Li} = \frac{E_b}{l} \begin{bmatrix} A & 0 & 0 \\ 0 & \frac{12I}{l^2} & \frac{-6I}{l} \\ 0 & \frac{-6I}{l} & 4I \end{bmatrix} \cdot l \begin{bmatrix} \cos^2 \alpha & \sin^2 \alpha & \frac{\sin \alpha \cos \alpha}{\cos^2 \alpha - \sin^2 \alpha} \\ -\sin \alpha \cos \alpha & \sin \alpha \cos \alpha & \frac{2}{0} \\ 0 & 0 & 0 \end{bmatrix}_i \cdot \begin{bmatrix} \epsilon_{xx} \\ \epsilon_{yy} \\ \gamma_{xy} \end{bmatrix} \quad (5.87)$$

where E_b is the Young's modulus for the beam.

If the local strain energy for an element is given by w_{Li} , and:

$$w_{Li} = \mathbf{u}_{Li}^T \mathbf{F}_{Li} \quad (5.88)$$

then pre-multiplying (5.87) by \mathbf{u}_{Li}^T and making the same substitution for the local displacement as above, gives the following:

$$w_{Li} = hbE_b l \cdot \epsilon^T \cdot \begin{bmatrix} c^2 & -sc & 0 \\ s^2 & \frac{sc}{2} & 0 \\ sc & \frac{c^2 - s^2}{2} & 0 \end{bmatrix}_i \cdot \begin{bmatrix} 1 & 0 & 0 \\ 0 & \frac{h^2}{l^2} & \frac{-h^2}{2l} \\ 0 & \frac{-h^2}{2l} & \frac{h^2}{3} \end{bmatrix} \cdot \begin{bmatrix} c^2 & s^2 & \frac{sc}{2} \\ -sc & sc & \frac{c^2 - s^2}{2} \\ 0 & 0 & 0 \end{bmatrix}_i \cdot \epsilon \quad (5.89)$$

where the substitutions $A=bh$, $I=bh^3/12$, $c=\cos(\alpha)$, and $s=\sin(\alpha)$ have been made in addition to the lumping of scalar terms. Multiplying out the three central matrices gives:

$$w_{Li} = hbE_b l \cdot \epsilon^T \cdot \begin{bmatrix} c^4 + s^2 c^2 \left(\frac{h^2}{l^2} \right) & s^2 c^2 - s^2 c^2 \left(\frac{h^2}{l^2} \right) & sc^3 - \left(\frac{sc^3 - s^3 c}{2} \right) \left(\frac{h^2}{l^2} \right) \\ s^4 + s^2 c^2 \left(\frac{h^2}{l^2} \right) & s^3 c + \left(\frac{sc^3 - s^3 c}{2} \right) \left(\frac{h^2}{l^2} \right) & s^2 c^2 + \left(\frac{c^2 - s^2}{2} \right)^2 \left(\frac{h^2}{l^2} \right) \\ SYMM & & \end{bmatrix}_i \cdot \epsilon \quad (5.90)$$

Therefore from (5.86):

$$W_L = \frac{1}{4} \sum_6 w_{Li} \quad (5.91)$$

The trigonometric terms in equation (5.90) must therefore be summed over i , where $i=1$ to 6 , and $\alpha_i=(i-1)\pi/3$ radians. Summing these terms and substituting the values into (5.90) and subsequently into (5.91) gives:

$$W_L = \frac{1}{4}hbE_b l \cdot \boldsymbol{\epsilon}^T \cdot \begin{bmatrix} \frac{1}{4}\left(9+3\left(\frac{h}{l}\right)^2\right) & \frac{3}{4}\left(1-\left(\frac{h}{l}\right)^2\right) & 0 \\ \frac{3}{4}\left(1-\left(\frac{h}{l}\right)^2\right) & \frac{1}{4}\left(9+3\left(\frac{h}{l}\right)^2\right) & 0 \\ 0 & 0 & \frac{3}{4}\left(1+\left(\frac{h}{l}\right)^2\right) \end{bmatrix} \cdot \boldsymbol{\epsilon} \quad (5.92)$$

If we now consider the strain energy in the continuum; the volume of the hexagonal unit cell $= (\sqrt{3}/2)l^2b$, and therefore, from equation (5.85) the total strain energy in the continuum unit cell is given by:

$$W_c = \frac{1}{2} \frac{\sqrt{3}}{2} l^2 b \cdot \boldsymbol{\epsilon}^T \cdot \left(\frac{E}{1-\nu^2} \right) \begin{bmatrix} 1 & \nu & 0 \\ \nu & 1 & 0 \\ 0 & 0 & \frac{1-\nu}{2} \end{bmatrix} \cdot \boldsymbol{\epsilon} \quad (5.93)$$

Therefore, equating equations (5.93) and (5.92), and simplifying gives:

$$\left(\frac{h}{l} \right) \left(\frac{E_b}{\sqrt{3}} \right) \mathbf{Mat}_e = \mathbf{D} \quad (5.94)$$

where \mathbf{Mat}_e and \mathbf{D} are the elastic constitutive matrices for the beam and continuum respectively.

We may consider the Poisson's ratio represented by the lattice system, through examining the ratio of terms $\mathbf{Mat}_{e(1,2)}$ and $\mathbf{Mat}_{e(1,1)}$. Therefore:

$$\nu = \frac{\frac{3}{4}\left(1-\left(\frac{h}{l}\right)^2\right)}{\frac{3}{4}\left(3+\left(\frac{h}{l}\right)^2\right)} = \frac{1-\left(\frac{h}{l}\right)^2}{3+\left(\frac{h}{l}\right)^2} \quad (5.95)$$

This can be rearranged in terms of h to give:

$$h = l \sqrt{\frac{1-3\nu}{\nu+1}} \quad (5.96)$$

The relationship between the Young's modulus of the continuum and the beam may be obtained by comparing term $\mathbf{D}_{(1,1)}$ with the equivalent term in the beam $\mathbf{Mat}_{e(1,1)}$, allowing for the additional pre-multiplication terms as given in equation (5.94). Therefore:

$$\frac{E}{1-\nu^2} = \left(\frac{h}{l} \right) \left(\frac{E_b}{\sqrt{3}} \right) \frac{3}{4} \left(3 + \left(\frac{h}{l} \right)^2 \right) \quad (5.97)$$

Substituting in (5.95) for ν gives:

$$\frac{E}{E_b} = \left(1 - \frac{\left(1 - \left(\frac{h}{l} \right)^2 \right)^2}{3 + \left(\frac{h}{l} \right)^2} \right) \frac{\sqrt{3}}{4} \left(\frac{h}{l} \right) \left(3 + \left(\frac{h}{l} \right)^2 \right) \quad (5.98)$$

And simplifying:

$$\frac{E}{E_b} = 2\sqrt{3} \left(\frac{h}{l} \right) \frac{1 + \left(\frac{h}{l} \right)^2}{3 + \left(\frac{h}{l} \right)^2} \quad (5.99)$$

It should be noted that both equation (5.95) and (5.99) agree with those derived by Karihaloo et al. (2003), as previously given in equations (3.8) and (3.9), respectively.

The ratio of the Young's modulus of the continuum (E) and the beam (E_b) may then be written in terms of the Poisson's ratio, ν by substituting equation (5.96) into equation (5.99), and simplifying to give:

$$\frac{E}{E_b} = \sqrt{3}(1-\nu) \sqrt{\frac{1-3\nu}{\nu+1}} \quad (5.100)$$

When $\nu=0.2$ equation (5.100) gives $E/E_b=0.8$ which implies that the Young's modulus value used for the beam element must be 1.25 times greater than the Young's modulus of the continuum being modelled.

5.7 Summary and comparison of different failure criteria

This chapter has investigated various options for the lattice beam failure criterion. A brief overview of two existing criteria was initially given. These are the stress based criterion used by the Delft group and the strain based criterion used by Karihaloo et al. (2003). In order to avoid the use of empirical scaling factors, and also to try and achieve mesh orientation independence (i.e. an isotropic failure criterion), various criteria have been proposed and investigated. These criteria have included a Mohr-Coulomb criterion based on axial, shear and moment forces, a principal stress criterion, a Mohr-Coulomb criterion based on continuum stresses, and a modification thereof, and finally, a modified version of the M-C criterion based on beam stresses.

In developing these new failure criteria, a series of proofs, validations and verifications have been completed. A brief summary of these investigations, together with the main assumptions and results, are given below:

Continuum equivalence and isotropy of the Mohr-Coulomb failure criterion

The equivalence between the continuum stresses and the mid-plane stresses of a beam, and the isotropy properties of the criterion were examined in this investigation.

The main assumptions made in this investigation are that:

- The lattice star (Figure 5.2) is fixed to the underlying continuum, at the nodal points, to which a stress field is applied.
- The displacements at the centre of the star are assumed to be zero.
- Each beam is effectively restrained rotationally by the flexural stiffness of the other five beams connected to each of its ends.
- The stress state is uniaxial.

The main results from this investigation are that:

- For $\nu \neq 0$ the Mohr-Coulomb criterion can never predict a perfectly isotropic failure, since the normal strains, $\varepsilon_{\eta\eta}$ at the beam mid-planes are not considered.
- When the major principal axis is half way between two elements (*e.g.* $\theta=30^\circ$), both elements become simultaneously critical and therefore fail at an effective stress equal to the continuum stress, f_t , only when the shear/normal strength ratio, $\mu=\sqrt{3}$.
- For $\mu=\sqrt{3}$ the ‘correct’ beam (most in-line with the principal stress axis) always fails first and the maximum degree of anisotropy (difference between beam stress and continuum stress), for a rotating principal stress, is approximately 7%.
- If $h=l/\sqrt{3}$ (to model a global Poisson’s ratio of 0.2), then the shear stress calculated from the resultants matches the continuum shear stress when $A_\eta=A/3$.

Continuum equivalence and isotropy of the principal stress failure criterion

If the lattice represents an isotropic homogenous material, the most appropriate failure criterion becomes one based on principal stresses. This may be achieved if the normal strains, $\varepsilon_{\eta\eta}$ are considered at the mid-plane of every beam.

The main assumptions made in the development of this criterion are that:

- There are two ‘cross’ nodes located perpendicular to the direction of the beam at the mid-plane of the beam, or one in the case of a boundary element. This implies that the lattice mesh must have a regular periodic triangular configuration.
- The normal strain, $\varepsilon_{\eta\eta}$ can be calculated from the displacements of these ‘cross’ nodes.
- The beams connecting the ‘cross’ nodes to the end nodes of the beam being considered are intact, and therefore the value of $\varepsilon_{\eta\eta}$ calculated is representative of that in the underlying continuum.

The main results from this investigation are that:

- The principal stress criterion is isotropic for the two orthogonal cases of uniaxial stress considered. i.e. the magnitude and direction of the principal stress calculated at the mid-plane of each of the lattice beams, irrespective of their orientation, agrees very closely with the continuum stress state.
- The criterion is only truly accurate for the pre-damage elastic case, and as damage occurs the local Poisson’s ratio tends to zero and the most appropriate failure criterion becomes one which is based on beam stresses.

Modification of the Mohr-Coulomb criterion based on beam stresses to match continuum.

The purpose of this investigation was to establish whether a M-C based failure criterion could be developed, which was based on beam rather than continuum stresses, but which could also be modified so that it matched the true continuum stresses for a pristine lattice.

The main assumptions made in this investigation are that:

- The rotation is assumed to be zero due to the restraint of the five adjoining neighbouring elements.
- The stress terms for the beam and continuum may be compared, and the continuum stress values may be assumed to be correct.
- Uniaxial stress applies locally.

The main results from this investigation are that:

- The stress components may be matched if two correction factors, β_1 and β_2 , are used to correct the axial and shear components of the beam stress, respectively.

Strain energy equivalence between lattice and continuum

The geometric properties of the lattice beam have been derived from comparison of the strain energy stored in a lattice ‘star’ and the equivalent continuum unit cell, under a constant strain field.

The main assumptions made in this investigation are that:

- The dotted hexagon formed from the intersection of the lines normal to the beam mid-surfaces represents the unit cell of the continuum, as illustrated in Figure 5.2.
- The strain energy stored in a continuum unit cell may be compared to the strain energy stored in the six ‘half’ beams emanating from the centre of the unit cell.

The main results from this investigation are that:

- In order to model a Poisson’s ratio of 0.2, the required height of a lattice beam (assuming unit thickness) is $h=l/\sqrt{3}$.
- When $\nu=0.2$ the Young’s modulus value used for the beam element must be 1.25 times greater than the Young’s modulus of the continuum being modelled.

The seven failure criteria that have therefore been considered and discussed in this chapter are summarised in Table 5.1 below:

Table 5.1. Summary of failure criteria investigation

Failure criteria	Key Equations	Assumptions
1. Delft	$\sigma_t = \frac{F}{A} + \alpha \frac{(M_i , M_j)_{\max}}{W}$ $A = bh \text{ and } W = \frac{bh^2}{6}$	<ul style="list-style-type: none"> • Shear force considered implicitly • $\alpha=0.005$
2. Karihaloo et al. (2003)	$\varepsilon = \frac{1}{l} \left(\Delta_x \cos \theta + \Delta_y \sin \theta + \varphi_1 - \varphi_2 \frac{h}{2} \alpha_s \right)$	<ul style="list-style-type: none"> • Strains calculated from beam end node displacements. • $\alpha_s=0.005$
3. M-C beam forces	$\mu(\sigma - f_{tb}) + \tau = 0$ $\sigma_{eff} = \sigma + \frac{ \tau }{\mu} \quad \text{for: } 0 \leq \sigma_{eff} < f_{tb}$	<ul style="list-style-type: none"> • Stresses calculated from beam forces. • Axial stress includes component from centre moment.

	$\sigma = \frac{F}{A_\xi} + \frac{ M_c }{W}$	<ul style="list-style-type: none"> • $\tau = F_\eta / A_\eta$ • $A_\xi = A, A_\eta = A/3.$ • $\mu = \sqrt{3}$
4. principal stress	$\sigma_I = \frac{\sigma_{\xi\xi} + \sigma_{\eta\eta}}{2} + \sqrt{\left(\frac{\sigma_{\xi\xi} - \sigma_{\eta\eta}}{2}\right)^2 + \tau_{\xi\eta}^2}$ $\sigma = \mathbf{D}\varepsilon$	<ul style="list-style-type: none"> • Regular elastic lattice configuration. • $\varepsilon_{\eta\eta}$ is obtained from displacements of ‘cross’ nodes. • Beams connecting ‘cross’ nodes with end nodes of beam are intact.
5. M-C continuum stresses	$\mu(\sigma_{\xi\xi} - f_{tb}) + \tau_{\xi\eta} = 0$ $\sigma_{eff} = \sigma_{\xi\xi} + \frac{ \tau_{\xi\eta} }{\mu} \quad \text{for: } 0 \leq \sigma_{eff} < f_{tb}$ $\sigma_{\xi\xi} = \frac{E}{1-\nu^2}(\varepsilon_{\xi\xi} + \nu\varepsilon_{\eta\eta})$ $\tau_{\xi\eta} = \frac{E}{2(1+\nu)}\gamma_{\xi\eta}$	<ul style="list-style-type: none"> • Regular elastic lattice configuration. • $\varepsilon_{\eta\eta}$ is obtained from displacements of ‘cross’ nodes. • Beams connecting ‘cross’ nodes with end nodes of beam are intact. • $\mu = \sqrt{3}$
6. Modified M-C continuum stresses	<p>Main equations as 5 above, but:</p> $\sigma_{\xi\xi} = E\varepsilon_{\xi\xi} \text{ and } \tau_{\xi\eta} = \frac{E}{2(1+\nu)}\gamma_{\xi\eta}$	<ul style="list-style-type: none"> • $\varepsilon_{\eta\eta}$ is not used. • $\mu = \sqrt{3}$
7. Modified M-C beam stresses	<p>Main equations as 5 above, but:</p> $\sigma_{\xi\xi} = \beta_1 s_\xi$ <p>where $\beta_1 = \frac{E_c}{E_b}$ and $s_\xi = E_b \frac{u_\xi}{l}$</p> $\tau_{\xi\eta} = \beta_2 s_\eta$ <p>Where $\beta_2 = \frac{E_c}{E_b} \frac{1}{(1+\nu)} \left(\frac{l^2 \alpha_s}{h^2} \right)$ and</p> $s_\eta = E_b \frac{u_\eta}{l} \frac{h^2}{l^2 \alpha_s}$	<ul style="list-style-type: none"> • Nodal rotations assumed to be zero. • Axial and shear forces based on beam forces corrected to match the continuum values for elastic stage. • $A_\xi = A, A_\eta = A/3.$ • $\mu = \sqrt{3}$

In order to compare the failure criteria summarised in Table 5.1, two lattice examples have been considered. The first example is a simple uniaxial tension ‘unzipping’ test undertaken on a 10x10 mesh with 1mm beam elements. The boundary conditions for this test are given in Figure 5.10 below.

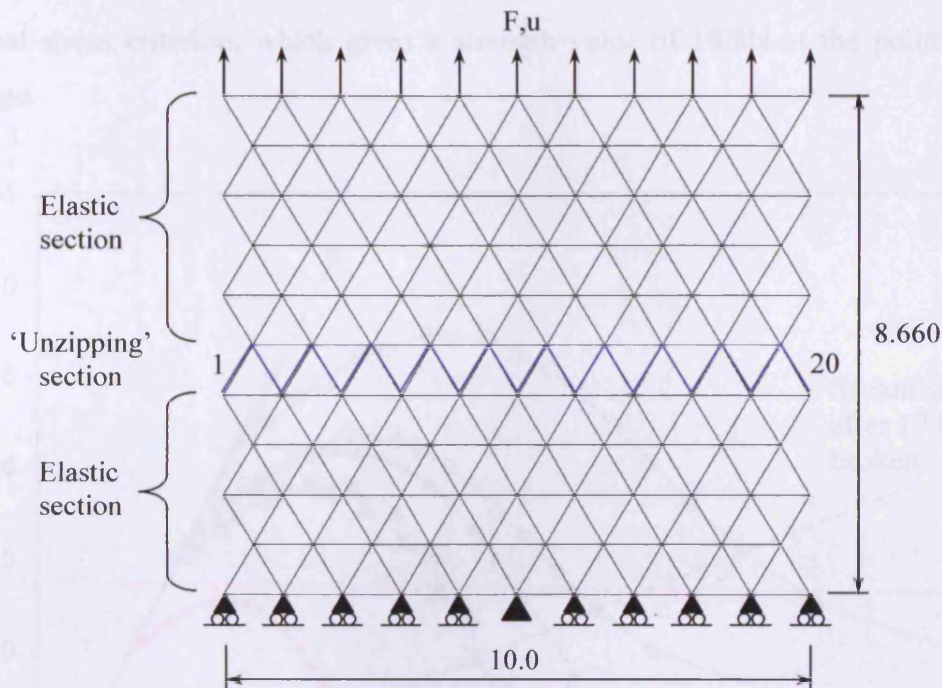


Figure 5.10. Boundary conditions for 'unzipping' uniaxial tension example

All of the elements are elastic (very high failure strengths) apart from the single line of 20 diagonal elements located in the central area of the specimen. These elements have been given a linear distribution of beam strengths from 2 to 11.5MPa, in 0.5MPa increments. As a result of this, the failure mode of the mesh for all simulations is identical. This is an 'unzipping' mode from left to right, i.e. element 1 fails first, followed by element 2, 3 then 4 etc. The values of E and ν used in the analysis are 31255MPa and 0.2 respectively.

All of the failure criteria summarised in Table 5.1 have been implemented in the numerical code, and a comparison of the force-displacement response produced by each of the criteria is given in Figure 5.11 below.

Since the lowest beam strength is 2MPa, and the cross-sectional area of the mesh is approximately 10mm^2 (assuming unit depth), the value of the force at the point of first beam breakage should be approximately 20N. It can be seen from Figure 5.11 that the actual force at first beam breakage varies considerably between the different failure criteria. The value is 31.6N for Karihaloo et al's criterion, and 25.1N for the Delft criterion, but only 16.1N for the M-C criterion with no corrections to match the continuum stresses (criterion 3). When these corrections are considered (criterion 7) the strength at first beam breakage is 21.5N, which is far more accurate. As expected, the three remaining criteria, which are also based on the continuum stress values at the mid-plane of the beam are all reasonably consistent, and are within approximately 7% of the expected value of 20N. The most appropriate criterion is the

principal stress criterion, which gives a strength value of 19.8N at the point of first beam breakage.

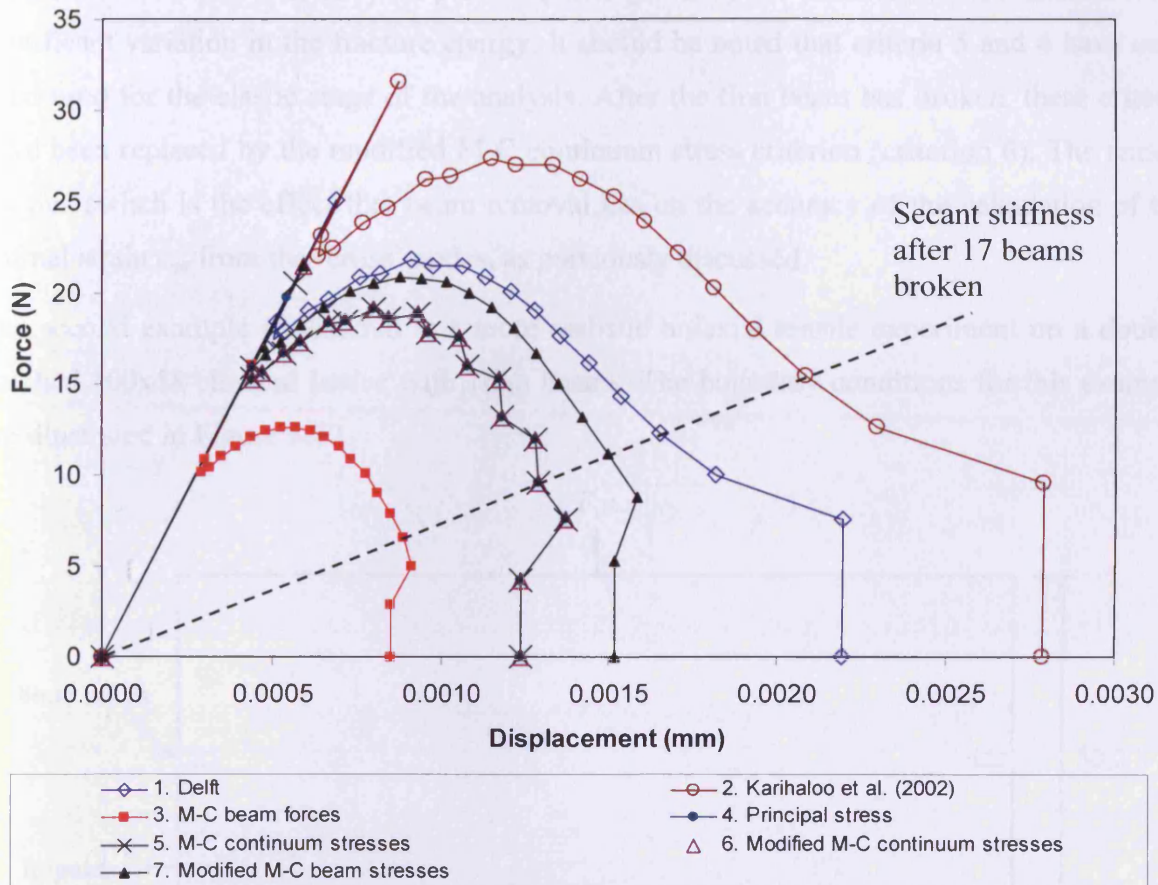


Figure 5.11. Force-displacement response of 'unzipping' uniaxial tension example

The order of beam breakages, and hence, the degradation of the lattice stiffness, is identical for all of the simulations presented in Figure 5.11. A different secant stiffness line may therefore be drawn from the origin to represent each of the 20 stages of damage that occur during the complete failure of the specimen shown in Figure 5.10. The secant stiffness line for the lattice after 17 beams have been removed, in an 'unzipping' manner, is shown in Figure 5.11. The force and displacement values of the lattice required to cause failure in the next beam (beam 18) for each of the different failure criteria may then be compared along this line. In addition, if the relative effects of the different criterion are compared along all of the secant stiffness lines, then it can be observed from Figure 5.11 that the relative effects of the different criteria remain reasonably constant until the end of the simulation when they deviate slightly. This deviation is probably due to the change of failure mode that occurs towards the

end of the simulation when the remaining beams are likely to experience greater rotational effects.

As a result of the above, the post-peak response given by the different failure criteria show significant variation in the fracture energy. It should be noted that criteria 5 and 4 have only been used for the elastic stage of the analysis. After the first beam has broken, these criteria have been replaced by the modified M-C continuum stress criterion (criterion 6). The reason for this switch is the effect that beam removal has on the accuracy of the calculation of the normal strain $\varepsilon_{\eta\eta}$ from the ‘cross’ nodes, as previously discussed.

The second example considered is a more realistic uniaxial tensile experiment on a doubly notched 100x58 element lattice with 1mm beams. The boundary conditions for this example are illustrated in Figure 5.12.

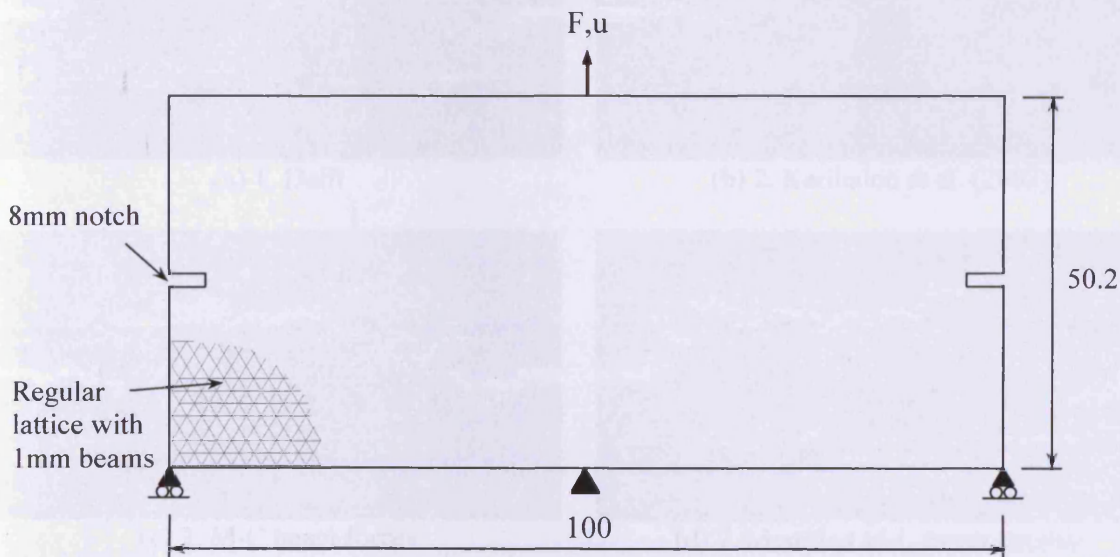


Figure 5.12. Boundary conditions for uniaxial tensile experiment on a doubly notched 100x58 lattice mesh with 1mm beam elements

The same values of E and ν have been used for this example as the previous one, but the beam strengths have been obtained from a statistical strength distribution. The statistical distribution used is given in equation (6.9) and is justified in full under section 6.7. The lowest beam strength in this distribution is 2MPa. It should be noted that exactly the same strength distribution (same input file) has been used for all of the simulations presented below.

This example is primarily aimed at investigating the effect that the choice of failure criterion has on the fracture pattern. The most appropriate criteria to investigate and compare, at a stage

of significant damage, are therefore considered to be the criteria based on stresses within the beams. The example outlined above has therefore been run with four different failure criteria. The four criteria considered are the Delft criterion, the strain based criterion of Karihaloo et al. (2003), the newly proposed M-C based criterion incorporating axial, shear and mid-beam moment contributions, and finally the version of the M-C beam stress criterion which has been corrected to match the continuum stresses in the elastic state. The fracture patterns produced by each of these criteria are shown in Figure 5.13 below. All of the fracture patterns are taken after 700 beams have been broken and removed, and the displacements have been scaled by 300 for the purpose of clarity

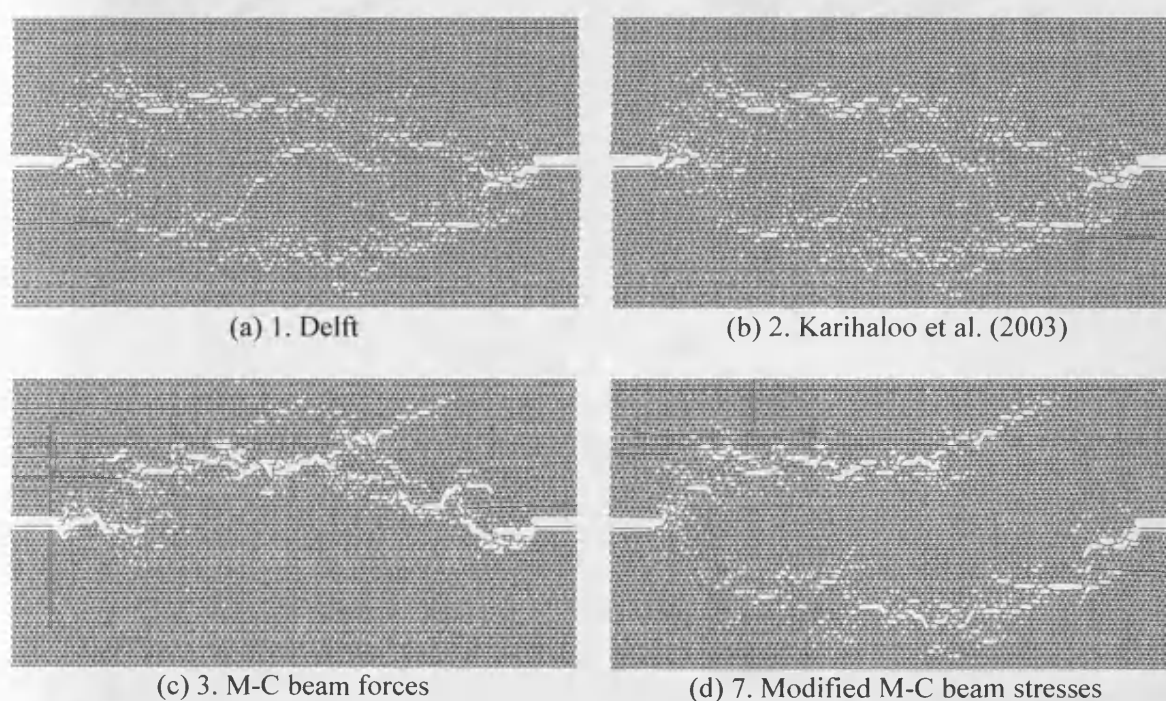


Figure 5.13. Fracture patterns for different failure criteria after 700 beams have broken

It can be seen from Figure 5.13 that the fracture patterns for the Delft and Karihaloo et al's criteria are very similar to each other. Both of these criteria have located an upper and lower path of weak beams from the statistical beam strength distribution, and as a result two distinct overlapping cracks have formed. The modified M-C fracture pattern has also captured the same two cracks, with a slight deviation in the upper crack, but the original M-C criterion, which includes the beam mid-span moment contribution, shows only the upper crack. This upper crack (Figure 5.13 (c)) has localised to a far greater extent than the other cracks in Figure 5.13, and has therefore developed into a macro crack which will eventually lead to complete specimen failure.

The complete force-displacement response for all four failure criteria is given in Figure 5.14 below:

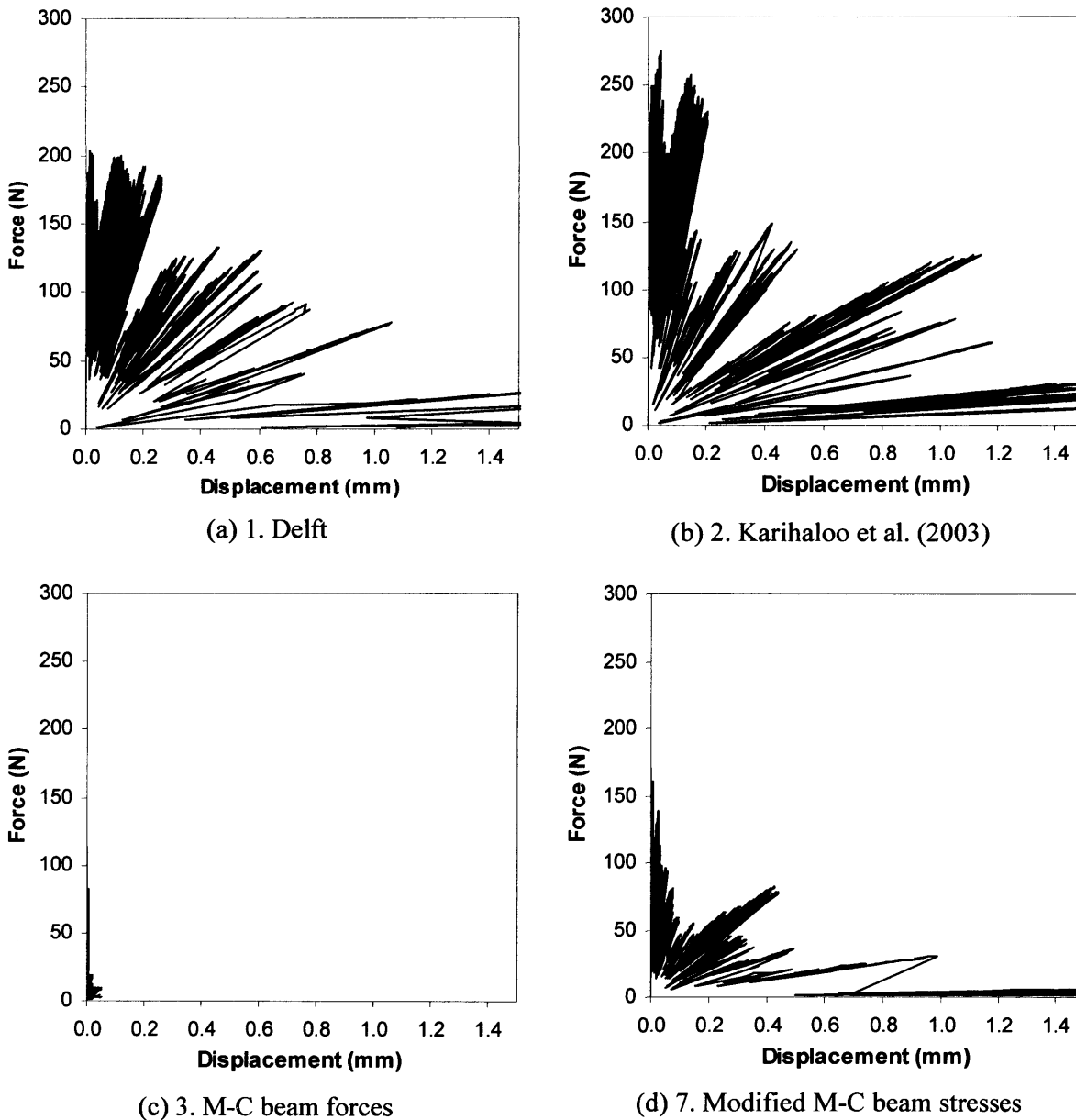


Figure 5.14. Force-displacement response for different failure criteria

In light of the observations made above, it is unsurprising therefore that the criterion which produces the lowest fracture energy response is criterion 3; the M-C criterion based on beam forces. This is considerably less than the fracture energy of the other three responses, due to the reduced amount of distributed cracking that occurs prior to localisation and development of the main macro crack. This is most likely due to the effective stress (equation (5.5)) in the beams being overestimated by the inclusion of the moment contribution, in addition to the shear and axial components, in the failure strength criterion. The order of the remaining three

criterion in terms of the amount of fracture energy required for specimen failure agrees with that suggested by the simpler example presented in Figure 5.11. The strain based criterion of Karihaloo et al. (2003) is seen to give the most ductile response. The increased ductility of this criterion, over the Delft criterion, is probably due to the fact that the criterion considers the difference in the beam end rotations, whereas the Delft criterion considers the maximum end moment.

Figure 5.15 gives the force-displacement values and secant stiffness of the lattice after 700 beams have broken and their stiffness have therefore been removed from the total stiffness of the system.

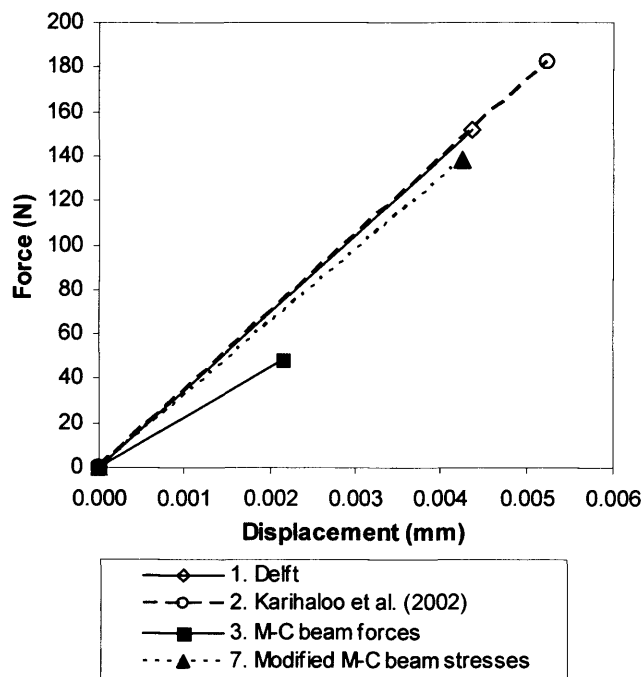


Figure 5.15. Force-displacement values and secant stiffness of lattice for different criteria after 700 beam removals

The graph therefore illustrates the result that would be obtained at the next iteration if the damaged lattices, as shown in Figure 5.13, were loaded to the point at which the next beam to fail becomes critical. This occurs when the effective stress in that beam equals the failure strength of the beam. Since all of the beams in the single data file used for this comparison have different beam strengths, and the order of beam breakages is generally different for each of the failure criteria, the element number of the next beam to break, and therefore its strength, will be different for each of the four cases considered here. As a result, the failure criteria cannot be compared in respect to the absolute value of the force and displacement at

the point of fracture of the 701st beam, however, the value of the secant stiffness is significant. This indicates the effect that the removal of the first 700 beams has had on the reduction of the overall global stiffness of the lattice system. Figure 5.15 shows that the secant stiffness is greatest for Karihaloo et al's criterion, followed closely by the Delft criterion, then the modified M-C criterion, and finally the modified M-C criterion. The secant stiffness for the latter is considerably less than that given by the three other criteria.

The stiffness of the lattice at any one point in its dissolution (damaging process) gives an indication of the diffusivity of damage, with more diffuse damage leading to a smaller reduction in the original elastic stiffness. Given this, the results of Figure 5.15 therefore agree with the fracture patterns observed in Figure 5.13. Karihaloo et al's criterion gives the greatest diffusivity and highest secant stiffness, and the lowest stiffness is given by the M-C criterion based on beam forces, which can be seen to produce the most localised cracking pattern with the lowest diffusivity of damage.

5.8 Conclusions and future work

This chapter has given an overview of the existing failure criteria that are used for the lattice modelling method, and has presented some new alternatives. The properties of the newly proposed criteria have been studied in some detail, through a series of investigations. These investigations, which have examined the isotropy of the criterion and the equivalence between beam and continuum stresses, have been summarised in section 5.7.

The newly proposed and existing criteria have then been compared in two separate examples; a simple 10x10 element lattice which fractures in a controlled 'unzipping' manner, and a more complex but realistic example of a uniaxial tension test on a 100mm by 50mm mortar plate, with randomly distributed beam strengths obtained from a statistical distribution.

Both examples have illustrated that the choice of failure criterion is extremely important since it exercises great influence over the results obtained for a lattice simulation with a given heterogeneity. The 'unzipping' example shows that even when the order of beam breakages is identical for all criteria, the mechanical force-displacement response obtained varies significantly depending on the criterion chosen. The second example has identified that when a more realistic lattice simulation, with random heterogeneity, is considered; the fracture patterns produced also differ significantly for the different criterion used. Since the force-displacement response of the system is dependant on the nature of the fracture pattern as well

as the criterion implemented, the fracture energy has also been shown to vary considerably depending on the failure criterion adopted.

Since it has been shown that the choice of criterion has a significant effect on both the fracture pattern and the fracture energy emitted, it is important that the criterion implemented has an underlying physical basis. If the mid-planes of the beams in a lattice are considered to represent particle interfaces, and furthermore, if the beams are considered to only break at these particle interfaces, then a failure criterion based on the theory of Mohr-Coulomb may be considered to have such a physical basis. The value of μ which has been derived from isotropic considerations in this chapter also has a physical representation, since it is defined as the axial shear strength ratio at an interface.

The failure criterion which therefore offers the greatest physical basis is the modified Mohr-Coulomb criterion based on beam stresses (criterion 7). In addition, this criterion may also be considered to be the most accurate of the four criteria which are based on stresses or strains obtained solely from the displacements of the end nodes of the beam being considered. This is due to the fact that the axial and shear stresses at the mid-surface of the beam have been theoretically equated and corrected to match the corresponding values at the same location in the continuum that the beam is intended to represent.

Future work should further investigate the relationship between the discrete lattice and the underlying continuum. In this respect, non-local failure criteria may be developed which take information from the displacement field of surrounding nodes. Alternatively, attention may be given to understanding the relationship between the moment component in a lattice beam and the micro rotation that this relates to in a higher order micropolar (Cosserat) continuum.

Chapter 6

Stochastic regularisation of lattice modelling

6.1 Introduction

The lattice beam modelling method has been shown to have the ability to offer very good qualitative observations of fracture processes in cementitious materials, as described in Chapter 3. However, the quantitative properties of the numerical method are somewhat limited, since it has been shown to exhibit both mesh orientation and mesh size dependency (Schlangen and Garboczi, 1997), in addition to being overly brittle in respect to the predicted force-displacement response (Schlangen, 1993).

The previous chapter has focused on improving the mesh orientation dependency of the method by developing failure criteria with improved isotropy characteristics. This chapter focuses on enhancing the quantitative force-displacement response provided by the model. Specific attention has been given to ensuring that the numerical results are more representative of experimental data, and that they are also objective i.e. independent of the mesh size used in the simulation.

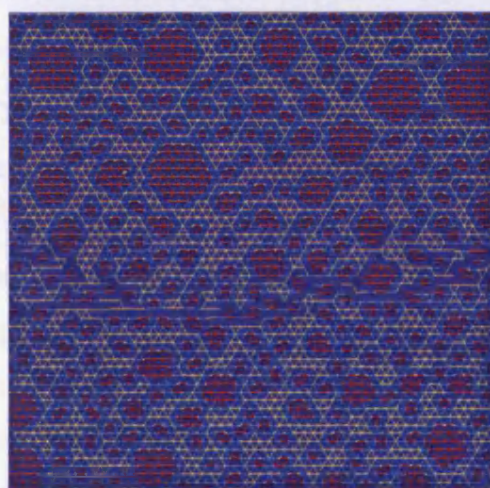
The pathological mesh size dependency of the ‘traditional’ lattice method is initially highlighted, through means of a simple tensile test on a concrete specimen containing mesostructure. A novel theory is then presented which is aimed at achieving a unique regularised mechanical softening response from the lattice through employing a statistical distribution of beam strengths (Joseph and Jefferson, 2006b and 2007).

6.2 Mesh size dependency

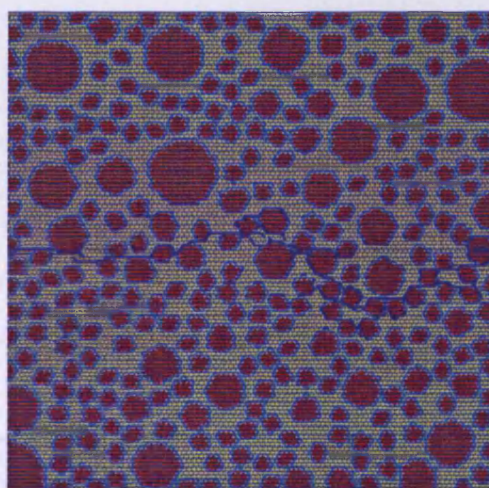
The mesh size dependency of the discrete lattice modelling method is an issue which has already been raised in the literature, as outlined in section 3.7.3. Schlangen and Garboczi (1997) examined the objectivity of the method for simple regular triangular lattice meshes with different beam length resolutions. In this study heterogeneity was modelled in a simple

manner by randomly assigning low (1.0) or high (3.0) strengths to the individual beams in the ratio of 1:3. It is therefore worth investigating whether the method of representing the material heterogeneity significantly affects the degree of mesh size dependency. A uniaxial tensile test on a 50mm square concrete specimen, doubly notched with 3mm deep notches, has therefore been considered. The heterogeneity is explicitly represented by a mesostructure overlay, generated in the manner described in section 4.2.2.

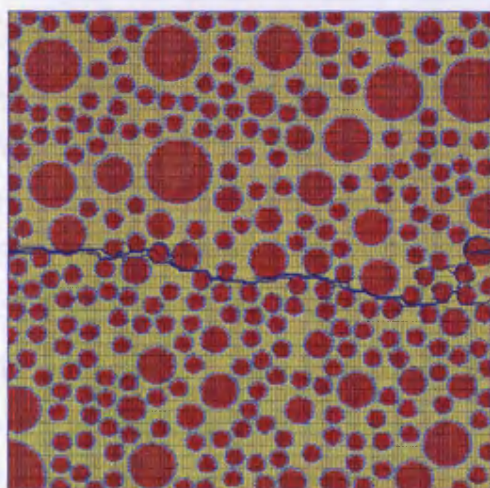
The concrete specimen has then been discretised into three different regular triangular lattice meshes. The beam length resolutions of these three meshes are 1mm, 0.5mm and 0.25mm, as shown in Figure 6.1 (a), (b) and (c), respectively.



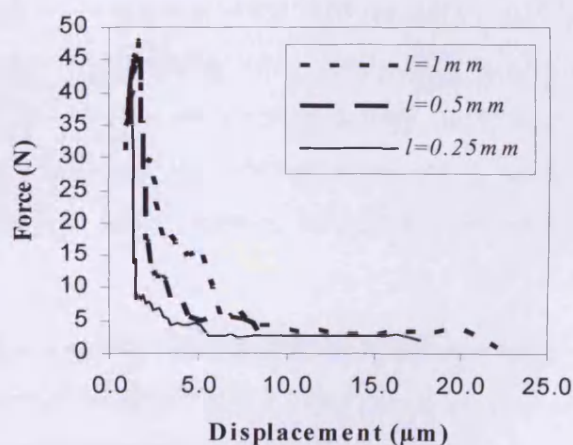
(a) $l = 1\text{mm}$ ($\lambda=50$)



(b) $l = 0.5\text{mm}$ ($\lambda=100$)



(c) $l = 0.25\text{mm}$ ($\lambda=200$)



(d) $P - \delta$ curves for varying beam lengths

Figure 6.1. Crack patterns and force-displacement curves for 50mm square notched specimens, modelled using varying lattice beam lengths of 1mm, 0.5mm, and 0.25mm.

The prescribed aggregate content, P_k for the mesostructure overlay shown in Figure 6.1 is 55%, and the maximum and minimum aggregate diameters are 8mm and 2mm, respectively. The stiffness and strength properties of the three mesostructure phases are $E_{agg} = 87.5GPa$, $E_{mat} = E_{ITZ} = 31.3GPa$, $f_{t,agg} = 10MPa$, $f_{t,mat} = 5MPa$, and $f_{t,ITZ} = 1.5MPa$. These have been taken to be the same as the typical parameters used in the literature for lattice simulations with particle overlay, as given in Table 3.1 (van Mier and van Vliet, 2003). The boundary conditions employed for this uniaxial tensile experiment are identical to those given for the simple tensile experiment presented in the previous chapter (Figure 5.10). The failure criterion implemented for this particular example is the Delft criterion as given by equation (5.1), with $\alpha=0.005$.

The force-displacement results for the three lattice discretisations are given in Figure 6.1(d). These results show that both the peak force and the fracture energy of the lattice system reduce as the mesh size decreases or the non-dimensional lattice size, λ as defined in equation (6.1), increases. The peak force reduces by approximately 12.5% from 48N to 42N as the lattice resolution reduces from 1mm to 0.25mm. The fracture energy also reduces by approximately 50% between 1mm and 0.5mm resolution, and a further 50% as the beam length reduces from 0.5mm to 0.25mm. It should also be noted that the load-displacement response for the 0.25mm regular lattice simulation agrees well with results published recently by Prado and van Mier (2003) on 60mm square specimens with an aggregate content, P_k , of 51%, and similar phase properties.

Since the fracture pattern for all three simulations is a horizontal crack with an approximately equal amount of deviation, then the crack area (considering unit depth) may also be considered to be approximately the same for all three cases. As a result, it may therefore be concluded that the specific fracture energy (energy released per unit area of crack), G_f , is not preserved with mesh refinement. The lattice method may therefore be deemed to exhibit pathological mesh size dependence.

The trend described above may be illustrated schematically for the case of a fine and coarse lattice mesh as shown in Figure 6.2. The fine mesh consists of $2n \times 2n$ elements which are of length, l , and the coarse mesh is made up of $n \times n$ elements of length $2l$. The geometric size of these mesh are therefore the same. In order to preserve the strain energy equivalence of the regular lattice with the continuum, as described in section 5.6, the cross-sectional height (h), and therefore area (A), of the beams must be proportional to the beam length, l (equation

(3.10)). The cross-sectional area of the short beams is therefore A , and that of the long beams is $2A$.

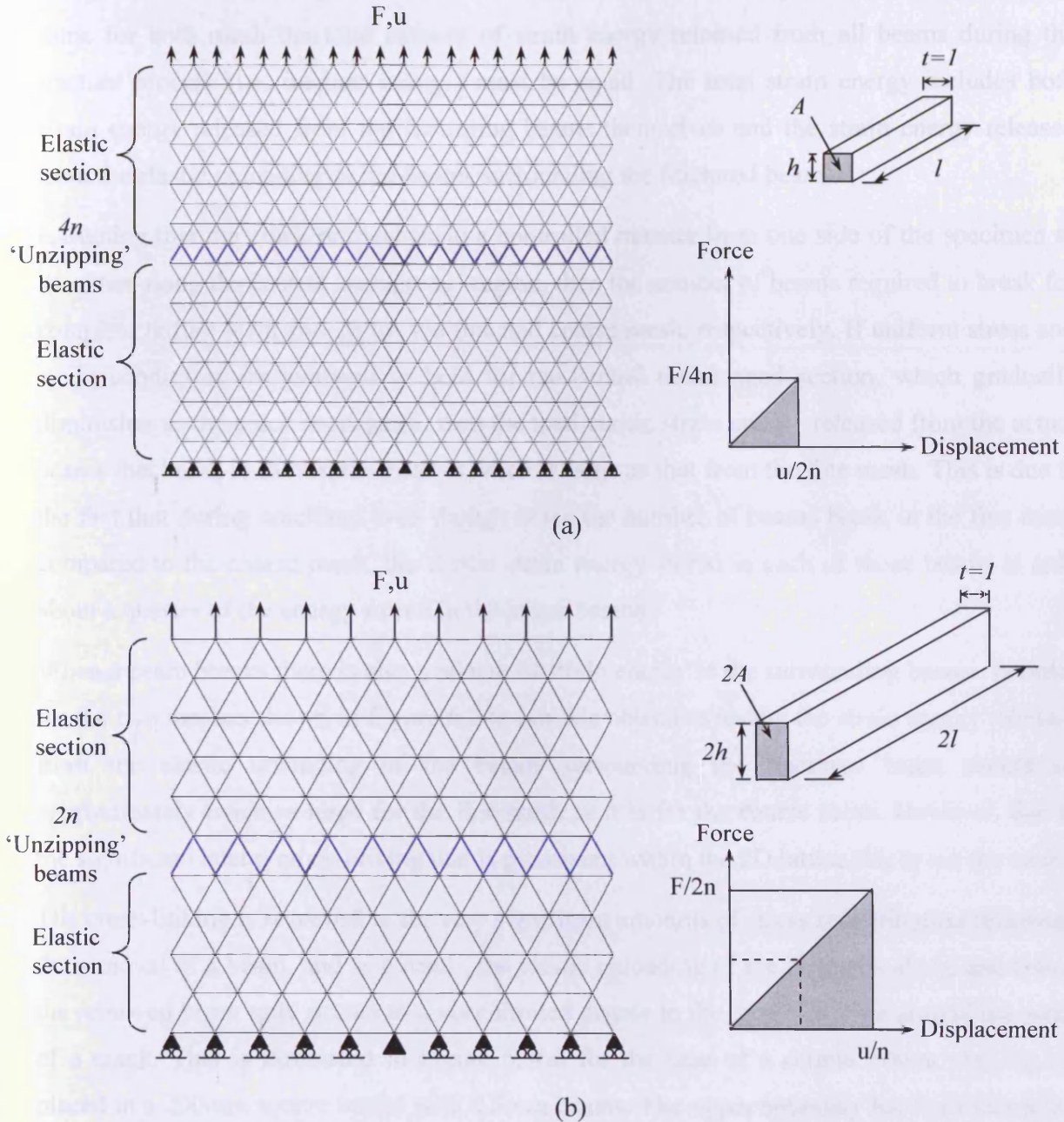


Figure 6.2. Schematic illustration of the effect of mesh resolution and lattice beam size on the approximate strain energy stored in a single beam for (a) a $2n \times 2n$ lattice and (b) an $n \times n$ lattice

If these two meshes are then loaded in uniaxial tension with a total force, F and an upper boundary displacement, u , it may be assumed that constant strain and stress states are set up. The axial force in a single diagonal beam is then approximately $F/4n$ and $F/2n$, and the elongation of a single diagonal beam, assuming identical stiffnesses, is $u/2n$ and u/n , for the fine mesh and coarse mesh, respectively.

From the shaded areas on the local element force-displacement graphs shown in Figure 6.2, it can be seen that the elastic strain energy stored in the longer beams is therefore four times the energy stored in the smaller beams. In order for the global load-displacement results to be the same for both mesh the total amount of strain energy released from all beams during the fracture process (i.e. fracture energy) must be equal. The total strain energy includes both strain energy released from the fracturing beams themselves and the strain energy released from the elastic unloading of the beams surrounding the fractured beam.

Assuming that the crack propagates in a controlled manner from one side of the specimen to the other along the central ‘unzipping’ region, then the number of beams required to break for complete failure is $4n$ and $2n$ for the fine and coarse mesh, respectively. If uniform stress and strain conditions are assumed to hold for the central undamaged section, which gradually diminishes as the crack propagates, then the total elastic strain energy released from the actual beams that break in the coarse mesh is twice as large as that from the fine mesh. This is due to the fact that during cracking, even though twice the number of beams break in the fine mesh compared to the coarse mesh, the elastic strain energy stored in each of those beams is only about a quarter of the energy stored in the larger beams.

When a beam breaks there is also a release of strain energy in the surrounding beams. In order for the two meshes shown in Figure 6.2 to provide objective results the strain energy released from the elastic unloading of the beams surrounding the fractured beam should be approximately twice as large for the fine mesh as it is for the coarse mesh. However, due to the significant lateral cross-linking that is prominent within the 2D lattice this is not the case.

The cross-linking is responsible for very significant amounts of stress redistribution following the removal of a beam, and as a result, the elastic unloading of the elements above and below the removed beam only occurs to a very limited degree in the localised zone around the wake of a crack. This is illustrated in Figure 6.3(a) for the case of a central 50mm slit-like cut placed in a 200mm square lattice with 0.5mm beams. The upper boundary has been subjected to a prescribed displacement of 0.01mm, and all resulting nodal displacements have been scaled by a factor of 1000 for the purposes of clarity. It should be noted that an analytical solution for a slit-like cut in an ‘infinite’ elastic body is available, as given by Karihaloo (1995). It should also be noted that the slightly unsymmetrical solution given in 6.3(a) is believed to be due to computational round-off. This stress redistribution is in direct contrast to the case of parallel multi-element strands (chains) which fully unload following the fracture

of one element of the strand. The fracture energy dissipation for this case would therefore be independent of mesh size resolution, as illustrated in Figure 6.3(b).

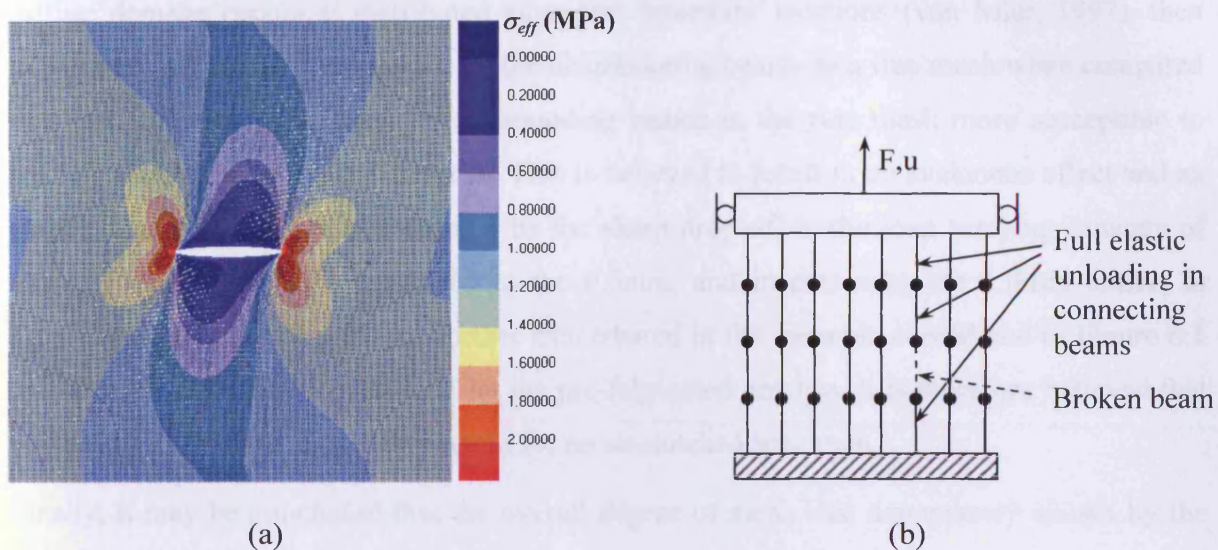


Figure 6.3. Illustration of the effect of cross-linking on stress redistribution: (a) Large amount of stress redistribution in 2D lattice and (b) no stress redistribution in a parallel chain model

In respect to the peak forces generated by the three mesh resolutions given in Figure 6.1, one would expect these to be equal, if the peak was associated with the point at which the first beam broke. This is because the material strengths of the three mesostructure phases have been kept identical for the three simulations, and the stress and strain in the elements at the elastic stage are expected to be the same irrespective of element length. This may be seen if we refer once again to the simplified example of Figure 6.2, where despite the forces and elongations being different in the two beam resolutions, the stress and strain are equal, and are given as $F/4nA$ and $u/2nl$, respectively. However, from Figure 6.1(d) it can be seen that there is an approximate decrease of 12.5% in the peak strength between the coarse and fine lattice meshes. This is because there is, in fact, some pre-peak hardening, and the amount of hardening is different for the different lattice resolution meshes.

One possible reason for this may be the effect that the lattice resolution has on the representation of the mesostructure; i.e. despite the prescribed aggregate content ($P_k=55\%$) being exactly the same for all three simulations shown in Figure 6.1, the actual ‘modelled’ content varies from 28% for $l=1mm$ to 45% for $l=0.25mm$. This is because the thickness and thus area of the ITZ layer reduces with beam length, l . A finer lattice resolution therefore leads to a finer representation of the weak ITZ layer surrounding the aggregate particles. However, a more likely reason is the fact that a finer lattice is also better able to capture the

high stress concentrations that occur at crack tips, as found in continuum fracture mechanics. Therefore, if a single ITZ beam is removed at the early stages of pre-peak hardening, when diffuse damage occurs at distributed aggregate boundary locations (van Mier, 1997), then higher stresses will be experienced by the neighbouring beams in a fine mesh when compared to a coarse mesh. This makes the surrounding beams in the fine mesh more susceptible to fracture than those in the coarse mesh. This is believed to result in an avalanche effect and an earlier onset of localisation, as shown by the sharp drop-off in the load carrying capacity of the 0.25mm lattice when compared to the 0.5mm, and in particular the 1.0mm lattice, in Figure 6.1(d). This effect is also further exacerbated in the example considered in Figure 6.1 by the stress concentrations caused by the pre-fabricated notches. It is therefore believed that the peaks would show closer agreement for an un-notched specimen.

Finally, it may be concluded that the overall degree of mesh size dependency shown by the example in Figure 6.1 is similar to that obtained in the simpler example studied by Schlangen and Garboczi (1997), as shown in Figure 3.12. The presence of mesostructure in the form of an explicit particle overlay does not appear in itself to eradicate or even reduce the inobjectivity of the model.

6.3 Options for regularisation

Having identified a major limitation of the traditional lattice model it is worth considering what options for regularising the specific fracture energy release may be gleaned from the literature. The main options that have been identified are:

1. Introducing a cohesive stress-strain or stress-crack opening relationship at the local element level, which has post-peak softening.
2. Using scaling factors to correct the peak load and ductility of the global load-displacement response.
3. Linking the smallest mesostructure particle size to the element size used in the mesh.
4. Using statistical distributions of beam strengths or stiffnesses.

The first option is that which is most commonly used in traditional finite element models. In fact the resolution length effect described in section 6.2 above is consistent with that found in finite element solutions for fracturing materials, and is the reason for the introduction of the Bažant and Oh crack band model (1983). Implementing this model within the lattice method would require the introduction of a tension softening relationship for all beams. Solving for

the internal displacements at every load step would then become a non-linear process. Whilst this is possible, and has in fact been implemented for the mortar phase by Karihaloo et al. (2003), the method significantly reduces the computational efficiency of the model, and as a result further increases its computational demand, which is already one of its main limitations (section 3.7.1). It should be noted that this method of achieving regularisation is also used in the RBSM (Bolander and Saito, 1998) as illustrated in Figure 2.24. However, the number of spring connections is far less in this model than the number of beams in a typical lattice model, and therefore the computational demand created by the non-linear solution is significantly less.

In addition, it is felt that regularising the lattice beam model in this manner compromises one of the fundamental philosophies of the method, as the author perceives it; namely, that the individual lattice elements should be of such a size that they may be considered to be brittle; i.e. the constitutive response of the small volume of material that each beam represents may be considered to be brittle when compared to the constitutive response of the structure as a whole. It is interesting to note that the systematic rupture of brittle elements during the dissolution of a lattice causes a discontinuous energy release which reflects the ‘energy jumps’ observed during cracking of actual experimental specimens. This is illustrated by the stepwise form of the softening tail in Figure 6.5(b).

The second option involves the use of scaling parameters to correct for the differences in peak load and ductility caused by the choice of lattice resolution. The scaling factors may be applied within the model at the failure criterion stage, as for the α and β factors used in the Delft criterion (equations (3.14) and (3.15)). Alternatively, the outputted force-displacement curves from the model may be scaled during the post-processing stage according to the lattice resolution used in the simulation. These scaling factors will be different, however, for every lattice resolution used. This has been addressed by physicists studying stress driven rupture in central force (pin jointed truss) lattice systems, where the lack of uniqueness in the system macro parameters, such as peak strength, and specific fracture energy, is an issue which has been recognised for some time (Krajcinovic, 1996). Here the size effect has been related to the non-dimensional lattice size λ , which is defined as:

$$\lambda = L/l \quad (6.1)$$

where L represents the geometric size of the lattice in the direction of uniaxial stress, and l represents the length of a link. Finite scaling laws may then be established whereby response curves for lattices of different size λ collapse onto a single master curve plotted in the $F\lambda^{-\beta}$ vs.

$u\lambda^{-\gamma}$ coordinate system. The exponents β and γ are fitting parameters that may be determined from multiple Monte-Carlo type numerical simulations, as described by Krajcinovic (1996). Whilst it is possible to correct the peak and tail of load-displacement graphs using scaling factors, the scientific basis for this is weak, and it is unlikely that the factors will be unique; i.e. they are likely to vary for different representations of heterogeneity, for example.

The third possibility for ensuring objectivity involves linking the smallest mesostructure particle size to the element size used in the mesh. For example, the smallest particle size modelled may be taken to be two or three times the element size. As the resolution of the simulation is increased and the element size is reduced, the size of the smallest mesostructure represented in the model is also reduced. The net effect of this is that the actual percentage of aggregate content modelled increases significantly with increasing lattice resolution. Prado and van Mier (2003) have shown that an increase in aggregate content, P_k , increases the fracture energy values until percolation of the weaker bond (ITZ) phase occurs. The main reason for the increase in fracture energy is believed to be due to the greater deviation that the crack must take in order to propagate across the specimen. If we consider the fracture pattern shown in Figure 6.1(c), then it becomes intuitive that if an additional amount of smaller strong aggregate particles are added to the simulation then these would serve to further ‘block’ the propagation of the crack. This would increase the overall tortuosity of the final through crack and also increase the fracture energy required to create this crack.

Increasing the percentage of aggregate inclusions in the manner described above is more likely to mask the mesh size dependency effect rather than correct for it, however. In addition, a method of regularising the fracture energy which is based on altering the total crack area is not going to achieve true objectivity in respect to the specific fracture energy, G_f ; i.e. the fracture energy per unit area of crack.

The final option for regularisation, as proposed here, involves the use of some form of statistical distribution of beam strengths or stiffnesses. The most common form of representing material inhomogeneity, currently used in the literature, is the particle overlay method as described previously in section 3.4.1. In this method pre-defined material strength and stiffness properties are assigned to the three separate phases that the concrete is assumed to comprise. Any stochastic variation of material properties within individual phases are omitted, since all elements of a particular phase are assigned the same properties. In real experimental specimens, of course, the strength and stiffness properties of these three phases are likely to fluctuate significantly and show considerable variation. This raises the possibility

of including a statistical distribution of beam strengths within the three mesostructure phases. Furthermore, due to the variation in material properties, the distinction between the different phases becomes less clear, and the possibility of replacing the mesostructure with a single statistical distribution may also be considered. In fact, van Mier et al. (2002) have already completed some early work in this area, as reviewed in section 3.4.2.

The use of some form of statistical variation of beam strengths therefore raises two interesting questions. Firstly, is it possible to achieve realistic force-displacement responses that are representative of actual experimental values? Secondly, through linking the statistical distribution of beam strengths to the element size is it possible to ensure that these force-displacement responses are independent of the mesh resolution?

6.4 1D parallel bar model

In order to address these questions it is first of all worthwhile considering the simplified case of a one dimensional parallel bar model. Since there is a tendency for cracks to localise into a single layer following the onset of damage, a uniaxial test on a two dimensional specimen, as given in Figure 6.1, may be considered in a simplified manner as a combination of an elastic region and a one dimensional parallel bar model, as illustrated in Figure 6.4.

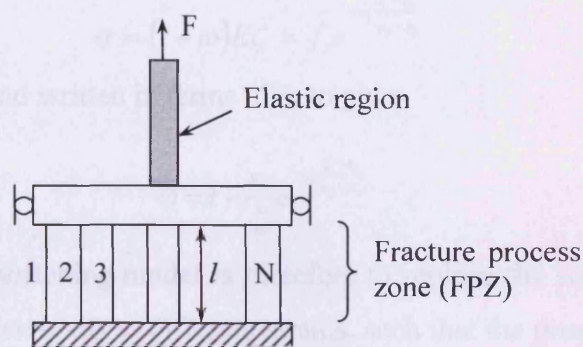


Figure 6.4. Simplified representation of fracture process zone with 1D parallel bar model

The N bars in the parallel bar model may then be considered to represent the elements in the fracture process zone over which the strain is assumed to localise. Krajcinovic (1996) discusses, in some detail, the application of a Weibull distribution of bar strengths to N bars in a loose bundle parallel bar model. Interestingly, the macro mechanical response of such a system under uniaxial tension is similar to that obtained from experimental observations on concrete specimens; i.e. a linear elastic region followed by pre-peak hardening, and post-peak softening. The form of the response curve is governed by the Weibull shape parameter, m ,

which is an indication of the material's strength variability; the larger the value of m the smaller the variability, and the more brittle the response of the parallel bar model.

Alternatively, it is also possible to work from a given softening curve back to a statistical distribution of bar strengths. A standard softening curve that is commonly used to represent the stress-strain relationship in the damage zone is the exponential softening curve, as illustrated in Figure 6.5(a). It can be seen from the experimental result in Figure 3.13 and also van Mier (1997) that the exponential function is suitable for capturing the tensile softening behaviour of cementitious materials. The softening relationship may therefore be written as:

$$\sigma = f_t e^{-c_1 \frac{\zeta - \varepsilon_t}{\varepsilon_0 - \varepsilon_t}} \quad (6.2)$$

where f_t is the average tensile strength, c_1 is the softening curve constant, ε_t is the strain at peak strength ($\varepsilon_t = f_t/E$), and ε_0 is the failure strain.

The constitutive relationship may also be written in terms of the damage parameter, ω as:

$$\sigma = (1 - \omega)E\varepsilon \quad (6.3)$$

where E is the Young's modulus of the material.

On the damage surface $\varepsilon = \zeta$ and (6.2) and (6.3) may be combined to give:

$$\sigma = (1 - \omega)E\zeta = f_t e^{-c_1 \frac{\zeta - \varepsilon_t}{\varepsilon_0 - \varepsilon_t}}$$

which may be simplified and written in terms of ω to give:

$$\omega = 1 - \frac{\varepsilon_t}{\zeta} e^{-c_1 \frac{\zeta - \varepsilon_t}{\varepsilon_0 - \varepsilon_t}} \quad (6.4)$$

The aim of the statistical softening model is therefore to replace the softening curve in each bar by a series of bars, which break at different strains, such that the proportion of broken bars in the zone of interest approximates the damage variable, ω . If there are N bars and at any point i bars are broken, and the strain at which a particular bar breaks is denoted by ζ_i , then noting that the current total strain on the damage surface is that associated with the strain at which bar i breaks, equation (6.4) may be written in a discrete form, giving:

$$\omega = \frac{i}{N} = \int_{\varepsilon_t}^{\varepsilon_0} p(\zeta) d\zeta = 1 - \frac{\varepsilon_t}{\zeta_i} e^{-c_1 \frac{\zeta_i - \varepsilon_t}{\varepsilon_0 - \varepsilon_t}} \quad (6.5)$$

which is a non-linear equation to be solved for ζ_i .

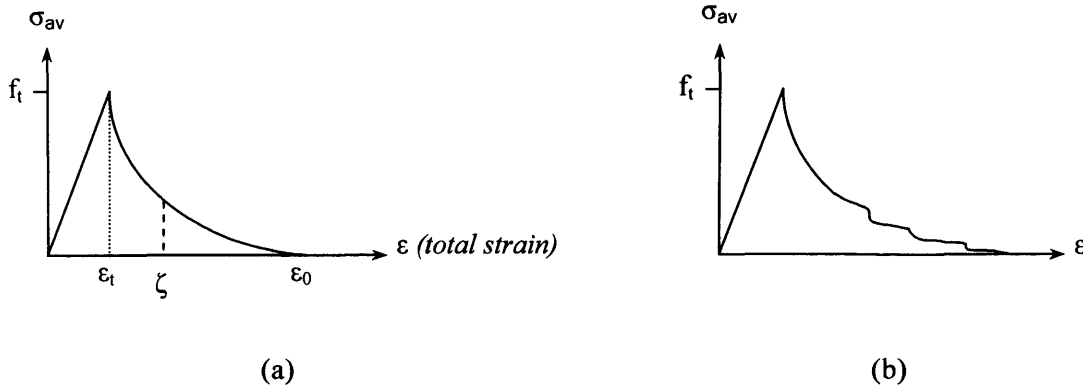


Figure 6.5. (a) Target idealised exponential softening curve. (b) Typical macro-mechanical response from discrete parallel bar model.

If a constant E -value is assumed for all bars in the FPZ then the bar strengths obtained from the solution of ζ_i for $n=1$ to N may be placed back into the parallel bar model. A typical response curve obtained from the model is shown schematically in Figure 6.5(b). In order for this response to be objective it should be independent of the bar length, l .

The key to achieving regularisation is maintaining an average-stress, σ_{av} versus crack opening displacement, u at localisation, irrespective of the resolution length, l . If this criterion is to be satisfied, then ε_0 must be a function of element length, as in the Bažant & Oh (1983) model;

$$\varepsilon_0 = \frac{u_0}{l} \quad (6.6)$$

where u_0 is the total crack opening at failure, and l is the length of elements in the fracture process zone.

Assuming that u_0 is an actual material parameter, ε_0 is therefore inversely proportional to the element length, l . The value of ε_0 specified on the tail of the softening curve (Figure 6.5(a)) therefore changes according to the element length being used. Furthermore, the distribution of bar strengths obtained from this specified softening curve, as given by equation (6.5), also changes with element length. As a result it is possible to maintain a global softening response from the model that is independent of the length of the elements in the FPZ.

It should be noted that a simple exponential decay function has been used above rather than a Weibull function, since the Weibull function does not allow the softening tail to be scaled whilst keeping the peak the same.

6.5 2D lattice model without mesostructure

The theory presented in the previous section may then be applied directly to a two dimensional lattice model subject to uniaxial tension, as illustrated in Figures 6.6 and 6.7 below. Figure 6.6 shows enlarged crack patterns for a notched 100mm by 50mm specimen which has been discretised using three different element lengths; 2mm, 1mm and 0.5mm. The beam failure strains, ζ_i have been obtained by solving equation (6.5) for $i = 1$ to N , where N is the total number of elements in the lattice mesh for the particular beam length resolution under consideration. The values of f_t and c_t have been taken to be 2MPa and 5.0, respectively, and the value of ε_0 has been calculated from equation (6.6) for the chosen beam length, l and a crack width opening, u_0 of 0.2mm. The beam strengths have then been obtained from the beam strains by multiplying by the Young's modulus of the material, taken to be that of the matrix (mortar); $E = 31255\text{MPa}$. Finally, the full range of beam strengths has been assigned to all beams in the specimen in a random manner. It should be noted that the failure criterion implemented in this simulation and the remaining simulations in this chapter is the Mohr-Coulomb criterion based on beam forces (criterion 3 in Table 5.1). It should also be noted that the shear area has not been corrected ($A_\eta = A$), and μ has been taken as 2.

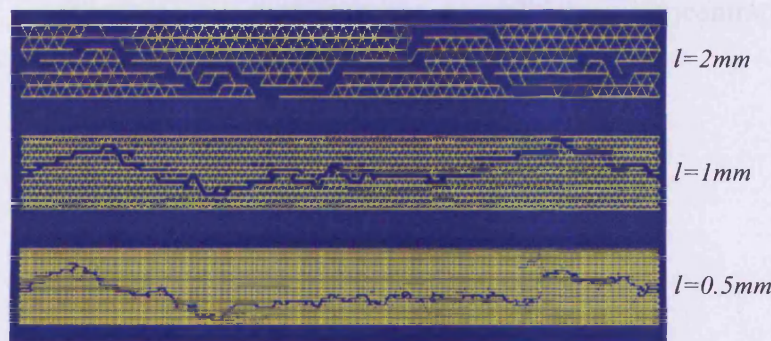


Figure 6.6. Enlarged crack patterns for three different beam length discretisations of a 100mm x 50mm notched specimen subject to uniaxial tension

It can be seen from Figure 6.6 that whilst the finer resolution lattice clearly shows more crack information, including some crack branching, the crack patterns for all three simulations agree reasonably well and exhibit similar amounts of fluctuation across the width of the specimen. Figure 6.7 shows, however, that the macro mechanical response of the system remains inobjective. A clear trend of diminishing fracture energy with decreasing beam length is still evident and this is of the same order as that observed originally for the traditional lattice model with mesostructure (Figure 6.1). The peak force for all three simulations is of the right order for a 100mm wide specimen, given an f_t of 2MPa and allowing for the reduction due to

the presence of notches. The value of the crack opening displacement, u_0 is, however, approximately two orders of magnitude less than the 0.2mm specified in the target softening curve. This indicates that all three force-displacement responses are overly brittle.

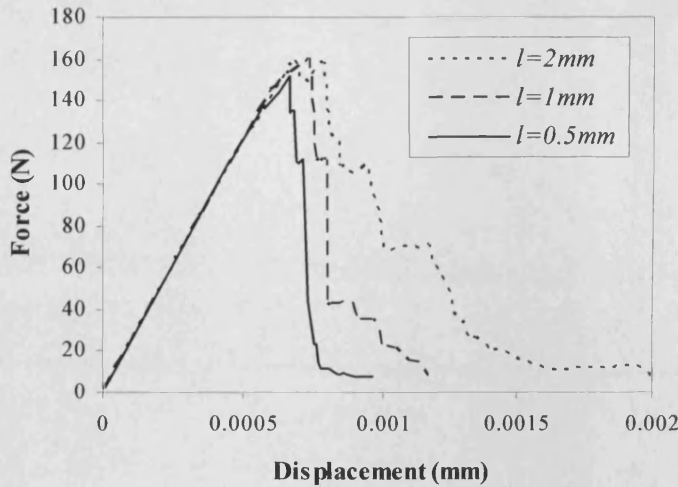


Figure 6.7. Force-displacement graph for three different beam length discretisations of a 100mm x 50mm notched specimen subject to uniaxial tension

The main reason for the over-brittleness and lack of objectivity observed above is that the parallel bar model is incapable of capturing the spatial stress concentrations and re-distributions that are prevalent within the two dimensional lattice model.

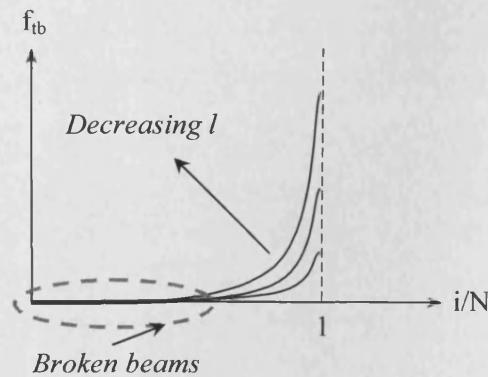


Figure 6.8. Illustration of beam strength (f_{ib}) variation with damage for varying lattice beam length

The adjustment of ε_0 to account for the lattice beam length used in the discretisation (eqn. (6.6)) does increase the strength of the strongest beams significantly, as illustrated in Figure 6.8. This does not, however, significantly influence the mechanical response during failure, since the propagating macro-crack tends to follow the path of 'weakest resistance' rather than localising into a pre-defined single layer of beams, as per the assumption made in Figure 6.4. As a result, only the lower portion of relatively low strength beams, as encircled in Figure 6.8,

are actually broken in the simulations. This is the reason for the over-brittleness of all three responses in Figure 6.7. In addition, since the strength difference between beams of varying length is very small in the lower region of the exponential curves of Figure 6.8, the trend of diminishing fracture energy with element length has not been corrected by any significant degree.

6.6 RME (Representative material element)

In order to adjust the one dimensional statistical regularization theory for application to a two dimensional lattice, it is useful to introduce the concept of a representative material element (RME). An RME is defined here as the smallest region of a specimen domain over which the full range of material strength variation may be considered to exist. In respect to the discrete lattice mesh the RME is the smallest area of lattice over which the full array of beam strengths may be found.

Since the lattice beam strengths are considered here to represent bond strengths within phases of the continuum; i.e. weak beams representing ITZ regions and strong beams representing aggregate regions, then the size of an RME is intrinsically linked to the size of an RVE (Representative volume element), commonly used in multiscale continuum FE models. It should be noted that the size of the RME, as for the RVE, is therefore considered to be linked to the degree of heterogeneity contained within the material. For a material containing a mesostructure, such as concrete, the maximum aggregate size is commonly used as a measure of the degree of heterogeneity. An RME size, in the order of 3-5 times the maximum aggregate size, as suggested for the case of the crack band model by Bažant & Oh (1983), has therefore been implemented in this model.

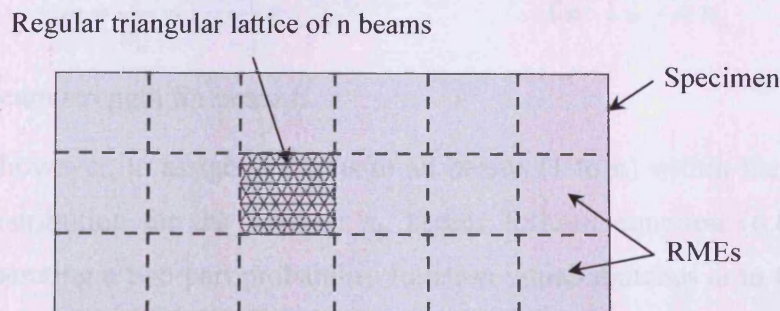


Figure 6.9. Division of specimen domain into RMEs containing n beams

The total discretised domain has therefore been segregated into RME regions as shown in Figure 6.9, and the full range of beam strengths, as obtained from equation (6.5), have been

distributed randomly over each and every RME. It should be noted that an RME is representative of a materials make-up rather than its constitutive behaviour, as is the case for an RVE. As a result, an RME is considered to exist post-localisation, unlike an RVE which is considered to break down after the strains have localised (Gitman, 2006), as described in section 2.5.2.

6.7 Double strength distribution over an RME

The challenge of achieving objective results in a two dimensional lattice may now be specifically considered as the need to regularize the energy released during damage of any given RME.

The number of beams that are fractured during complete failure of an RME, n_ω is given by;

$$n_\omega = a_\omega n \quad \text{with: } \frac{1.13}{\sqrt{n}} < a_\omega < 1 \quad (6.7)$$

where n is the total number of beams in an RME, and a_ω is the proportion of the total number of beams that are fractured.

The actual value of n_ω depends on the amount of fluctuation or the tortuosity that the crack exhibits as it propagates through the RME, and also the amount of distributed beam breakages that occur prior to crack localisation. The lower limit on a_ω is therefore derived for the case of zero tortuosity whereby a single horizontal row of diagonal elements break, as illustrated in the unzipping example shown in Figure 5.10.

If the damage is now considered to be complete (i.e. $\omega=1$) when n_ω beams (rather than n beams) have broken, then equation (6.5) may be re-written as;

$$\omega = \frac{j}{n_\omega} = 1 - \frac{\varepsilon_t}{\zeta_j} e^{-c_1 \frac{\zeta_j - \varepsilon_t}{\varepsilon_0 - \varepsilon_t}} \quad \text{for: } 1 \leq j \leq n_\omega \quad (6.8)$$

where ζ_j is the beam strength for beam j .

It is necessary, however, to assign strengths to all beams (1 to n) within the RME, in such a way that the distribution for the weakest n_ω beams follows equation (6.8). This may be achieved by generating a two-part probability function which matches ω in the range 1 to n_ω and then increases thereafter. It should be noted that since the function given in (6.8) tends towards a horizontal asymptote at $\zeta=\varepsilon_0$ (Figure 6.10), it is not possible to extrapolate this function to produce a complete distribution for n beams. The second part of the probability

curve, as illustrated in Figure 6.10, is therefore defined as a Weibull function, with constant $m=12$:

$$P(\zeta) = \underbrace{\frac{j}{n} = 1 - \frac{n_w}{n} \left(\frac{\varepsilon_t}{\zeta_j} e^{-c_1 \frac{\zeta_j - \varepsilon_t}{\varepsilon_0 - \varepsilon_t}} \right)}_{\text{Part 1}} - \underbrace{\left(\frac{n - n_w}{n} \right) e^{-\left(\frac{\zeta_j - \varepsilon_t}{4\varepsilon_0} \right)^m}}_{\text{Part 2}} \quad \text{for: } 1 \leq j \leq n \quad (6.9)$$

It should be noted that a Weibull form of the function has been adopted here for convenience only.

The beam strengths derived from the double strength distribution given by equation (6.9) may be considered to retain some form of physical relevance to the underlying mesostructure, despite this not being modelled explicitly in the present model. The weaker beams from the first part of the distribution may be considered to represent the ITZ and weaker mortar elements that fracture during propagation of the macro crack. The stronger beams from the second part of the distribution have little numerical significance, since they should not break according to the theory, however, physically they may be considered to represent the stronger mortar and aggregate phases that serve to ‘block’ the propagation of the crack.

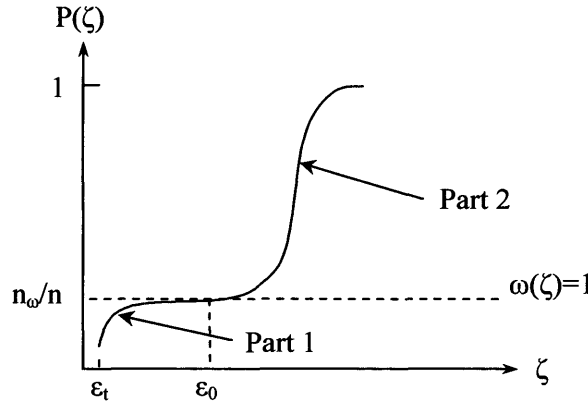


Figure 6.10. Schematic representation of the two-part probability function.

6.8 Percolation limit

The full array of beam strengths obtained from solving the double strength distribution, given in equation (6.9), for $i=1$ to n , are allocated randomly to the n beams within the RME. The number of beams that actually fracture during complete failure of an RME has previously been defined as n_w . This should be of the order of \sqrt{n} for a predominantly one dimensional

crack propagating through a two dimensional RME containing n beams. According to the theory, the beam strengths of the n_w beams that fail should come from the lower part (part 1) of the probability function illustrated in Figure 6.10. However, for this to be the case, the actual number of lower strength distribution beams that must be scattered across the two dimensional RME must be significantly greater than n_w .

The number of beams which therefore break during complete damage of an RME, n_w is considerably less than n_p ; the number of beams that are required to be distributed in order to achieve a percolation path of ‘low strength’ beams across an RME. For a random distribution of lower strength beams across a two dimensional lattice RME, n_p is defined as:

$$n_p = a_p n \quad (6.10)$$

where a_p is the percolation limit expressed as a fraction of the total number of beams n in an RME.

Herrmann & Roux (1990) discuss at some length percolation theory in relation to the conductance of lattice networks. It should be noted, however, that the stress concentration effects contained within structural lattice networks are not present in conductance networks. These effects serve to further complicate any theoretical determination of the percolation limit from the mechanical response of the system, since this is dependent on whether the stress driven crack path coincides with the percolation path.

The effect of the percolation limit, a_p on the post-peak softening response of a notched 100mm x 50mm specimen with a lattice resolution, $l = 0.5\text{mm}$, is given in Figure 6.11. The boundary conditions for this uniaxial test are as given in Figure 6.12. It can be seen from Figure 6.11 that as a_p is reduced and hence the number of beams drawn from the lower part of the two-part strength distribution, n_p is decreased, the ductility of the softening curve increases significantly. Unlike conductance networks, structural lattices do not offer infinite resistance below some percolation limit, p_c . Instead, the post peak response becomes increasingly ductile as a result of the need for an increasing proportion of beams from the upper strength distribution to be broken for complete failure. Conversely, if a_p is increased and the proportion of beams drawn from the lower strength distribution becomes too large, the post peak response becomes overly brittle. This is because too many percolation paths then exist and as a result the stronger beams from the lower strength distribution, which control the softening tail, remain unbroken.

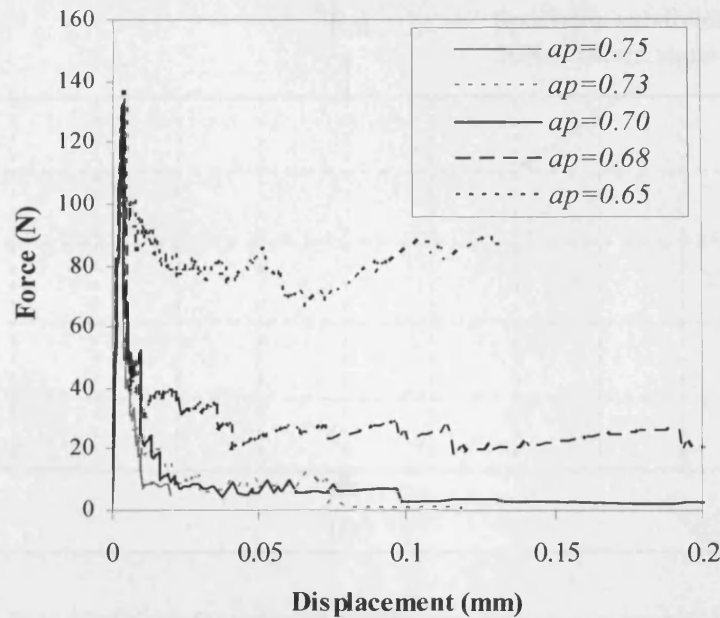


Figure 6.11. Sensitivity of the post-peak softening response to the percolation threshold, a_p .

From Figure 6.11 it is apparent that an a_p of 0.7 produces a post peak response which is comparable to the chosen input curve parameters ($f_t=2\text{MPa}$, $u_0=0.2\text{mm}$), and which is representative of a typical cementitious material (van Mier, 1997). It should be noted that a peak load of 140N equates to a peak stress, over the un-notched area, of 1.6MPa. This is less than the peak target stress of 2MPa, due to the initial stress concentrations created by the 8mm notches located at either side of the specimen.

6.9 Objectivity of double strength distribution

The degree of objectivity offered by the double strength distribution theory applied to a two dimensional lattice without explicit mesostructure may now be examined. Figure 6.13 shows the force-displacement curves for three different element length discretisations of a 100mm x 50mm DEN mortar specimen. This specimen is subjected to uniaxial tension as illustrated in Figure 6.12. The values of f_t , u_0 and a_p used in these simulations are 2MPa, 0.2mm and 0.7, respectively. The specimen has been segregated into 50No. 10mm square RMEs which are each allocated the full range of beam strengths as obtained from equation (6.9). The size of the RME has been taken to be five times a maximum particle size of 2mm, which is typical for a mortar.

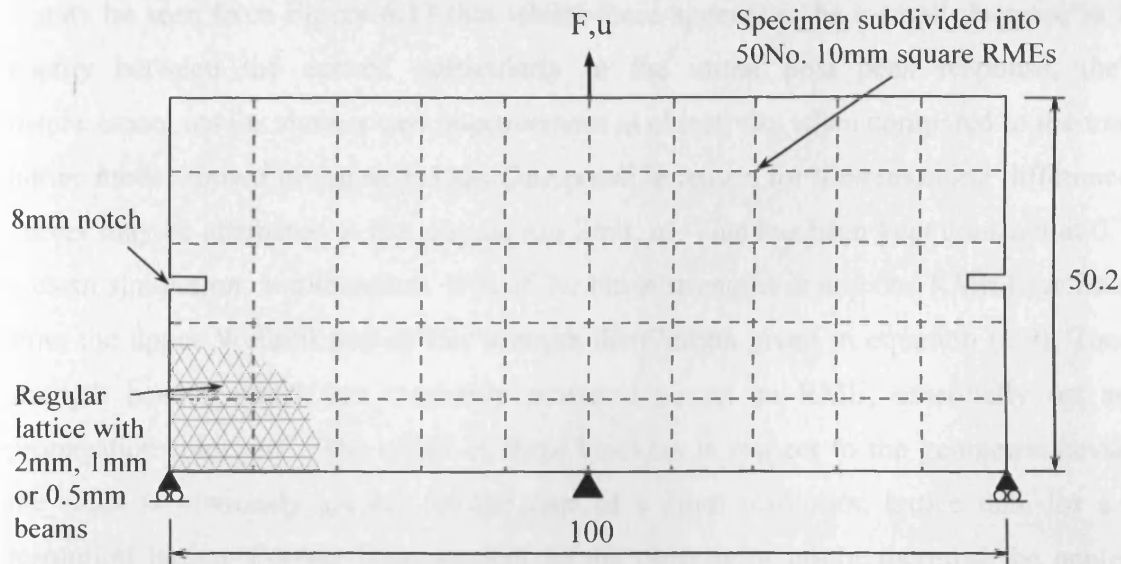


Figure 6.12. Boundary conditions for uniaxial tensile experiment on a doubly notched 100x50mm specimen discretised using three different lattice resolutions: 2mm, 1mm and 0.5mm

It should be noted that, in addition to the beam length, only the height of the beams have been altered between the lattice simulations shown in Figure 6.13. This is required in order to maintain a global Poisson's ratio of 0.2, as given by equation (3.10). It should also be noted that eight separate simulations have been completed for each of the three lattice resolutions chosen. Each of these simulations has a different random distribution of beam strengths across the RMEs. However, only three typical force-displacement responses have been shown in Figure 6.13 for the purposes of clarity.

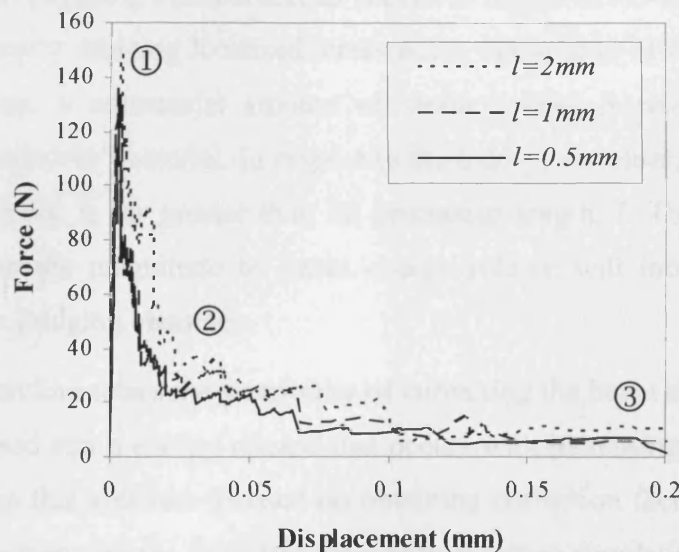


Figure 6.13. Three typical force-displacement graphs for 100mm x 50mm notched specimens with varying mesh resolutions of 2mm, 1mm, and 0.5mm.

It may be seen from Figure 6.13 that whilst there appears to be a small decrease in fracture energy between the curves, particularly in the initial post peak response, the force-displacement results show a vast improvement in objectivity when compared to the traditional lattice model shown in Figure 6.1(d). One possible reason for the remaining difference in the curves may be attributed to the percolation limit, a_p . This has been kept constant at 0.7 in the present simulation, and therefore 30% of the beam strengths in any one RME have been taken from the upper Weibull part of the strength distribution given in equation (6.9). These high strength beams, which are randomly scattered across an RME, essentially act as crack propagation ‘blockers’. The effect of these blockers in respect to the geometric deviation of the crack is obviously greater for the case of a 2mm resolution lattice than for a 0.5mm resolution lattice. Further improvement in the objectivity might therefore be achieved by making a_p a function of the element length, l in order to allow for this effect.

The general over-brittleness of the curves shown in Figure 6.7 for the one dimensional statistical theory has also been corrected in the modified double strength distribution theory. This is evident in the far larger displacement values obtained for the tail of the softening curves, which are now of the same order as the 0.2mm crack opening displacement (u_0) specified in the target exponential softening curve. All three curves are still nevertheless slightly over brittle in the immediate post-peak softening response, when compared to the idealised target exponential curve. The primary reason for the very significant energy drops observed in this region is believed to be due to the breakage of early crack bridges that have formed across the propagating macrocrack, as shown in Figure 6.14. These bridges ‘serve to pull material in’ thereby creating localised stress bulbs either side of the crack. When these bridging beams break a substantial amount of strain energy is released due the elastic unloading of this ‘pulled-in’ material. In respect to the theory, therefore, the ‘effective length’ of this bridging element is far greater than its geometric length, l . The amount of material pull-in and therefore the magnitude of strain energy release will increase with increasing beam strength of the bridging elements.

This observation therefore raises the possibility of correcting the beam strength distribution to allow for the increased strain energy release that occurs with increasing beam strength. Early investigation work in this area has focused on obtaining correction factors by comparing the output force-displacement graphs from two dimensional lattice simulations with the idealised exponential target softening curve. However, obtaining a smooth correction function from

these correction factors has been found to require the completion of a very large number of simulations in order to account for the random allocation of heterogeneity in the model.

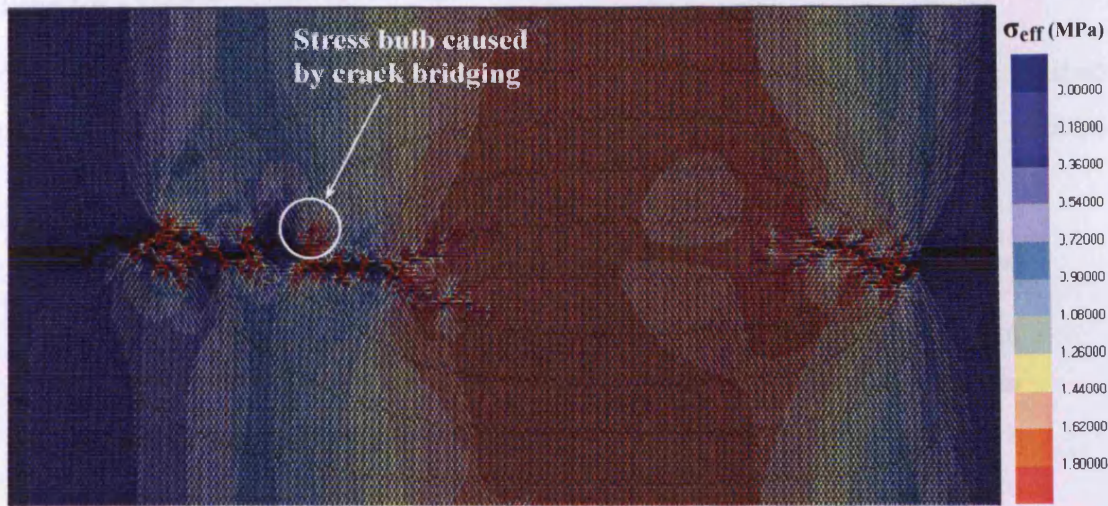


Figure 6.14. Detailed effective stress plot around a propagating macrocrack illustrating the stress the stress bulbs caused by crack bridging

The peak load in Figure 6.13 has also been maintained at approximately 140N, which is considered reasonable, given the specified f_t value of 2MPa and allowing for the stress concentrations caused by the notches, as previously discussed. The peak value is nevertheless observed to reduce slightly with reducing beam length, as originally observed for the traditional lattice model in Figure 6.1(d). Since the minimum strength of the beams has been set at 2MPa irrespective of the lattice resolution used, then the ability of the finer mesh to better capture the high stress concentrations around the notch tips has only been implicitly allowed for in the current version of the statistical beam strength theory. Some indication of the magnitude of this resolution affect is given by the linear elastic fracture mechanics (LEFM) problem shown in Figure 6.3(a). The maximum stress in the beams surrounding the crack tip is twice as large for a 1mm element length discretisation as it is for the 2mm case.

In addition to producing vastly improved quantitative results, the method also appears to maintain good qualitative results in respect to predicting feasible crack evolution. The fracture patterns for all three lattice resolutions were found to be realistic for a uniaxial tensile test, and were also observed to have a degree of tortuosity that was of the order of the 10mm RME size chosen. In statistical terms, this implies that for a percolation limit, a_p of 0.7 the macro crack was able to locate a percolation path through individual RMEs that contained beams that were primarily drawn from the lower part of the strength distribution given in equation (6.9). The size of the RME was specifically chosen to be five times the maximum aggregate

size, and since this is also recognised in the literature (Gitman, 2006) to approximate the size of the fracture process zone, then it is felt that the degree of tortuosity given by the model is realistic for a mortar specimen.

The evolution of the fracture pattern for the finest resolution ($l=0.5\text{mm}$) lattice is illustrated in Figure 6.15. The three stages of crack propagation correspond to the locations indicated by the numbers on Figure 6.13.

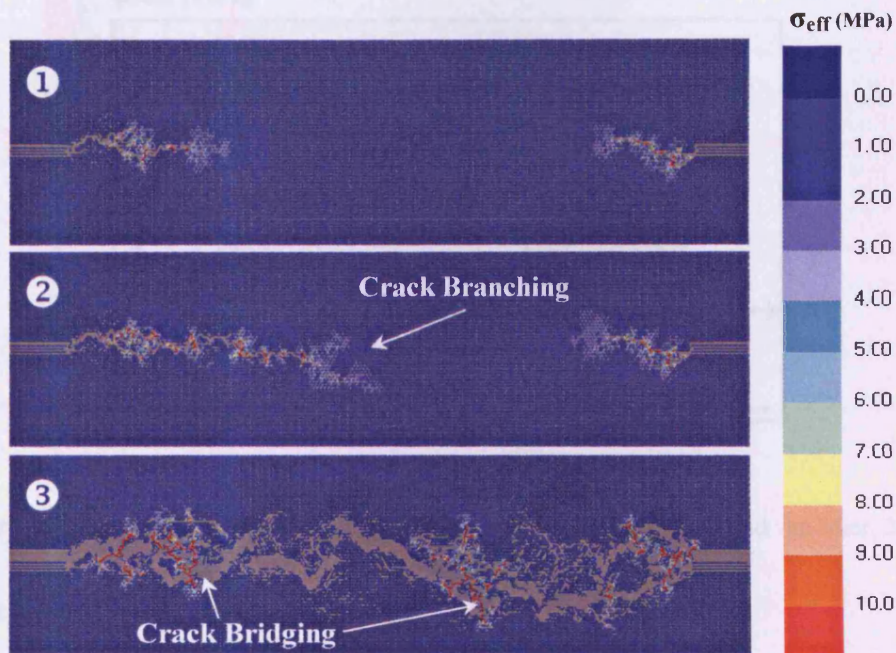


Figure 6.15. Enlarged views of typical fracture evolution for 100mm x 50mm notched specimen with a 0.5mm mesh resolution (see Figure 6.13 for respective mechanical response)

Figure 6.15, in conjunction with Figure 6.13, illustrates that the model has captured three distinct phases of crack evolution, namely: (i) initial crack propagation from the notch tip at peak response; (ii) crack branching during the softening phase, and; (iii) crack bridging at the tail of the softening curve. In the present model these three distinct phases can be attributed primarily to: (i) the stress concentration around the notch tips; (ii) the availability of multiple percolation paths containing weaker beams at crack tips, and; (iii) the cross-linking of the segregated specimen parts with higher strength lattice beams.

These phases are also representative of actual fracture processes that have been captured in experimental observations using optical microscopy, fluorescent impregnation, AE monitoring and photoelastic coating techniques (van Mier, 1997). Prado and van Mier (2003) categorise these fracture processes into three distinct stages, namely microcrack growth,

macrocrack growth and crack bridging and branching, as schematised in Figure 6.16. The fracture pattern illustrated in Figure 6.15 may therefore be considered to capture the second and third stages; however the initial microcracking stage is negligible in the present simulation. This is because the large stress concentrations around the notch tips predispose the beams in the immediate vicinity to failure, thereby severely limiting the amount of distributed microcracking, and therefore pre-peak hardening that occurs.

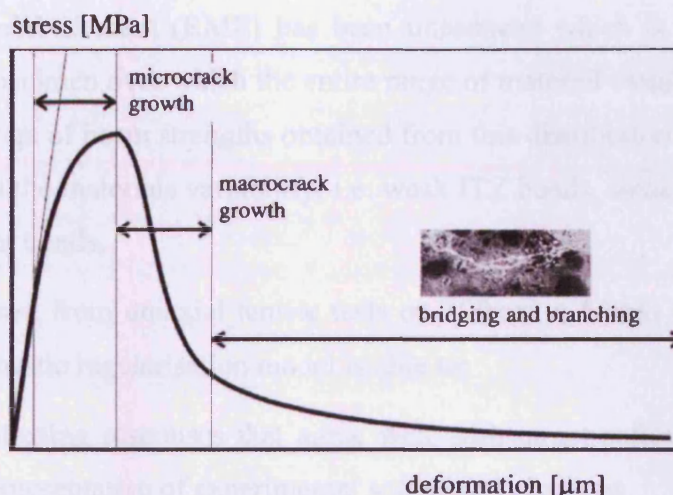


Figure 6.16. Fracture processes in concrete under uniaxial tension (Prado and van Mier, 2003)

6.10 Conclusions and future work

Lattice models have been recognised for some time as having the ability to disclose important information about the physical processes occurring during the fracture of cementitious materials. The quantitative limitations of the model, which include over-brittleness and mesh size dependence of the force-displacement response, have, however, limited its wider application.

This chapter has presented and discussed the reasons for the non-uniqueness of the traditional lattice method and the range of options that may be implemented in order to address this problem. The key to achieving regularisation has been identified as the need to maintain an average-stress, σ_{av} versus crack opening displacement, u at localisation, irrespective of the lattice resolution length, l . In order to achieve this, particular attention has been given to the development of a regularisation theory based on the statistical distribution of beam strengths. The underlying aim of the statistical softening model is to replace the softening curve in each bar by a series of bars, which break at different strains, such that proportion of bars broken in the localised zone approximates the damage variable, ω .

A statistical distribution was initially proposed which represents the localised fracture process zone as a bundle of one dimensional parallel bars. The strengths of these bars are obtained by solving the discrete form of a target exponential softening curve, whose tail is taken to be a function of the element length, l .

The theory has then been recast into a double strength distribution format to account for the additional spatial effects prevalent in two dimensional lattices. In doing so, the concept of a representative material element (RME) has been introduced which is considered to be the smallest area of a specimen over which the entire range of material variability can be expected to be found. The range of beam strengths obtained from this distribution may be considered to physically represent the materials variability; i.e. weak ITZ bonds, weak-strong mortar bonds, and strong aggregate bonds.

Initial results obtained from uniaxial tensile tests on 100mm x 50mm DEN specimens have shown that the stochastic regularisation model is able to:

1. Predict softening responses that agree well with target softening curves, which in turn are representative of experimental softening behaviour.
2. Produce softening responses that are largely independent of mesh size.
3. Give realistic fracture patterns with a fracture process zone comparable to the chosen size of the representative material elements, without explicitly representing the mesostructure.
4. Capture the main phases of crack formation, namely macrocrack growth, crack branching and crack bridging.

In addition, the nature of the post peak response has also been found to be sensitive to the percolation limit, a_p . A percolation limit of 0.7 (70% of all beams drawn from the lower strength distribution) has been determined to give an optimal post-peak response for a lattice resolution of 0.5mm.

Analysis of the initial results from the model has also indicated that the main issues to be considered when applying this theory to two dimensional lattices are:

1. The effect of the lattice resolution size on the ability of the mesh to capture stress concentrations at pre-fabricated notches and crack tips.
2. The existence of multiple percolation, and therefore cracking paths.

3. The relationship between the percolation limit, a_p and the element length, l .
4. The increase in ‘effective length’ of the beams as damage progresses.

It is believed that by randomly distributing beams drawn from the lower strength distribution, up to the percolation limit, the issues of multiple cracking paths and stress concentrations affecting the choice of crack path are significantly reduced. During damage evolution, it is therefore believed that the vast majority of the broken beams are representative of the entire lower part of the dual strength distribution, as assumed in the theoretical derivation.

The effect of element length on the percolation limit, and the increase in ‘effective length’ of the beams as damage progresses are not considered explicitly in the present model, however, and will therefore be explored in future work. Due to the underlying statistical basis of the present regularisation model, future work should also focus on detailed quantification of the degree of regularisation offered by the model. This should be completed through undertaking large numbers of repetitive simulations with different random distributions of heterogeneity for different mesh resolutions. In addition, the effect of combining the statistical theory with an explicit mesostructure overlay will also be explored.

One further topic that future development of the model might also focus on is the inclusion of the Weibull size effect. The current theory has already introduced and utilised the concept of an RME in respect to distribution of material heterogeneity. However, in the present model the average tensile strength, f_t for every RME is considered to be identical. If the average tensile strength is therefore given a Weibull distribution of its own, as illustrated in equation (6.11) and by Figure 6.17, then the model would feasibly be able to capture the Weibull size effect as discussed by Bažant (2005).

$$P(f_t) = \frac{m}{f_{t0}} \left(\frac{f_t - f_{tu}}{f_{t0}} \right)^{m-1} e^{-\left(\frac{f_t - f_{tu}}{f_{t0}} \right)^m} \quad \text{for: } f_t > 0 \quad (6.11)$$

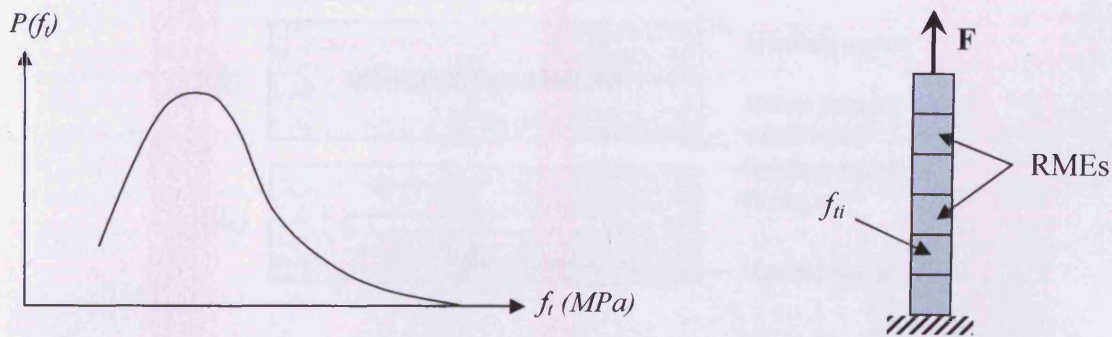


Figure 6.17. Schematic illustration of Weibull distribution of average tensile strengths, f_t of RMEs

Chapter 7

Experimental study on self-healing cementitious materials

7.1 Introduction

The amount of experimental data relating to the autonomic healing of cementitious materials within the literature is currently very limited, as noted in Chapter 2. Therefore, in order to facilitate the development of a numerical model to simulate the autonomic healing process, it was deemed necessary to first undertake an experimental programme, for which all observations and data would be available. These include:

1. Width, nature and location of cracks;
2. Viscosity and degree of migration of glue, and;
3. The strength and stiffness of specimens pre- and post-healing.

The autonomic healing concept investigated in this work is illustrated in Figure 7.1.

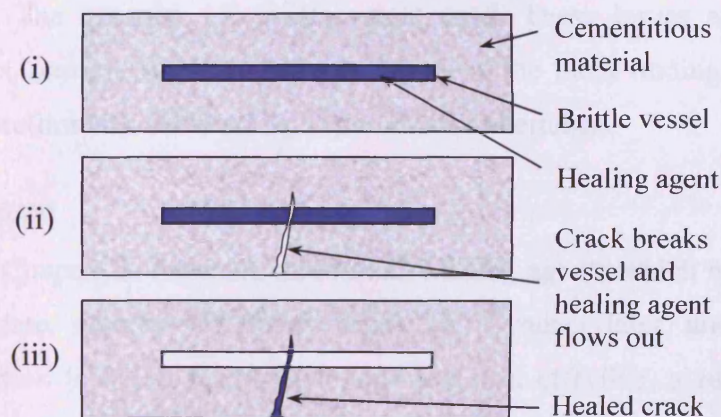


Figure 7.1. Autonomic healing concept

The concept is based on the principle that crack formation in the cementitious matrix also causes brittle adhesive-filled capsules or tubes, embedded within the matrix, to crack. The contents of the capsules or tubes are thereby released into the crack plane where the agent is intended to cure and heal the damaged host matrix. This concept was originally proposed for cementitious materials by Dry (1994), as noted in section 2.3.2.1.

The primary objectives of this experimental work are therefore:

1. To design, produce and embed a healing mechanism within a cementitious matrix;
2. To determine the degree of actuation of the healing mechanism in response to damage caused by external loading, and;
3. To establish the degree to which the healing mechanism restores, or improves, the original mechanical properties of the cementitious matrix.

This chapter initially outlines the main issues associated with achieving adhesive based self-healing within small scale laboratory specimens, as identified by the preliminary experimental investigation work. Details of the development of a successful self-healing experimental method are then given, followed by the presentation and analysis of the results of a series of self-healing experiments conducted on reinforced mortar prismatic beams.

7.2 Preliminary investigations

A substantial amount of preliminary experimental work has been completed prior to the development of a successful self-healing experimental method, as outlined in Joseph and Jefferson (2007). The various aspects that have been investigated include: (i) The type of healing agent; (ii) The method of encapsulation; (iii) The form of the host cementitious matrix, and; (iv) The quantity of reinforcement used. These issues are discussed in the following sections, and are followed by a summary of the main findings obtained from the final two sets of preliminary self-healing experiments undertaken.

7.2.1 Healing agent

As referred to in Chapter 2, there are three main healing agents which have been utilised in the literature to date, namely: (i) Epoxy resins; (ii) Cyanacrylates, and; (iii) Alkali-silika solutions. In addition to being readily available and cost effective, a suitable agent for the autonomic healing of cementitious materials should:

1. Have the ability to be readily encapsulated within an internal or external supply system;
2. Be sufficiently mobile to allow migration to the areas of damage following release;
3. Have sufficient mechanical properties on curing, ideally equal to or greater than the properties of the cementitious matrix, in order to resist crack re-opening, and;
4. Have sufficient longevity, and compatibility with the cementitious matrix, over the lifetime of the structure.

It should be noted that only the first three requirements have been specifically addressed during the preliminary investigation work on the selection of a suitable healing agent. The final criterion will be important, however, in determining the optimal long term solution.

Three different adhesives were selected and examined for their suitability as potential healing agents; an epoxy resin and two types of cyanoacrylate. The epoxy resin tested was a Tecroc products injection grout TG07 (Tecroc, 2004). The cyanoacrylates examined were SICOMET 9000; a methoxyethyl based product from Henkel Sichel-Werke (Henkel Sichel-Werke, 1997), and Rite Lok EC-5; an ethyl based adhesive produced by 3M Ltd (Appendix A).

The suitability of these adhesives were evaluated in a largely qualitative manner, based on:

1. Their initial workability, viscosity, and curing period,
2. Their mechanical ability to bond both smooth and rough concrete surfaces together, and;
3. Their longevity within an encapsulated system.

The epoxy injection grout, despite its current use as a remedial crack injection and repair method for concrete, was rejected for two reasons: (i) its viscosity of 200 centipose, despite being low for an epoxy resin, is only capable of filling cracks down to 100 microns (Tecroc, 2004), and (ii) its two-part system cures in the absence of air, which makes it unsuitable for internal encapsulation, or for use in an external circulatory supply system, where good post-encapsulation longevity (i.e. extended pot-life) is required. It should be noted that Mihashi et al. (2000) examined the feasibility of separate storage of the two epoxy resin components, adjacent to one another within a cementitious matrix. They concluded that insufficient mixing on release resulted in poor curing and therefore poor mechanical performance of the adhesive. This system was therefore not examined during the preliminary investigation stage of these experiments.

Both of the cyanoacrylates examined performed well, and offered good workability due to low viscosities, quick curing times in the order of seconds, and mechanical strengths significantly greater than the parent cementitious matrix. In addition, both cyanoacrylates were single agent and had good pot-lives; i.e. providing the moisture content of the capsule was low and it was adequately sealed, then no significant degradation of the adhesive, in terms of viscosity, was observed over a period of 60 days post-encapsulation.

Rite Lok EC-5 cyanoacrylate was chosen as the most suitable healing agent for achieving self repair within a mortar matrix, and was therefore used for the duration of the experimental programme described in section 7.3. The data sheet for this cyanoacrylate is included under Appendix A. Rite Lok EC-5 was chosen because of its suitability at bonding a wide range of substrates including ceramics, and for its wicking ability due to its extremely low viscosity; 1-10 centipose, compared to 15-25 centipose for SICOMET 9000. This increases its potential self-healing capability due to its ability to infiltrate micro-cracks within the cementitious matrix. As indicated on the data sheet (Appendix A), it has a full cure time of 24 hours and a tensile strength (ISO 6922) of 20MPa after curing.

7.2.2 Encapsulation method

In the absence of a readily available source of hollow spherical microcapsules, and a suitable technique for encapsulating healing agents within them, all preliminary investigations focused on the use of hollow capillary tubes, as illustrated in Figure 7.2. These are small diameter quartz or borosilicate glass tubes traditionally used for the sampling and storage of blood in the medical industry. They obtain their name from the high capillary attractive forces that exist between the walls of the tube due to their small internal diameter.

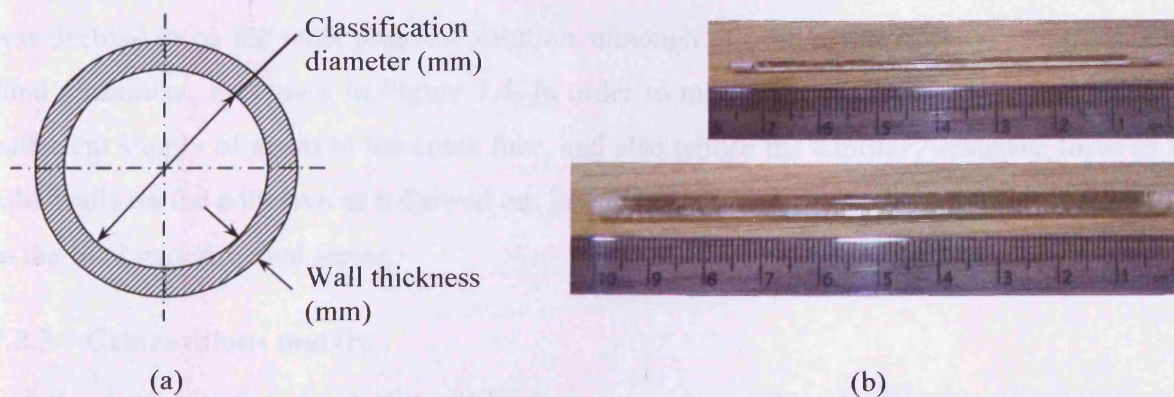


Figure 7.2. (a) Borosilicate capillary tube cross-sectional details, and; (b) Pictures of 1.5mm and 3.0mm diameter tubes filled with cyanoacrylate and plugged with wax

75mm long tubes of 0.8mm ID (internal diameter) and 1.5mm ID, and 100mm long tubes of 3mm ID were internally encapsulated within prismatic mortar beams during the preliminary experiments. The specification details for these tubes are given in Table 7.1.

Table 7.1. Specifications of capillary tubes used in preliminary experiments

Classification diameter (mm)	0.8	1.5	3.0
Wall material	Borosilicate glass		
Wall thickness (mm)	-	-	0.5
Length (mm)	75	75	100
Total internal capacity of single tube, excluding wax end plugs (µl)	34	118	650

Two different configurations of capillary tubes were explored. These included: (i) a single layer of 5No. tubes, and; (ii) a double layer of 10 tubes (2 layers of 5No.), placed evenly across the beam, as illustrated in Figure 7.3.

In all cases the tubes were filled with adhesive by rotating the tube to a near horizontal position and using the capillary attractive force of the tube itself to draw up the liquid. The ends were then sealed by inserting the tube into a soft wax compound. This method of filling was found to minimise the amount of air trapped within the tubes. In the control specimens, the adhesive was replaced with an ink tracing die, although the same filling procedure was utilised.

Various methods for placing the tubes within the mortar during the casting process were also explored including the use of wire supporting frames. However, in order to ensure sufficient compaction of the mortar around the capillary tubes, manual placement of the tubes in layers was deemed to be the most practical solution, although this did result in some variation in the final placement, as shown in Figure 7.4. In order to minimise tube breakages, and provide a sufficient supply of agent to the crack face, and also reduce the capillary resistive force of the tube walls on the adhesive as it flowed out into the crack, the largest 3mm ID tubes were used in the final experimental series.

7.2.3 Cementitious matrix

For the purpose of proving the self-healing concept, small scale laboratory specimens of dimensions 75x75x255mm were used during the entire experimental programme, as illustrated in Figure 7.3. In order to achieve a more homogenous material at this specimen

scale the beams were cast using mortar as oppose to concrete. The maximum aggregate size was limited to 2mm, and the maximum aggregate to specimen dimension ratio was therefore limited to 1:35. Following a series of trial mixes, a ratio of 0.6 : 1 : 3.5 (water : OPC : sand), by weight, was found to offer suitable workability in respect to achieving sufficient material compaction around the reinforcing bar and capillary tubes. This mix design was used for all subsequent sets of experiments (apart from set 1), as shown in Table 7.3.

7.2.4 Reinforcement

The purpose of reinforcing the mortar beams is to control the rate of crack opening in the specimens during the three-point bending test. The self-healing system is also envisaged to be applicable to reinforced concrete. The minimum level of reinforcement specified in Eurocode 2 (BS EN1992, 2004) for reinforced concrete beams is $0.13\% bd$; where b is the beam breadth and d is the depth to the centre of the reinforcement. This equates to a 3mm diameter bar for the beam dimensions adopted in these experiments, as given in Figure 7.3.

A smooth 3.15mm diameter high yield steel reinforcing bar was therefore used in the preliminary experiments to satisfy the minimum level of reinforcement. Higher levels of reinforcement were also examined during both the preliminary and final experimental programme, as described in section 7.3. A smooth 6.7mm diameter high yield steel bar was used to provide the higher amounts of reinforcement in the more heavily reinforced beams.

Three 250mm long samples of the 3.15mm diameter and the 6.7mm diameter steel bar have been tested in a tensile testing machine in line with the recommendations of BS4449 (2005). The mean mechanical properties for both bar materials are given in Table 7.2 below:

Table 7.2. Summary of the mean mechanical properties for the 3.15mm ϕ and the 6.7mm ϕ high yield steel reinforcement bars

Diameter (mm)	Profile	Elastic modulus (GPa)	0.2% Proof stress (MPa)	Ultimate strength (MPa)	Elongation at failure (%)
3.15	Smooth	205.2	563.1	597.3	12.0
6.70	Smooth	192.3	526.1	576.3	12.7

7.2.5 Summary of preliminary investigation work

Following various individual studies on the healing agent, encapsulation mechanism, cementitious matrix and reinforcement, as described previously, two sets of experiments were

completed. These preliminary experiments consisted of two sets of 6 beams, with each set comprising 4 self-healing (SH) and 2 control (C) beams, tested under three-point loading. The first set contained a single layer of 5No. 100mm long capillary tubes, and the second set contained 10No. capillary tubes, placed in two layers, as illustrated in Figure 7.3. For both sets of experiments, capillary tubes of 3mm internal diameter were used.

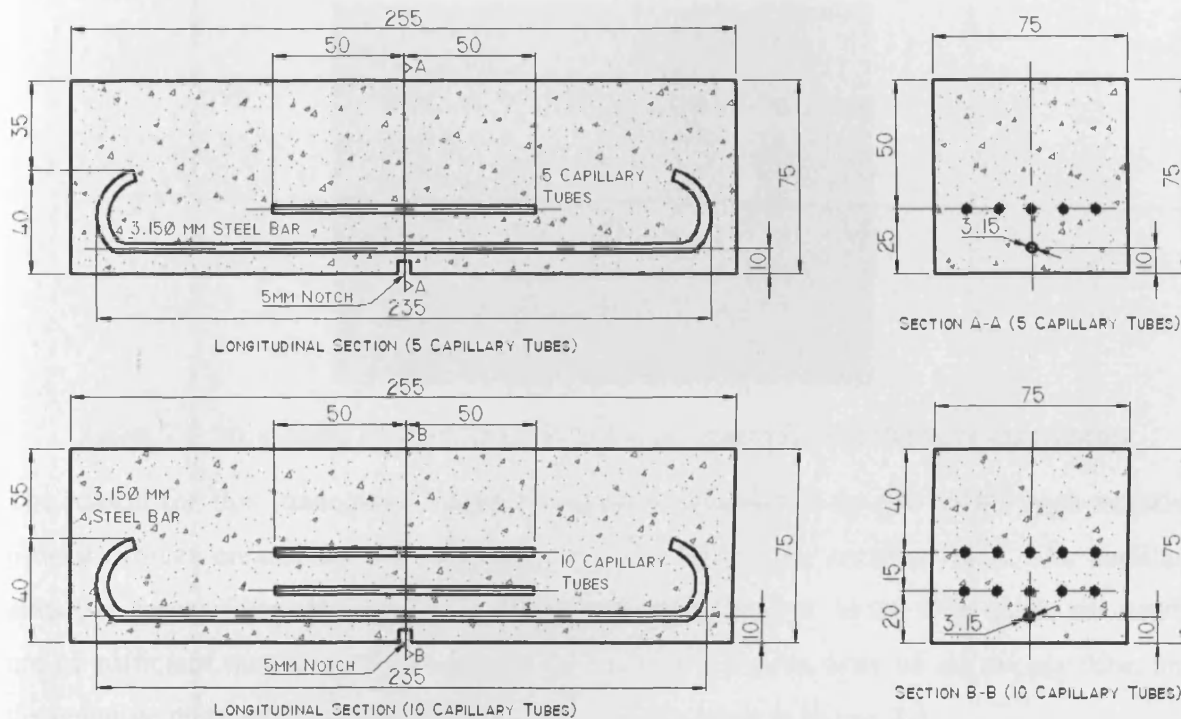


Figure 7.3. Specimen configuration for the two sets of preliminary experiments containing (a) a single layer, and (b) a double layer of 5No. 100mm long, 3mm diameter glass capillary tubes

The tubes in the SH beams were filled with Rite-Lok EC5 cyanoacrylate, and the tubes in the control beams were filled with ink, before being sealed with wax plugs, prior to casting. All beams were subjected to a two-stage, three-point bending, test procedure, in an identical manner to that undertaken in the final experimental procedure described in section 7.3.3, and illustrated in Figure 7.8. The two-stage test includes the creation of some degree of initial damage during the first loading cycle, followed by a period of healing, after which the beam is loaded to complete failure during the second loading cycle.

Results from these two sets of preliminary experiments showed some evidence of a small amount of healing in one of the four SH beams containing a double layer of tubes, but overall it was concluded that the glue had not been drawn into the cracks in sufficient quantity to allow for any significant amount of healing to occur. This conclusion was supported by the very limited extent of ink penetration which was observed on the crack faces of the control

beams, as illustrated in Figure 7.4. It should also be noted that the glue has a slightly higher viscosity than the ink, and is therefore likely to have penetrated the crack to an even lesser degree than the ink. No obvious glue deposition was observed on the crack faces of the SH beams, but large quantities of liquid glue and ink were observed to remain in both sections of the capillary tubes following complete fracture of all of the specimens.

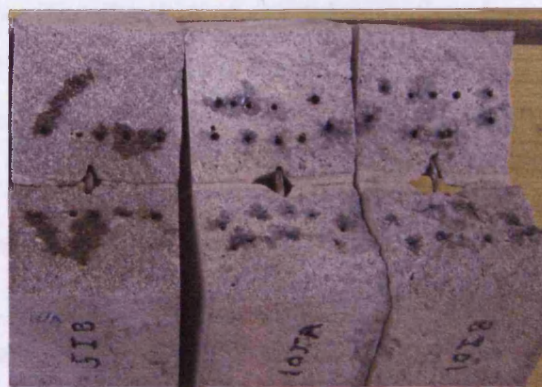


Figure 7.4. Ink staining on crack faces of control specimens from preliminary experiments

The reason for this inadequate release of agent is believed to be due to the high negative pressure forces created by the wax plugs at either end of the capillary tube. The capillary attractive force of the opening crack, and the gravitational force on the fluid mass, are clearly not of sufficient magnitude to overcome the capillary resistive force of the supply tube, and the negative pressure force due to the sealed ends, as shown in Figure 7.5.

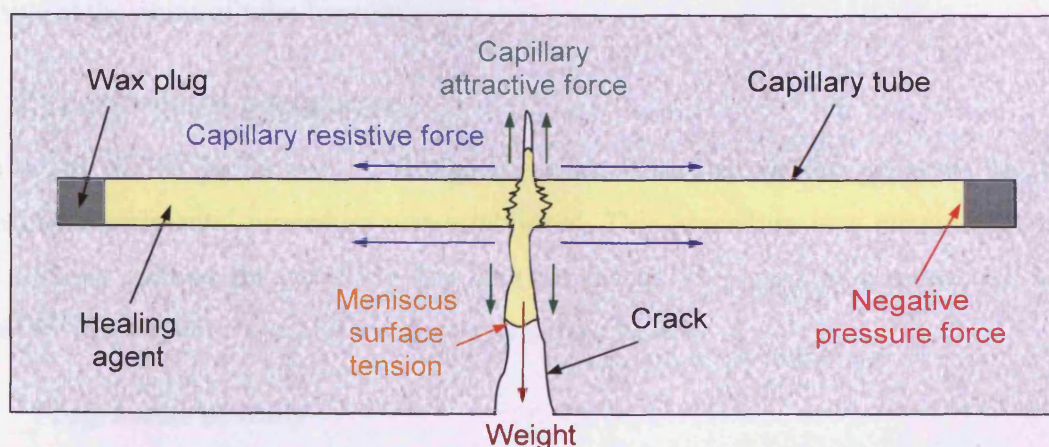


Figure 7.5. Schematic illustration of the main forces acting on an internally encapsulated healing agent

The small amount of ink migration shown in Figure 7.4 is therefore believed to be attributed to the release of ink from the localised vicinity of the crack site of the capillary tube. The amount of ink released in this area may be affected to some degree by the nature of the tube fracture. Li et al. (1998) have shown that the primary failure mechanism for a capillary tube

lying perpendicular to a crack is clean and discrete. This failure mechanism becomes more of a compound fracture when the angle between the axis of the tube and the direction of the crack decreases, thus increasing the likelihood of releasing a greater volume of agent. These two distinct failure mechanisms have been shown previously in Figure 2.10. The tubes in the three-point bending preliminary experiments described above, are subject primarily to a tensile failure mechanism. The fracture of the tubes is therefore more likely to follow the tensile failure shown in Figure 2.10(a) than the flexural failure shown in Figure 2.10(b). This was confirmed by observations of the fractured ends of the capillary tubes shown in Figure 7.4.

It should also be noted that the issue of high negative pressure forces inhibiting the release of agent is less likely to be as pronounced in the case of encapsulation within an ECC (Engineered Cementitious Composite), as discussed by Li et al (1998). This is due to the fact that the fibre reinforcement causes controlled cracking at multiple sites in the cementitious matrix (Figure 2.13(b)). Also, in work undertaken by Williams et al. (2007), on self-healing within laminated composites, the hollow holding vessel is sheared along its length as a result of the delaminating mode of failure, thus no significant negative pressure forces are apparent.

To overcome the above difficulties, longer capillary tubes have been encapsulated in the final experimental setup (section 7.3), whose ends extend outside of the beam and are open to the atmosphere, thus removing the strong resistance of the negative pressure force on the adhesive at the point of tube fracture.

7.3 Experimental procedure

As a result of the preliminary investigation work described in the previous section, the following experimental procedure was established. This procedure was considered to be the most suitable method for gathering key data for the development of a model for adhesive based self-healing within reinforced mortar prismatic beams.

7.3.1 Programme of study

The experimental programme of study undertaken to date has comprised six sets of experiments. The specimen configuration for each of these sets of experiments is outlined in Table 7.3. All of these experiments have involved three-point bend testing of reinforced prismatic mortar beams.

Table 7.3. Summary of specimen configuration for the full testing programme

	Set 1. Notched, lightly reinforced	Set 2. Notched, lightly reinforced	Set 3. Notched, moderately reinforced	Set 4. Notched, heavily reinforced	Set 5. Un- notched, lightly reinforced	Set 6. Notched, lightly reinforced, varied loading rate
No. of Beams	2 Ctrl & 4 SH	2 Ctrl & 4 SH	2 Ctrl & 4 SH	2 Ctrl & 4 SH	2 Ctrl & 4 SH	1 Ctrl & 3 SH at each loading rate
Age at first test	28 days	28 days	28 days	70 days	28 days	70 days
Mix ratio by weight (water:OPC:sand)	0.55:1:3.5	0.6:1:3.5	0.6:1:3.5	0.6:1:3.5	0.6:1:3.5	0.6:1:3.5
Cube strength, f_{cu} (MPa)	-	27.9 (After 28 days)	24.1 (After 28 days)	35.7 (After 70 days)	24.2 (After 28 days)	33.0 (After 70 days)
Specific fracture energy, G_f (N/mm)	-	-	0.068 (After 28 days)	0.096 (After 70 days)	-	0.077 (After 70 days)
Cylinder splitting strength, f_{split} (MPa)	-	2.4 (After 28 days)	2.0 (After 28 days)	3.6 (After 70 days)	2.2 (After 28 days)	3.5 (After 70 days)
Reinforcement (see Table 7.2 for properties)	1No. 3.15mm ϕ high yield steel bar	1No. 3.15mm ϕ high yield steel bar	2No. 3.15mm ϕ high yield steel bar	1 No. 6.7mm ϕ high yield steel bar	1No. 3.15mm ϕ high yield steel bar	1No. 3.15mm ϕ high yield steel bar
Adhesive supply system	4No. 3mm ID capillary tubes, open at one end	4No. 3mm ID capillary tubes, open at both ends	4No. 3mm ID capillary tubes, open at both ends	4No. 3mm ID capillary tubes, open at both ends	4No. 3mm ID capillary tubes, open at both ends	4No. 3mm ID capillary tubes, open at both ends
5mm deep notch	Yes	Yes	Yes	Yes	No	Yes
Stroke loading rate (mm/s)	0.003	0.003	0.003	0.003	0.003	0.00075, 0.003 and 0.012

The influence of various parameters on the self-healing behaviour of the beams has been investigated. The parameters that have been considered include:

1. The level of reinforcement;
2. The monotonic stroke controlled rate of loading, and;
3. The effect of pre-notching.

It can be seen from Table 7.3 that sets 1, 2, 3 and 5 have been tested after 28 days, and sets 4 and 6 have been tested after 70 days. It should be noted that this delay in the experimental programme was due to unforeseen mechanical failure of the testing equipment. This delay has, nevertheless, provided the opportunity to examine a fourth parameter, namely:

4. The effect of specimen age on the autonomic-healing ability of the beams.

In addition to the self-healing (SH) and control beam (C) tests, as described in the following sections, material tests have also been completed for the majority of the experimental sets. Three material tests have been undertaken, including:

1. Cube strengths, f_{cu} – Based on 100mm cubes tested in accordance with BS1881-Part 116 (1983).
2. Cylinder splitting strengths, f_{split} – Based on 100mm diameter, 200mm long cylinders tested in accordance with BS1881-Part 117 (1983). It should be noted that the true tensile strength of the mortar, f_t may be considered to be approximately $0.9f_{split}$ (Neville, 1995).
3. Specific fracture energy, G_f – Based on 255x75x75mm prisms, pre-notched to 10mm, and tested in three-point bending with a span of 200mm. The specific fracture energy has been calculated from the force-central deflection response of the beams in line with the guidance provided by RILEM Committee FMC-50 (1985).

The results of these material tests, where available, are given in Table 7.3. It should be noted that the material test specimens have been cast from the same mortar mix that the self-healing and control beams have been cast from. All beams and material specimens were also tested at the same age, as specified in Table 7.3.

7.3.2 Specimen preparation procedure

The self-healing and control specimens for each of the experimental sets given in Table 7.3 have been prepared in a similar manner to the first set of tests on lightly reinforced notched beams, as illustrated in Figure 7.6.

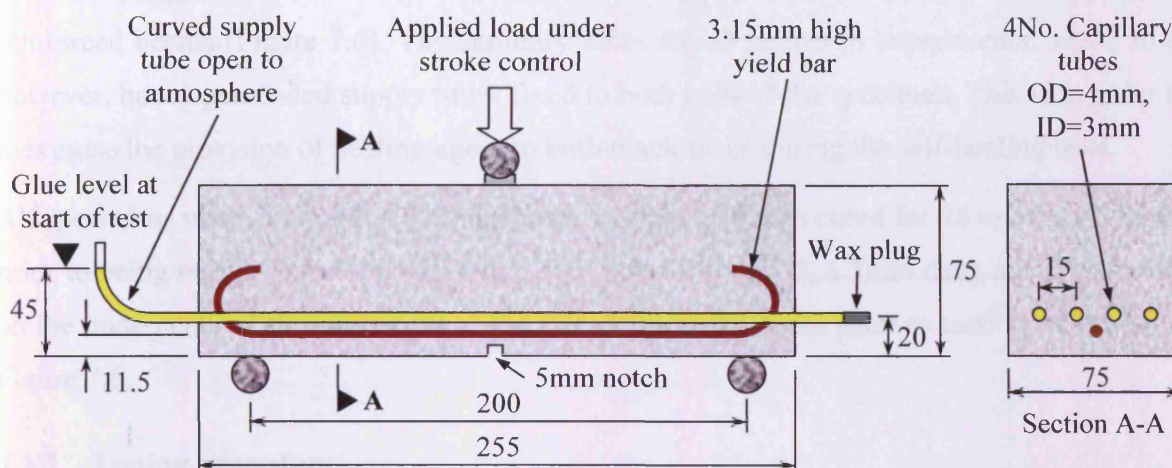


Figure 7.6. Specimen arrangement for set 1 experiments on lightly reinforced notched beams. (Note: Experimental sets 2 to 6 have an open curved supply tube at both ends of the specimen)

The set 1 beams are reinforced with a single 3.15mm diameter high yield steel bar placed on 10mm brick spacing blocks, as shown in Figure 7.7. Since the bar has a smooth profile, shear anchorage is provided by the bent section at either end of the bar. Experimental sets 2, 5 and 6 have an identical reinforcement arrangement. For set 4 the 3.15mm bar is replaced with a larger 6.7mm diameter bar, and for set 3 the single 3.15mm bar is replaced with two 3.15mm bars, spaced at a horizontal distance of 30mm apart.

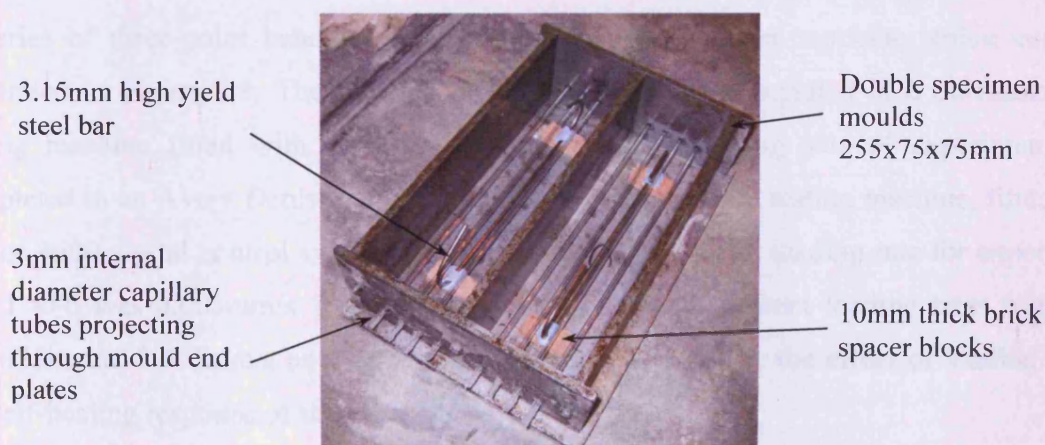


Figure 7.7. Illustration of glass tube and reinforcement configuration for set 1 experiments

The healing agent, for all SH specimens in all experimental sets, is supplied via 4 No. 3mm diameter hollow capillary tubes, placed in a single layer, 20mm from the bottom of the beam. These tubes are inserted through lubricated pre-drilled holes in the mould end plates prior to casting, as illustrated in Figure 7.7. The capillary tubes were open to the atmosphere on one side and plugged with wax on the other side for the first set of tests on notched, lightly reinforced beams (Figure 7.6). The capillary tubes for all beams in experimental sets 2 to 6, however, have open ended supply tubes fixed to both ends of the specimen. This is in order to maximise the provision of healing agent to both crack faces during the self-healing tests.

All specimens were demoulded 24 hours after casting, and then cured for 28 or 70 days in air, prior to being tested. For all experimental sets, apart from set 5, a 5mm deep notch was sawn on the underneath of the specimens at the mid-point of the beam prior to testing, as shown in Figure 7.6.

7.3.3 Testing procedure

Prior to testing, all of the capillary tubes within the SH specimens were filled with Rite-Lok EC5 cyanoacrylate to a level of 25mm above the centre-line of the tube (Figure 7.6). In order to minimise air voids, adhesive was injected into the tubes using a syringe.

The four capillary tubes in each of the two control beams were also filled and sealed in an identical manner, but with the adhesive being replaced by an ink tracing die of low viscosity (approximately 3 centipose). It should be noted that the amount of adhesive or ink placed in the supply system prior to testing was approximately 10ml for each specimen, and that this amount was fixed, and not replenished during the testing procedure.

A series of three-point bend tests were then completed under machine stroke control as illustrated in Figure 7.8. The first set of experiments was completed in a Shimadzu AG-1 testing machine fitted with a 20kN load cell. The remaining sets of experiments were completed in an Avery Denison 7152 universal servo hydraulic testing machine, fitted with a Dartec 9600 digital control system, and a 600kN load cell. The loading rate for experimental sets 1 to 5 was 0.003mm/s. For experimental set 6 three different loading rates were used; 0.00075mm/s, 0.003mm/s and 0.012mm/s, in order to examine the effect of loading rate on the self-healing response of the beams.

For all tests, the central deflection of the beam was measured using a transducer supported via an aluminium armature, connected to the centreline of one side of the beam (Figure 7.8). This method of measuring central deflection ensured that ‘bedding in’ effects, as indicated in the

stroke results for the preliminary experiments, were not captured. For all notched experiments, the crack mouth opening displacement (CMOD) was also recorded, in addition to the central deflection and load, using a clip gauge with a 5mm range.

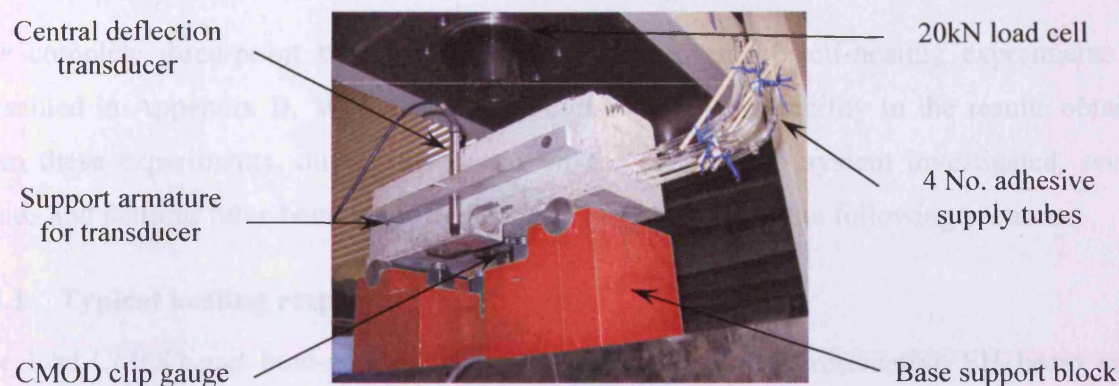


Figure 7.8. Testing arrangement for set 1 experiments on lightly reinforced notched beams

All of the control beams and self-healing beams, for all sets of experiments, were subjected to a two cycle loading process. In the first loading cycle the beam was loaded until it reached its initial peak value, at which point a sharp drop in the strength of the beam was recorded at the same time as a macro crack was observed to propagate from the underside of the beam. The test was then continued until the beam regained its initial peak strength, and a CMOD value of at least 0.3mm had been reached. At this point, the specimen was unloaded under stroke control, at the same constant rate used in the loading part of the cycle. A typical response from the first cycle of loading for a SH and control beam is given by the light red (SH beam) and blue (Control) lines shown in Figure 7.10.

In the second loading cycle the beams were tested at the same loading rate to failure, or until a central deflection value in excess of 3mm was recorded. For the control specimens the second loading cycle was completed immediately after the first loading cycle, and for the SH specimens the second loading cycle was delayed for a period of 24 hours, in order to allow full curing of the cyanoacrylate adhesive to occur. A typical response from the second loading cycle for a SH and control beam is given by the dark red (SH beam healed) and blue (Control) lines shown in Figure 7.10.

It should be noted that the only exception to the two cycle testing procedure described above was for the first experimental set. The control beams for the set 1 experiments were tested to failure in a single loading cycle, and whilst the SH beams were tested in two loading cycles, as described above, the unloading curves from the first cycle were not recorded. A typical

response for a SH and control beam from the first set of experiments is illustrated in Figure 7.9.

7.4 Results and discussion

The complete three-point bending results for all six sets of self-healing experiments are presented in Appendix B. Whilst there is inevitably some variability in the results obtained from these experiments, due to the nature of the self-healing system investigated, several trends and features have been identified. These are presented in the following sections.

7.4.1 Typical healing response

The load-CMOD and load-central deflection response of a representative SH beam and a control beam are presented in Figure 7.9.

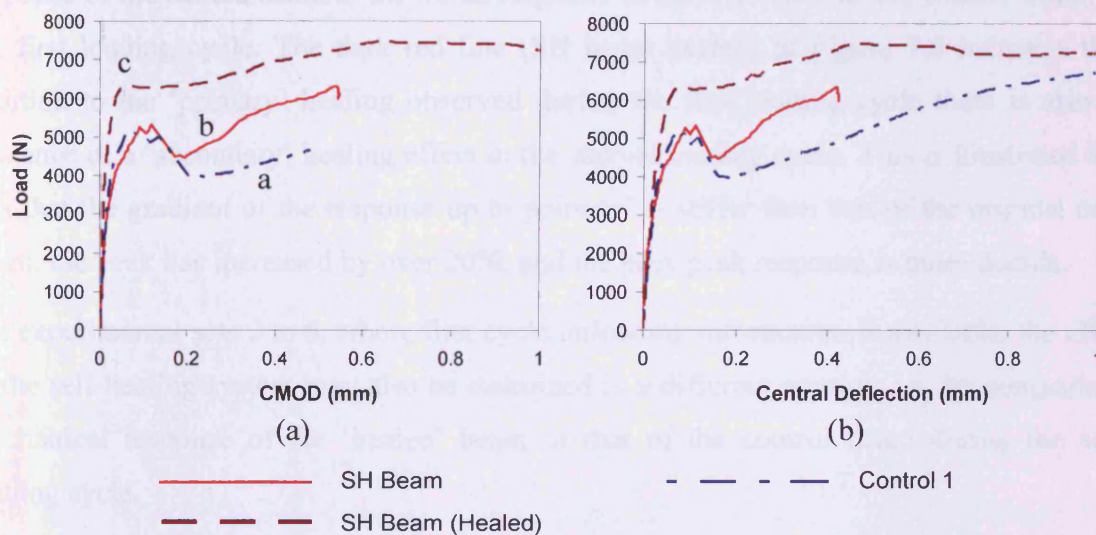


Figure 7.9. (a) Load-CMOD and (b) Load-central deflection response for SH beam 4 and Control beam 1 from set 1

It may be seen that, for both the control specimen and the first test on SH beam 4, there is some pre-peak non-linearity due to microcracking between about 4 and 5.2kN. This is followed by a sudden drop of approximately 0.7kN over a CMOD increase of approximately 0.1mm for the self-healing beam, compared with about 1.1kN over 0.13mm for the control beam. This drop is caused by the brittle fracture of the four borosilicate capillary tubes which emit a distinctive breaking sound during testing. Thereafter, the primary load carrying mechanism is performed by the steel reinforcement and the stiffness of the control beam is given by the gradient of the line at point 'a' in Figure 7.9(a). It should be noted that a lightly

reinforced beam without the glass tubes would also show a drop, but it is likely to be less pronounced.

It can be observed from Figure 7.9 that, even during the first test on SH beam 4, there is some evidence of ‘primary’ healing. This is apparent in the increased gradient of the line at point ‘b’ when compared to the equivalent gradient of the control at point ‘a’. Cyanoacrylates are acidic solutions which have the ability to cure rapidly within a period of seconds, and it is believed that the conditions within the mortar, including the presence of moisture and the alkaline environment, further accelerate the curing process, and are therefore responsible for the rapid primary healing observed in the majority of the tests.

After the SH beam has been unloaded and left to cure for a period of 24 hours, the efficacy of the passive autonomic healing mechanism may be examined, by comparing the mechanical response of the healed beam to the initial response of the SH beam, or the control beam, from the first loading cycle. The dark red line (SH beam healed) in Figure 7.9 indicates that in addition to the ‘primary’ healing observed during the first loading cycle there is also clear evidence of a ‘secondary’ healing effect in the second loading cycle. This is illustrated by the fact that the gradient of the response up to point ‘c’ is stiffer than that of the original control beam, the peak has increased by over 20%, and the post-peak response is more ductile.

For experimental sets 2 to 6, where first cycle unloading information is available, the efficacy of the self-healing system may also be examined in a different manner; i.e. by comparing the mechanical response of the ‘healed’ beam to that of the control beam during the second loading cycle.

The difference between the two methods of examining the efficacy of the self-healing process may therefore be attributed to whether or not the second loading cycle results for the SH beam include the permanent CMOD or central displacement set values, as obtained at the end of the first loading cycle. Both of these methods of plotting the data are illustrated for SH beam 1 from the second set of experiments on lightly reinforced notched beams, as given in Figure 7.10.

Further evidence of the primary healing effect is shown in Figure 7.10, both by the increased stiffness response of the SH beam following tube breakage, and the increased stiffness of this beam during unloading. The latter results in an approximate doubling of the permanent set value for the SH beam, compared to the control beam, following unloading. The reason for the stiffer unloading response is believed to be due to the rapid curing and hardening of the

adhesive that has entered the crack, which then serves to act as a ‘wedge’ between the crack surfaces on unloading.

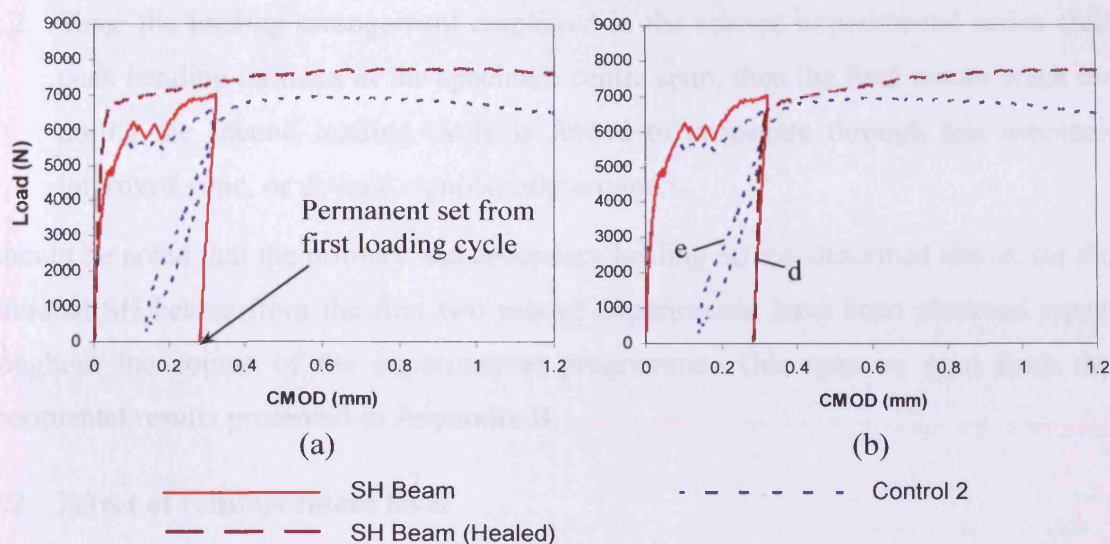


Figure 7.10. Load-CMOD response for SH beam 1 and Control beam 2 from set 2; (a) without, and (b) with the permanent set from the first loading cycle considered

Interestingly, on reloading after a period of 24 hours, the high level of stiffness observed during the unloading of the SH specimen is maintained, as illustrated by line ‘d’ in Figure 7.10(b). If the gradient of SH beam response ‘d’ is compared to the gradient of the control response ‘e’, then it is clear that the 0.3mm crack created during the first loading cycle has been healed. The reloading of the SH specimen must, therefore, result in new crack formation, or a peeling apart of the newly bonded original crack faces. Qualitative evidence of the occurrence of both of these situations is presented in section 7.4.6.2. As a result of the above, the hysteresis loop for the SH beam is also therefore far less than that of the control beam.

In Figure 7.10(a) the permanent set obtained from the first loading cycle on the SH beam is removed, and the second loading cycle response is plotted from the origin. The response of this set 2 SH beam post-healing, when compared to the virgin response of the control beam, is similar to that illustrated previously for the SH beam from set 1 (Figure 7.9(a)), and once again shows an increase in stiffness, peak strength and post-peak ductility. This apparent ‘enhancement’ of the post-healed beam properties, when compared to the virgin properties, is believed to be due to two reasons:

1. The very low viscosity cyanoacrylate is believed to not only flow onto the crack faces and to the crack tip under the influence of capillary forces, but is also believed to infiltrate the region of micro-cracks within the FPZ, behind the crack faces, thus

creating a cementitious-polymer composite, with improved mechanical properties, in the central region of the beam.

2. Since the loading arrangement employed in the current experimental series creates a peak bending moment at the specimen centre span, then the final macro crack created during the second loading cycle is forced to propagate through this mechanically improved zone, or deviate significantly around it.

It should be noted that the primary and secondary healing effects described above, for the two individual SH beams from the first two sets of experiments, have been observed repeatedly throughout the course of the experimental programme. This may be seen from the full experimental results presented in Appendix B.

7.4.2 Effect of reinforcement level

Three levels of beam reinforcement have been examined in the experimental programme, as detailed in Table 7.3. These include reinforcement configurations consisting of a single 3.15mm bar, two 3.15mm bars, and a single 6.7mm diameter bar. The levels of reinforcement provided by each of these configurations are 0.16%, 0.32% and 0.72%, respectively.

The force-CMOD response for a typical SH beam from experimental sets 2, 3 and 4 are given in Figure 7.11. It can be seen from this figure that the strength of the control beams, after initial cracking of the mortar and glass tubes, increases with an increase in the percentage of reinforcement, as expected.

The main effect that the level of reinforcement has on the self-healing behaviour is evident in the gradient of the primary healing response that occurs immediately after the fracture of the glass tubes. It can be seen from Figure 7.11 that as the level of reinforcement increases so does the gradient of the primary healing line. The reason for this trend is believed to be due to the rate at which the macro crack opens. For higher levels of reinforcement the rate of crack opening is slower, and therefore, the adhesive, which has flowed into the crack, and is in the process of hardening, is effectively being loaded at a slower rate. When an adhesive layer is being loaded in tension at the same time as it's curing, it is to be expected that a slower loading rate will result in a stiffer response, since the bonds have more time to form.

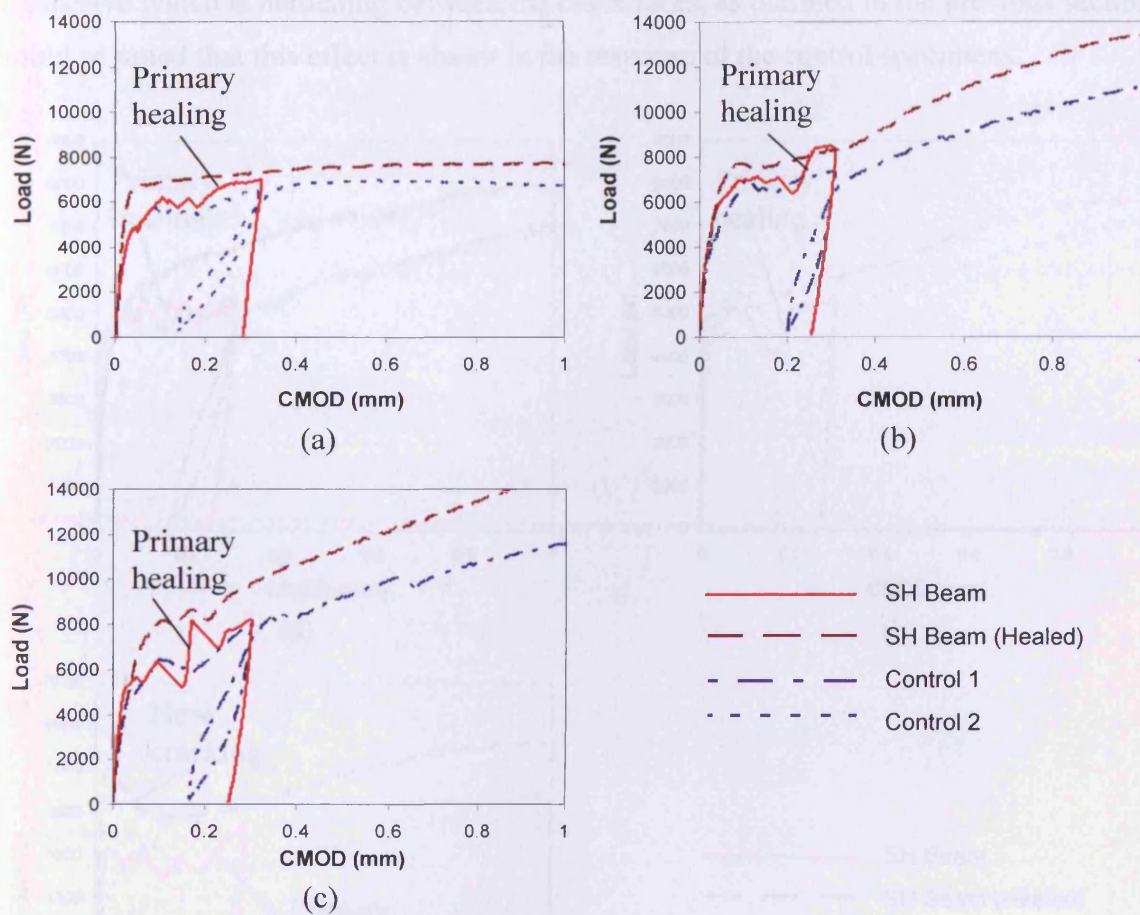


Figure 7.11. Load-CMOD response for (a) SH beam 1 from set 2, with a single 3.15mm reinforcing bar, (b) SH beam 3 from set 1, with two 3.15mm reinforcing bars, and (c) SH beam 4 from set 4, with a single 6.7mm reinforcing bar

7.4.3 Effect of loading rate

The effect of the stroke loading rate has been examined for lightly reinforced prismatic beams in experimental set 6. Three different rates of loading have been examined, each of which are four times faster than the previous loading rate. The rates, which were used for both the first and second loading cycles, are 0.00075mm/s, 0.003mm/s and 0.012mm/s.

The force-CMOD response for three typical SH beams, from experimental set 6, tested at different loading rates, are presented in Figure 7.12. It may be seen from this figure that the main effect of the loading rate on the self-healing behaviour is once again evident in the gradient of the primary healing response. As the monotonic rate of stroke controlled loading is increased, the stiffness of the primary healing response decreases. This trend is again believed to be due to the effect that the loading rate has on the stiffness response of the layer

of adhesive which is hardening between the crack faces, as outlined in the previous section. It should be noted that this effect is absent in the response of the control specimens.

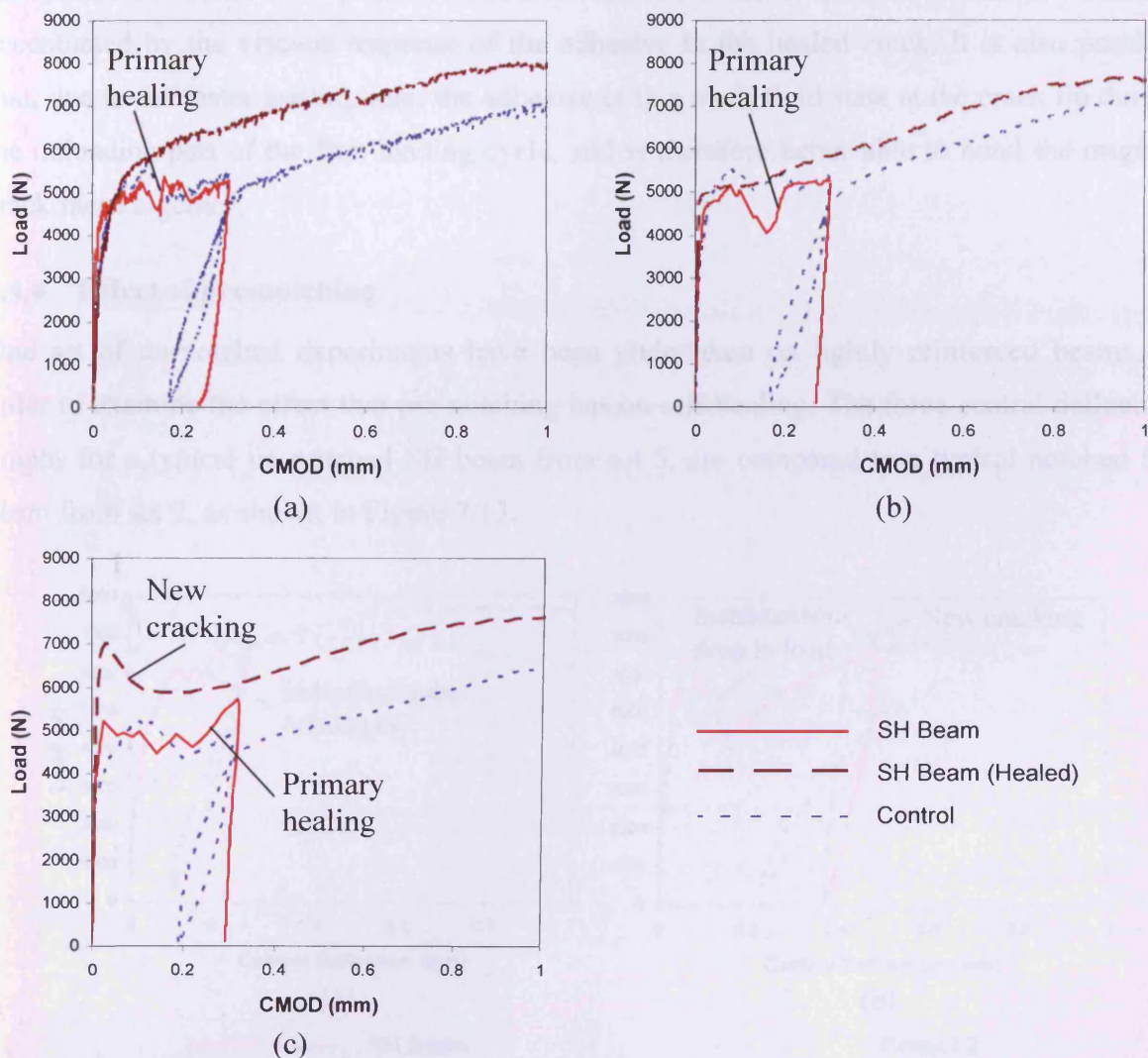


Figure 7.12. Load-CMOD response for (a) SH beam 1 from set 6, tested at a rate of 0.00075mm/s, (b) SH beam 4 from set 6, tested at a rate of 0.003mm/s, and (c) SH beam 7 from set 6, tested at a rate of 0.012mm/s.

The second loading cycle response of the highest loading rate specimen (Figure 7.12(c)) also shows a loading rate effect on the secondary healing behaviour. The stiffness, peak and post-peak ductility of the 'healed' response of the SH beam is greater than the virgin response of the control specimen, as described in section 7.4.1. However, in addition, there is a significant drop in the peak strength, from 7kN to 6kN, which is further evidence of new crack formation. The reason for the significantly higher peak and subsequent drop in strength is believed to be due to the higher loading rate that SH beam 7 was tested at, since this response is reminiscent of the increase in tensile strength seen in standard concrete tests conducted at

increased strain rates. It should be noted, however, that the control beam response in Figure 7.12(c) does not show the same strain rate effect, despite being subject to the same loading rate as the SH beam. It is possible, therefore that the strain rate effect for the SH beam is accentuated by the viscous response of the adhesive in the healed crack. It is also possible that, due to the faster loading rate, the adhesive is in a more fluid state at the crack tip during the unloading part of the first loading cycle, and is therefore better able to bond the original crack faces together.

7.4.4 Effect of pre-notching

One set of un-notched experiments have been undertaken on lightly reinforced beams, in order to examine the effect that pre-notching has on self-healing. The force-central deflection graphs for a typical un-notched SH beam from set 5, are compared to a typical notched SH beam from set 2, as shown in Figure 7.13.

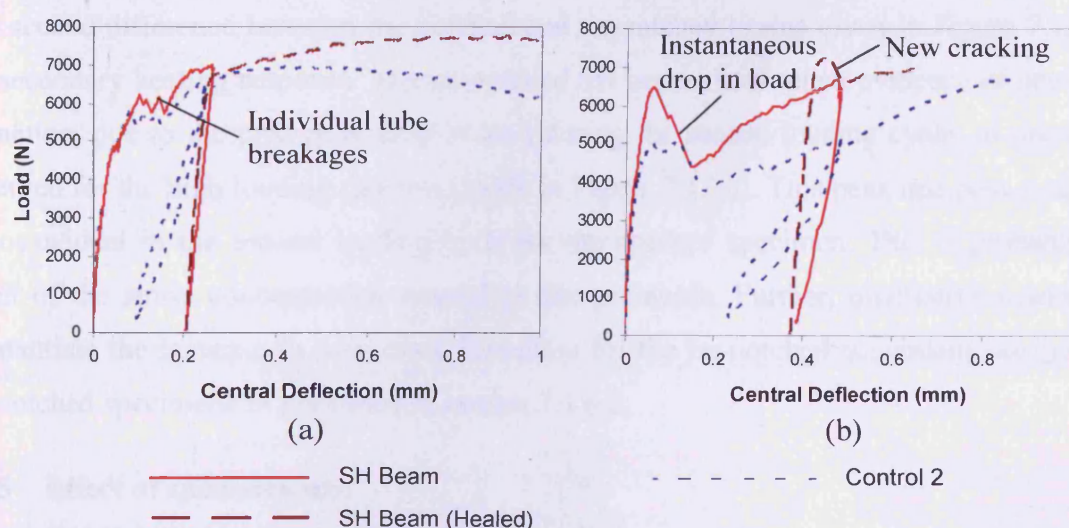


Figure 7.13. Load-central deflection response, including permanent set, for (a) Notched SH beam 1 from set 2, and (b) Un-notched SH beam 1 from set 5.

Figure 7.13 illustrates two distinct differences in the mechanical response of the notched and un-notched beams. The first difference is in the initial post-peak response of both the control and the SH beams. It can be seen that the immediate post-peak drop in strength is far greater for the un-notched specimens than for the notched specimens. This is because the 5mm pre-notch not only reduces the amount of material below the reinforcement level, but also acts as a crack initiator. The stress concentration created by the notch therefore results in an earlier onset of cracking, which is evident in the greater pre-peak non-linearity, for both the SH beam and Control beam, in Figure 7.13(a).

Of greater interest, however, is the effect that the more energetic crack propagation, in the un-notched beams, has on the fracture of the four capillary tubes. In Figure 7.13(b), the large post-peak drop of approximately 2kN occurs almost instantaneously due to the simultaneous rupture of all four capillary tubes, whereas in Figure 7.13(a) the tubes break individually, thereby producing a ‘saw tooth’ response. The net effect of this is that at the point of first glue release into the crack plane, the central deflection of the un-notched beam is approximately 0.15mm, compared to 0.1mm for the notched SH beam. Since the CMOD responses for all experiments closely follow the central deflection response (see Appendix B), then the crack width will also be greater for the un-notched specimen compared to the notched specimen. The smaller crack width at first tube breakage and the slower crack opening response, which in turn results in a longer primary healing period, are therefore believed to be the main reasons for the increased primary healing behaviour of the notched beam compared to the un-notched beam.

The second difference between the notched and un-notched beams given in Figure 7.13 is in the secondary healing response. The un-notched SH beam shows clear evidence of new crack formation, due to the post-peak drop in load during the second loading cycle, as previously observed for the high loading rate test shown in Figure 7.12(c). This peak and post-peak drop is not evident in the second loading cycle for the notched specimen. This is probably as a result of the stress concentration created by the pre-notch. Further, qualitative evidence to substantiate the increase in new crack formation for the un-notched specimens compared to the notched specimens is presented in section 7.4.6.2.

7.4.5 Effect of specimen age

As detailed in Table 7.3, four of the experimental sets (sets 1, 2, 3 and 5) have been tested at 28 days, whilst the remainder (sets 4 and 6) have been tested at an age of 70 days. In order to ascertain whether the age of the specimen has an effect on its autonomic healing ability, SH beams 4, 5 and 6 from experimental set 6 may be compared with the SH beams from set 2.

It has been concluded, from comparison of these experimental results, that there are no clear discernable trend differences that emerge in the self-healing response, due to the age of the mortar beams. This is not surprising since, unlike autogenous healing which is intrinsically linked to the age of the specimen (Schlangen et al., 2006), the efficacy of the autonomic healing response is dependent primarily on the viscosity and curing abilities of the adhesive, and the quality of the delivery system.

7.4.6 Qualitative results

In addition to the quantitative trends presented above there are also many qualitative observations which serve to demonstrate the occurrence of the self-healing process.

7.4.6.1 Glue flow

During all experiments, on both the self-healing and control beams, the distinct sound of capillary tube fracture was noted. The individual fracture of the four tubes was observed to coincide with an instantaneous drop in strength of the specimen, as previously discussed. For the control specimens the sound of tube fracture was followed within 20-30 seconds by a distinct flow of tracing die to the side faces of the beams, as shown in Figure 7.14(a). This is a clear indication of the capillary suction effect caused by the propagating crack.



(a)



(b)

Figure 7.14. (a) Ink migration during testing of lightly reinforced, notched control specimen (b) Glue flow during testing of lightly reinforced, notched self-healing specimen

The migration of cyanoacrylate during loading of the self-healing specimens is less pronounced than the ink tracing die, due to its colourless appearance and higher viscosity. Figure 7.14(b) clearly indicates, however, that the adhesive has flowed from the capillary tubes and has entered the crack plane. It should be noted that despite there being a large amount of adhesive available within the reservoir (approximately 10ml), only about 0.1-0.3ml was initially observed to flow into the crack, following the fracture of the capillary tubes. This value was estimated from the observed glue level drop in the curved supply tubes shown in Figure 7.6. A further drop in the glue level was then generally recorded as the crack widened and surplus adhesive was observed to flow from the underside of the beam in the locality of the notch, as shown in Figure 7.14(b).

It should also be noted that despite the rapid curing abilities of cyanoacrylate, when deposited in thin layers which are in contact with moisture and oxygen, when stored in larger volumes

its curing rate is significantly slower. The cyanoacrylate which remained in the supply tubes following testing was observed to remain in liquid form for over a week, despite being open to the atmosphere. As a result, many of the specimens released additional adhesive during the second loading cycle. This observation suggests that it may be possible to capture a tertiary healing effect from the fixed supply system used in these experiments, although this has not been investigated in the current work.

Visual confirmation of glue flow into the crack plane is illustrated for the case of two SH beams from the first set of experiments in Figure 7.15. Similar glue migration patterns were obtained for all of the self-healing beams tested. It can be seen from Figure 7.15 that the extent of the spread of the adhesive is linked to the effectiveness of the mechanical healing results obtained from the three-point bend tests. SH beam 1 exhibited very little self-healing due to specific problems with its supply system, and as a result the adhesive capillary rise appears to have been in the order of only 10mm. Conversely, SH beam 4, which exhibited increased stiffness, peak strength, and ductility (Figure 7.9) shows a significantly greater adhesive capillary rise, which is in the order of 30mm.

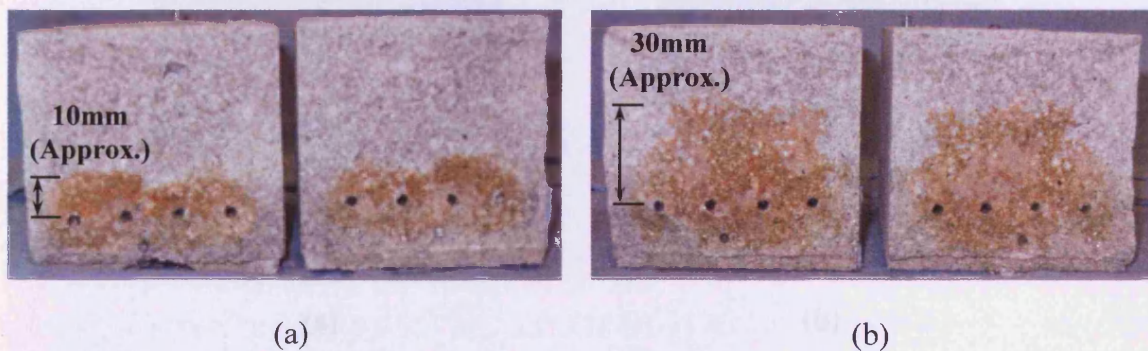


Figure 7.15. Glue migration and effective zone of healing for experimental set 1 on notched, lightly reinforced mortar beams (a) SH beam 1, and (b) SH beam 4

It should be noted that the dark orange discoloration shown in Figure 7.15 is the actual cured colour of the cyanoacrylate found on the final crack face, and has not been dyed or digitally enhanced in any form. Preliminary investigations undertaken on Rite-Lok EC5, as described in section 7.2.1, found the adhesive to dry in a colourless layer on both cast (smooth) and cracked (rough) surfaces of mortar specimens. In addition, the adhesive was not observed to visibly react in any way with the constituents of the beam, namely; sand, cement, water, steel or glass. The discolouration is therefore believed to arise when the layer of adhesive is mechanically loaded, and therefore strained, as the original crack surfaces begin to peel apart. This theory has not been specifically tested in the current work, however.

The staining pattern of the ink tracing die from the control specimens offers a far less realistic indication as to the area infiltrated by the adhesive during healing, since not only is the viscosity less than that of the adhesive, it is also readily absorbed into the mortar and produces only a light staining effect. It should be noted that as a result of the limited benefit that the ink tracing die was deemed to offer, the capillary tubes in the control specimens for experimental sets 2-6 were left empty during testing.

7.4.6.2 New crack formation

Further qualitative evidence of the efficacy of the autonomic healing process is given by the clear indication of new crack formation for both notched and un-notched specimens. Figure 7.16 shows the original and final crack patterns on the side face of two notched SH beams from the first set of experiments.

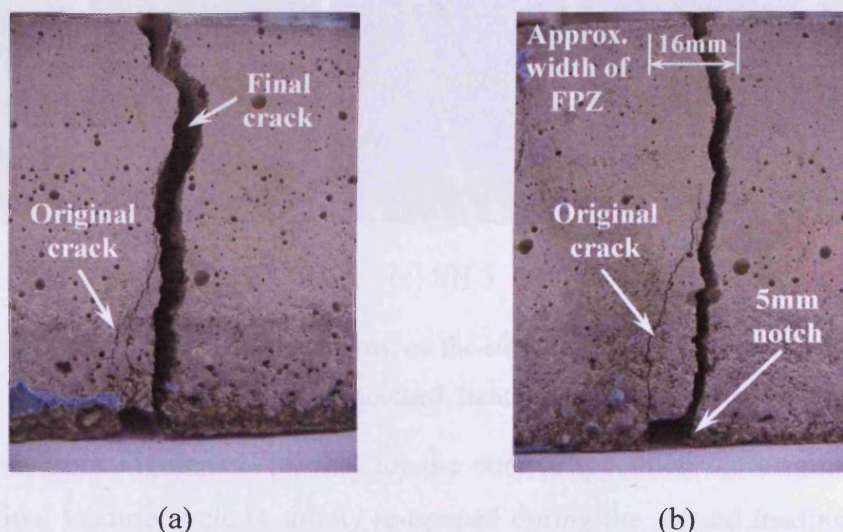


Figure 7.16. Original and final crack patterns on the side face of (a) SH beam 2, and (b) SH beam 3, for the first experimental round on notched, lightly reinforced beams

It is clear from Figure 7.16 that despite the stress concentration created by the notch, the final cracking path for the self-healing specimens is different from the original macro-crack created during the first loading cycle. This new crack formation was not observed to occur in either of the control specimens, and therefore, this is clear evidence of the effectiveness of the bonding capabilities of the ethyl cyanoacrylate, when used within a mortar matrix.

These new crack formations also explain why there appear to be areas towards the boundaries of the final fracture surfaces, shown in Figure 7.15, that have very limited adhesive coverage. This is somewhat misleading, since on closer inspection it may be seen that new crack

surfaces are formed during the second loading cycle, and therefore any adhesive released into the original crack would not necessarily be evident on the final fracture surface.

New crack formations were also observed for the fifth set of experiments on un-notched, lightly reinforced prismatic beams. The original and final fracture patterns for all four SH beams, created during the first and second cycles of loading, respectively, are shown in Figure 7.17. It should be noted that the photographs have been taken at an angle of 45° and therefore show both the side and underside faces of the beams. The original fracture patterns, created during the first loading cycle, have also been highlighted in red for the purpose of clarity.

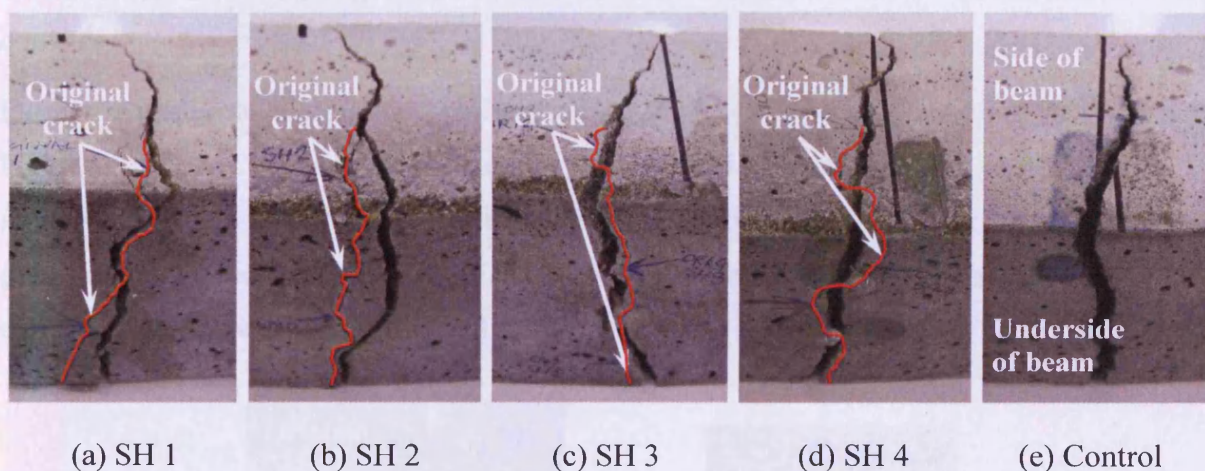


Figure 7.17. Original and final crack patterns, on the side and underside faces, from the fifth set of experiments on un-notched, lightly reinforced beams.

It may be seen from Figure 7.17(e) that for the control specimen the original crack formed during the initial loading cycle is simply re-opened during the second loading cycle, without the occurrence of any additional cracking.

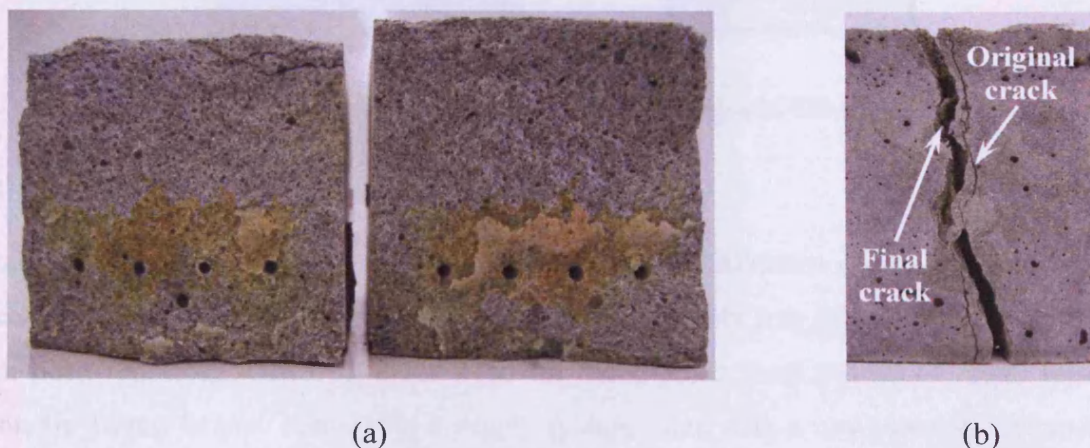


Figure 7.18. SH beam 3 from set 5: (a) Glue migration and effective zone of healing, and; (b) Original and final crack patterns on underside of beam

The spread of adhesive on the original crack face has also been observed for the un-notched specimens, as illustrated for SH beam 3 in Figure 7.18(a). The capillary rise of the adhesive appears to be approximately 20mm, and less extensive than that observed for the first set of experiments on notched beams (Figure 7.15(b)). It should be noted, however, that due to the absence of the stress concentration caused by the pre-sawn notch, the degree of new crack formation is far higher for the un-notched specimens than for the notched specimens. The original and final crack patterns on the underneath of all the beams are completely different, as illustrated in Figure 7.17 and Figure 7.18(b). As a result of this, the glue migration pattern shown in Figure 7.18(a) only reflects the areas of the original and final fracture planes which coincide.

Further evidence of the bonding abilities of the Rite-Lok EC5 cyanoacrylate are shown in Figure 7.19. It can be seen that the surplus glue released from the delivery system during the first loading cycle has effectively bridged the final through crack. In addition, evidence of glue stringing, which is created when the two crack surface are separated during the adhesive curing period, has also been identified.

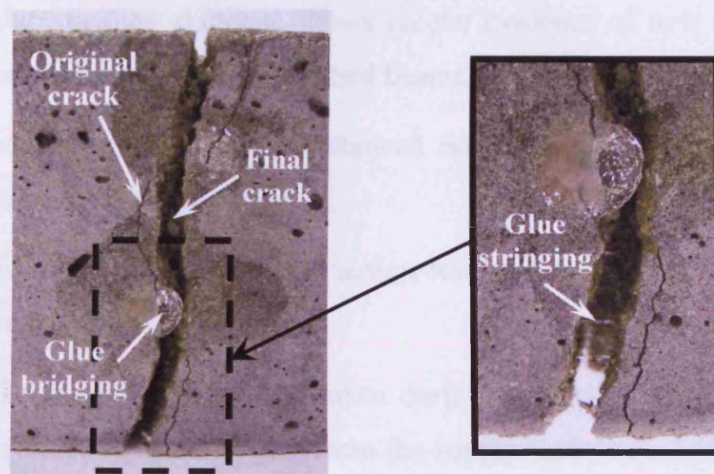


Figure 7.19. Glue bridging and stringing on the underside of SH beam 4 from set 5

7.5 Conclusions and future work

Details of the preliminary and final experimental work undertaken on the autonomic healing of cementitious materials has been given in this chapter. Six sets of self-healing experiments have been reported, which have involved the three-point bend testing of small reinforced prismatic mortar beams, containing a supply system filled with a low viscosity cyanoacrylate healing agent.

Force-CMOD and force-central deflection results from these experiments have shown that two stages of healing have been observed to occur. A primary healing response occurs during the first loading cycle after the glass capillary supply tubes have fractured, and a secondary healing response occurs during the second loading cycle, after the adhesive has fully cured.

The effect of various parameters on the efficacy of the SH response have also been investigated as part of the experimental programme, including reinforcement level, loading rate, pre-notching, and the age of the specimen. The following trends and features have been observed to occur:

1. The stiffness of the primary healing response is observed to increase with increasing percentage of reinforcement, due to the slower crack opening rate;
2. The stiffness of the primary healing response is observed to decrease with increasing loading rate, due to the faster crack opening rate, relative to the glue set time;
3. The initial post-peak drop in strength is greater for the un-notched beams compared to the notched beams, and the stiffness of the primary healing response is therefore less;
4. The secondary healing response shows greater evidence of new cracking for the un-notched beams compared to the notched beams, and;
5. The age of the mortar specimens showed no discernable effect on the nature and efficacy of the self-healing response.

The quantitative evidence of a self-healing action was also reinforced by several qualitative observations. These include:

1. Distinct cracking of the capillary tubes during the first loading cycle, followed by immediate release of healing agent from the supply reservoir;
2. Evidence of the capillary suction effect, resulting in ink and glue flow to the side faces of the beams;
3. Glue migration patterns on the final cracked faces of the self-healing beams;
4. Evidence of new crack formation, created during the second loading cycle, for both notched and un-notched specimens, and;
5. Evidence of adhesive bonding resulting in crack bridging and stringing.

It may be concluded, therefore, from both the quantitative and qualitative observations noted above, that the primary objectives of the experimental work, as outlined in the introduction

(section 7.1) have been met, in addition to the overall aim of providing quantitative data for the development of a numerical model.

The ability of an externally supplied low viscosity cyanoacrylate, to heal, and, in certain circumstances enhance the strength of the cementitious material, makes it an interesting technique for possible future commercial exploitation. The capacity of the system to offer rapid primary healing, in addition to long term secondary material healing, greatly increases its flexibility, and makes it akin to the far more sophisticated biological healing systems such as blood clotting and scar tissue creation.

The efficacy of the autonomic healing system presented in this chapter has been examined solely in terms of the mechanical properties, such as strength and stiffness, of the mortar beams pre and post-healing. The durability issues of concrete, as presented in Chapter 1, are primarily related to increased permeability caused by various microcracking processes. Whilst the mechanical self-healing demonstrated in this chapter is also likely to decrease the permeability of the specimens, and therefore improve their durability, this needs to be confirmed in future work.

Chapter 8

Modelling of self-healing cementitious materials

8.1 Introduction

The overall mechanical response observed during the self-healing experiments described in Chapter 7, is a complex combination of individual physical and chemical processes. The migration of glue from a cracked supply tube is dependent not only on the crack width opening, which is constantly growing for a monotonically increasing stroke displacement controlled test, but also on the viscosity of the glue, which is also increasing as the glue begins to cure. The speed of the curing process itself is in turn dependent not only on the type of adhesive, but on the thickness of the adhesive layer, the moisture content and alkalinity of the mortar, and the ambient temperature at which healing occurs.

This complex physical-chemical process may be captured through the development of a non-linear coupled phenomenological based constitutive model. Alternatively, the main physical processes may be captured in a simplified manner using a physically based discrete modelling method (Joseph et al., 2008a and 2008b). It is the latter approach that has been explored in this chapter.

The lattice beam modelling method, as outlined in Chapter 3, has therefore been used in this chapter to model the autonomic healing process that has been quantified in the experimental work presented in Chapter 7. The preliminary modelling work presented here is therefore aimed at investigating whether or not the lattice modelling method is capable of capturing the main mechanical behaviour observed during the self-healing experiments.

8.2 Lattice modelling of the self-healing process

The lattice modelling method used in this chapter to model the autonomic healing process is essentially the same as that described in Chapter 3 with some adjustments made to the algorithm to allow for the implementation of the healing process.

Since cracks are modelled discretely in the lattice approach, crack openings are therefore determined automatically. For a notched beam tested under three-point loading the CMOD may therefore be obtained directly from the model. The value of the CMOD can therefore be used as the criterion for governing the breakage of the glass capillary tubes, and hence the onset of healing. Once the capillary tubes have broken, it is assumed that the flow of the adhesive is controlled by the varying aperture of the crack at that location.

Glue setting may then be modelled in a staged manner whereby broken beams are replaced with ‘healed’ beams at predefined CMOD limits. The height of glue rise, and therefore, determination of which broken beams are to be healed, is obtained from the non-uniform capillary flow theory described in section 8.2.3. The healed beams are considered to be composite beams comprising part mortar and part glue. The axial stiffness of these composite beams is therefore determined from the axial stiffness of the mortar part and the glue part combined in series. The length of the glue part is determined by the width of the opening at the beam location just prior to healing.

8.2.1 Healing algorithm in 1D

The numerical algorithm, as outlined above, is illustrated schematically in Figure 8.1 for the simple case of a 1D parallel bar model comprising two elements supported between two rigid bar supports. The support bar on the left is fully fixed and the one on the right is only allowed to translate in the x-direction. The elements have identical stiffness ($k_1=k_2$), but the tensile strength of element 1 is less than element 2 ($f_{t1}<f_{t2}$).

The system is initially subject to a prescribed displacement (u_p), and resists this displacement with a stiffness, k ($k=k_1+k_2$), as illustrated by line (i) in Figure 8.1(b). When the stress in element 1 reaches its tensile strength (f_{t1}), element 1 breaks and its stiffness is removed from the system. The difference in the distance between the supports and the unstrained length of element 1 is defined as the crack mouth opening displacement (CMOD) for this simple 1D model.

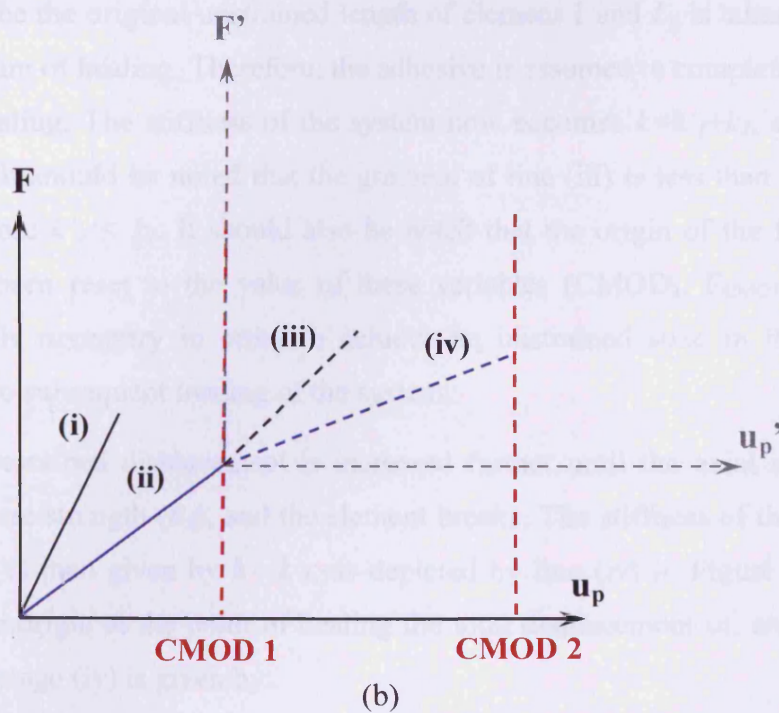
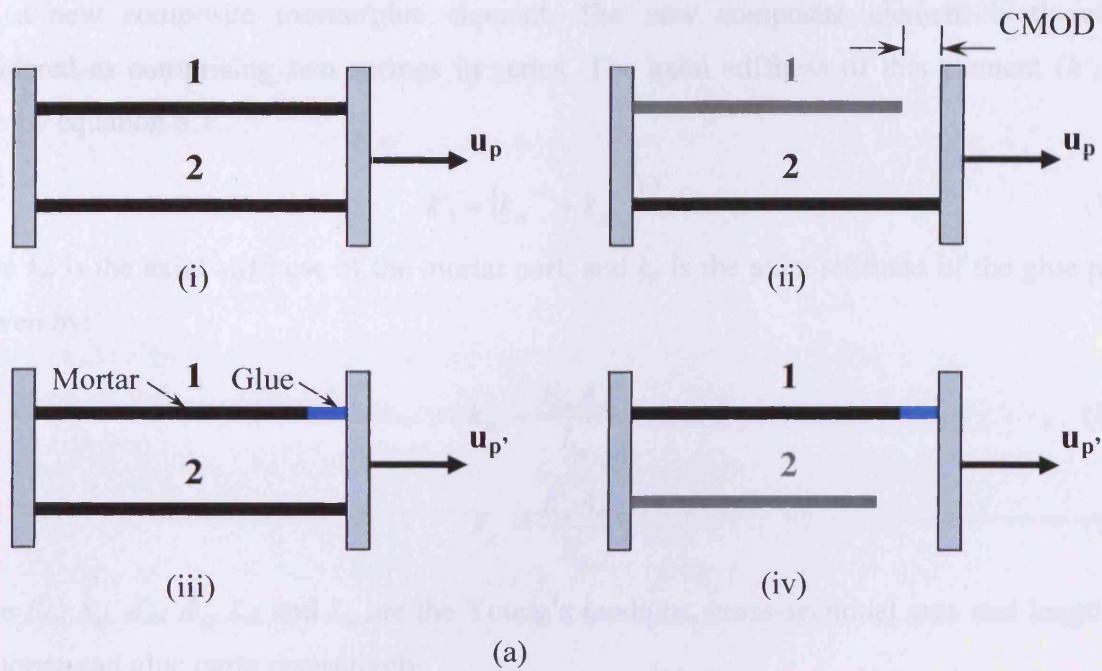


Figure 8.1. Schematic illustration of (a) healing process in a 1D parallel bar model, and (b) mechanical response of model pre- and post-healing

As the prescribed displacement (u_p) increases further, the CMOD increases by the same amount. The stiffness of the system at this point is $k=k_2$ as represented by the gradient of line (ii) in Figure 8.1(b). When the value of the CMOD reaches the predefined healing point (CMOD 1 in Figure 8.1(b)) element 1 is healed. This involves replacement of the element

with a new composite mortar/glue element. The new composite element is therefore considered as comprising two springs in series. The axial stiffness of this element (k'_1) is given by equation 8.1.

$$k'_1 = (k_m^{-1} + k_g^{-1})^{-1} \quad (8.1)$$

where k_m is the axial stiffness of the mortar part, and k_g is the axial stiffness of the glue part, as given by:

$$k_m = \frac{E_m A_m}{L_m} \quad (8.2)$$

And:

$$k_g = \frac{E_g A_g}{L_g} \quad (8.3)$$

where E_m , E_g , A_m , A_g , L_m and L_g are the Young's modulus, cross-sectional area and length of the mortar and glue parts respectively.

L_m is taken to be the original unstrained length of element 1 and L_g is taken to be the CMOD value at the point of healing. Therefore, the adhesive is assumed to completely fill the crack at the time of healing. The stiffness of the system now becomes $k=k'_1+k_2$, as given by (iii) in Figure 8.1(b). It should be noted that the gradient of line (iii) is less than line (i) since $E_g < E_m$, and therefore $k'_1 < k_1$. It should also be noted that the origin of the force-displacement response has been reset to the value of these variables ($CMOD_1$, F_{CMOD_1}) at the point of healing. This is necessary in order to achieve an unstrained state in the new composite element prior to subsequent loading of the system.

Finally, the prescribed displacement is increased further until the axial stress in element 2 equals the failure strength (f_{t2}), and the element breaks. The stiffness of the system from this point onwards is then given by $k= k'_1$, as depicted by line (iv) in Figure 8.1(b). Due to the resetting of the origin at the point of healing the total displacement of, and force within, the system during stage (iv) is given by:

$$u_p = CMOD_1 + u_p' \quad (8.4)$$

And:

$$F = F_{CMOD_1} + F' \quad (8.5)$$

8.2.2 Extension of healing algorithm to 2D

The 1D healing theory, as explained above, may be extended for use in a 2D lattice simulation. In this respect, element 1 can be considered to represent the group of beams that initially break and are subsequently healed when the CMOD reaches the predefined healing

point. Element 2 can then be considered to represent the group of elements that break after healing, when the specimen is tested to failure.

The point at which healing occurs (CMOD 1) takes on a physical meaning in the two dimensional case. In the 2D model CMOD 1 is the value of the CMOD when the capillary tubes are said to have broken and healing is considered to have begun. It should be noted that CMOD 1 is a predefined value and is based on the average CMOD value at which the capillary tubes are heard to break during the experiments. At the point at which healing is considered to occur and the selected broken beams are healed, the value of the opening at the location of the broken beams varies depending on the location of the beam. The width of the opening, which is also the length of the glue segment in the composite healed element, is therefore defined as the difference between the extended length of the original beam (assuming that it never broke) and the length of the original unstressed beam element. The length of the glue part (L_g) in the composite elements is therefore far less for elements healed at the top of the crack during stage (viii) (Figure 8.1(b)) than at the bottom of the crack just above the notch. The composite healed elements at the bottom of the crack are therefore less stiff than those at the top of the crack. This is because a greater L_g results in lower stiffness for the glue segment k_g and for the beam as a whole k_l' , as shown by equations 8.1 and 8.3.

It should be noted that the 1D methodology described above when applied to a 2D lattice simulation can be extended to allow for multiple healing events at a range of predefined CMOD values. The nodal displacements would have to be zeroed at every healing point in order to ensure that the newly healed elements are unstrained at each point of healing. The nodal displacement values and system forces recorded prior to each healing point could then be summed, as shown for the 1D case in equations 8.4 and 8.5, to obtain the overall mechanical response of the system. In essence this procedure means that the overall non-linear mechanical response of the system can be modelled as a series of linear simulations.

8.2.3 Glue flow theory

When the borosilicate glass tubes crack the adhesive is free to flow into the crack. This occurs in a downward and upward direction. In both the downward and upward directions the capillary attractive force of the narrow crack draws the adhesive out of the tubes. In the downward direction this is assisted by gravity, and conversely in the upward direction gravity resists the flow of adhesive. The main forces acting on the adhesive following the cracking of the tubes are illustrated in Figure 7.5. For the purpose of this model the adhesive is assumed

to migrate fully in the downward direction, and therefore all fractured lattice elements situated below the level of the tubes are automatically healed. This assumption is consistent with experimental evidence of free glue flow out of the bottom of the beam shortly following the cracking of the tubes (Figure 7.14(b)).

In order to model the flow of adhesive in the upward direction, however, the balance of capillary and gravitational effects must be considered. The approach utilised within this model is therefore based on capillary flow through non-uniform sections (Young, 2004) and is similar to that employed by Roels et al. (2003) for modelling moisture flow in discrete cracks in building materials. This involves using a 1D moving front model in which both capillary and gravity forces are considered. The governing equations are Darcy's equation of flow and mass continuity.

The two main crack faces (Figure 8.2) which are opening up about a hinge at the top of the mortar beam, when under three-point loading, are simply considered in this model as plates with a linearly varying spacing.

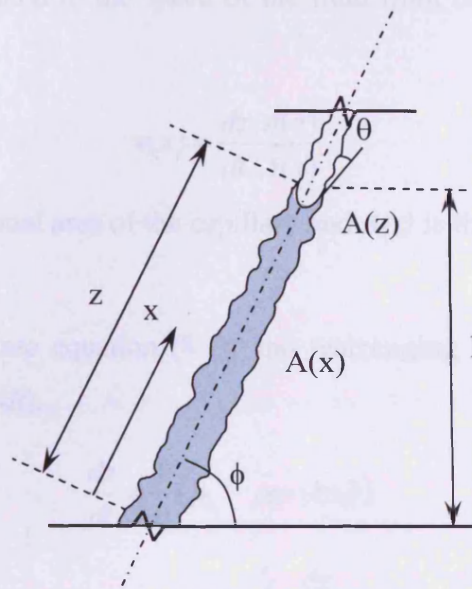


Figure 8.2. Illustration of the flow of adhesive in a crack

The velocity of the viscous flow $v(x)$ inside a capillary tube or between two plates can be given by the basic 'Darcy like' flow equation:

$$v(x) = -\frac{k}{\mu} \left(\frac{dP}{dx} + \rho g \sin \phi \right) \quad (8.6)$$

where μ is the viscosity, P the pressure, g the gravity, ϕ the inclination angle of the capillary/crack (Figure 8.2) and ρ and k are the density and permeability of the adhesive respectively.

Rearranging equation (8.6) and integrating from the reservoir to the meniscus interface gives:

$$\mu \int_0^z \frac{v}{k} dx = p_c - \rho g z \sin \phi \quad (8.7)$$

where z is the distance of the fluid front from the reservoir and p_c is the capillary potential. The capillary potential for a plane opening of width b is given by:

$$p_c = \frac{2\gamma \cos \theta}{b} \quad (8.8)$$

where θ is the angle that the meniscus forms with the wall of the opening (or face of the crack), as shown in Figure 8.2, and γ is the surface tension of the fluid. For a non-uniform cross-section ($b=b(x)$) the capillary potential depends on the position of the interface.

The velocity can also be related to the speed of the fluid front based on the conservation of mass:

$$v(x) = \frac{dz}{dt} \frac{A(z)}{A(x)} \quad (8.9)$$

where $A(x)$ is the cross-sectional area of the capillary and $A(z)$ is the cross-sectional area at the meniscus interface.

Substituting equation (8.9) into equation (8.7), and rearranging gives an expression for the flow velocity at the front (dz/dt):

$$\frac{dz}{dt} = \frac{1}{\eta} (p_c - \rho g z \sin \phi) \quad (8.10)$$

where:

$$\eta = \mu A(z) \int_0^z \frac{dx}{k A(x)} \quad (8.11)$$

From equation (8.10) it can be seen that the flow velocity at the front is zero when the capillary potential drawing the fluid up the crack is matched by the weight of the fluid acting downwards. Therefore, by placing $dz/dt=0$ in equation (8.10) and substituting the expression given in equation (8.8) for p_c , the rise height h may be defined as:

$$h = z \sin \phi = \frac{2\gamma \cos \theta}{b \rho g} \quad (8.12)$$

The theory given above has been implemented within a relatively simple time-stepping algorithm for tapering cracks, as shown in Figure 8.3.

- Choose Δt
- Start with very small $z=z_0$
- Evaluate η
- $t = t + \Delta t$
- $\Delta z = \frac{\Delta t}{\eta} (p_c - \rho g z \sin \phi)$
- $z = z + \Delta z$
- If $\Delta z < tol$ exit, otherwise continue
- Repeat process with smaller Δt to ensure that the solution is time-step converged

Figure 8.3. Time-stepping algorithm to calculate z versus t

The algorithm has been evaluated in MathCAD, and rise height versus time graphs for two different crack openings have been calculated, as given in Figure 8.4.

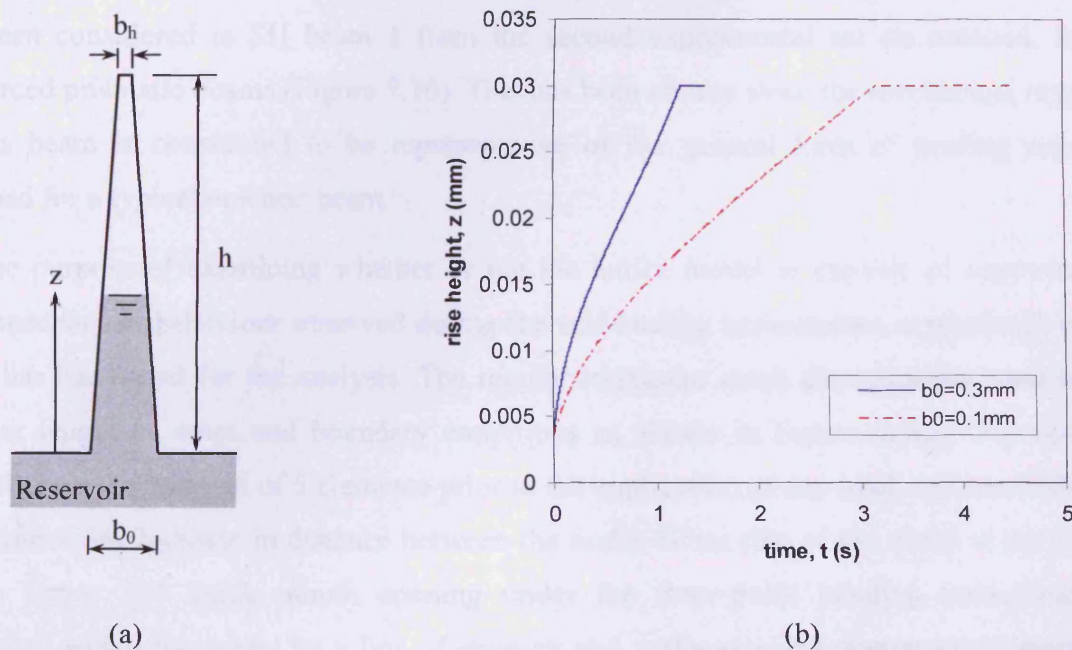


Figure 8.4. (a) Idealised vertical tapering crack, and (b) Rise height versus time for two different crack openings, b_0

The parameters used for the glue in the above calculation are viscosity, $\mu = 5 \text{ mPa.s}$, density, $\rho = 1060 \text{ kg/m}^3$, meniscus angle, $\theta = 0^\circ$ and surface tension, $\gamma = 0.033 \text{ N/m}$. The viscosity was obtained from the adhesive data sheet (Appendix A), and the surface tension was determined experimentally from measured glue rises in capillary tubes of known diameter. The maximum

experimentally observed crack height was 30mm above the level of the supply tubes, as illustrated in Figure 7.15(b). This was therefore taken to be the height of the cavity, h , in the above simulations. The crack opening at the top of the cavity, b_h , was assumed to be a nominal 0.01mm.

It can be seen from Figure 8.4(b) that for both sizes of crack opening ($b_0=0.1mm$ and $0.3mm$) the glue rises to the maximum rise height, h . More significantly, for both examples, this occurs within a period a few seconds. As a result of these findings, all of the broken beams in the lattice model, up to the total rise height, h , have been healed in an instantaneous manner, as described in the following section.

Finally, it should be noted that ‘sink’ terms, associated with glue going into the surrounding area (fpz), have been ignored in the current theory.

8.3 2-D modelling example

In this section a 2-D lattice simulation is used to model the self-healing response of a typical adhesive healed mortar beam, as described in Chapter 7. The specific experimental beam that has been considered is SH beam 1 from the second experimental set on notched, lightly reinforced prismatic beams (Figure 7.10). This has been chosen since the mechanical response of this beam is considered to be representative of the general form of healing response obtained for a typical notched beam.

For the purpose of examining whether or not the lattice model is capable of capturing the main mechanical behaviour observed during the self-healing experiments, a relatively coarse mesh has been used for the analysis. The regular triangular mesh discretisation used has an element length of 4mm and boundary conditions as shown in Figure 8.5(a). The notch is modelled via the removal of 5 elements prior to the application of any load, and the CMOD is measured as the increase in distance between the nodes either side of the notch at the bottom of the beam. The crack mouth opening under the three-point bending arrangement is controlled within the model by a line of stronger and stiffer steel reinforcement elements, as illustrated in Figure 8.5 (a). The strength and stiffness values for the mortar, steel and glue phases used in the model are given in Table 8.1.

Table 8.1. Material properties used in the numerical simulation

	Strength, f_t (MPa)	E-value (MPa)
Mortar	1 - 6.5	15800
Steel	597 (from Table 7.2)	205200
Glue	20	3500

The strength of the ethyl cyanoacrylate used in the model is taken from the RiteLok EC5 data sheet as given in appendix A. The Young's modulus of the adhesive is taken to be 3500 MPa, as suggested by Kim et al. (2006). The strength and stiffness values used for the steel have been obtained from tensile testing of the 3.15mm reinforcing bar used in the experiments, as described under section 7.2.4. The lattice beam analysis is a 2D plane stress simulation with a beam width of 1mm. Therefore, in order to account for the single 3.15mm diameter steel reinforcing bar used in the 75mm wide experimental beam, the steel lattice element cross-sectional area (A_s) has been reduced to 0.104mm^2 ($A_s = \pi(3.15/2)^2/75$). It should be noted that in reality this element is a composite element comprising part steel and part mortar (either side of the steel). Once the beam becomes cracked up to the level of the steel the stiffness of the mortar part is then lost and the stiffness of the element is based on the stiffness of the steel alone. Since consideration of the mortar part makes only a small difference to the initial stiffness of the beam, and also to maintain simplicity of the algorithm, the horizontal elements at the level of the steel have been considered to be steel only elements.

The E-value for the mortar phase has been estimated from three point bending fracture energy tests that were conducted on plain mortar beams cast from the same mortar mix used in the self-healing experiments. Based on the average central deflection of the fracture energy beams in the elastic region, the E-value of the mortar has been back calculated to be approximately 15,800 MPa as given in Table 8.1.

In order to capture the shape and tortuosity of the crack that propagates upwards from the notch, the central band of mortar elements are assigned randomly distributed strengths selected from a predefined strength range. The strength range used for the simulation presented in Figures 8.5 and 8.6 is 1 to 6.5 MPa. The width of this central band of mortar elements, whose strength is drawn from this range, has been set to 16mm, as illustrated in Figure 8.5(a). The remainder of the mortar elements are then set to elastic (i.e. very high failure strengths). The choice of the width of the central band is based on the estimated width of the fracture process zone (fpz) obtained from the experimental investigation, as illustrated

in Figure 7.16(b). This simplified method of introducing heterogeneity into the current model also allows for subsequent post-healed cracking to deviate away from the original crack, as observed experimentally in Figure 7.16(b).

Figure 8.5(b) illustrates the development of initial cracking, healing, and final crack formation of the three-point bend beam under the prescribed displacement (u_p), and the boundary conditions shown in Figure 8.5(a). The displacements shown in the meshes of Figure 8.5(b) have been scaled by a factor of 50 for the purpose of clarity.

Meshes (i) to (vii) illustrate the development of the macro crack which propagates from the notch upwards, to a distance of approximately 50mm above the base of the beam. At this point the value of the CMOD reaches 0.05mm and all of the previously broken mortar beams are healed and replaced with composite mortar/glue elements, as outlined previously in the description of the model algorithm. It should be noted that from Figure 8.6(a) the first capillary tube fractures in the experimental test at a CMOD of approximately 0.1mm. The healing in the model has, however, been initiated at a CMOD value of 0.05mm. This is due to the inability of the model to capture some of the non-linear processes which increase the ductility of the experimental response. These are discussed in more detail later in this section.

The healing in this simulation occurs instantaneously, in one stage, and is applied to all previously broken beams. The reason for the decision to heal instantaneously is based on the idealised glue rise calculations (section 8.2.3), and experimental evidence; in particular, the occurrence of ink staining very shortly (several seconds) after tube fracture (Figure 7.14(a)) and the rapid rate dependent primary healing effect observed in the SH experiments. This evidence indicates that the adhesive is not only drawn up the crack very quickly but also cures rapidly. The fixture time according to the RiteLok EC5 data sheet (Appendix A) is 5-15 seconds, however, this is likely to be further accelerated by the alkaline environment of the mortar and the presence of moisture. The decision to heal in one stage is justified by the large reservoir of adhesive that is provided by each and every one of the individual capillary tubes, and also the relatively short time period over which all four capillary tubes are heard to crack. Therefore, it is felt that there is a readily available and plentiful source of adhesive available at the crack faces within a few seconds of the first tube breaking. Finally, the justification for healing all of the broken beams shown in mesh (vii) (Figure 8.5(b)) is based upon the observed glue rise of approximately 30mm above the capillary tube level (50mm above the base of the beam), as shown in Figure 7.15(b).

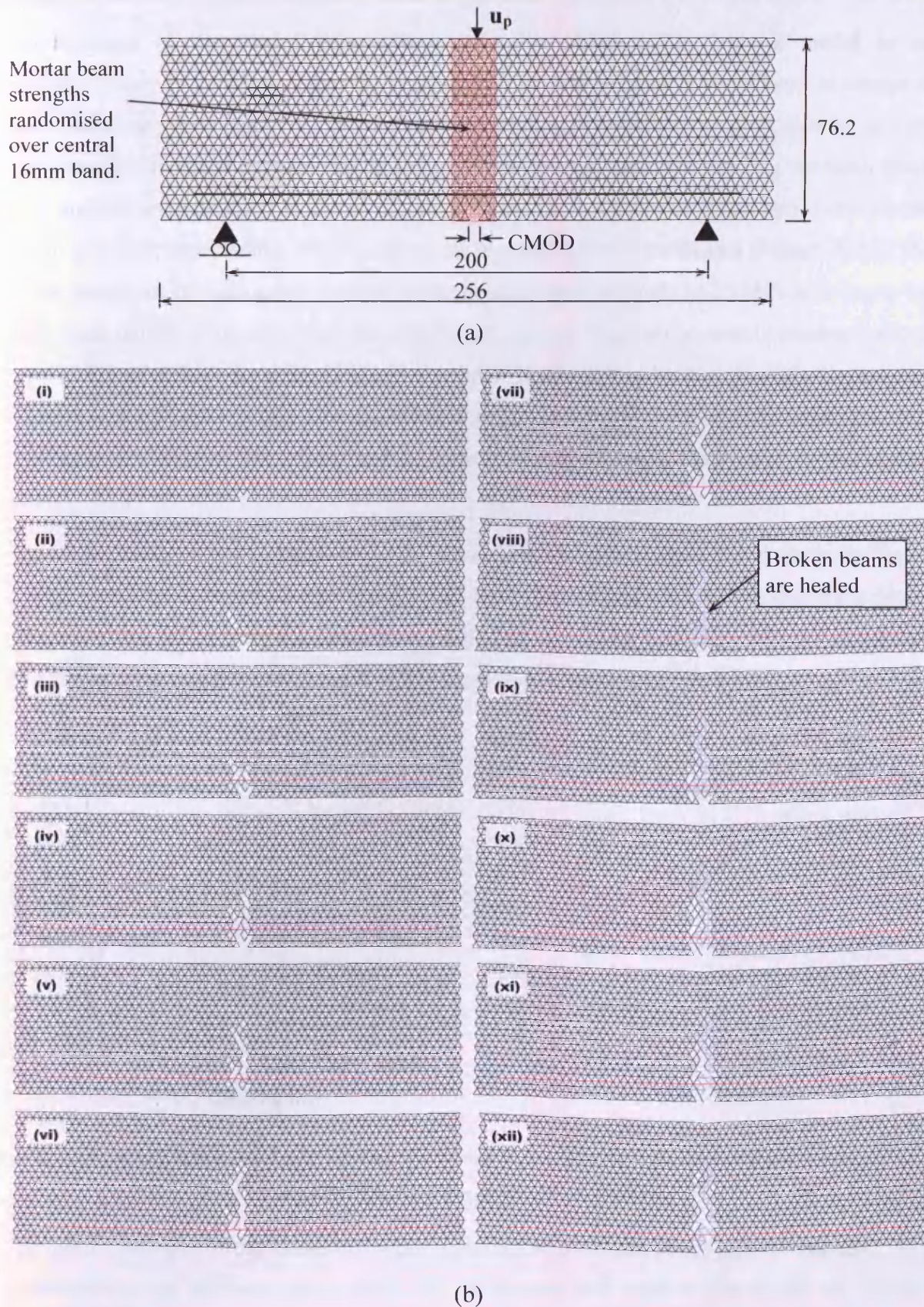


Figure 8.5. Coarse mesh discretisation of SH beam: (a) Boundary conditions, and; (b) Development of initial cracking, healing, and final crack formation.

The strength of the healed composite mortar/glue phase in the current model is set instantaneously to 20 MPa following healing. Whilst this element is considered to comprise two distinct separate parts for the purpose of modelling, in reality, the glue, due to its very low viscosity, is likely to permeate into the fracture process zone surrounding the main crack face. Indirect experimental evidence of this is found in the observed differences between the initial and final post-healing crack patterns on the side faces of the beams (Figure 7.16). The effect, therefore, of setting the strength of the healed beam elements to 20 MPa is to cause the final crack pattern to deviate from the initial crack pattern. This can be seen in meshes (viii) to (xii) in Figure 8.5(b). In mesh (xii) the specimen is effectively broken through. Its residual strength is due to the triangulation caused by the mortar hinge at the top of the beam, the steel reinforcement bridging the crack, and the elastic mortar elements either side of the central band.

The force-displacement response from the simulation shown in Figure 8.5 is given in Figure 8.6(b). Since the lattice beam analysis is a 2D plane stress simulation of unit depth the forces obtained from the simulation have been multiplied by 75 so that they may be compared directly with the experimental results of SH beam 1, as shown in Figure 8.6(a).

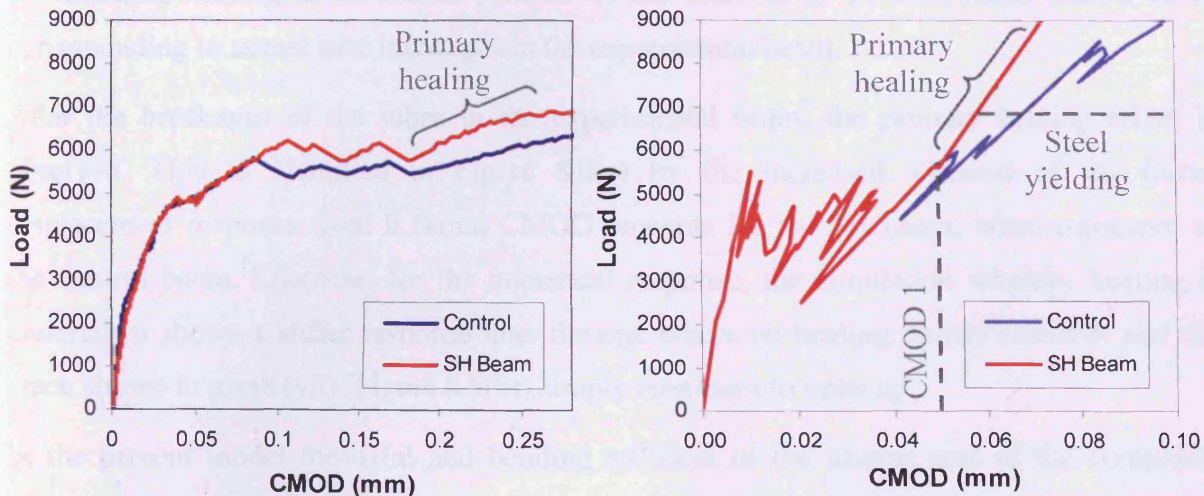


Figure 8.6. (a) Experimental and (b) Numerical load – CMOD response for a notched mortar beam subject to adhesive based autonomic healing

The initial stiffness of the lattice response agrees well with the experimental response. This confirms that the stiffness values used for the mortar and steel in the model are correct. Between 0mm and 0.05mm CMOD the response of the experimental beam shows a gradually increasing drop-off in stiffness as a result of initial micro-cracks which then coalesce to form a larger macrocrack. During the same period the numerical response is significantly stiffer

and oscillates considerably. The increased stiffness is largely due to the limits of the current model, in that the mortar elements outside of the central FPZ band are considered to be perfectly elastic. The model is therefore not able to adequately capture initial microcracking which serves to reduce the stiffness of the beam. The oscillatory response is due in the main to the very coarse mesh used in this analysis, and also the omission of any form of smoothing, as illustrated in Figure 3.1. The value of the load towards the end of this initial stage is nevertheless predicted correctly by the model at about 5kN.

The response of the experimental beam between 0.05mm and 0.18mm CMOD is largely due to the combined effect of the four borosilicate tubes and the steel reinforcement. The stiffness increase between 0.05mm and 0.1mm CMOD is due to the action of the steel and glass, and the discontinuities, signified by the drops in the force-displacement response, are a result of the individual tubes breaking. There is also possibly a degree of steel/mortar slip occurring during this period as a result of the smooth steel bars that were used as reinforcement in the experiment. Since, neither the non-linear effects of the glass tubes breaking nor the steel/mortar slip are included in the model it is not able to capture the additional ductility in the force-displacement response that these processes provide. For this reason the value chosen for initiating healing in the model (CMOD 1) has been set to 0.05mm rather than a value corresponding to actual tube breakages in the experimental beam.

After the breakages of the tubes in the experimental beam, the primary healing effect is observed. This is identified in Figure 8.6(a) by the increased stiffness of the force-displacement response from 0.18mm CMOD onwards for the SH beam, when compared to the control beam. Likewise, for the numerical response, the simulation whereby healing is undertaken shows a stiffer response than the one where no healing occurs (control) and the crack shown in mesh (vii) (Figure 8.5(b)) simply continues to open up.

In the present model the axial and bending stiffness of the mortar part of the composite mortar/glue element has been reduced to account for the loss of stiffness that will occur in this area due to microcracking of the mortar in the FPZ around the macro crack. The axial and bending stiffness of the mortar part have therefore been pre-multiplied by a microcracking factor, m . The axial stiffness of the mortar part for example, as given in equation 8.2, then becomes:

$$k_m' = mk_m = m \frac{E_m A_m}{L_m} \quad (8.13)$$

The value of m used in the simulation shown in Figure 8.6(b) is 0.1. It can be seen from this figure that the stiffness of the beam post-healing is significantly less than the initial stiffness of the beam pre-damage. However, this post-healing stiffness is also substantially greater than the primary healing response obtained in the experiments (even after allowing for the different x-axis scales in Figure 8.6). It is possible to further reduce the gradient of the primary healing response with an even lower value of m . However, it is felt that the main reasons for the overly high stiffness of the model at this point are the absence of the non-linear effects of steel yielding and slip, and the overestimate of the degree of healing.

Both the healing and control responses of Figure 8.6(a) begin to plateau out at approximately 7kN due to the yielding of the steel reinforcement. The numerical results shown in Figure 8.6(b), however, show a continuation in the load carrying capacity of the beam since the Young's modulus of the steel remains constant in the current model. In respect to the second point, since the model is a 2D plane stress model, healing all of the beams up to a level of 30mm above the capillary tubes is equivalent to full healing across the entire width of the beam in the experiment. However, as indicated by the glue migration pattern on the face of the experimental beam (Figure 7.15(b)), the adhesive flow is mainly confined to the middle two thirds of the crack face.

8.4 Conclusions and future work

The results presented in this chapter have shown that the lattice modelling method is capable of capturing the main mechanical behaviour which has been observed during the self-healing experiments on three-point bending of adhesive filled mortar beams. The initial stiffness and pre-healing strength is captured correctly, as is the fracture pattern pre- and post-healing. The increasing stiffness of the self-healing beams, relative to the control, caused by the primary healing in the experiments is also captured by the model.

Whilst the qualitative predictions are good, the quantitative properties of the current model require improvement. The inability of the current model to capture the early microcracking, and the full scope of damage in the fracture process zone around the macro crack, means that the force CMOD response is overly stiff pre- and post-healing. In addition, the current model is not able to capture the non-linear effects of tube breakages, steel bar slip and steel yielding. As a result of this, the overall numerical response is overly brittle, and the predicted ultimate load carrying capacity of both the healing and control beams is too high.

Future development work is required in order to improve the quantitative characteristics of the model. Implementation of the stochastic theory presented in Chapter 6 to all mortar elements should allow for diffuse microcracking around the main macro crack, thereby reducing the pre- and post-healing stiffness of the beam. In addition, inclusion of the non-linear effects of steel bar slip and yielding would improve the ductility of the mechanical response. It should be noted that it is possible to model the stiffness reduction that both of these processes cause in a similar manner to that currently used for capturing the stiffness change during the healing process. The effect of steel slip or yield may therefore be captured by reducing the stiffness of the elements surrounding the steel bar, or the steel elements themselves, when pre-defined CMOD values are reached in the analysis.

Further model development is also required in respect to the coupling of the flow theory with the lattice model. It is envisaged that in future models glue setting will be modelled using a time dependent function, with the strength of the composite healed elements developing over time, rather than instantaneously. This will allow the rate dependency effect of the primary healing process, as discussed in section 7.4.3, to be captured by the model. In addition, a 'sink' term is required to be added to the flow theory, to allow for the volume of glue entering the fracture process zone around the main crack.

Chapter 9

Conclusions and future outlook

This chapter summarises the general conclusions that may be drawn from the present investigation and comments on the future outlook of the research. For specific conclusions and future work suggestions readers are directed to these sections at the end of each of the individual work chapters.

The research objectives, as outlined in the introduction to this thesis, were to:

1. Undertake novel autonomic healing experiments to better understand the kinematics of the healing process, and to obtain reliable data on the mechanical properties of the healed material for the development of numerical models;
2. Improve the quantitative abilities of the discrete lattice beam modelling method in respect to modelling the damage of cementitious materials, and;
3. Model the fracture and autonomic healing process within cementitious materials using the discrete lattice beam modelling method.

In respect to each of these three objectives, the following research has been undertaken, which has led to the following conclusions being made:

1. An experimental programme has been designed, developed and completed, which has examined the efficacy of adhesive based autonomic healing within small scale reinforced mortar beams. The main conclusions of which are that:
 - Both primary and secondary healing effects occur within the self-healing beams, during the first and second loading cycles, respectively, which can result in improved mechanical properties of the composite;
 - The primary healing response improves with increasing reinforcement level, and decreasing load rate, and;

- The quantitative self-healing response is confirmed by qualitative observations that show clear evidence of crack healing due to glue flow on the crack face, and new crack formation.
2. The main quantitative limitations of the traditional lattice modelling method have been identified as: (i) Computational demand; (ii) Mesh orientation dependency; (iii) Mesh size dependency, and; (iv) Over-brittleness. The first two have been addressed, respectively, through implementation of an efficient FE computational algorithm, and development of a Mohr-Coulomb based failure criterion which minimises mesh orientation dependence. The second two limitations have been addressed by the development of regularisation theory based on the statistical distribution of beam strengths. The aim of this theory is to achieve realistic and objective softening curves from the lattice simulations, irrespective of the mesh resolution used. The main findings of these research areas are that:
- The implementation of efficient assembly and solver routines are extremely important in a lattice FE code, since the global stiffness matrix is very sparse and the number of DOF are generally very high;
 - The choice of failure criterion used in the lattice model is very important since it can effect both the predicted fracture pattern and the force-displacement response;
 - A Mohr-Coulomb failure criterion, when based upon the mid-plane beam stresses, which are in turn corrected to match the continuum stresses at this point, is considered to offer the best accuracy, and have the greatest underlying physical basis;
 - The double strength distribution of beam strengths, distributed randomly over RMEs, significantly improves the objectivity of the softening response obtained for different mesh resolutions, and improves the over-brittleness of this response when compared to experimental results, and;
 - The stochastic regularisation theory, despite not having an explicit mesostructure overlay, is still able to capture the main phases of crack formation, namely macrocrack growth, crack branching and crack bridging.
3. The self-healing response recorded during the experimental programme has been modelled using the discrete lattice beam modelling method. This has been undertaken

in a simple manner by replacing broken beams with the properties of healed beams at a pre-defined CMOD value. The main conclusions of this modelling work are that:

- The lattice model is capable of capturing the main stages of the mechanical behaviour of the experimental self-healing beams, including the initial stiffness, pre-healing strength and the stiffness increase during primary healing;
- The initial crack pattern is realistic for a three-point bending test, and the post-healed crack pattern deviates away from the initial crack, reflecting the new cracking observed during the experiments, and;
- The quantitative predictions of the model may be improved by including the non-linear effects of tube breakages, steel bar slip and steel yielding.

As discussed in Chapter 2, the lattice modelling method has been recognised for some time as having the ability to offer good qualitative predictions of fracture evolution under varying loading conditions. It is for this reason that the model has been used by researchers in many different fields of engineering to model materials with different types of heterogeneity. Nevertheless, it is felt that the quantitative limitations of the method, which include both mesh orientation and mesh size dependency, have inhibited further widespread application of the model.

As a consequence of the improvements made to the quantitative properties of the model, as outlined by the research presented in this thesis, the future outlook for the lattice method is considered to be positive. Further development and quantification of the stochastic regularisation theory, and integration of this theory within simulations containing explicit representation of mesostructure, is likely to improve this outlook even further, as will further analysis of the equivalence between the underlying continuum and its discrete representation.

The application of the lattice method to the modelling of the autonomic healing process in a cementitious material is, in the understanding of the author, the first time that the model has been used to capture the self-healing behaviour in any material. The ability of this relatively simple model to capture the main phases of the self-healing response, serves as further evidence of its flexibility, and augurs well for its future application at capturing various self-healing phenomenon.

The autonomic healing system developed and investigated in this thesis clearly offers a successful mechanism for restoring, and, in certain circumstances, enhancing the mechanical properties of the composite. The infiltration of the cyanoacrylate into, and around, the

macrocrack is likely to also reduce the permeability, and, therefore, improve the durability of the new composite material. This, however, requires confirmation during future work. The rapid flow and curing ability of the low viscosity cyanoacrylate, which is evident in the primary healing strength gain, also suggests that the method might be applicable to healing damage created under dynamic situations, such as in earthquakes.

There are two main issues which need to be addressed, however, before this self-healing mechanism can move towards commercialisation. The first issue relates to the practical feasibility of the healing system, and the second issue relates to the attitude of the client.

The feasibility of the brittle glass delivery system is clearly the biggest drawback of the present method, in respect to on-site structural applications. The most robust system currently available, probably involves the inclusion of adhesive filled microcapsules within the concrete mix during casting. Recent self-healing research within sandwich structures (Williams et al., 2007) and polymers (Wu et al., 2007) has, however, moved away from micro-encapsulation towards the development of continuous supply networks that allow healing agent reserves to be replenished frequently. In light of this, two possible supply systems, which would improve the future outlook of the autonomic healing process in concrete, are suggested in Figure 9.1.

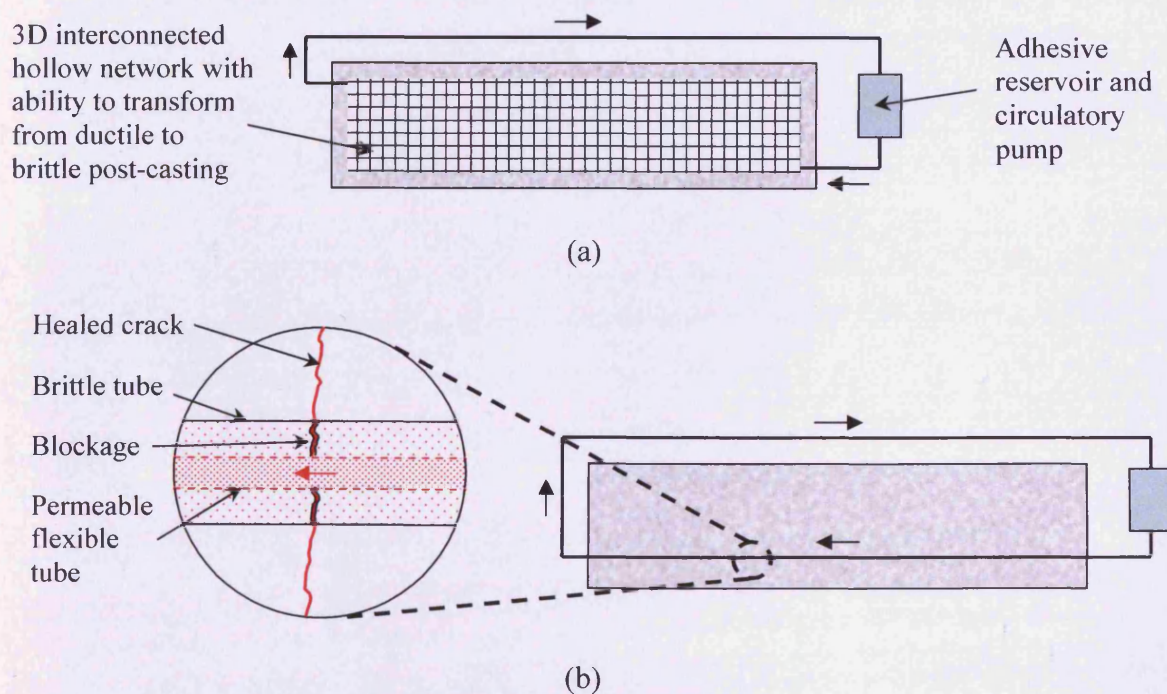


Figure 9.1. Future options for development of SH delivery system in concrete: (a) Ductile network with ability to turn brittle post-casting, and (b) Two-part supply tube which prevents blockages

The second issue, and possibly the biggest issue, which requires addressing prior to widespread uptake of this, or any other self-healing material, is the attitude of the client. Any system which involves some form of modification to the constituents, or manufacture, of an engineering material will result in an additional initial cost. However, providing the long term efficacy of the system in respect to improving the materials durability is proven, these initial costs should be more than offset by the long term savings from reduced repair and maintenance. Clients must, therefore, be prepared to evaluate the whole life costs, both financial and environmental, of their structures, before they are likely to seriously consider the adoption of these new and emerging self-healing materials.

References

- Abreu, M.M., Lemos, J.V., Carmeliet, J. and Schlangen, E. (2007). Modelling compressive cracking in concrete by a modified lattice model. *Fracture Mechanics of Concrete and Concrete Structures (FraMCoS-6)*, Vol 1: New Trends in Fracture Mechanics of Concrete, Catania, Italy, June 2007, pp. 453-460.
- Alava, M.J., Nukala, P.K.V.V. and Zapperi, S. (2006). Statistical models of fracture. *Advances in Physics*, 55(3-4), pp. 349-476.
- Arslan, A., Ince, R. and Karihaloo, B.L. (2002). An improved lattice model for concrete fracture. *Journal of Engineering Mechanics*, 128(1), pp. 57-65.
- Barbero, E.J. and Lonetti, P. (2003). Application of continuum damage healing mechanics to self-healing composites. 2003 ASME International Mechanical Engineering Congress. American Society of Mechanical Engineers, Washington, DC., U.S., Nov 2003.
- Barrett, R., Berry, M., Chan, T., Demmel, J., Donato, J., Dongarra, J., Eijkhout, V., Pozo, R., Romine, C. and van der Vorst, H. (1994). *Templates for the solution of linear systems: Building blocks for iterative methods*. Society for industrial and applied mathematics.
- Bazant, Z.P. and Planas, J. (1997). *Fracture and size effect in concrete and other quasi-brittle materials*. CRC Press, Boca Raton, USA.
- Bazant, Z.P. and Oh, B.H. (1983). Crack band theory for fracture of concrete. *Materials and Structures*, 16(93), pp. 155-177.
- Bazant, Z.P., Tabarra, M.R., Kazemi, T. and Pijaudier-Cabot, G. (1990). Random particle model for fracture of aggregate or fibre composites. *Journal of Engineering Mechanics*, 116(8), pp. 1686-1705.
- Bazant, Z.P. (2005). *Scaling of Structural Strength*. 2nd ed. Elsevier Ltd., Oxford, U.K.
- Beranek, W.J. and Hobbelman, G.J. (1998). Recent developments of the lattice model for in-plane loading of masonry walls. *Proceedings of the Brick Masonry Society*, 8, pp. 135-141.
- Bolander, J.E. and Saito, S. (1998). Fracture analyses using spring networks with random geometry. *Engineering Fracture Mechanics*, 61(5-6), pp. 569-591.
- Bolander, J.E. and Le, B.D. (1999). Modelling crack development in reinforced concrete structures under service loading. *Construction and Building Materials*, 13(1-2), pp. 23-31.
- Bolander, J.E., Hong, G.S. and Yoshitake, K. (2000). Structural concrete analysis using rigid-body-spring networks. *Computer-Aided Civil and Infrastructure Engineering*, 15(2), pp. 120-133.
- Bolander, J.E., Yip, M., Moriizumi, K. and Kunieda, M. (2001). Rigid-body-spring network modelling of cement-based composites. *Fracture Mechanics of Concrete Structure, FraMCoS-4*, Cachan-Paris, France, pp. 773-780.
- Bolander, J.E. and Berton, S. (2004). Cohesive zone modelling of fracture in irregular lattices. *Fracture Mechanics of Concrete Structure, FraMCoS-5*, Vail, Colorado, USA, pp. 989-994.
- Bolander, J.E. and Sukumar, N. (2005). Irregular lattice model for quasistatic crack propagation. *Physical Review B*, 71(094106), 12 pp.
- Brown, E.N., Sottos, N.R. and White, S.R. (2002). Fracture testing of a self-healing polymer composite. *Experimental Mechanics*, 42(4), pp. 372-379.
- Brown, E.N., Kessler, M.R., Sottos, N.R. and White, S.R. (2003a). In situ poly(urea-formaldehyde) microencapsulation of dicyclopentadiene. *Journal of Microencapsulation*, 20(6), pp. 719-730.

- Brown, E.N., Moore, J.S., White, S.R. and Sottos, N.R. (2003b). Fracture and fatigue behaviour of a self-healing polymer composite. *Bioinspired Nanoscale Hybrid Systems*, Dec 2-4 2002, 735. Materials Research Society, Boston, MA, United States, pp. 101-106.
- Brown, E.N., White, S.R. and Sottos, N.R. (2004). Microcapsule induced toughening in a self-healing polymer composite. *Journal of Materials Science*, 39(5), pp. 1703-1710.
- Brown, E.N., White, S.R. and Sottos, N.R. (2005a). Retardation and repair of fatigue cracks in a microcapsule toughened epoxy composite - Part I: Manual infiltration. *Composites Science and Technology*, 65(15-16), pp. 2466-2473.
- Brown, E.N., White, S.R. and Sottos, N.R. (2005b). Retardation and repair of fatigue cracks in a microcapsule toughened epoxy composite - Part II: In situ self-healing. *Composites Science and Technology*, 65(15-16), pp. 2474-2480.
- Bruyere, K., Morestin, F., Brunet, M., Mitton, D. and Rumelhart, C. (1998). Cancellous bone strength prediction using 2D spring lattice. *Journal of Biomechanics*, 31(1), pp. 61.
- BS 1881 – Part 116. (1983). Testing concrete. Method for determination of compressive strength of concrete cubes.
- BS 1881 – Part 117. (1983). Testing concrete. Method for determination of tensile splitting strength.
- BS 4449. (2005). Steel for the reinforcement of concrete. Weldable reinforcing steel. Bar, coil and decoiled product. Specification.
- BS EN1992. (2004). Eurocode 2: Design of concrete structures – Part 1-1: General rules and rules for buildings.
- Budiansky, B. and O’Connell, R.J. (1976). Elastic moduli of a crack solid. *International Journal of Solids and Structures*, 12, 81–97.
- Burt, N.J. and Dougill, J.W. (1977). Progressive failure in a model heterogeneous medium. *Journal of the Engineering Mechanics Division*, 103(3), pp. 365-376.
- Caballero, A., López, C.M. and Carol, I. (2006). 3D meso-structural analysis of concrete specimens under uniaxial tension. *Computer Methods in Applied Mechanics and Engineering*, 195(52), pp. 7182-7195.
- Carol, I., López, C.M. and Roa, O. (2001). Micromechanical analysis of quasi-brittle materials using fracture-based interface elements. *International Journal for Numerical Methods in Engineering*, 52(1-2), pp. 193-215.
- Chiaia, B., Vervuurt, A. and van Mier, J.G.M. (1997). Lattice model evaluation of progressive failure in disordered particle composites. *Engineering Fracture Mechanics*, 57(2-3), pp. 301-318.
- Coates, R.C., M.G. Coutie, and F.K. Kong (1999). *Structural Analysis*. 3rd ed. Chapman and Hall, London.
- Copuroglu, O, Schlangen, E., van Breugel, K. and Fraaij, A.L.A. (2005). Frost salt scaling modelling of cement paste. *International Conference on Concrete Repair, Rehabilitation and Retrofitting, ICCRRR ’05*, Cape Town, South Africa. 1. pp. 127-133.
- Curtin, W.A. and Scher, H. (1990). Brittle fracture in disordered materials: A spring network model. *Journal of the Materials Research Society*, 5, pp. 535-553.
- Cusatis, G., Bažant, Z.P. and Cedolin, L. (2006). Confinement-shear lattice CSL model for fracture propagation in concrete. *Computer Methods in Applied Mechanics and Engineering*, 195(52), pp. 7154-7171.

- Cusatis, G., Bažant, Z.P. and Cedolin, L. (2003a). Confinement-shear lattice model for concrete damage in tension and compression: I. Theory. *Journal of Engineering Mechanics*, ASCE, 129(12), pp. 1439-1448.
- Cusatis, G., Bažant, Z.P. and Cedolin, L. (2003b). Confinement-shear lattice model for concrete damage in tension and compression: II. Computation and validation. *Journal of Engineering Mechanics*, ASCE, 129(12), pp. 1449-1458.
- Cusatis, G. and Cedolin, L. (2007). Two-scale study of concrete fracturing behaviour. *Engineering Fracture Mechanics*, 74(1-2), pp. 3-17.
- Daux, C., Moës, N., Dolbow, J., Sukumar, N. and Belytschko, T. (2000). Arbitrary branched and intersecting cracks with the extended finite element method. *International Journal for Numerical Methods in Engineering*, 48(12), pp. 1741-1760.
- Davids, W.G. and Landis, E. (2003). Lattice models for the prediction of load-induced failure and damage in wood. *Wood and Fibre Science*, 35(1), pp. 120-134.
- de Borst, R. (2002). Fracture in quasi-brittle materials: a review of continuum damage-based approaches. *Engineering Fracture Mechanics*, 69(2), pp. 95-112.
- de Borst, R. and Mühlhaus, H-B. (1991). Continuum models for discontinuous media, in *Fracture Processes in Concrete, Rock and Ceramics*, J.G.M. van Mier, J.G. Rots and A. Bakker (eds.), Chapman & Hall, London/New York, pp. 601-618.
- de Borst, R., Sluys, L.T., Mühlhaus, H.B. and Pamin, J. (1993). Fundamental issues in finite element analyses of deformation. *International Journal of Engineering Computation*, 10, pp. 99-121.
- Dry, C.M. (1994). Matrix cracking repair and filling using active and passive modes for smart timed release of chemicals from fibres into cement matrices. *Smart Materials and Structures*, 3(2), pp. 118-123.
- Dry, C.M. (1996a). Procedures developed for self-repair of polymeric matrix composite materials. *Composite Structures*, 35, pp. 263-269.
- Dry, C.M. (1996b). Release of smart chemicals for the in-service repair of bridges and roadways. In *proceedings of Smart Materials, Structures, and MEMS*, The International Society for Optical Engineering, Bangalore, India, Dec 1996, 3321, pp. 140-144.
- Dry, C.M. (1996c). Smart bridge and building materials in which cyclic motion is controlled by internally released adhesives. In *proceedings of Smart Structures and Materials 1996: Smart Systems for Bridges, Structures, and Highways*. Society of Photo-Optical Instrumentation Engineers, San Diego, CA, USA, Feb 1996, 2719, pp. 247-254.
- Dry, C.M. (1996d). Smart earthquake-resistant materials: using time-released adhesives for damping, stiffening, and deflection control. In *proceedings of 3rd Int. Conference on Intelligent Materials and 3rd European Conference on Smart Structures and Materials*. Society of Photo-Optical Instrumentation, Lyon, France, June 1996, 2779, pp. 958-967.
- Dry, C.M. (2000). Three designs for the internal release of sealants, adhesives, and waterproofing chemicals into concrete to reduce permeability. *Cement and Concrete Research* 30(12), pp. 1969-1977.
- Dry, C. and Corsaw, M. (2003). A comparison of bending strength between adhesive and steel reinforced concrete with steel only reinforced concrete. *Cement and Concrete Research* 33(11), pp. 1723-1727.
- Dry, C. and Unzicker, J. (1998). Preserving performance of concrete members under seismic loading conditions. In *proceedings of Smart Structures and Materials 1998: Smart Systems for Bridges*,

- Structures, and Highways. The International Society for Optical Engineering, San Diego, CA, United States, Mar 1998, 3325, pp. 74-80.
- Dry, C. (2004). Self-healing materials. An MIT Enterprise: Technology Review. <http://www.technologyreview.com/forums/forum.asp?forumid=208> [Accessed: 07/ 2005].
- DTI. (2006). Construction statistics annual report 2006. London TSO.
- Duxbury, P.M., Beale, P.D. and Moukarzel, C. (1995). Breakdown of two-phase random resistor networks. *Physical Review B*, 51(6), pp. 3476-3488.
- Edvardsen, C. (1999). Water permeability and autogenous healing of cracks in concrete. *ACI Materials journal*, 96(4), pp. 448-454.
- FEMMASSE. (2008). Finite element module MLS. Femmassee BV. www.femmasse.com [Accessed: 10/2008].
- Feng, Z. (2003). Micromechanics-based multiscale lattice modelling of fatigue cracking in hot mixed asphalt. PhD Thesis, North Carolina State University, Raleigh, USA.
- Fischer, J. (2001). The molding of the world. *U.S. News & World Report*. 25th June, 2001. p. 45.
- Frantziskonis, G.N., Konstantinidis, A.A. and Aifantic, E.C. (2001). Scale-dependent constitutive relations and the role of scale on nominal properties. *European Journal of Mechanics - A/Solids*, 20(6), pp. 925-936.
- Freyermuth, C.L. (2001). Life-cycle cost analysis for large segmental bridges. *Concrete International*, 23(2), pp. 89-95.
- Gitman, I.M. (2006). Representative volumes and multi-scale modelling of quasi-brittle materials. PhD thesis, Delft University of Technology, Delft, The Netherlands.
- Gugliotta, G. (2001). A plastic that 'heals' itself: Innovation could extend life of everyday items. *The Washington Post*. A12. Thursday, February 15th, 2001.
- Häfner, S., Eckardt, S., Luther, T. and Könke, C. (2006). Mesoscale modelling of concrete: Geometry and numerics. *Computers and Structures*, 84, pp. 450-461.
- Helmer, M. (2001). Plastic, heal thyself: Fatigued materials have a new self-help cure. *Nature Science Update*. 15th February, 2001.
- Henkel Sichel-Werke. (1997). Technical data sheet for SICOMET 9000. Henkel Sichel-Werke Ltd. www.henkel.com [Accessed: 10/2008].
- Herrmann, H.J., Hansen, A. and Roux, S. (1989). Fracture of disordered, elastic lattices in two dimensions. *Physical review B*, The American Physical Society, 39(1), pp. 637-648.
- Herrmann, H.J. and Roux, S. (eds.). (1990). Statistical models for the fracture of disordered media. Elsevier/North Holland, Amsterdam, The Netherlands.
- Herrmann, H.J. (1991). Patterns and scaling in fracture. In *Fracture Processes in Concrete, Rock and Ceramics*, Vol 1: Microscopic Materials Studies and Materials Engineering, pp. 195-211.
- Hillerborg, A. (1985). Numerical methods to simulate softening and fracture of concrete. In *Fracture Mechanics of Concrete: Structural Applications and Numerical Calculation*, G.C. Sih and A. DiTommaso (eds.). Martinus Nijhoff Publishers, Dordrecht, pp. 141-170.
- Hosoda, A., Kishi, T., Arita, H. and Takakuwa, Y. (2007). Self-healing of crack and water permeability of expansive concrete. 1st international conference on self-healing materials. Noordwijk, Holland, April 2007.

- Hou, P. (2007). Lattice model applied to the fracture of large strain composite. *Theoretical and Applied Fracture Mechanics*, 47, pp. 233-243.
- Hrennikoff, A. (1941). Solution of problems of elasticity by the framework method. *Journal of Applied Mechanics*, 12, pp. 169-175.
- Ince, R., Arslan, A. and Karihaloo, B.L. (2003). Lattice modelling of size effect in concrete strength. *Engineering Fracture Mechanics*, 70, pp. 2307-2320.
- Ingraffea, A. R. and Saouma, V. (1985). Numerical modelling of discrete crack propagation in reinforced and plain concrete, in *Fracture Mechanics of Concrete*, G.C. Sih and A. DiTommaso (eds.), EAFM series, Martinus Nijhoff publishers, Dordrecht, pp. 171-222.
- Jacobsen, S. and Sellevold, E.J. (1996). Self-healing of high strength concrete after deterioration by freeze/thaw. *Cement and Concrete Research*, 26(1), pp. 55-62.
- Jagota, A. and Bennison, S.J. (1994). Spring-network and finite element models for elasticity and fracture. In *Non-Linearity and Breakdown in Soft Condensed Matter*, K.K. Bardhan et al. (eds.), Springer, Berlin, 437, pp. 186-201.
- Jefferson, A.D. (2003a). Craft: a plastic-damage-contact model for concrete. I. Model theory and thermodynamic considerations. *International Journal of Solids and Structures*, 40(22), pp. 5973-5999.
- Jefferson, A.D. (2003b). Craft: a plastic-damage-contact model for concrete. II. Model implementation with implicit return-mapping algorithm and consistent tangent matrix. *International Journal of Solids and Structures*, 40(22), pp. 6001-6022.
- Joseph, C. and Jefferson, A.D. (2006a). State of the art report on self-healing materials. Cardiff School of Engineering, Internal Report No. 3131.
- Joseph, C. and Jefferson, A.D. (2006b). Stochastic regularisation of lattice modelling for the failure of cementitious composites. *Proceedings of the Joint Conference of the Association for Computational Mechanics in Engineering (UK) and The Irish Society for Scientific and Engineering Computation*, Belfast, Ireland, April 2006, pp. 219-222.
- Joseph, C. and Jefferson, A.D. (2007). Stochastic regularisation of lattice modelling for the failure of quasi-brittle materials. *Fracture Mechanics of Concrete and Concrete Structures (FraMCoS-6)*, Vol 1: *New Trends in Fracture Mechanics of Concrete*, Catania, Italy, June 2007, pp. 445-452.
- Joseph, C., Jefferson, A.D. and Cantoni, M. (2007). Issues relating to the autonomic healing of cementitious materials. 1st international conference on self-healing materials. Noordwijk, Holland, April 2007.
- Joseph, C., Jefferson, A.D. and Lark, R.J. (2008a). Lattice modelling of cementitious materials with engineered self-healing properties. *Proceedings of the 16th Conference of the Association for Computational Mechanics in Engineering (UK)*, Newcastle, U.K., April 2008.
- Joseph, C., Jefferson, A.D. and Lark, R.J. (2008b). Lattice modelling of autonomic healing processes in cementitious materials. *Proceedings of 8th World Congress on Computational Mechanics (WCCM8)*, Lido, Venice, Italy, June/July 2008.
- Kabat, J. (2001). Plastic Surgery. *Wired Magazine*. <http://www.wired.com/wired/archive/9.06/eword.html?pg=3> [Accessed: July 2004].
- Karihaloo, B. L. (2003). Failure of Concrete. In *Comprehensive Structural Integrity*, B. L. Karihaloo and W.G. Knauss (eds.), Volume 2, Chapter 10, Elsevier, Oxford,, pp. 477-548.
- Karihaloo, B.L., Shao, P.F. and Xiao, Q.Z. (2003). Lattice modelling of the failure of particle composites. *Engineering Fracture Mechanics*, 70(17), pp. 2385-2406.

- Karihaloo, B.L. (1995). *Fracture mechanics and structural concrete*. 1st ed. John Wiley & Sons, New York.
- Kessler, M.R., Sottos, N.R. and White, S.R. (2003). Self-healing structural composite materials. *Composites Part A: Applied Science and Manufacturing*, 34(8), pp. 743-753.
- Kim, D.W., Lee, Y.S., Oh, Y.T. and Chu, C.N. (2006). Prevention of exit burr in microdrilling of metal foils by using a cyanoacrylate adhesive. *The International Journal of Advanced Manufacturing Technology*, 27(11-12), pp 1071-1076.
- Kishi, T., Ahn, T., Hosoda, A., Suzuki, S. and Takaoka, H. (2007). Self-healing behaviour by cementitious recrystallisation of cracked concrete incorporating expansive agent. 1st international conference on self-healing materials. Noordwijk, Holland, April 2007.
- Krajcinovic, D. (1996). *Damage Mechanics*. North-Holland series in Applied Mathematics and Mechanics, J.D. Achenbach et al. (eds.), Elsevier, Amsterdam.
- Kuentz, M., Leuenberger, H. and Kolb, M. (1999). Fracture in disordered media and tensile strength of microcrystalline cellulose tablets at low relative densities. *International Journal of Pharmaceutics*, 182(2), pp. 243-255.
- Kunin, I.A. (1982). *Elastic media with microstructure vol. I*. Springer-Verlag, Berlin, Germany.
- Leite, J.P.B., Slowik, V. and Apel, J. (2007). Computational model of mesoscopic structure of concrete for simulation of fracture processes. *Computers and Structures*, 85, pp. 1293-1303.
- Leite, J.P.B., Slowik, V. and Mihashi, H. (2004). Computer simulation of fracture processes of concrete using mesolevel models of lattice structures. *Cement and Concrete Research*, 34(6), pp. 1025-1033.
- Lemaitre, J. and Chaboche, J.L. (1990). *Mechanics of solid materials*. Cambridge University Press, Cambridge.
- Li, V.C., Yun Mook, L. and Yin-Wen, C. (1998). Feasibility study of a passive smart self-healing cementitious composite. *Composites Part B: Engineering*, 29(6), pp. 819-827.
- Li, Z., Perez Lara, M.A. and J.E. Bolander. (2006). Restraining effect of fibres during non-uniform drying of cement composites. *Cement and Concrete Research*, 36(9), pp. 1643-1652.
- Lilliu, G. and van Mier, J.G.M. (2007). On the relative use of micro-mechanical lattice analysis of 3-phase particle composites. *Engineering Fracture Mechanics*, 74(7), pp. 1174-1189.
- Lilliu, G. and van Mier, J.G.M. (2003). 3D lattice type fracture model for concrete. *Engineering Fracture Mechanics*, 70(7-8), pp. 927-941.
- LUSAS. (2008). Lusas finite element program version 13.5. Finite Element Analysis Ltd. <http://www.lusas.com/index.html> [Accessed: 10/2008].
- Maiti, S. and Geubelle, P.H. (2006). Cohesive modelling of fatigue crack retardation in polymers: Crack closure effect. *Engineering Fracture Mechanics*, 73(1), pp. 22-41.
- Man, H-K. and van Mier, J.G.M. (2008). Influence of particle density on 3D size effects in the fracture of (numerical) concrete. *Mechanics of Materials*, 40(6), pp. 470-486.
- Meakin, P. (1991). Simple models for material failure and deformation. In *Fracture Processes in Concrete, Rock and Ceramics*, J.G.M. van Mier, J.G. Rots and A. Bakker (eds.), Chapman & Hall, London/New York, pp. 213-229.
- Meakin, P., Li, G., Sanders, L.M., Louis, E. and Guinea, F. (1989). A simple two-dimensional model for crack propagation. *Journal of Physics, A: Math. Gen.*, 22, pp. 1393-1403.

- Melenk, J.M., Babuska, I. (1996). The partition of unity finite element method: Basic theory and applications. *Computer Methods in Applied Mechanics and Engineering*, 39, pp. 289-314.
- Mihashi, H., Kaneko, Y., Nishiwaki, T. and Otsuka, K. (2000). Fundamental study on development of intelligent concrete characterized by self-healing capability for strength. *Transactions of the Japan Concrete Institute*, 22, pp. 441-450.
- Mihashi, H. and Nomura, N. (1992). Microcracking and tension-softening properties of concrete. *Cement and Concrete Composites*, 14, pp. 91-103.
- Moukarzel, C. and Duxbury, P.M. (1994). Failure of three-dimensional random composites. *Journal of Applied Physics*, 76(7), pp. 4086-4094.
- Neville, A.M. (1995). *Properties of Concrete*, 4th ed., Longman, Essex.
- Nilson, A.H. (1968). Nonlinear analysis of reinforced concrete by the finite element method. *Journal Proceedings of the American Concrete Institute*, 65(9), pp. 757-766.
- Nishiwaki, T., Mihashi, H., Jang, B-K. and Miura, K. (2006). Development of self-healing system for concrete with selective heating around crack. *Journal of Advanced Concrete Technology*, 4(2), pp. 267-275.
- Nooru-Mohamed, M.B., Schlangen, E. and van Mier, J.G.M. (1993). Experimental and numerical study on the behaviour of concrete subjected to biaxial tension and shear. *Advanced Cement Based Materials*, 1(1), pp. 22-37.
- Nooru-Mohamed, M.B. (1992). Mixed-mode fracture of concrete: an experimental approach. PhD Thesis, Delft Technical University, Delft, The Netherlands.
- Oliver, J., Huespe, A.E., Pulido, M.D.G. and Chaves, E. (2002). From continuum mechanics to fracture mechanics: the strong discontinuity approach, *Engineering Fracture Mechanics*, 69(2), pp. 113-136.
- Oliver, J., Huespe, A.E. and Samaniego, E. (2003). A study on finite elements for capturing strong discontinuities. *International Journal for Numerical Methods in Engineering*, 56(14), pp. 2135-2161.
- Ostoja-Starzewski, M. and Stahl, D.C. (2000). Random fibre networks and special elastic orthotropy of paper. *Journal of Elasticity*, 60(2), pp. 131-149.
- Ostoja-Starzewski, M. (2002). Lattice models in micromechanics. *Applied Mechanics Reviews*, 55(1), pp. 35-60.
- Parrod, P. (2002). A lattice model for fibrous materials. MSc thesis, The University of Maine, Orano, USA.
- PCA. (2008). http://www.cement.org/tech/faq_cracking.asp [Accessed: 10/2008].
- Peerlings, R.H.J., de Borst, R., Brekelmans, W.A.M. and de Vree, J.H.P. (1996). Gradient-enhanced damage for quasi-brittle materials. *International Journal for Numerical Methods in Engineering*, 39, pp. 3391-3403.
- Pijaudier-Cabot, G. and Bažant, Z.P. (1987). Nonlocal damage theory. *ASCE Journal of Engineering Mechanics*, 10, pp. 1512-1533.
- Prado, E.P. and van Mier, J.G.M. (2003). Effect of particle structure on mode I fracture process in concrete. *Engineering Fracture Mechanics*, 70(14), pp. 1793-1807.
- Press, W.H., Teukolsky, S.A., Vetterling, W.T. and Flannery, B.P. (1996). *Numerical recipes in Fortran 77: the art of scientific computing*. Cambridge University Press, Cambridge, UK.
- Rashid, Y.R. (1968). Analysis of prestressed concrete pressure vessels. *Nuclear Engineering and Design*, 7(4), pp. 334-344.

- Reinhardt, H-W. and Joos, M. (2003). Permeability and self-healing of cracked concrete as a function of temperature and crack width, *Cement and Concrete Research*, 33, pp. 981-985.
- Remmers, J.J.C. and de Borst, R. (2007). Numerical modelling of self-healing mechanisms. In *Self-healing materials: an alternative approach to 20 centuries of material science*, S. van der Zwaag (ed.), Springer, The Netherlands, pp. 365-380.
- RILEM Committee FMC-50. (1985). Determination of the fracture energy of mortar and concrete by means of three point bending tests on notched beams. *Material and Structures*, 18(106), pp. 285-290.
- Rocha, M.M. and Riera, J.D. (1991). On size effects and rupture of non-homogenous materials, in *Fracture Processes in Concrete, Rock and Ceramics*, J.G.M. van Mier, J.G. Rots and A. Bakker (eds.), Chapman & Hall, London/New York, pp. 451-460.
- Roels, S., Vandersteen K. and Carmeliet, J. (2003). Measuring and simulating moisture uptake in a fractured porous medium. *Advances in Water Resources*, 26, pp. 237-246.
- Rossi, P. and Richer, S. (1987). Numerical modelling of concrete cracking based on a stochastic approach. *Materials and Structures*, 20(5), pp. 334-337.
- Rots, J.G. (1993). Computational modelling of concrete fracture. PhD thesis, Delft University of Technology, Delft, The Netherlands.
- Rule, J.D., Brown, E.N., Sottos, N.R., White, S.R. and Moore, J.S. (2005). Wax-protected catalyst microspheres for efficient self-healing materials. *Advanced Materials*, 17(2), pp. 205-208.
- Şahmaran, M. and Li, V.C. (2008). Durability of mechanically loaded engineered cementitious composites under highly alkaline environments. *Cement and Concrete Composites*, 30(2), pp. 72-81.
- Schlangen, E. (2005). Self-healing phenomena in cement-based materials. RILEM. http://www.rilem.org/tc_shc.php [Accessed: 11/2005].
- Schlangen, E. (1993). Experimental and numerical analysis of fracture processes in concrete. PhD Thesis, Delft Technical University, Delft, The Netherlands.
- Schlangen, E. and van Mier, J.G.M. (1992a). Experimental and numerical analysis of micromechanisms of fracture of cement-based composites. *Cement and Concrete Composites*, 14, pp. 105-118.
- Schlangen, E. and Garboczi, E.J. (1997). Fracture simulations of concrete using lattice models: Computational aspects. *Engineering Fracture Mechanics*, 57(2-3), pp. 319-332.
- Schlangen, E. and van Mier, J.G.M. (1992b). Simple lattice model for the numerical simulation of fracture of concrete materials and structures. *Materials and Structures*, 25(9), pp. 534-542.
- Schlangen, E., Koenders, E.A.B. and van Breugel, K. (2007). Influence of internal dilation on the fracture behaviour of multi-phase materials. *Engineering Fracture Mechanics*, 74(1-2), pp. 18-33.
- Schlangen, E. and Copuroglu, O. (2005). Modelling of deterioration mechanisms in concrete and mortar. *Proceedings of the 5th International Conference on Computation of Shell and Spatial Structures*, Salzburg, Austria, Jun 2005.
- Schlangen, E. and van Breugel, K. (2005). Prediction of tensile strength reduction of concrete due to ASR. *Third International Conference on Construction Materials, Performance, Innovations and Structural Implications, ConMat '05*, Vancouver, Canada, Aug 2005.
- Schlangen, E. and Garboczi, E.J. (1996). New method for simulating fracture using an elastically uniform random geometry lattice. *International Journal of Engineering Science*, 34(10), pp. 1131-1144.

- Schlangen, E. and van Mier, J.G.M. (1995). Crack propagation in sandstone: Combined experimental and numerical approach. *Rock Mechanics and Rock Engineering*, 28(2), pp. 93-110.
- Schlangen, E., Ter Heide, N and van Breugel, K. (2006). Crack healing of early age cracks in concrete, In *Measuring, Monitoring and Modelling Concrete Properties*, Springer, The Netherlands, pp. 273-284.
- Schmets, A.J.M. (2003). Self-healing: an emerging property for new materials. *Leonardo Times*. <http://www.selfhealingmaterials.nl/Self%20Healing%20Materials%20article.pdf> [Accessed: 12/2005].
- Sharp, S.R. and Clemena, G.G. (2004). State of the art survey of advanced materials and their potential application in highway infrastructure. Charlottesville: Virginia Transportation Research Council. pp. 1-41.
- Shewchuk, J. R. (1994). An introduction to the conjugate gradient method without the agonising pain. Technical Report:CS-94-125. Carnegie Mellon University, Pittsburgh, PA, USA. <http://www.cs.cmu.edu/~quake-papers/painless-conjugate-gradient.pdf> [Accessed: 10/2008].
- Sika (2001). Technical data sheet for SikaDur 52 epoxy crack injection resin. Sika Ltd. <http://www.rssonline.org/datasheets/SIKADUR%2052.PDF> [Accessed: 10/2008].
- Stankowski, T. (1990). Numerical simulation of progressive failure in particle composites. PhD Thesis, University of Colorado, Boulder, CO, U.S.A.
- Stinson, S. (2001). Plastic mends its own cracks: Microcapsules in composite release healing agent when stressed. *Chemical & Engineering News*, 79(8), p. 13.
- Sukumar, N, Moes, N, Moran, B, and Belytschko, T. (2000). Extended finite element method for three-dimensional crack modelling. *International Journal for Numerical Methods in Engineering*, 48(11), pp. 1549-1570.
- Tan, L., Schlangen, E. and Ye, G. (2007). Simulation of failure in hydrating cement particles systems. *Key Engineering Materials*, 348-349, pp. 737-740.
- Tecroc (2004). Technical data sheet for epoxy injection grouts TG6, TG7, and TG10. Tecroc Products Ltd. http://www.tecroc.com/Technical_Data_Sheets/15_EPOXY_INJECTION_GROUT.pdf [Accessed: 10/2008].
- Ter Heide, N., Schlangen, E. and van Breugel, K. (2005). Experimental Study of Crack Healing of Early Age Cracks, In proceedings of Knud Højgaard conference on Advanced Cement-Based Materials, Technical University of Denmark, June 2005.
- Termonia, Y., Meakin, P. and Smith, P. (1985). Theoretical study of the influence of the molecular weight on the maximum tensile strength of polymer fibres. *Macromolecules*, 18, pp. 2246-2252.
- Valente, S. (1991). Influence of friction on cohesive crack propagation. In *Fracture Processes of Concrete and Ceramics*, J.G.M. van Mier, J.G. Rots and A. Bakker (eds.), Chapman & Hall, London/New York, pp. 695-704.
- Van der Zwaag, S. (2007). Self-healing materials: an alternative approach to 20 centuries of material science. Springer, The Netherlands.
- van Mier, J.G.M., Schlangen, E. and Vervuurt, A. (1995). Lattice type fracture models for concrete. In *Continuum Models for Materials with Microstructure*, H-B. Müllhaus (ed.), John Wiley & Sons Ltd., New York, pp. 341-377.
- van Mier, J.G.M., Schlangen, E. and Vervuurt, A. (1996). Tensile cracking in concrete and sandstone: Part 2 – effect of boundary rotations. *Materials and Structures*, 29(186), pp. 87-96.

- van Mier, J.G.M., Chiaia, B.M. and Vervuurt, A. (1997). Numerical simulation of chaotic and self-organizing damage in brittle disordered materials. *Computer Methods in Applied Mechanics and Engineering*, 142(1-2), pp. 189-201.
- van Mier, J.G.M. (2004). Discussion on "Lattice modelling of size effect in concrete strength by Ince, R., Arslan, A. and Karihaloo, B.L., *EFM*, 70, pp. 2307-20". *Engineering Fracture Mechanics*, 71, pp. 1625-1628.
- van Mier, J.G.M. and van Vliet, M.R.A. (2003). Influence of microstructure of concrete on size/scale effects in tensile fracture. *Engineering Fracture Mechanics*, 70(16), pp. 2281-2306.
- van Mier, J.G.M. (1997). *Fracture processes of concrete: assessment of material parameters for fracture models*. CRC Press, Inc.
- van Mier, J.G.M., van Vliet, M.R.A. and Wang, T.K. (2002). Fracture mechanisms in particle composites: statistical aspects in lattice type analysis. *Mechanics of Materials*, 34(11), pp. 705-724.
- van Oss, H.G. (2005). Background facts and issues concerning cement and cement data. Open-file report 2005-1152. US Dept. of the Interior and US Geological Survey. <http://pubs.er.usgs.gov/usgspubs/ofr/ofr20051152> [Accessed: 10/2008].
- Van Vliet, M.R.A. (2000). *Size effect in tensile fracture of concrete and rock*. PhD Thesis, Delft Technical University, Delft, The Netherlands.
- van Vliet, M.R.A. and van Mier, J.G.M. (1996). Comparison of lattice type fracture models for concrete under biaxial loading regimes. In *Size-Scale Effects in the Failure Mechanisms of Materials and Structures*, A. Carpinteri (ed.), E & FN Spon, London, pp. 43-57.
- Vasic, S, Smith, I. and Landis, E. (2005). Finite element techniques and models for wood fracture mechanics. *Wood Science Technology*, 39(1), pp. 3-17.
- Vervuurt, A. (1997). *Interface fracture in concrete*. PhD Thesis, Delft Technical University, Delft, The Netherlands.
- Vervuurt, A., van Mier, J.G.M. and Schlangen, E. (1994). Analyses of anchor pull-out in concrete. *Materials and Structures*, 27(5), pp. 251-259.
- Vervuurt, A., Schlangen, E. and van Mier, J.G.M. (1996). Tensile cracking in concrete and sandstone: Part 1 – basic instruments. *Materials and Structures*, 29(185), pp. 9-18.
- Vonk, R.A., Rutten, H.S., van Mier, J.G.M. and Fijneman, H.J. (1991). Micromechanical simulation of concrete softening. In *Fracture Processes in Concrete, Rock and Ceramics*, J.G.M. van Mier, J.G. Rots and A. Baker (eds.), Chapman & Hall/E & FN Spon, London, pp. 129-138.
- Walraven, J. C. (1980). *Aggregate interlock: a theoretical and experimental analysis*. PhD thesis, Delft University of Technology, Delft, The Netherlands.
- Wang, J., Navi, P. and Huet, C. (1992). Numerical study of granule influences on the crack propagation in concrete. *Fracture Mechanics of Concrete Structure, FraMCos-1*, Z.P. Bažant (ed.), pp. 373-378.
- Wang, J., Navi, P. and Huet, C. (1997). Numerical analysis of crack propagation in tension specimens of concrete considered as a 2D multicracked granular composite. *Materials and Structures*, 30(1), pp. 11-21.
- Westerbeek, T. (2005). Self-healing materials. Radio Netherlands. <http://www2.rnw.nl/rnw/en/features/science/050801rf?view=Standard> [Accessed: 11/ 2005].
- White, S.R., Sottos, N.R., Geubelle, P.H., Moore, J.S., Kessler, M.R., Sriram, S.R., Brown, E.N. and Viswanathan, S. (2001). Autonomic healing of polymer composites. *Nature*, 409, pp. 794-797.

- White, S.R. (2005). University of Illinois at Urbana Champaign: Autonomic Healing Research. <http://www.autonomic.uiuc.edu/index.html> [Accessed: 11/2005].
- Williams, G., Trask, R. and Bond, I. (2007). A self-healing carbon fibre reinforced polymer for aerospace applications. *Composites: Part A*, 38, pp. 1525-1532.
- Williams, H.R., Trask, R.S. and Bond, I.P. (2007). Design of vascular networks for self-healing sandwich structures. 1st international conference on self-healing materials. Noordwijk, Holland, April 2007.
- Wisby, G. (2001). U. of I. researchers find material that heals itself. *Chicago Sun-Times*. Thursday, 15th February, 2001.
- Wu, W., Hansen, C., Aragon, A., Sottos, N.R., White, S.R., Geubelle, P. and Lewis, J. (2007). Direct ink writing of microvascular networks. 1st international conference on self-healing materials. Noordwijk, Holland, April 2007.
- Xiao, Q.Z. and Karahaloo, B.L. (2006). Asymptotic fields at frictionless and frictional cohesive crack tips in quasibrittle materials. *Journal of Mechanics of Materials and Structures*, 1(5), pp. 881-910.
- Yamada, K., Hosoda, A., Kishi, T. and Nozawa, S. (2007). Crack self-healing properties of expansive concretes with various cements and admixtures. 1st international conference on self-healing materials. Noordwijk, Holland, April 2007.
- Yip, M., Li, Z., Liao, B-S. and Bolander, J.E. (2006). Irregular lattice models of fracture of multiphase particulate materials. *International Journal of Fracture*, 140(1-4), pp. 113-124.
- Yip, M., Mohle, J. and Bolander, J.E. (2005). Automated modelling of 3-D structural components using irregular lattices. *Computer-Aided Civil and Infrastructure Engineering*, 20(6), pp. 393-407.
- Young, W-B. (2004). Analysis of capillary flows in non-uniform cross-sectional capillaries. *Colloids and Surfaces A: Physicochemical and Engineering Aspects*, 234(1-3), pp. 123-128.
- Yunovich, M. and Thompson, N.G. (2003). Corrosion of highway bridges: Economic impact and control methodologies. *Concrete International*, 25(11), pp. 52-57.
- Zapperi, S., Vespignani, A. and Stanley, H.E. (1997). Plasticity and avalanche behaviour in microfracturing phenomena. *Nature*, 388, pp. 658-660.
- Zhong, W. and Yao, W. (2008). Influence of damage degree on self-healing of concrete. *Construction and Building Materials*, 22(6), pp. 1137-1142.
- Zubelewicz, A. and Bažant, Z.P. (1987). Interface element modelling of fracture in aggregate composites. *Journal of Engineering Mechanics, ASCE*, 113(11), pp. 1619-1630.

Appendix A – Data sheet for Rite-Lok EC5 cyanoacrylate

This appendix contains the data sheet for Rite-Lok EC5 cyanoacrylate. This adhesive has been used exclusively as the healing agent in the final self-healing experimental programme presented in section 7.3.



RITE-LOK™ Cyanoacrylate Adhesive EC5

Product Data Sheet

Updated : February 2007
Supersedes : New

Product Description

RITE-LOK EC5 is a low viscosity (5 cPs) Ethyl Cyanoacrylate based adhesive. EC5 is suitable for bonding a wide range of materials where very fast cure speed is required.

Key Features

EC5 is specially formulated for high strength, general purpose bonding of most plastics, rubbers, metals and other common substrates. Recommended for use on assemblies with very close fitting parts and smooth, even surfaces. Can be used as a post-assembly adhesive to wick into parts.

Physical Properties

Base	Ethyl
Soluble In	Acetone, MEK
Viscosity (cps)	Range 1-10 Typical Value 5
Specific Gravity	1.06
Colour	Clear

Performance Characteristics

Maximum Gap Fill (best results are obtained with very thin bond lines)	0.05mm
Fixture Time	5-15secs
Tensile Strength (ISO 6922)	20 N/mm ²
Full Cure	24hrs
Speed of Cure	The speed of cure of cyanoacrylates varies according to the substrate to be bonded. Acidic surfaces such as paper and leather will have longer cure times than most plastics and rubbers.
Moisture Resistance	Low resistance to high levels of moisture and humidity over time.
Service Temperature Range	-50 to +80°C

Date: February 2007
RITE-LOK
Cyanoacrylate Adhesive EC5

Additional Product Information	RITE-LOK Activators AC11 and AC12 may be used in conjunction with RITE-LOK cyanoacrylates where cure speed needs to be accelerated. Cure speeds of less than 2 seconds can be obtained with most RITE-LOK cyanoacrylates. The use of an activator can reduce the final bond strength by up to 30%.
Application Techniques	Bond speed is very fast so ensure that parts are properly aligned before bonding. RITE-LOK Activators may be required if there are gaps or porous surfaces. Some plastics may require application of RITE-LOK AC77 Primer. Ensure parts are clean, dry and free from oil and grease. Product is normally hand applied from the bottle. Apply sparingly to one surface and press parts firmly together until handling strength is achieved. As a general rule, as little cyanoacrylate as possible should be used – over application will result in slow cure speed and lower bond strength.
Storage Conditions	Once opened, keep the adhesive in a cool, dry place away from direct sunlight. Under such conditions shelf life at room temperature will be 12 months. Refrigeration to 5°C gives optimum storage stability.
Shelf Life	12 months from date of despatch by 3M when stored in the original carton at 21°C
Precautionary Information	Refer to product label and material Safety Data Sheet for health and safety information before using the product. For information please contact your local 3M Office. www.3M.com
For Additional Information	To request additional information or to arrange for sales assistance, call 0870 6080050 Address correspondence to: 3M United Kingdom PLC, 3M House, 28 Great Jackson Street, Manchester, M15 4PA
Product Use	All statements, technical information and recommendations contained in this document are based upon tests or experience that 3M believes are reliable. However, many factors beyond 3M's control can affect the use and performance of a 3M product in a particular application, including the conditions under which the product is used and the time and environmental conditions in which the product is expected to perform. Since these factors are uniquely within the user's knowledge and control, it is essential that the user evaluate the 3M product to determine whether it is fit for a particular purpose and suitable the user's method or application.
Note	Values presented have been determined by standard test methods and are average values not to be used for specification purposes. Our recommendations on the use of our products are based on tests believed to be reliable but we would ask that you conduct your own tests to determine their suitability for your applications. This is because 3M cannot accept any responsibility or liability direct or consequential for loss or damage caused as a result of our recommendation

3M and RITE-LOK are trademarks of the 3M Company.

Industrial Adhesives & Tapes Division

© 3M United Kingdom PLC 2000

3M United Kingdom PLC
3M House,
28 Great Jackson Street,
Manchester,
M15 4PA

Product Information :
Tel 0870 60 800 50
Fax 0870 60 700 99

3M Ireland
3M House, Adelphi Centre,
Upper Georges Street,
Dun Laoghaire, Co. Dublin, Ireland

Customer Service :
Tel (01) 280 3555
Fax (01) 280 3509

Appendix B – Self-healing experimental results

This appendix contains the force-CMOD and force-central displacement results for all six sets of experiments which make up the full self-healing experimental programme reported in Chapter 7. A summary of the specimen configurations for the different sets of experiments has been presented previously in Table 7.3, and is reproduced in Table B.1 for convenience.

It should be noted that the results of the second loading cycle, after full adhesive curing has taken place, are presented in two formats; with and without the permanent set from the first loading cycle included. This has been done for sets 2-6 inclusive, where unloading data is available for the first loading cycle (initial damage phase) of the experiment. The purpose of presenting the data in these two formats is to allow the mechanical response of the self-healed beams to be compared to both the corresponding control beam response, and the initial virgin response (first cycle loading) of the self-healing beam itself.

Table B.1. Summary of specimen configuration for the full testing programme

	Set 1. Notched, lightly reinforced	Set 2. Notched, lightly reinforced	Set 3. Notched, moderately reinforced	Set 4. Notched, heavily reinforced	Set 5. Unnotched, lightly reinforced	Set 6. Notched, lightly reinforced, varied loading rate
No. of Beams	2 Ctrl & 4 SH	2 Ctrl & 4 SH	2 Ctrl & 4 SH	2 Ctrl & 4 SH	2 Ctrl & 4 SH	1 Ctrl & 3 SH at each loading rate
Age at first test	28 days	28 days	28 days	70 days	28 days	70 days
Mix ratio by weight (water:OPC:sand)	0.55:1:3.5	0.6:1:3.5	0.6:1:3.5	0.6:1:3.5	0.6:1:3.5	0.6:1:3.5
Cube strength, f_{cu} (MPa)	-	27.9 (After 28 days)	24.1 (After 28 days)	35.7 (After 70 days)	24.2 (After 28 days)	33.0 (After 70 days)
Specific fracture energy, G_f (N/mm)	-	-	0.068 (After 28 days)	0.096 (After 70 days)	-	0.077 (After 70 days)
Cylinder splitting strength, f_{split} (MPa)	-	2.4 (After 28 days)	2.0 (After 28 days)	3.6 (After 70 days)	2.2 (After 28 days)	3.5 (After 70 days)
Reinforcement (see Table 7.2 for properties)	1No. 3.15mm ϕ high yield steel bar	1No. 3.15mm ϕ high yield steel bar	2No. 3.15mm ϕ high yield steel bar	1 No. 6.7mm ϕ high yield steel bar	1No. 3.15mm ϕ high yield steel bar	1No. 3.15mm ϕ high yield steel bar
Adhesive supply system	4No. 3mm ID capillary tubes, open at one end	4No. 3mm ID capillary tubes, open at both ends	4No. 3mm ID capillary tubes, open at both ends	4No. 3mm ID capillary tubes, open at both ends	4No. 3mm ID capillary tubes, open at both ends	4No. 3mm ID capillary tubes, open at both ends
5mm deep notch	Yes	Yes	Yes	Yes	No	Yes
Stroke loading rate (mm/s)	0.003	0.003	0.003	0.003	0.003	0.00075, 0.003 and 0.012

B.1 Set 1: Notched, lightly reinforced beams

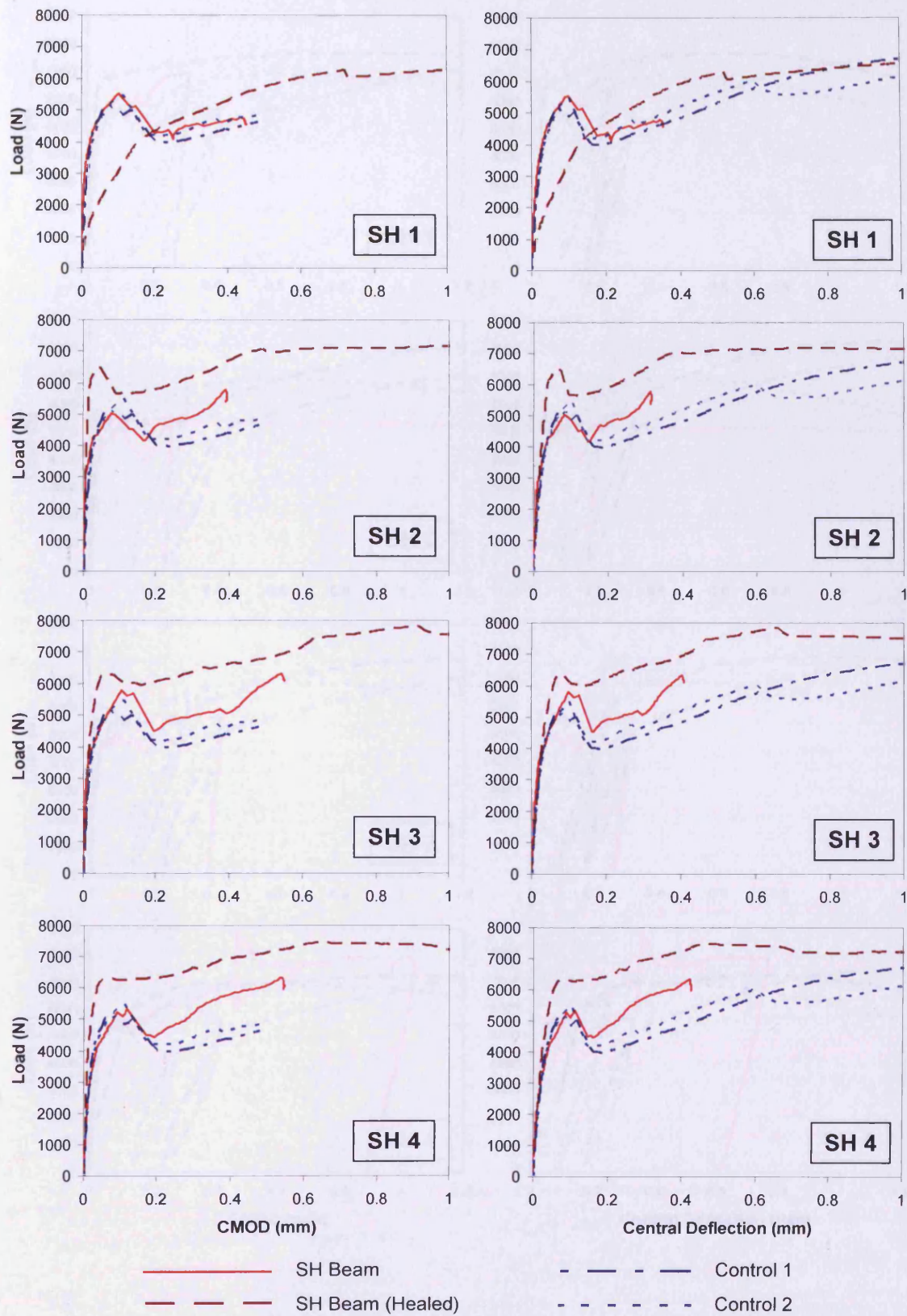


Figure B.1. Load-CMOD and load-central deflection for set 1

B.2 Set 2: Notched, lightly reinforced beams

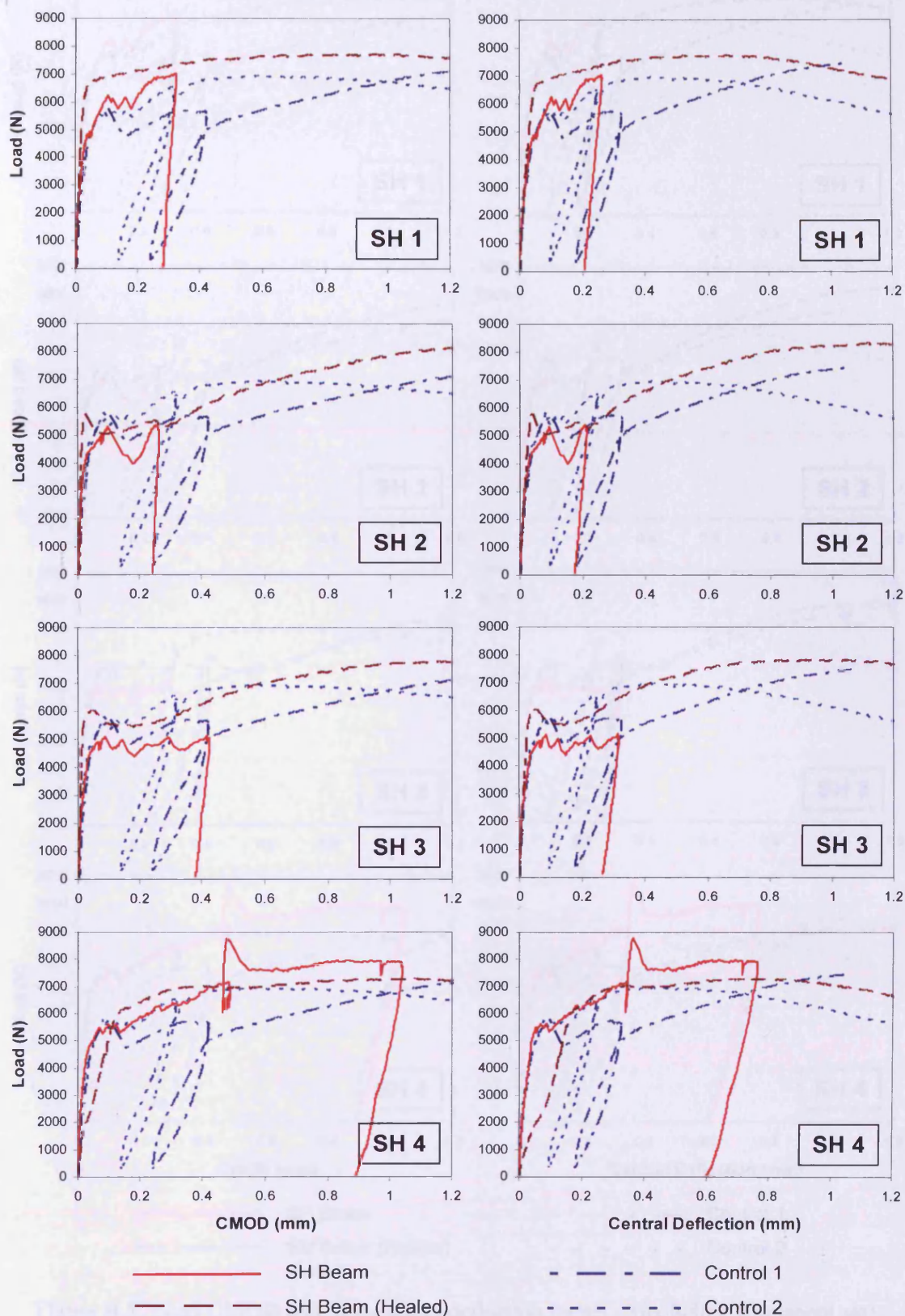


Figure B.2. Load-CMOD and load-central deflection for set 2

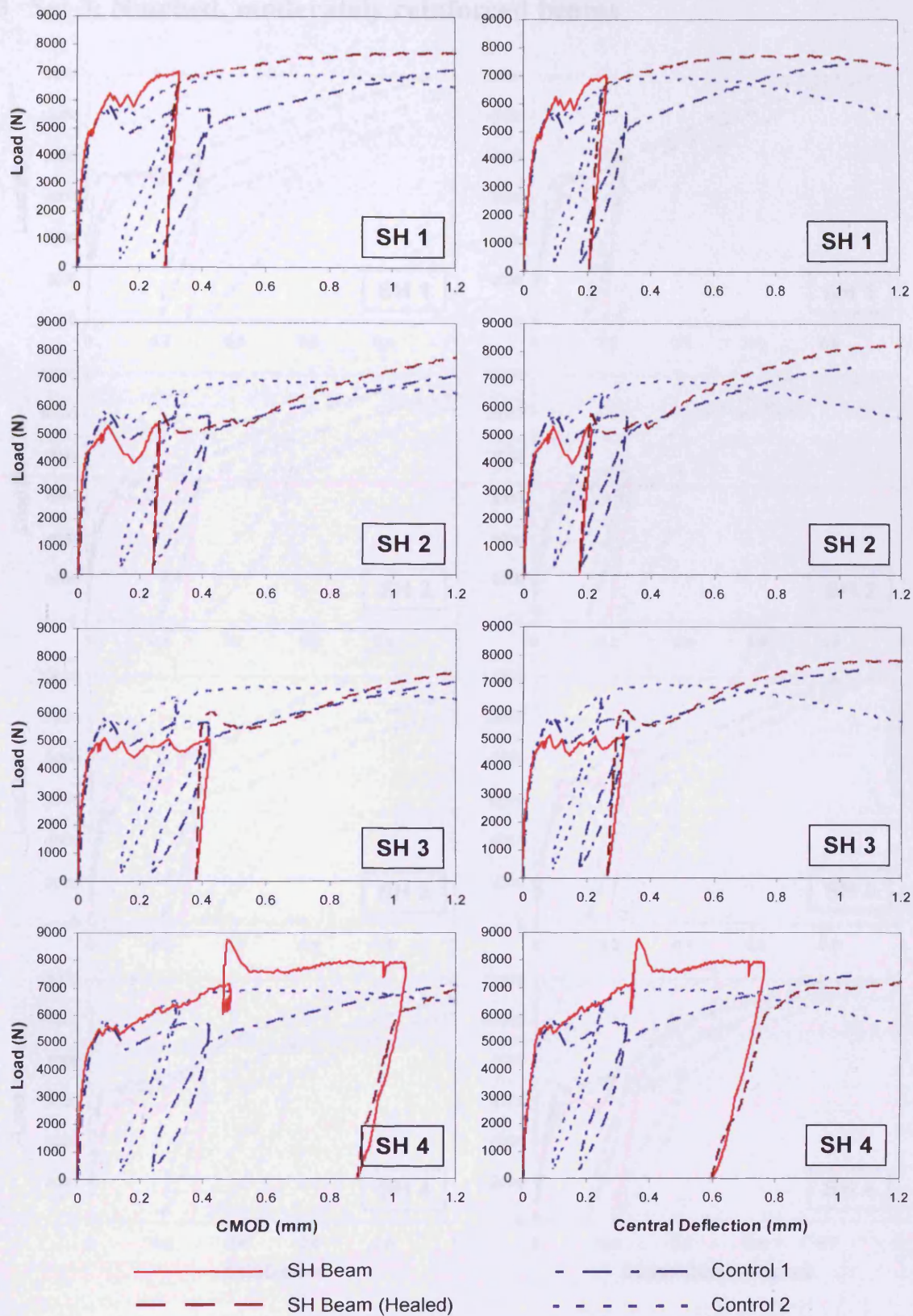


Figure B.3. Load-CMOD and load-central deflection for set 2 (including permanent set)

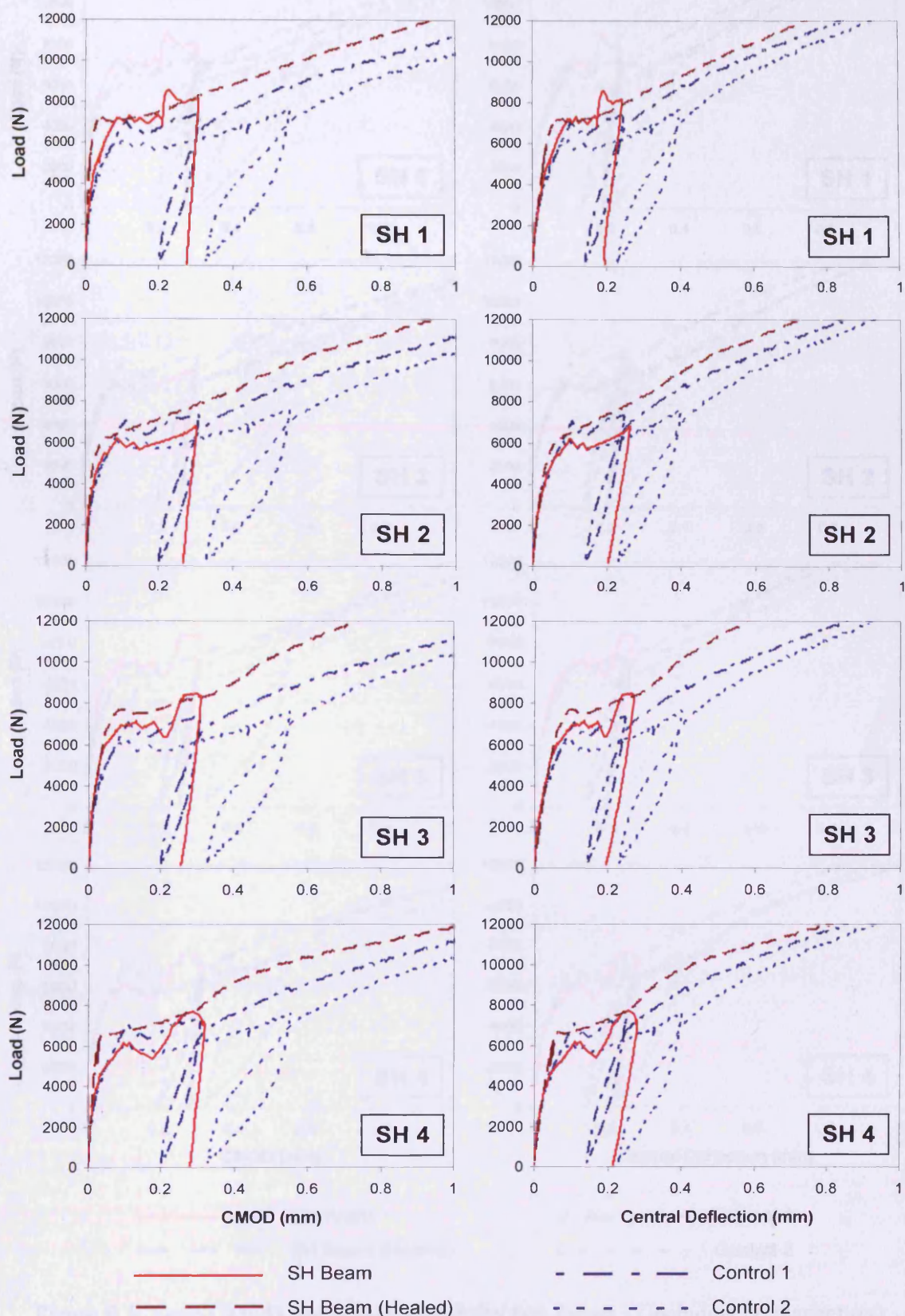
B.3 Set 3: Notched, moderately reinforced beams

Figure B.4. Load-CMOD and load-central deflection for set 3

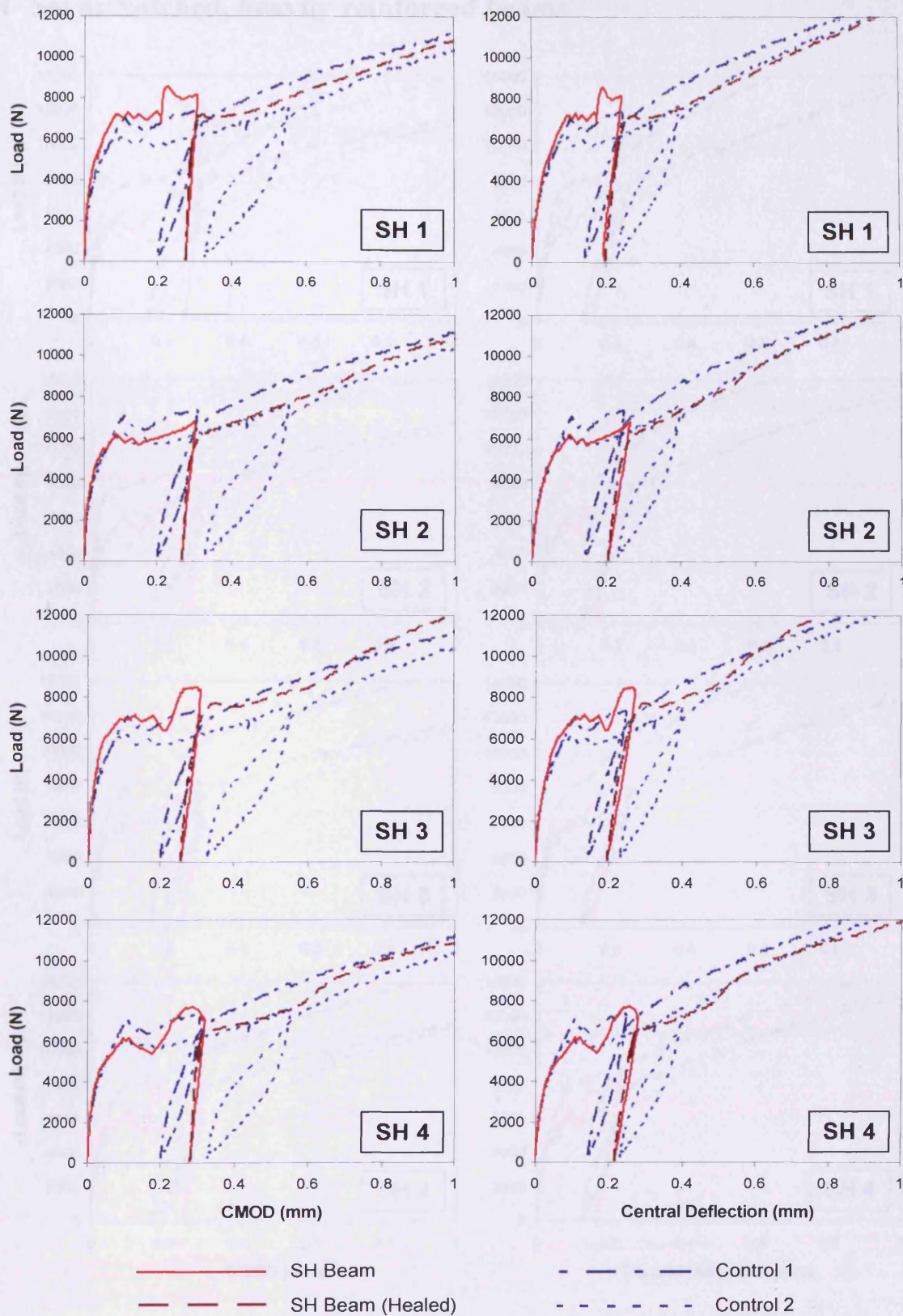


Figure B.5. Load-CMOD and load-central deflection for set 3 (including permanent set)

B.4 Set 4: Notched, heavily reinforced beams

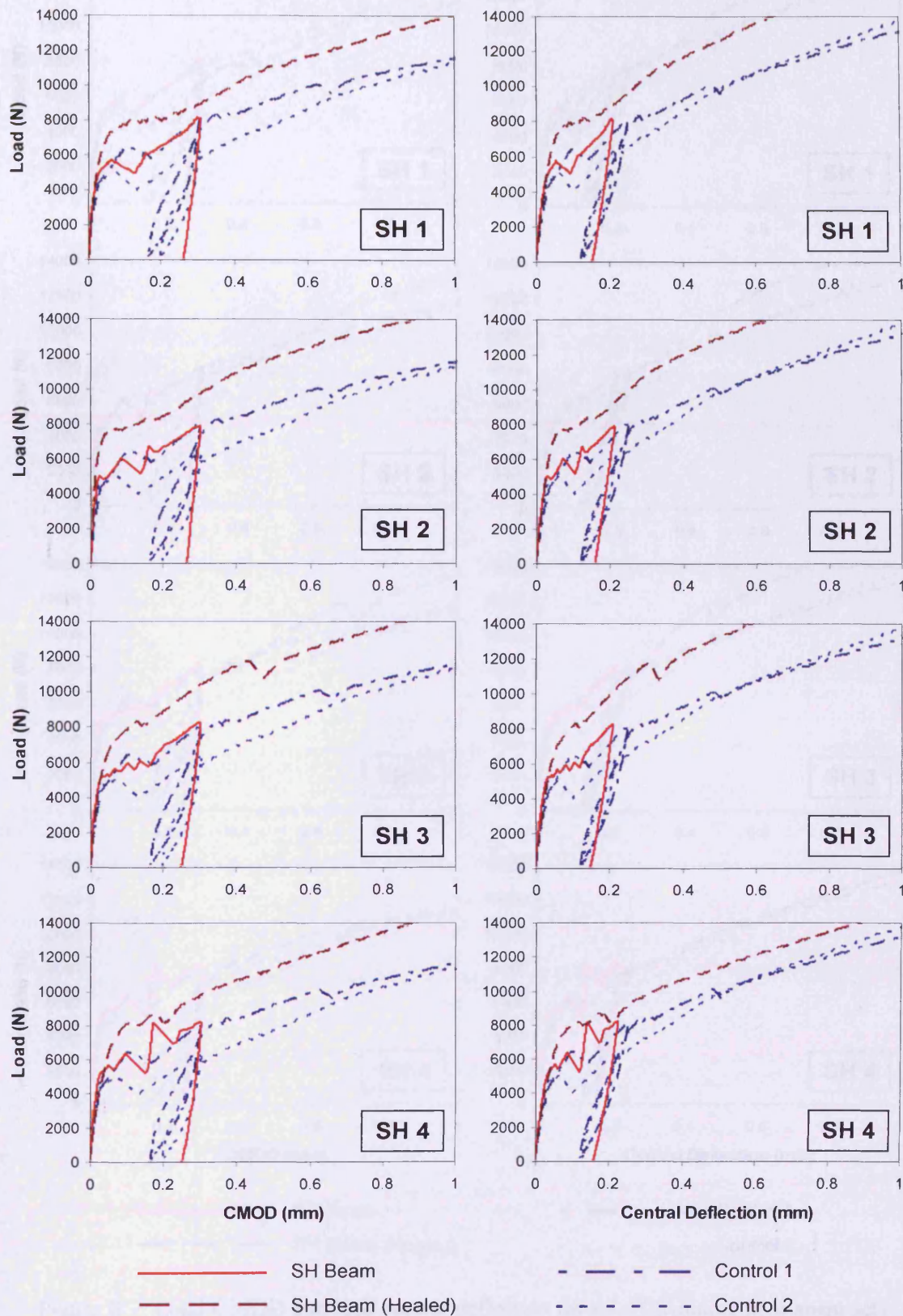


Figure B.6. Load-CMOD and load-central deflection for set 4

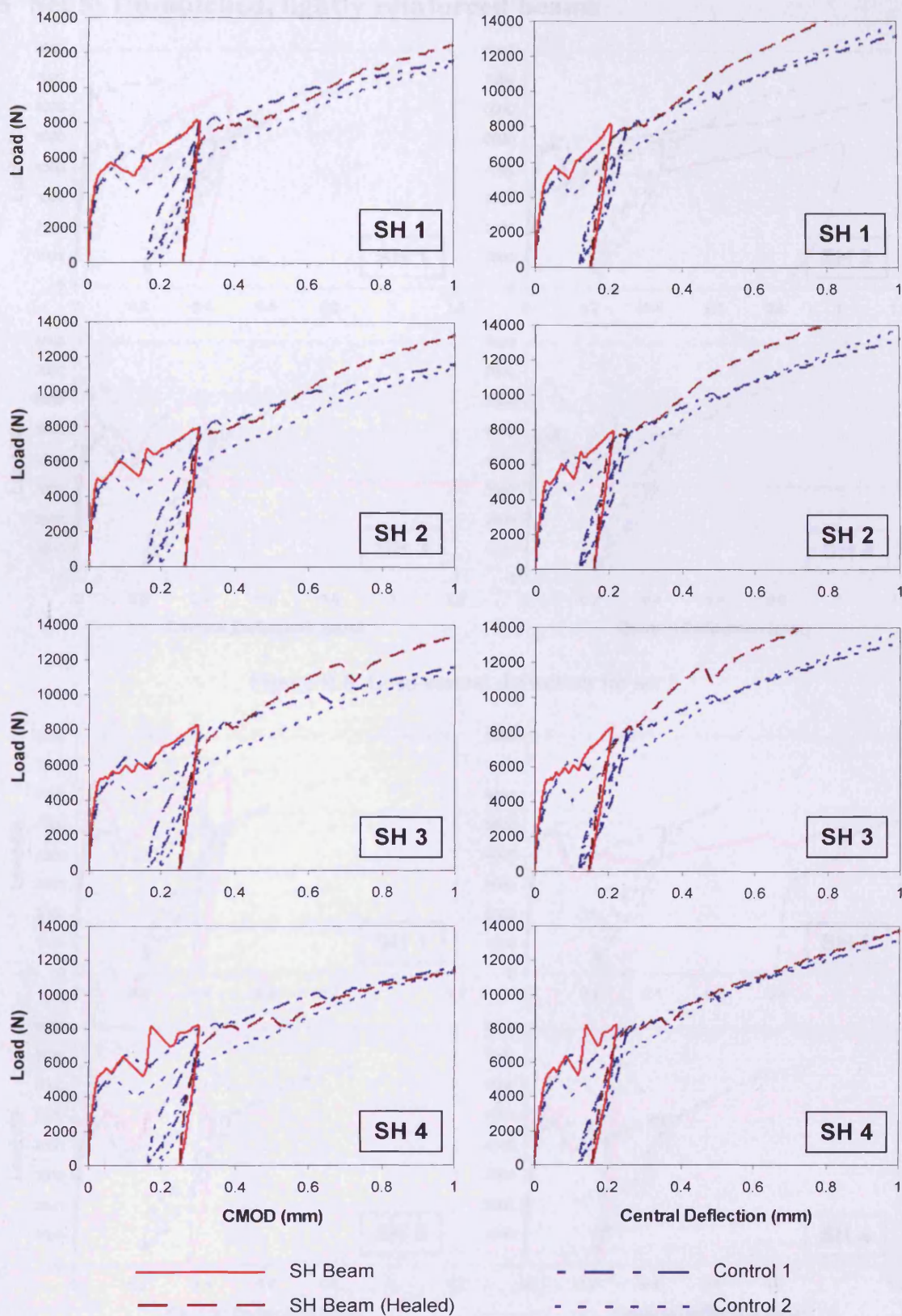


Figure B.7. Load-CMOD and load-central deflection for set 4 (including permanent set)

B.5 Set 5: Un-notched, lightly reinforced beams

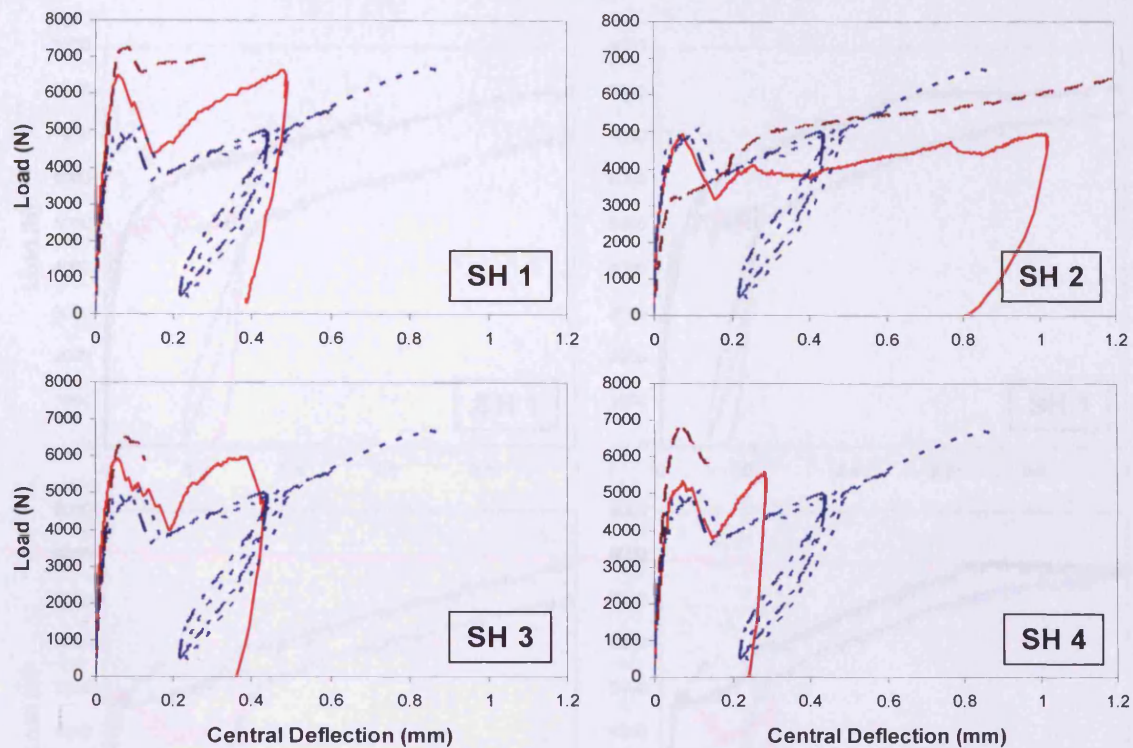


Figure B.8. Load-central deflection for set 5

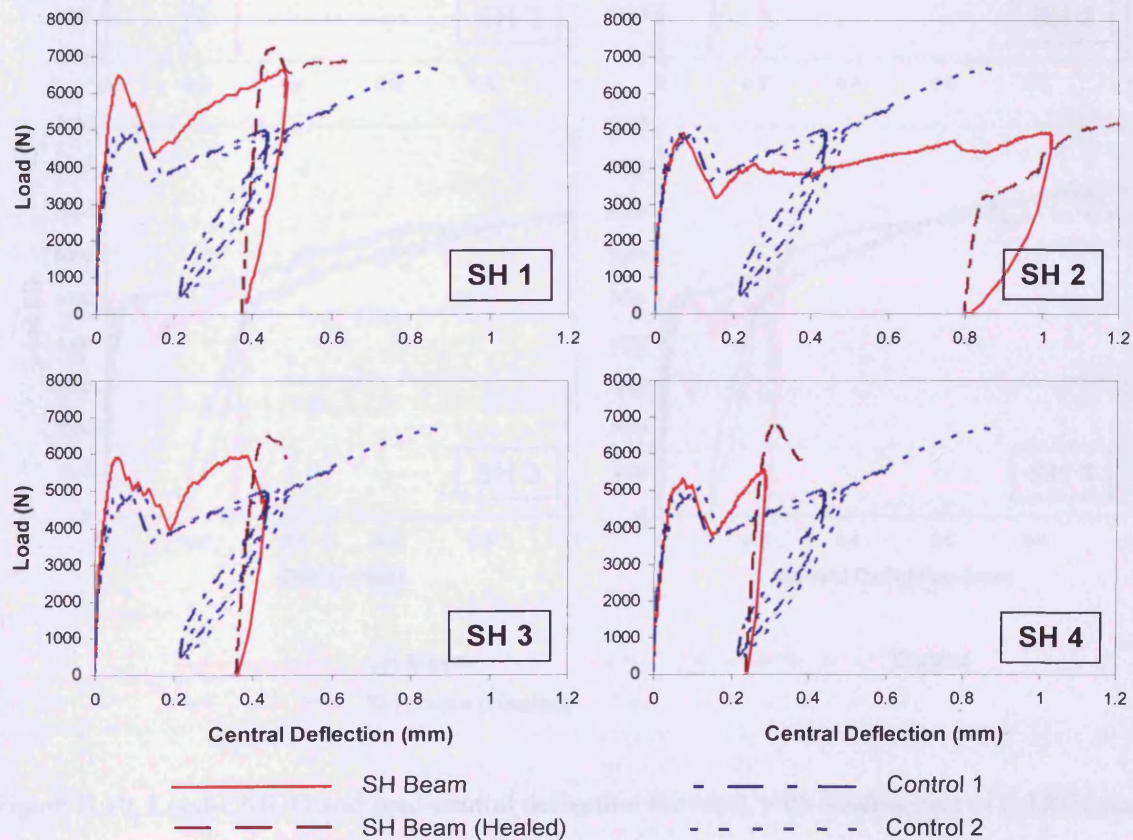
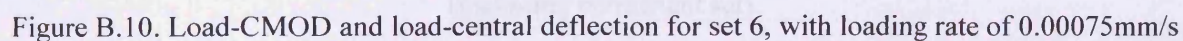


Figure B.9. Load-central deflection for set 5 (including permanent set)



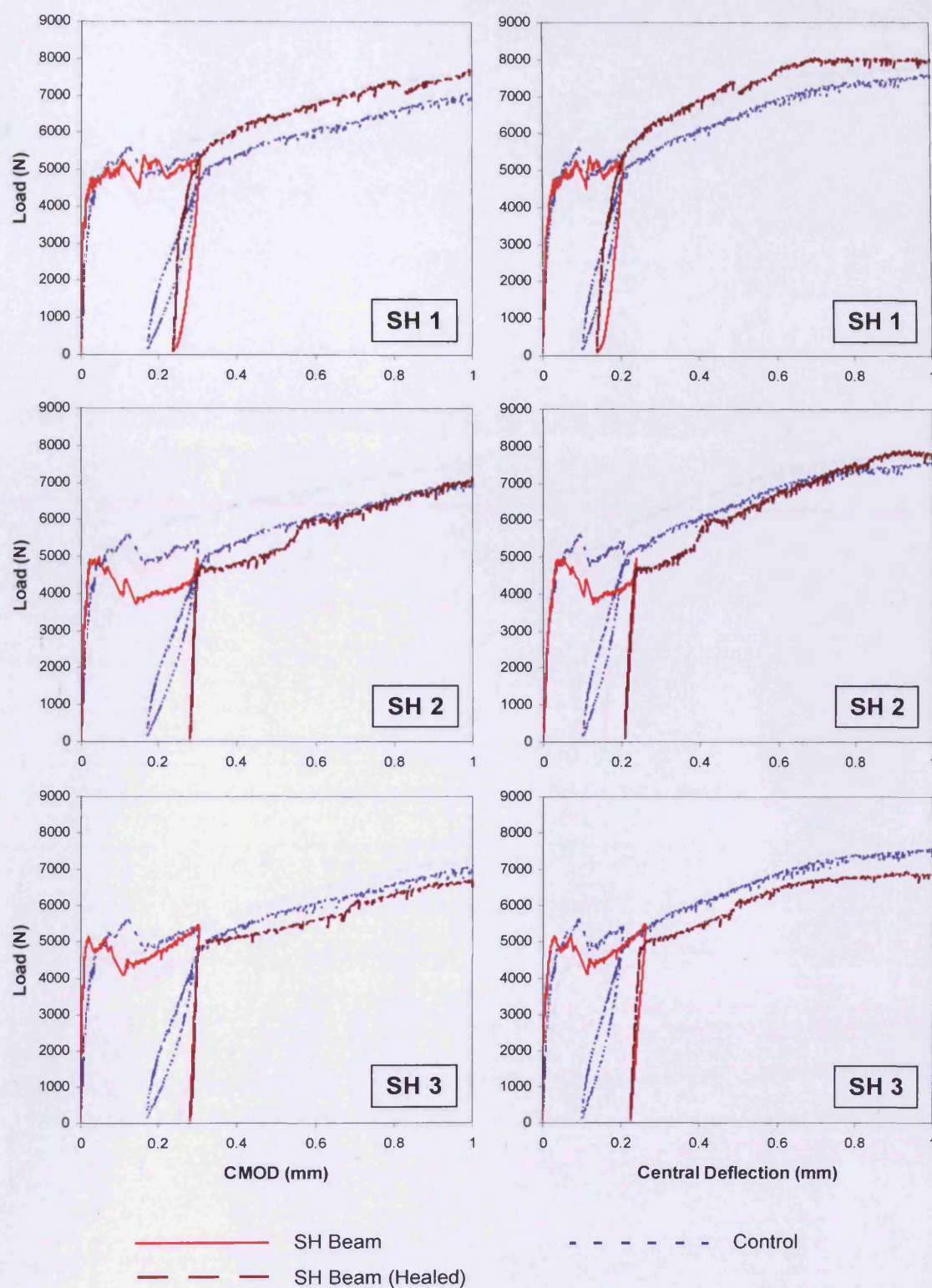


Figure B.11. Load-CMOD and load-central deflection for set 6, with loading rate of 0.00075mm/s (including permanent set)

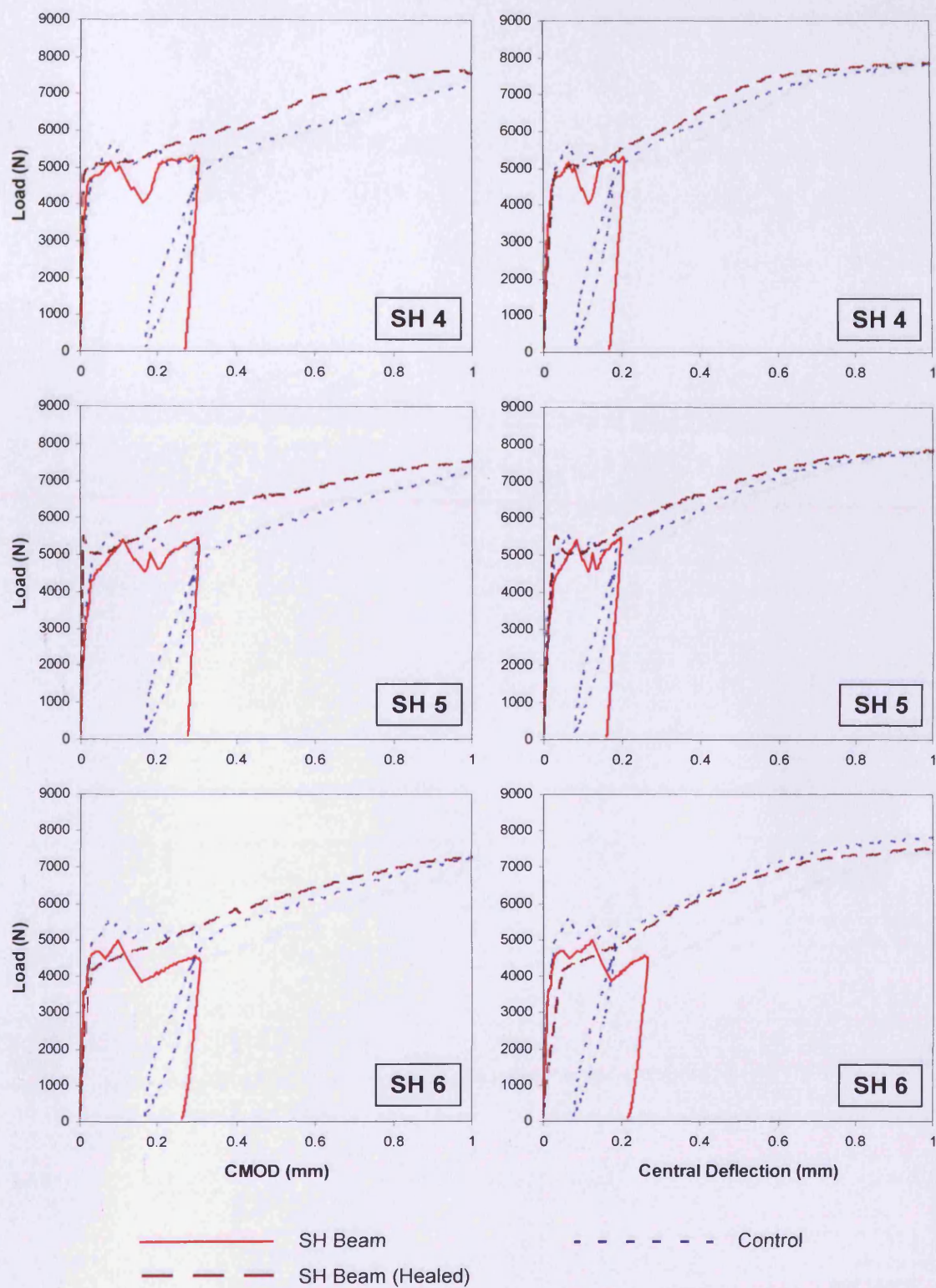


Figure B.12. Load-CMOD and load-central deflection for set 6, with loading rate of 0.003mm/s

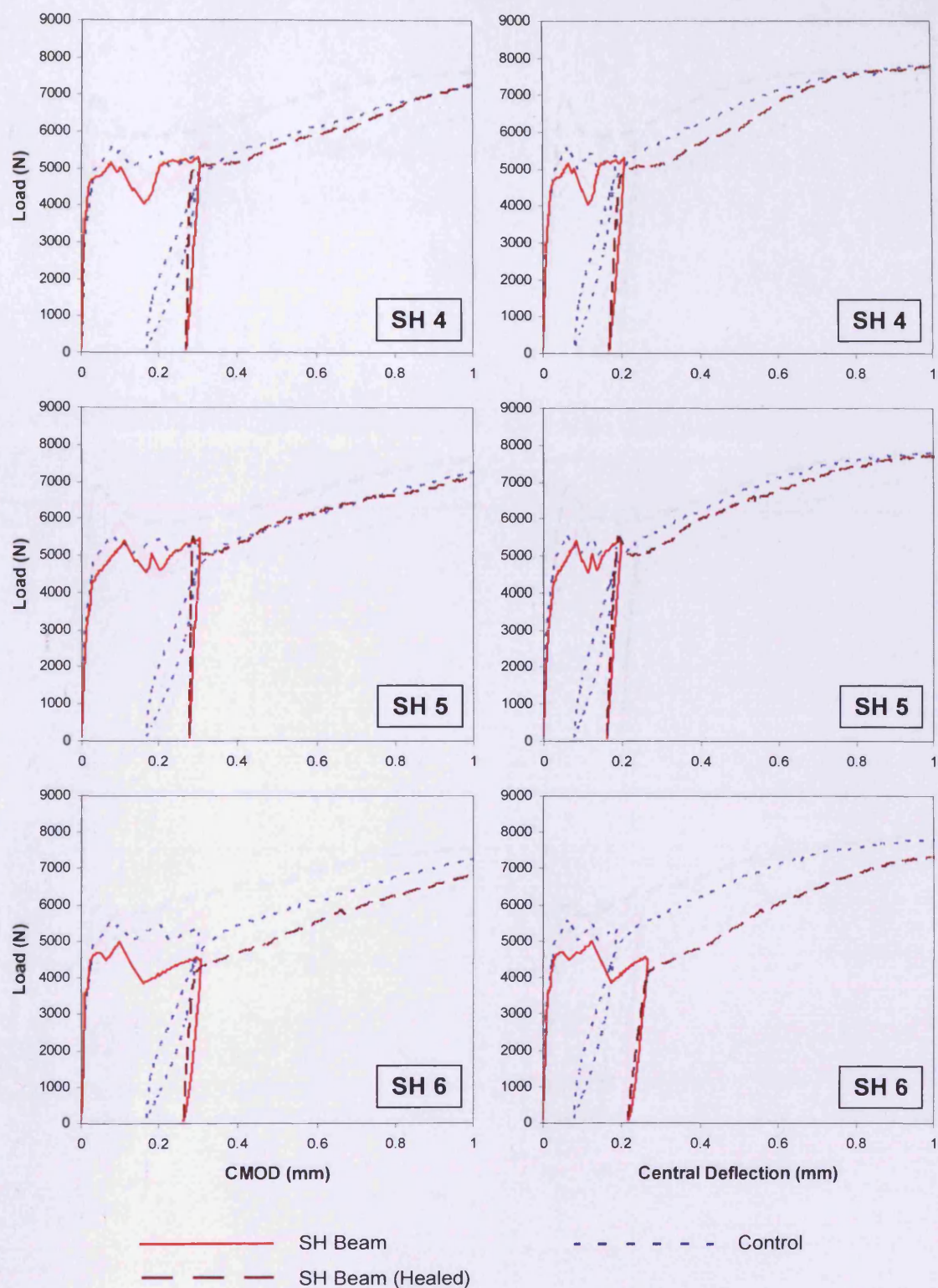


Figure B.13. Load-CMOD and load-central deflection for set 6, with loading rate of 0.003mm/s (including permanent set)

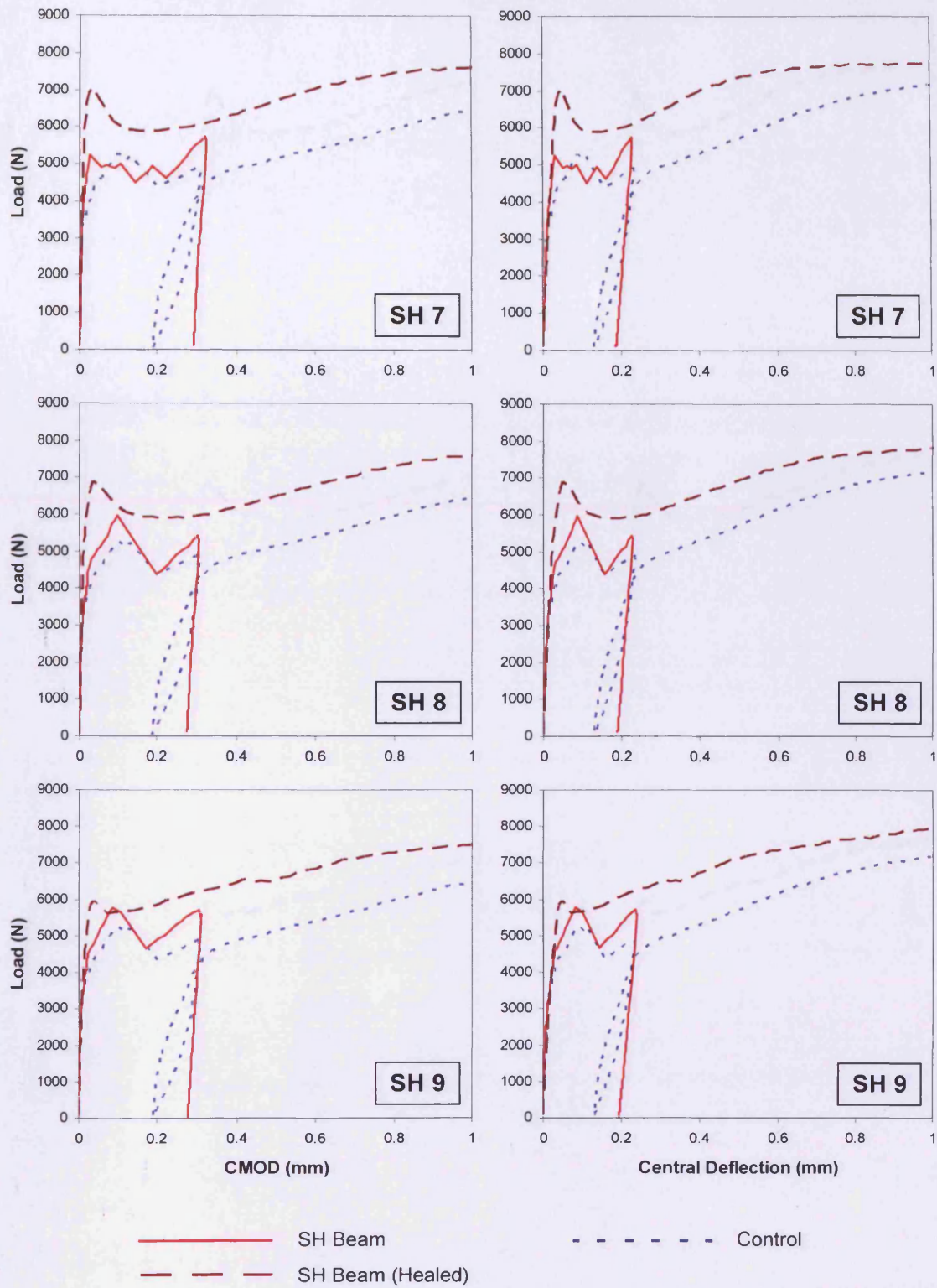


Figure B.14. Load-CMOD and load-central deflection for set 6, with loading rate of 0.012mm/s

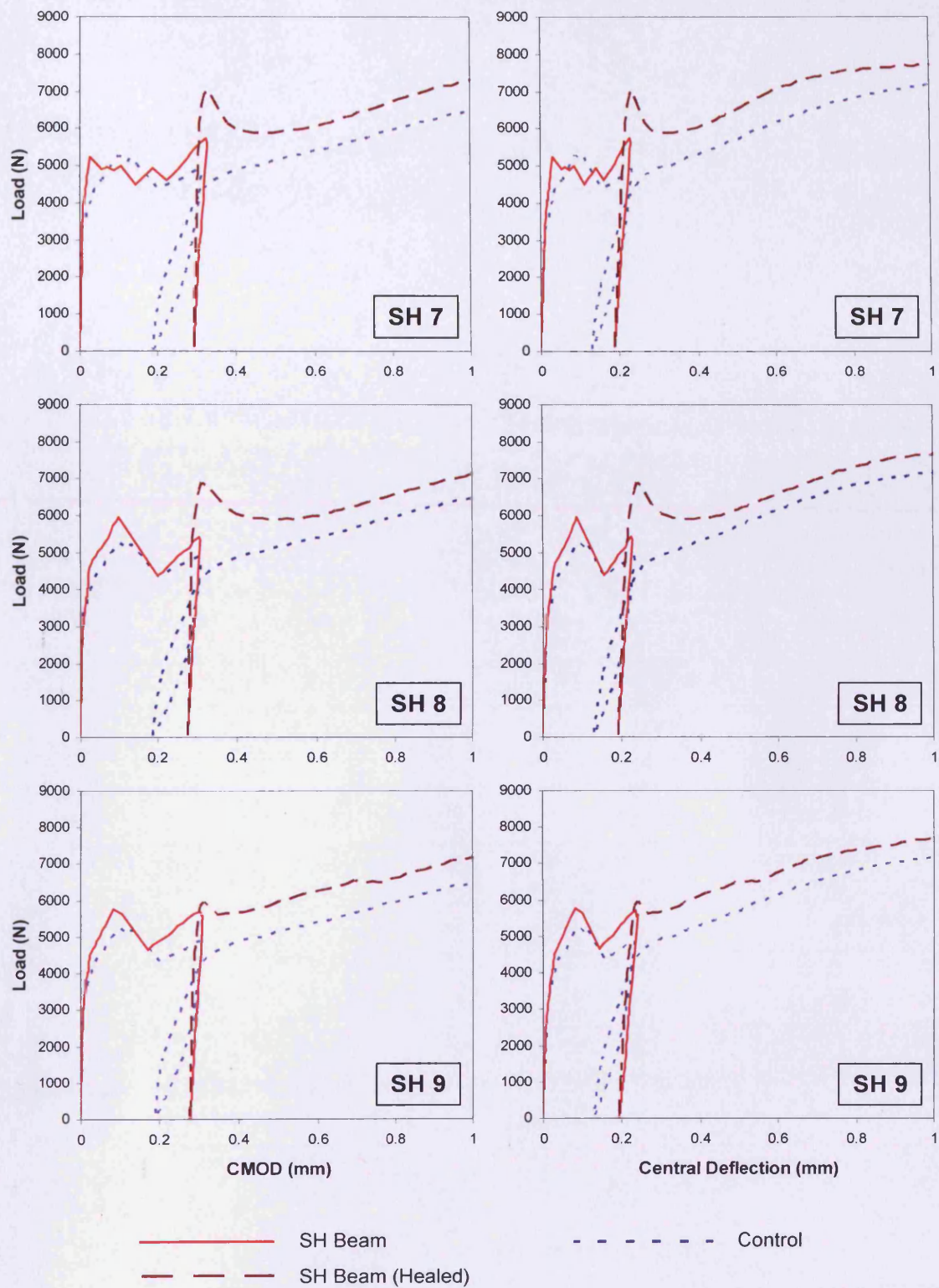


Figure B.15. Load-CMOD and load-central deflection for set 6, with loading rate of 0.012mm/s (including permanent set)